Fundamental Studies and Applications of Fluxional Carbon Cages

YUZHEN WEN

Durham University

Department of Chemistry

Fundamental Studies and Applications of Fluxional Carbon Cages

Yuzhen Wen

A Thesis Submitted for the Degree of Doctor of Philosophy

August 2024

Dedicated to my family

& everyone who has supported me when I was down

Table of Contents

CHAPTER 3: PREFERNTIAL CRYSTALLISATION OF RAPIDLY INTERCONVERTING DIASTEREOISOMERS

CHAPTER 4: MOLECULAR GLASS PROPERTIES OF FLUXIONAL CARBON CAGES

Abstract

Fluxional carbon cages, such as bullvalene and barbaralane, are molecules which possess ‘shapeshifting’ properties through the rapid and reversible Cope rearrangements inside their carbon skeletons. The existence of fluxional carbon cages has proven that a dynamic structural library can exist in a single rigid molecule and their isomerism distribution could be biased through covalent or noncovalent bonding. Over the last 60 years, the development of fluxional carbon cages has been mostly focused on fundamental studies such as synthesis and computational modelling. There have been several examples of their fluxional properties being utilised in chemical and physical application, while their potential to be biological systems and functional materials has been rarely discovered.

Based on the most advanced synthetic methods of bullvalenes and barbaralanes, we have explored both their fundamental properties and potential applications. The noncovalent control over the dynamic chirality of 9-substituted barbaralanes was achieved in both solid and solution states and proved by X-ray diffractions and NMR spectroscopy, which explored the potential of barbaralanes building the induced-fit model. Various barbaralane oligomers were prepared and their dynamic preferential crystallisations were observed and analysed for future predictions of their crystalline behaviours. Molecular glasses analogues of bullvalenes were synthesised and characterised, with their thermal properties were studied via differential scanning calorimetry and polarised microscopy, in which their spontaneous adjustment of crystallinity degree could lead them to be potential functional materials.

Declaration

The scientific work described in this Thesis was carried out in the Chemistry Department at Durham University between October 2020 and April 2024, as well as in the Chemistry Department at University of York between February 2023 and April 2024. Unless otherwise stated, it is the work of the author and has not been submitted in whole or in support of an application for another degree or qualification at this or any other University or institute of learning.

Signed:

Yuzhen Wen

Date: 01/08/2024

Conferences Attended and Presentations Given

1. Durham Chemistry PG Symposium, Durham University, UK, June 2022.

Poster presentation: *Noncovalent Control over Dynamic sp^3 Stereochemistry*

2. 7th International Conference on Molecular Sensors & Molecular Logic Gates (MSMLG 2022), Dublin, Ireland, July 2022

Poster presentation: *Noncovalent Control over Dynamic sp^3 Stereochemistry*

3. The Early Career Researcher Macrocyclic and Supramolecular Chemistry (ECR MASC), Loughborough University, UK, July 2022

Poster presentation: *Noncovalent Control over Dynamic sp^3 Stereochemistry*

4. 17th International Symposium on Macrocyclic and Supramolecular Chemistry (ISMSC 2023), Reykavík, Iceland, June 2023

Poster presentation: *Dynamic Preferential Crystallisation of Rapidly Interconverting Diastereoisomers*

5. Chemistry@York Research Conference, University of York, UK, July 2023

Oral presentation: *Dynamic Preferential Crystallisation of Rapidly Interconverting Diastereoisomers*

6. 5th ERC Grantees Conference, Edinburgh, UK, July 2023

Poster presentation: *Dynamic Preferential Crystallisation of Rapidly Interconverting Diastereoisomers*

7. RSC Macrocyclic and Supramolecular Chemistry Meeting (MASC) 2023, University of Birmingham, UK, December 2023

Poster presentation: *Dynamic Preferential Crystallisation of Rapidly Interconverting*

Diastereoisomers

8. Invited Talk, Xiamen University, China, January 2024

Oral presentation: *Fundamental Studies and Applications of Shapeshifting Molecules*

9. 18th International Symposium on Macrocyclic and Supramolecular Chemistry (ISMSC 2024), Hangzhou, China, May 2024

Poster presentation: *Noncovalent Control over Dynamic sp^3 Stereochemistry*

Awards, Grants and Scholarships

1. PhD Scholarship of China Scholarship Council (CSC), July 2020 | 3.5-year tuition fee waiver and living stipend for international students + £3000 research grant per year.

2. St Chad's College SCR Conference Grant, June 2022 | Individual award of £100 to present research at the 7th International Conference on Molecular Sensors & Molecular Logic Gates (MSMLG 2022).

3. St Chad's College SCR Academic Development Fund, June 2023 | Individual award of £100 to present research at the 17th International Symposium on Macrocyclic and Supramolecular Chemistry (ISMSC 2023).

4. Best Oral Presentation in the Chemistry@York Conference, July 2023 | 'Dynamic Preferential Crystallisation of Rapidly Interconverting Diastereoisomers', acknowledgement of the effective talk of research in the 'Molecular Materials' section.

Acknowledgements

Then we burned the bridges we've crossing over

Just to see the firelight

And the innocent are getting over being old tonight

—Take That, '*When We Were Young*'

Paul McGonigal. Thanks for the top-level academic guidance on a stupid PhD student, as well as the precious care on an international student who came to the UK alone. I have learned not only how to deal with everything with the highest standard, but also how to be independent and initiative. I have not yet, but will make you proud one day.

Durham University and Funding Agencies. I am grateful for the PhD funding offered by Durham University and China Scholarship Council, including the waiver of the expensive tuition fee, the living stipend for 3.5 years, and the abundant research grants.

CG235 and E214. It has been a unique experience working in two different unis and share the lab with different groups. It is always great to get useful suggestions and have multiple group activities. I have learned about not only the various culture of different countries, but also the diversity of human beings.

Alyssa Avestro. Thanks for the continuous inspirations and encouragements you brought to me when I lose faith on my career. I will miss all the bubble tea and Chinese food we had together!

Academic and Technical Staff. My PhD work is strongly supported by these names: thanks James Walton and Matt Kitching for being my co-supervisors, Juan Aguilar for the best NMR service in the world, Dimitry Yufit for the great XRD results, Iman Khazal for all the small things in the lab, etc.

Friends in Durham Chemistry. It is extremely lucky to have a great Chinese mafia in the small department which I could have lunch and hang out with. Special thanks to Haijing Wang and Shuyue Luan for all the hotpots and European travels.

Yulong Sun. Thanks for being a big brother (or uncle, whatever) and giving the precious advice on my career. I wish I could have as much knowledge and money as you.

Pokemon Fellas. Being a Pokemon VGC player is definitely my most unique experience, and meeting the best teammates in the world is even more valuable. I have had great memories with you guys: training on showdown, catching Mewtwo in Barcelona, karaoke in Liverpool, hiking in Edinburgh…I cannot enjoy the game and make progress so much without this team, and I wish I could attend the World Championship with you one day.

Shan Jiang and the Jiang group. Thanks for warmly inviting me for a lovely visiting. It is great to learn from totally different research and bring in my experience while working with a bunch of nice people playing Stardew Valley.

Andrew Sue. Thanks for having me in the research lab in December 2017 and directing my path in the field of supramolecular chemistry. I could always get useful suggestions from the perspective of both a mentor and a friend.

My family. I cannot be luckier to be born in a family which highly values education. You could have saved your average incomes but you choose to spend them on my educational fees over and over again. In such environment I have grown up to be a person with knowledge, but more importantly, a person who has dignity and always distinguish between right and wrong.

Abbreviations

Ac	Acetyl
AIBN	Azobisisobutyronitrile
ASAP	Atmospheric solids analysis probe
br	Broad
Bu	Butyl
CD	Cyclodextrin
COSY	Correlation spectroscopy
CTE	Coefficient of thermal expansion
d	Doublet
DCE	1,2-Dichloroethane
DFT	Density functional theory
DIPEA	*N*,*N*-Diisopropylethylamine
DMAP	4-(Dimethylamino)pyridine
DMF	Dimethylformamide
DMSO	Dimethyl sulphoxide
DSC	Differential scanning calorimetry
ESI	Electrospray ionisation
Et	Ethyl
HMBC	Heteronuclear multiple-bond correlation spectroscopy
HPLC	High-performance liquid chromatography
HR	High resolution
HSQC	Heteronuclear single-quantum correlation spectroscopy
IPr	1,3-Bis(2,6-diisopropylphenyl)imidazol-2-ylidene
LDA	Lithium Diisoproylamide
m	Multiplet
Me	Methyl
Mosher's Acid	α-Methoxy-α-trifluoromethylphenyl acetic acid
M.P.	Melting point
MS	Mass spectromet
NBS	*N*-bromosuccinimide
NMR	Nuclear magnetic resonance

NOESY	Nuclear overhauser effect spectroscopy
Ph	Phenyl
q	Quartet
rt	Room temperature
s	Singlet
ssNMR	Solid-state nuclear magnetic resonance
t	Triplet
TFA	Trifluoroacetic acid
THF	Tetrahydrofuran
TLC	Thin-layer chromatography
UV	Ultraviolet
VT	Variable-temperature
VT NMR	Variable-temperature nuclear magnetic resonance
XRD	X-ray diffraction

Note: conventional abbreviations for units, physical quantities and stereochemical terms are not included here.

General Experimental Methods

Materials: All reagents were purchased from commercial suppliers (Sigma-Aldrich, Fluorochem, Alfa Aesar or Tokyo Chemical Industry) and used without further purification.

Instrumentation and Analytical Techniques: Analytical thin-layer chromatography (TLC) was performed on neutral aluminium sheet silica gel plates (Fluka, 60778-25EA) and visualised under UV irradiation (254 nm). Nuclear magnetic resonance (NMR) spectra were recorded using a Bruker Advance (III)-400 (^{1}H 400.130 MHz and ^{13}C 100.613 MHz), Varian Inova-500 (^{1}H 500.130 MHz and ^{13}C 125.758 MHz), Varian VNMRS-600 (^{1}H 600.130 MHz and ^{13}C 150.903 MHz) or a Varian VNMRS-700 (^{1}H 700.130 MHz and ^{13}C 176.048 MHz) spectrometer, at a constant temperature of 298 K unless otherwise stated. For variable-temperature (VT) measurements, operating temperatures were calibrated using an internal calibration solution of MeOH and glycerol. Chemical shifts (δ) are reported in parts per million (ppm) relative to the signals corresponding to residual non-deuterated solvents [$CDCl_3$: δ = 7.26 or 77.16, D_2O δ = 4.79]. Coupling constants (*J*) are reported in Hertz (Hz). 13C NMR Experiments were proton-decoupled, whereas ^{19}F NMR experiments are coupled and referenced to an internal standard, hexafluorobenzene (HFB, δ = 164.99 ppm), unless otherwise stated. Assignments of ^{1}H and ^{13}C NMR signals were accomplished by two-dimensional NMR spectroscopy (COSY, NOESY, HSQC, HMBC). NMR spectra were processed using MestReNova version 14.0. Data are reported as follows: chemical shift; multiplicity; coupling constants; integral and assignment. Low-resolution atmospheric solids analysis probe (ASAP)-MS were performed using a Waters Xevo QTOF equipped with an ASAP. High-resolution electrospray (HR-ESI) and ASAP (HR-ASAP) mass spectra were measured using a Waters LCT Premier XE high resolution, accurate mass UPLC ES MS (also with ASAP ion source). Melting points (M.P.) were recorded using a Gallenkamp (Sanyo) apparatus and are uncorrected.

Thesis Layout

Chapter 1 introduces basic studies of fluxional carbon cages, detailing their special properties, development of synthetic pathways and methods of analysing and accessing them. It also explores the applications of fluxional carbon cages, particularly bullvalene, highlighting how to utilise their shapeshifting abilities either occurs spontaneously, or in response to different environments. Chapter 2 demonstrates the control of dynamic sp^3 stereochemistry of barbaralanes via noncovalent interactions in both solid and solution state. Chapter 3 discusses the synthesis of barbarlane oligomers which exhibit diastereoisomerism and observations of their crystalline behaviour. Chapter 4 discusses the synthesis of di-substituted bullvalenes and investigations on their molecular glass properties. Chapters 2－4 have been formulated in a style suitable for publication at a later date, including a focussed discussion of the key data followed by a more comprehensive account of the data in Experimental Sections and Appendices.

CHAPTER 1 | INTRODUCTION OF SHAPESHIFTING MOLECULES

Synopsis

This introductory chapter centres on the fundamental concept of fluxional carbon cages. It explains how their 'shapeshifting' properties emerge and discusses how minor structural changes in the core of the fluxional carbon cage can lead to the formation of varying numbers of degenerate and nondegenerate isomers. Early investigations on the synthesis of bullvalenes and barbaralanes are summarised, followed by the development of more advanced and effective syntheses, and systematic studies of their dynamic behaviours using the combination of NMR spectroscopy and computational modelling which help to distinguish their isomerism distributions. Applications of fluxional carbon cages mainly focus on utilising their dynamic ability to form certain shapes or adjust complicated systems, including analytes, piezoelectric materials and antibiotics.

1.1 Fluxional Carbon Cages and Cope Rearrangement

The Cope rearrangement, first reported by Arthur C. Cope,[1] is a [3,3]-sigmatropic rearrangement reaction involving 1,5-dienes. In this process, a σ-bonded atom or group flanked by one or more π-electron systems moves to a new location while the C-C bonds redistribute. Although the process is a pericyclic reaction, it can be assumed that the reaction undergoes a transition state with the same energy and structure as the diradical even though the diradical is not usually a true intermediate. In terms of stereochemistry, the reaction appears to pass through a chair-like transition state (Scheme 1.1).

Scheme 1.1. The mechanism of Cope rearrangement.

The term "fluxional carbon cages" refers to a series of chemical compounds such as bullvalene[2] (**1**), the barbaralyl cation[3] (**2**), barbaralane[4] (**3**) and semi-bullvalene[5] (**4**). (Figure 1.1a) These fluxional carbon cages all have dynamic structures due to the rapid Cope rearrangements occurring within the molecules, which change the relative positions of atoms or functional groups, resulting in thousands of degenerate isomers without breaking the carbon skeleton. Amongst the fluxional family, barbaralane **3** and semibullvalene **4** are relatively simple, as they can only convert between two isomers because the olefin only exists on the two arms of the carbon cage, and when the π bond rearranges, each methine group maintains a substantially unchanged position (Figure 1.1b). In contrast, bullvalene **1** has an additional olefin, which opens the third arm of the carbon cage for sigmatropic rearrangement, allowing each carbon to change its relative position with other carbons through a series of sequential sigmatropic rearrangements, resulting in more than 1 million possible degenerate isomers (Figure 1.1c).

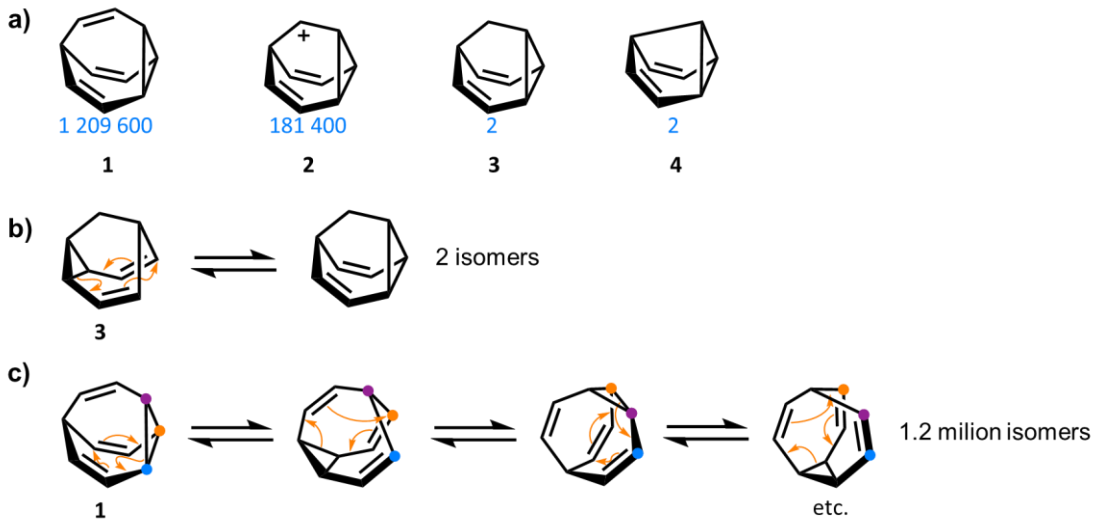

Figure 1.1. (a) The structures of bullvalene **1**, the barbaralyl cation **2**, barbaralane **3** and semi-bullvalene **4** with the number of their degenerate isomers; (b) The Cope rearrangement of barbaralane **3**; (c) The Cope rearrangement of bullvalene **1**.

The structure of fluxional carbon cages, although seemingly complicated, could be simplified to a cage with 'three faces', i.e. bullvalene could be deconstructed into a ten-carbon cage composed of three alkene bridges connected by an sp^3 carbon, with a cyclopropane ring on each side. Each 'face' of the cage is identical, providing the molecule with a three-fold axis of symmetry. (Figure 1.2)

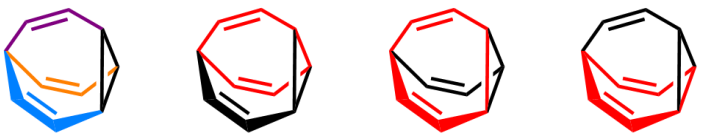

Figure 1.2. Illustrations of three alkene bridges of bullvalene and the three-fold axis of symmetry.

In unfunctionalised fluxional carbon cages, valence isomers are degenerate, meaning they have equivalent constitutions. However, when one or more hydrogen atoms of these molecules are substituted with another group, the degeneracy is broken, imparting shapeshifting properties to the molecules (Figure 1.3a). In the case of 9-substituted barbaralanes, the two degenerate isomers happen to be a pair of stereoisomers and endows the molecule with sp^3 dynamic chirality, which refers to a situation where the barbaralane can rapidly interconvert between two

enantiomers and does not exhibit fixed chirality over time (Figure 1.3b). In the case of di-substituted bullvalenes, the rearrangements change the relative positions of substituents, leading to an oscillation between rod-like and twisted shapes (Figure 1.3c).

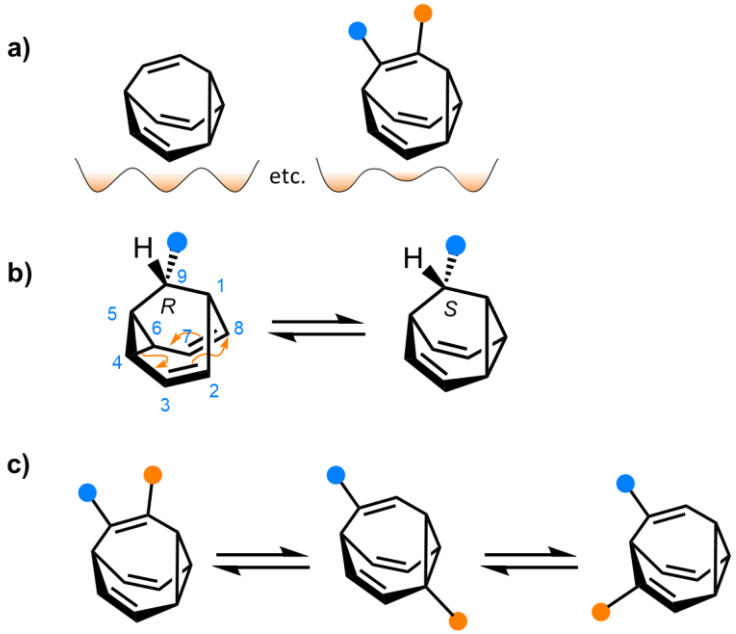

Figure 3. a) An unfunctionalised degenerate bullvalene vs functionalised nondegenerate bullvalene; b) The dynamic chirality of 9-substituted barbaralanes; c) Different shapes of di-substituted bullvalenes due to the Cope rearrangements.

1.2 Bullvalene

The structure of bullvalene was first predicted by Doering and Roth in 1963, elucidated by the sharp singlet in its ^{1}H-NMR spectrum, they believed that "all ten carbon atoms must inevitably wander over the surface of a sphere in ever-changing relationship to each other". [1a] In the same year, Schröder produced bullvalene by photolysis of a dimer of cyclooctatetraene **5**, with benzene as the sole by-product.[1b] (Scheme 1.2)

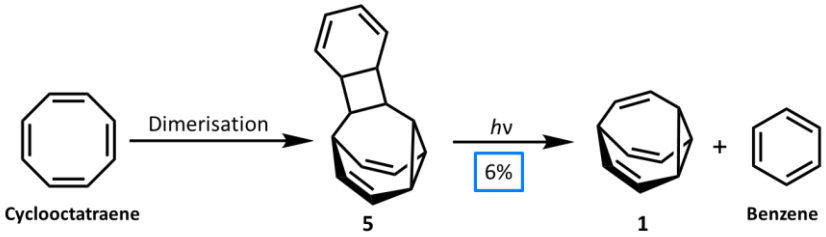

Scheme 1.2. The first synthesis of bullvalene (**1**) reported by Schröder.

During the 1960s and 1970s, various synthetic routes towards mono- and di-substituted bullvalenes were reported by Doering, Scott, Serrotosa and Schröder.[6] For example, Doering's route starts with the treatment of barbaralone **6** with diazomethane in a one-carbon homologation to give bullvalone **8** and its isomeric aldehyde **7**. Reduction of **8** with sodium borohydride gives alcohol **9** which was then acetylated with acetic anhydride at 130 °C. The final step is pyrolysis at 345 °C to get the desired bullvalene **1**. Serrotosa then developed a similar route which also goes through the formation of bullvalone and its isomeric aldehyde, then the bullvalone **8** was treated with p-toluenesulphonyl hydrazine in acetic acid to give tosylhydrazone **11**. Anionic fragmentation with methyllithium in benzene at 0 °C and then UV irradiation of bicyclo[4.2.2]deca-2,4,7,9-tetraene **12** leads to bullvalene **1** in 82% yield of the final step (Scheme 1.3).

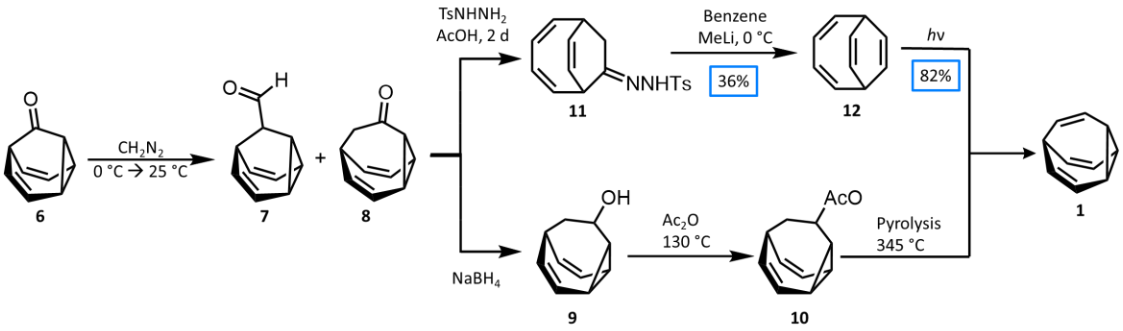

Scheme 1.3. Synthetic pathways towards bullvalane (**1**) produced by Doering and Serratosa.

The synthetic pathways towards tri- and tetra-substituted functionalised bullvalenes have been investigated since the 1990s.[7] A concise method accessing tetra-substituted bullvalenes was developed in 2006 by Bode and co-workers[7c]. It has been used in obtaining more elaborately-substituted bullvalenes, and investigations of their rearrangement and equilibrium properties. Bode's route starts with the Mukaiyama–Michael addition of cycloheptadienone **13** to give the enone **14**, followed by radical bromination, oxidation with *N*-methylmorpholine-*N*-oxide, deprotection with trifluoroacetic acid and dichloromethane, then intramolecular cyclopropanation catalyzed by a Lewis acid to give triketone **18**. From here, two of the carbonyl groups of the triketone were selectively added with allylmagnesium bromide to produce a 3:2 mixture of *meso*- and *D, L*-compound **19**, which could both be transformed into tetra-

substituted bullvalene **20** by the treatment of thionyl chloride and pyridine. (Scheme 1.4)

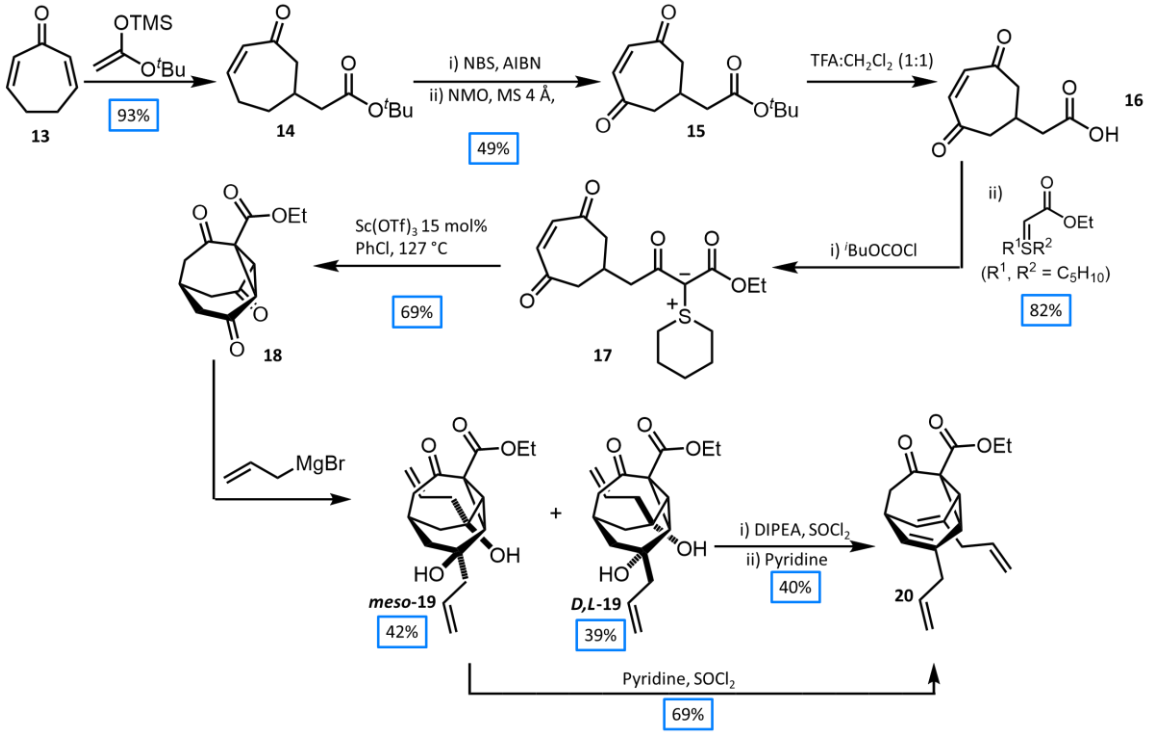

Scheme 1.4. Synthesis of the tetra-substituted functionalised bullvalene **20** reported by Bode and co-workers

In the 2010s, metal-catalyzed cyclization was used to access bullvalene derivatives. Au(I)-catalyzed and Co(I)-catalyzed reactions to prepare bullvalene precursors have been respectively reported by Echavarren[8] and Fallon[9]. In Echavarren's route, gold(I)-catalyzed oxidative cyclization of 7-(substituted ethynyl)-1,3,5-cycloheptatrienes yields barbaralone **22**, which undergoes a homologation reaction with the lithium anion of (trimethylsilyl)diazomethane to give bullvalone **24**, and then reduction with nBu_3SnH and $Pd(PPh_3)_4$ to afford unsubstituted bullvalene **1**, or via lithium diisopropylamide and bis(trifluoromethanesulfonyl)aniline (Comins' reagent) to give mono- and di-substituted bullvalenes **25**. (Scheme 1.5)

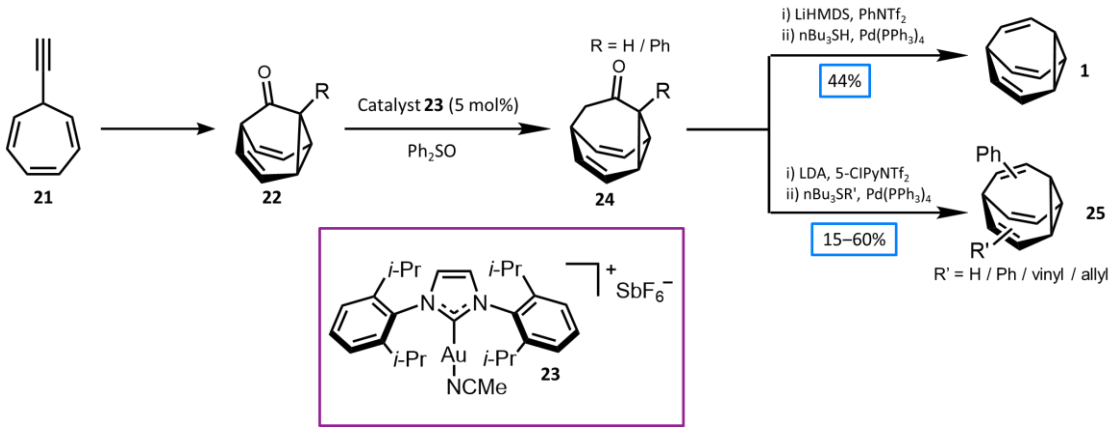

Scheme 1.5. The synthetic route towards bullvalenes reported by Echavarren.

In Fallon's route, in the presence of CoI_2(dppe)/ZnI_2/Zn catalyst, the cyclooctatetraene **26** undergoes a [6 + 2] cycloaddition with alkynes **27** to produce the bicyclo[4.2.2]deca-2,4,7,9-tetraene (BDT) intermediate **28**, which undergoes a di-π-methane photoisomerisation under UV irradiation to give the bullvalene derivatives **29** in yields between 40—81%. (Scheme 1.6) This is by far the most efficient synthesis of bullvalene derivatives.

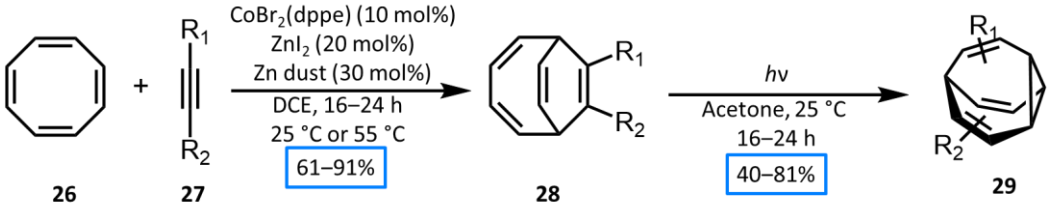

Scheme 1.6. The most concise synthetic route of bullvalenes reported by Fallon.

Fallon's initial synthetic route towards bullvalenes only applies for limited types of substituents, i.e. for aromatic substituted BDT **30**, it would process the di-π-methane rearrangement to form lumibullvalene **31**. (Scheme 1.7a) To expand the pool of products, Fallon then reported the synthesis of boronate ester-substituted bullvalenes **33** using boronate ester-substituted alkynes **32**, which could then be modified with various substitutents. The synthesis of di- and tri-substituted bullvalenes **35** through the [6 + 2] cycloaddition of trimethylsilyl-substituted cyclooctatetraenes **34** was also discovered, including the first synthesis of heterogeneously trisubstituted bullvalenes.[10] (Scheme 1.7b)

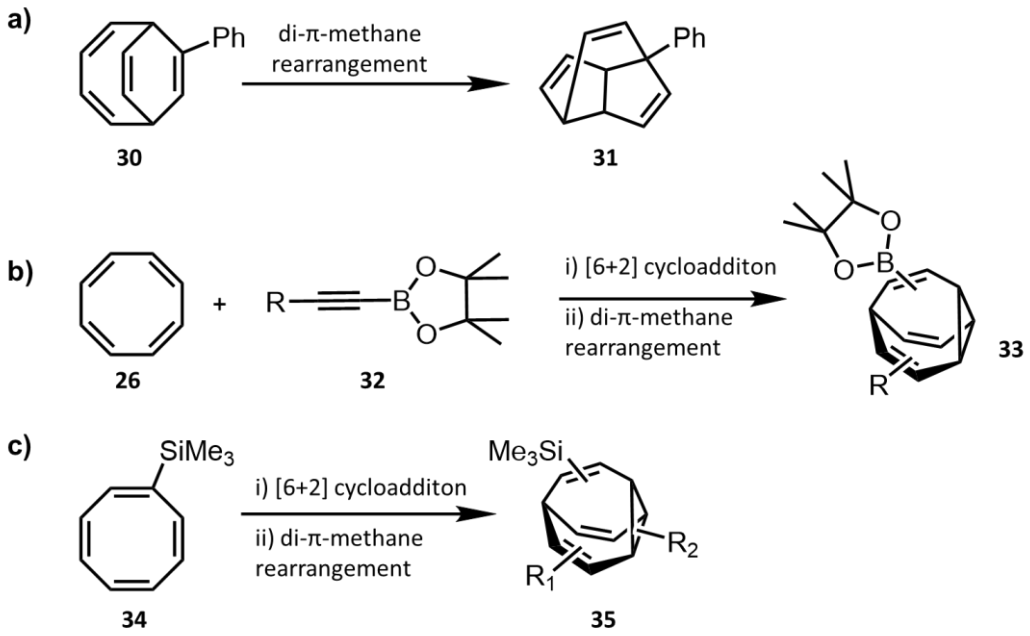

Scheme 1.7. a) The formation of lumibullvalene **31** from phenyl BDT **30**; b) Synthesis of boronate ester bullvalenes **33**; c) Synthetic route of di- and trisubstituted bullvalenes.

To study the structure library of bullvalenes and their substitution patterns, several systems of labelling the atoms and positions of bullvalene have been created[11]. An isomer coding system was reported by Bode,[11ab] in which every possible isomer is given a ten-digit code referring to the position of the carbon atom and the number represents the type of substituent (Figure 1.4a). In *silico* modelling, especially DFT calculations have been particularly useful in rationalising the behaviour of shape-shifting mixtures due to its ability to optimize molecular geometries, calculate relative energies and predict equilibrium populations. The correlated and conformational isomerism of bullvalene was studied by McGonigal,[11c] in which a more simplified way of labelling the positions of substituents were used: the positions on each alkene bridge are marked in order from α (the sp^3 carbon connecting the three alkene bridges) to δ (cyclopropane ring), and this simplified label system will be applied on the description of substituted bullvalenes throughout the thesis (Figure 1.4b).

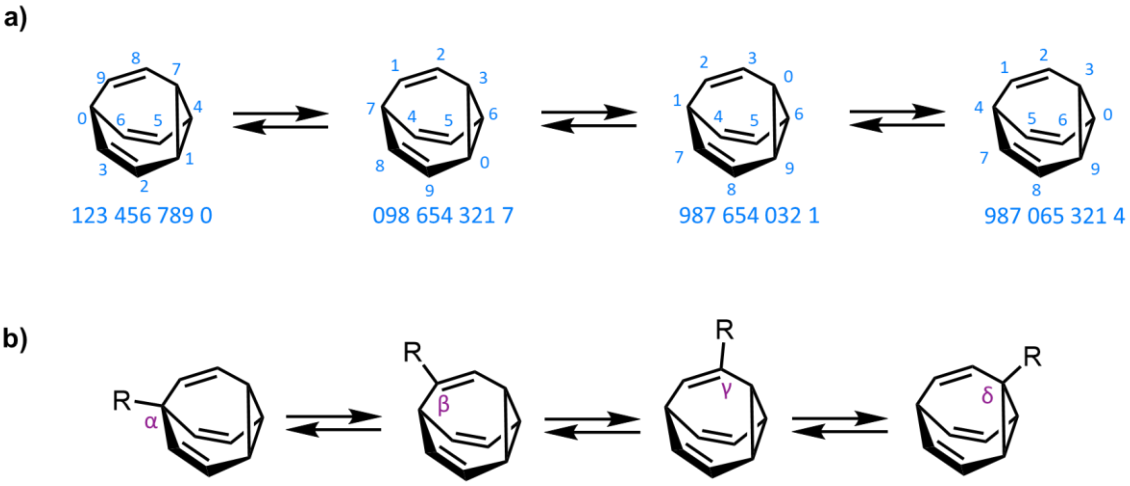

Figure 1.4. (a) Bode's coding system for the mono-substituted bullvalene isomer network analysis. (b) The labelling of substituent positions on bullvalene.

1.3 Barbaralanes

Barbaralane is a rigid nine-carbon tricyclic diene. Similar to bullvalene, it is also composed of three bridges and one cyclopropane ring, however, one of the ethylene arms is replaced by a methine group, allowing it to fluctuate between only two degenerate isomers. Thus, the structures of barbaralanes are relatively easy to study, and their shapeshifting properties and equilibrium could be investigated as they are tractable systems.

The first member of the barbaralane family reported was the carbonyl-containing derivative barbaralone **6**, which was prepared as an intermediate when Doering attempted to improve the synthesis of bullvalene in 1963.[12] The key step of the synthetic route is the insertion of an intramolecular carbene into the central double bond of the cycloheptatriene ring system, resulting in the formation of the carbonyl derivative. (Scheme 1.8) The route starts with the Buchner reaction of ethyl diazoacetate and benzene to obtain cycloheptatriene **36**. The ester is hydrolyzed to carboxylic acid **37** and then converted to acid chloride **38** using thionyl chloride. Diazomethane is used to react with the acid chloride to give diazomethyl ketone **39**. Finally, the ketone is treated with copper (II) sulfate in the mixture of benzene and hexane under reflux to produce ketocarbene, which can form the babaralone **6** in the intramolecular cyclopropanation reaction.

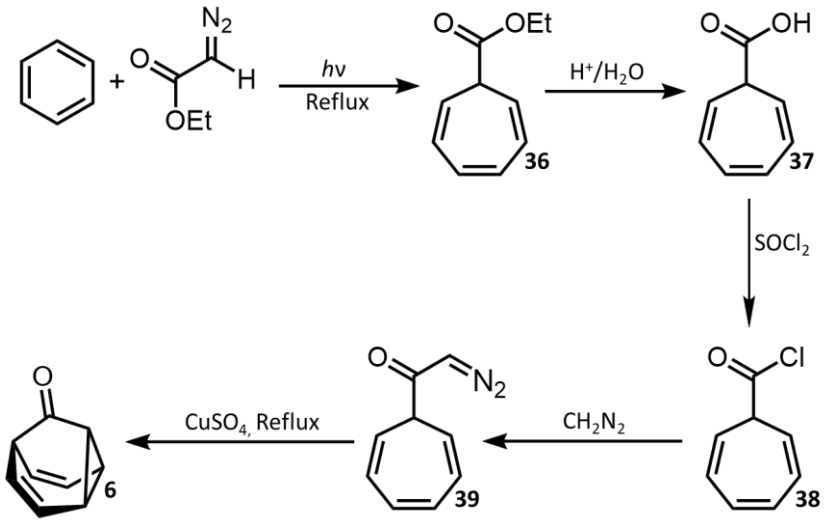

Scheme 1.8. Synthesis of barbaralone (**6**) reported by Doering and Roth

A series of synthetic routes towards babaralanes were reported during the 1980s and 1990s, e.g. Heckel's route starts from a Schmidt reaction of 2-adamantanone to give the carboxylic acid, followed by decarboxylation, allyl bromination and base-catalyzed ring closure to provide barbaralone, and then eliminated to barbaralane.[4a] Quast obtained 2,6-substituted barbaralane **48** via a Grignard reaction of bicyclo[3.3.1]nonane-2,6-dionen **44**, followed by dehydration, bromination and cyclisation with a zinc-copper couple.[13] These routes towards barbaralanes all require multiple steps, as well as dangerous reagents. (Scheme 1.9)

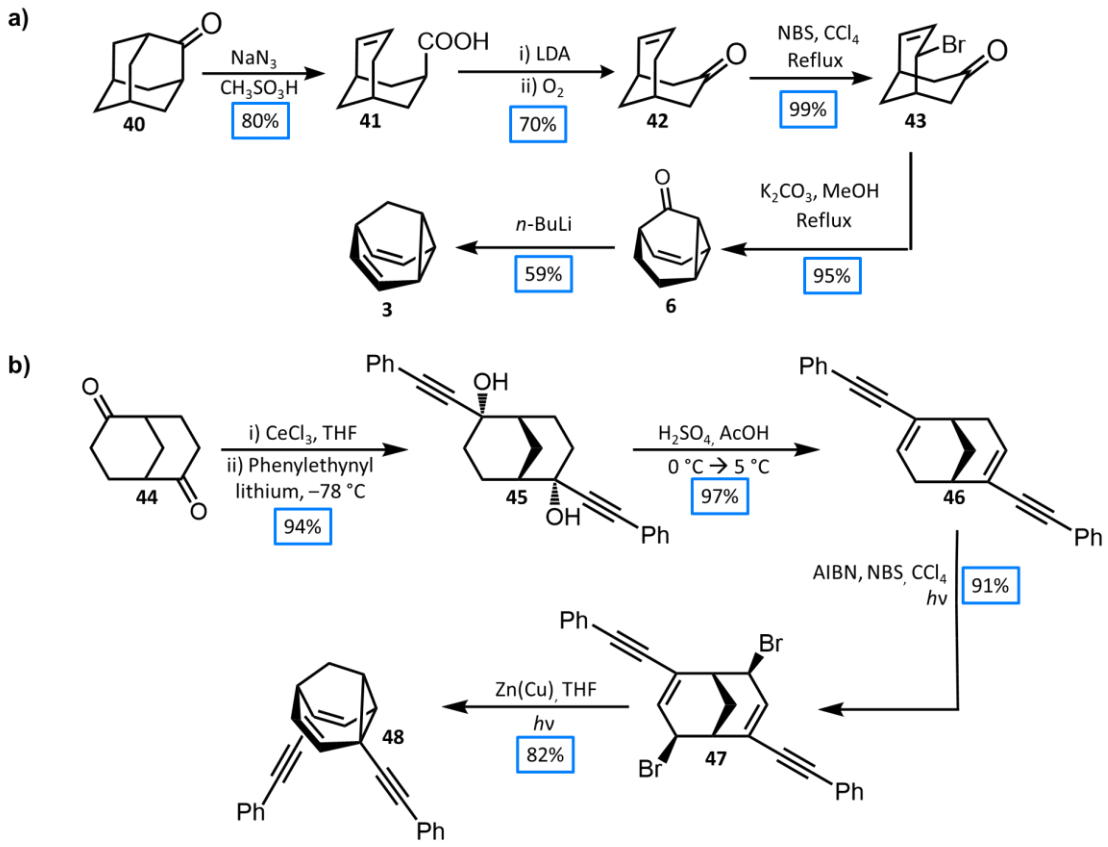

Scheme 1.9. a) Synthesis of barbaralane (**6**) from 2-adamantanone (**40**) reported by Henkel. b) Synthesis of 2,6-bis(phenylethynyl)barbaralane (**48**) developed by Quast.

From the 2010s, cationic gold complexes have been used in the synthesis of barbaralanes as they can promote enyne cyclisations under mild conditions while exerting particular control over competitive reaction pathways, and stabilize intermediates with carbenoid character.[8] The cycloisomerisations of alkynyl cycloheptatrienes and the mechanism of the resulting indene formation by using different gold catalysts and π-Lewis acids were reported by Echavarren in 2012, in which alkynyl cycloheptatriene **49** is first prepared by nucleophilic addition of an acetylide to tropylium tetrafluoroborate, and in the presence of a gold(I) catalyst **50**, it cycloisomerises to a gold-stabilised fluxional barbaralyl cation **51**. The barbaralyl cation will transform irreversibly to indenes without nucleophiles, but if intercepted with an external nucleophile (such as methanol), the barbaralane methyl ether **52** can be isolated with only a small amount of indenyl by-products. (Scheme 1.10)

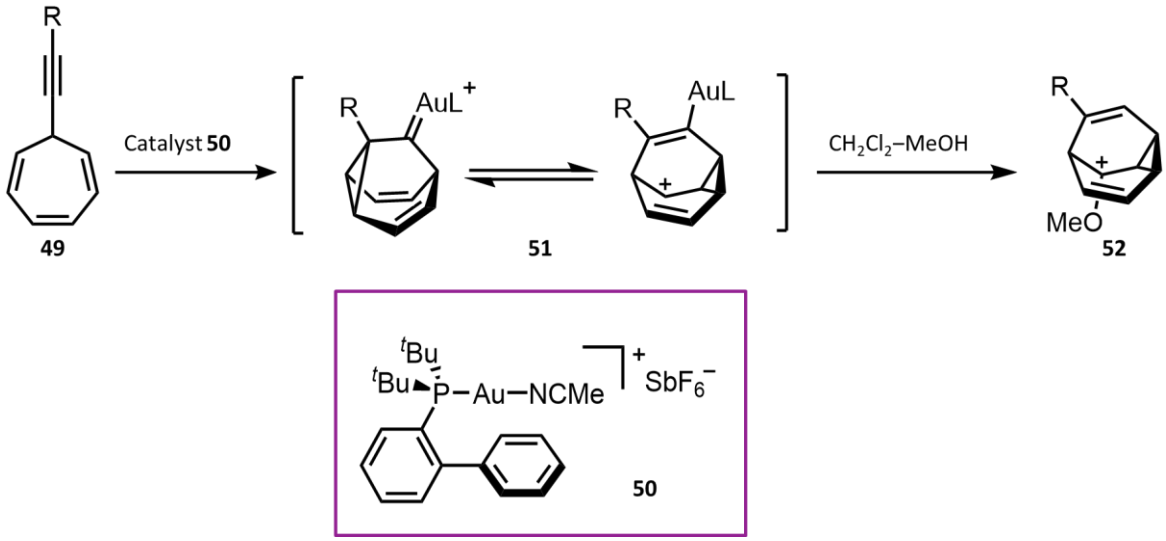

Scheme 1.10. General procedure to synthesise substituted barbaralane methyl ethers (**52**) from alkynyl cycloheptatrienes (**49**).

Echavarren's two-step barbaralane synthesis was further improved in 2016 to obtain barbaralone and its 1-substituted derivatives.[14] First activation and coordination to the alkyne triple bond occurs, which effectively promotes cyclization, followed by an attack of the external oxidant to provide α-oxo gold(I) carbene, which is then oxidized in situ for intramolecular cyclopropane to give barbaralones. Several different gold(I) catalysts and oxidants were tested and diphenyl sulphoxide and (acetonitrile)[(2-biphenyl) di-tert-butylphosphine]gold(I) hexafluoroantimonate **23** gave the highest yields. A series of substituted barbaralones **22** were successfully prepared via this synthetic route, with yields varing from 45% to 95%, and barbaralone itself reached a yield of 97%. This is by far the simplest and most versatile pathway to prepare barbaralone. (Scheme 1.11)

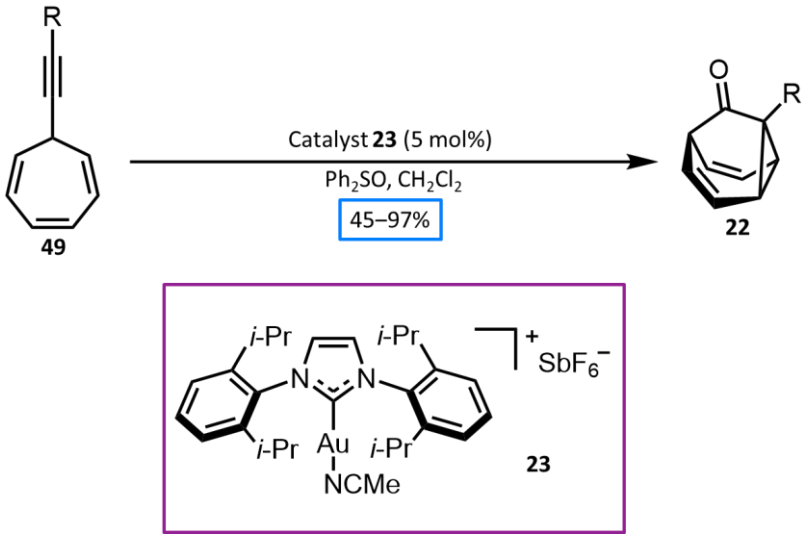

Scheme 1.11. General procedure to synthesize substituted barbaralones (**22**) from substituted alkynyl cycloheptatrienes (**49**) developed by Echavarren

1.4 Fundamental Studies of Fluxional Carbon Cages

Apart from synthetic pathways, the research of fluxional carbon cages over the last few decades has been mainly about studying their fundamental fluxional properties via both chemical and computational methods. For barbaralanes, the analysis and control of the dynamic chirality have been thoroughly demonstrated by McGonigal.[15,16] The shape-selective crystallisation of barbaralanes was reported in 2018, in which a series of di-substituted barbaralanes **53**/**53'** were prepared and characterised. DFT calculations indicated that the regioisomer **53** is more favoured in the solution state. However, XRD results showed that two of the barbaralanes gave energy-unfavoured regioisomers in the crystalline state, which is due to the adaption of their molecular size and shape[15]. (Figure 1.4)

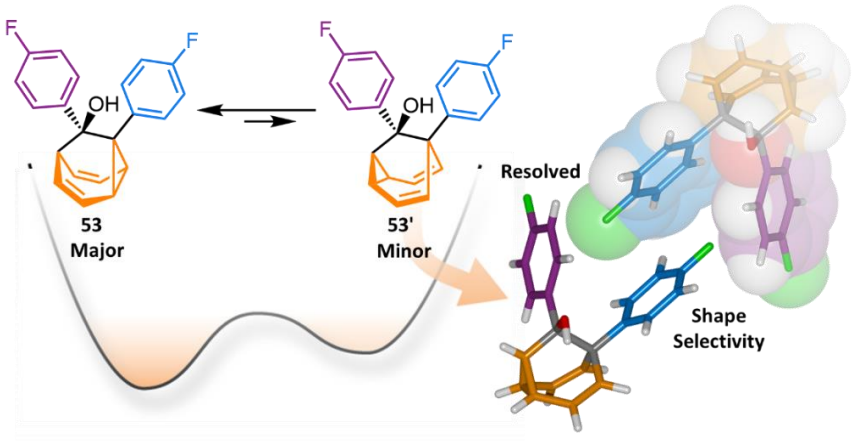

Figure 1.4. Illustration of shape-selective crystallisation and the crystal structures of five di-substituted barbaralanes.

The covalent control of dynamic sp^3 stereochemistry of barbaralanes was reported in 2023. The internal enantiomerisation of barbaralanes could be stopped, restarted or slowed by external reagents such as covalent chiral additives or chiral metal ligands.[16] The extent of dynamic Cope rearrangements controlled by neighbouring chiral centres was determined via DFT calculations, NMR spectroscopy and X-ray crystallography. The stereochemical information could also transmit to the metal ion (i.e. Ru(II) and Pd (II) ions) via covalent ligand backbone or ion pairing, which leads to the potential to create chiral-at-metal stereogenic centres, where chirality is imparted to a metal center, enabling enantioselective transformations in asymmetric synthesis (Figure 1.5).

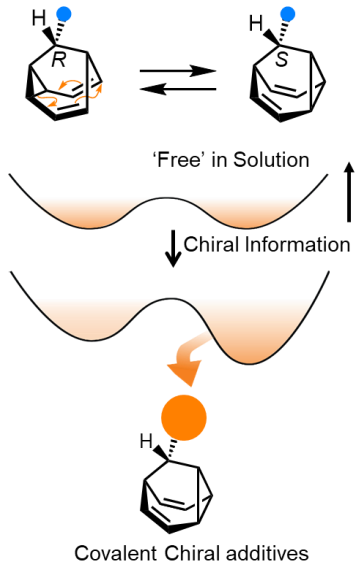

Figure 1.5. Illustration of covalent control over the dynamic chirality of barbaralanes.

The freezing of Cope rearrangements and dynamic preferential crystallisations of fluxional carbon cages was first demonstrated by Herges.[17] The homotropylidene dihydrobullvalene **5** was prepared via dimerization of cyclooctatetraene using the same conditions of Schröder's first synthetic route towards bullvalene. As one of the alkene bridges was substituted and turned into sp^3-C atoms, the product **5** could not be regarded as a bullvalene, but a barbaralane-like derivative that interconverts between two enantiomers. Dynamic enantiomerism of **5** is observed in the solution state, and in the crystalline state, it is proved to be a conglomerate as only one enantiomer is present in the single crystals precipitating from the racemic solution (Figure 1.6a). A bullvalene dimer **54** was also synthesised via dimerization of **5**, and XRD result indicated that only the *meso* diastereoisomer is present in the single crystals (Figure 1.6b).

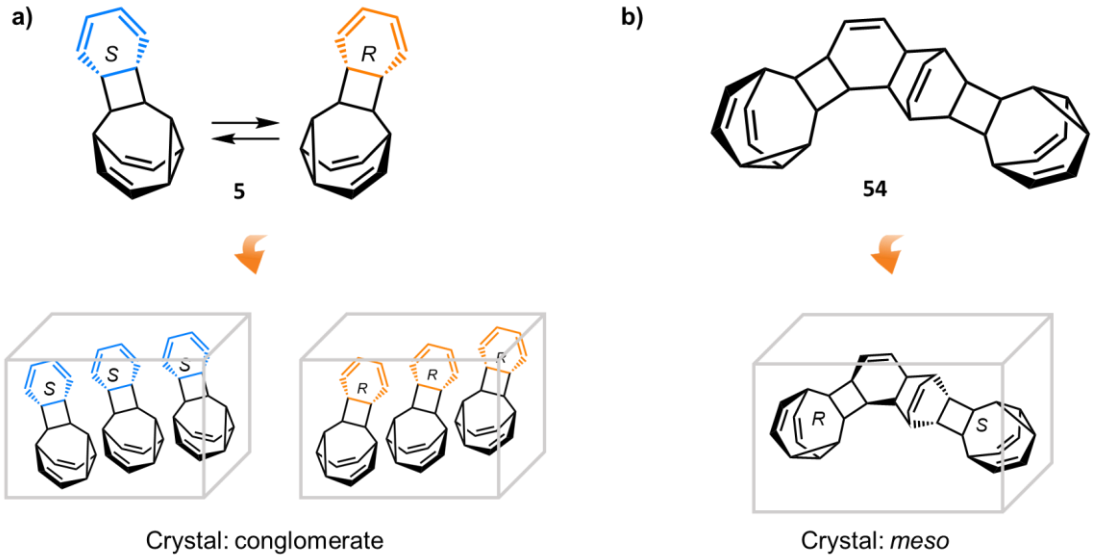

Figure 1.6. a) The dynamic enantiomerism of bullvalene **5** and its crystalline behaviour; b) The chemical structure of bullvalene dimer **54** and its crystal structure.

The potential of stereogenic bullvalenes to spontaneously racemise was observed by Bode.[18] A racemic, static bullvalone was prepared via the addition of phenyl Grignard reagent to triketone **55**, followed by elimination, allylation, and further elimination. The structure of the final product was suggested by 2D-NMR spectroscopy to be the rearranged regioisomer **58** instead of the expected **59** (Scheme 1.12). The isomer **58** was then proved to be racemic and static via chiral HPLC resolution and circular dichroism.

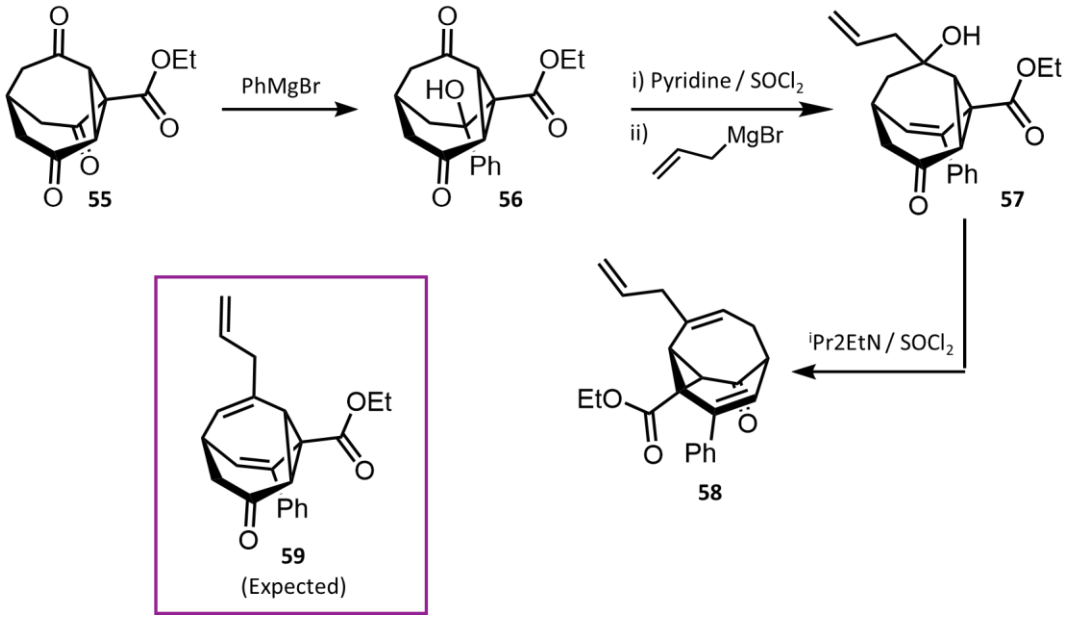

Scheme 1.12. Bode's synthetic route of racemic bullvalone **58**.

In Fallon's 2019 report of tri-substituted bullvalenes, the isomerism populations of di- and tri-substituted bullvalenes were studied using low-temperature NMR spectroscopy.[10b] The results demonstrated that although various isomers of substituted bullvalenes exist in theory, two isomers take up almost all the distribution: For di-substituted bullvalenes **60**, two substituents flank the bridgehead position in both the major isomer **60a** (ββ) and minor isomer **60b** (βγ). Tri-substituted bullvalenes **35** shows a similar isomerism behaviour, in which the substituents takes up the three alkene bridges separately, and far away from the cyclopropane ring. (Figure 1.7) The crystal structures of di-substituted bullvalenes were obtained and analysed, and the minor isomer could be resolved in the solid state due to shape-selectivity, which matches up with McGonigal's previous report of shape-selectivity of barbaralanes.[15]

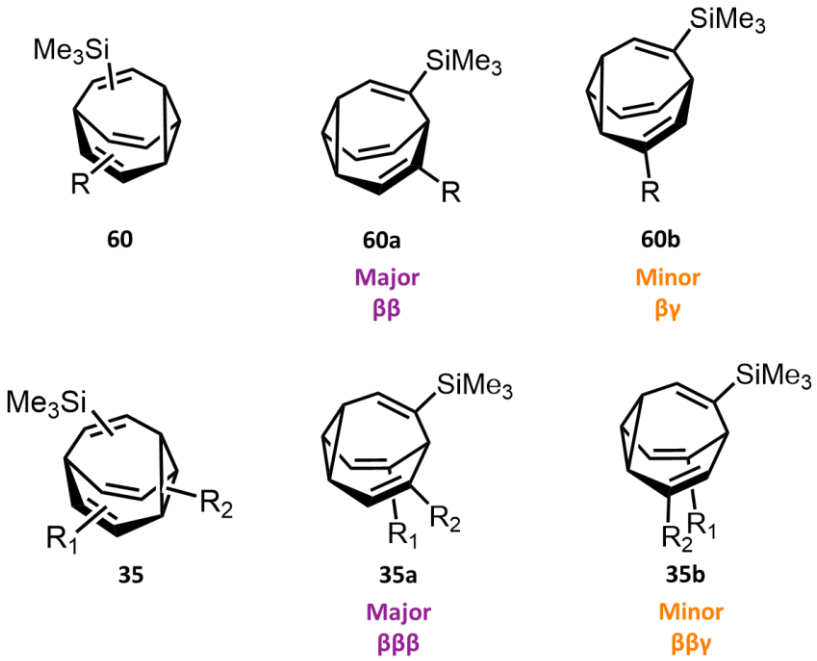

Figure 1.7. The isomerism populations of di- and tri-substituted bullvalenes studied by Fallon.

The host-guest interactions of macrocycles and bullvalenes were investigated by Fallon and co-workers via computational modelling.[19] Three different cyclodextrins were chosen to capture both the unsubstituted and mono-substituted bullvalenes. The interaction potential energy between the host and guest is systematically evaluated first for different binding positions, and the most favourable ones are further subjected to unrestrained MD simulation to determine the most common binding modes. (Figure 1.8) The computational results showed that β-cyclodextrin has the strongest binding with bullvalenes. However, the simulations did not properly consider the rapid interconversion of bullvalenes in the process of binding with cyclodextrins, and the conclusion could actually be proved via simple NMR spectroscopy.

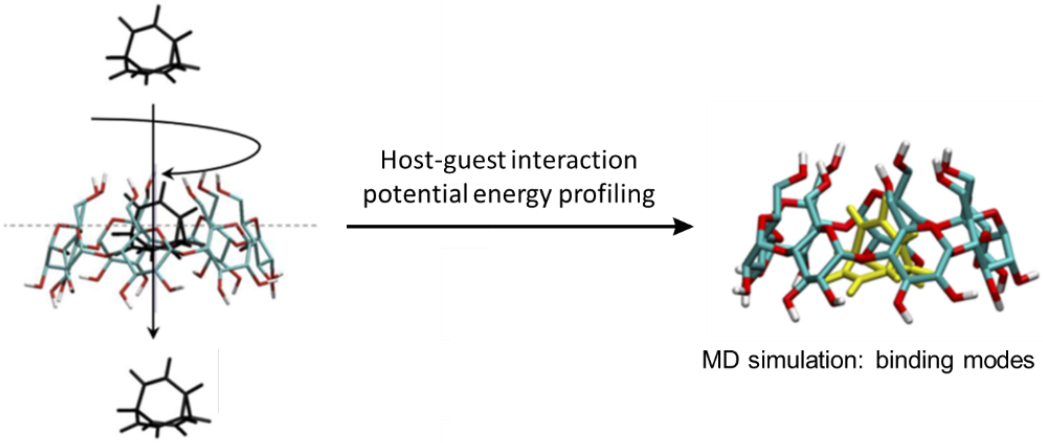

Figure 1.8. Simulation of host-guest interactions of cyclodextrins and bullvalenes.

Fallon has also demonstrated the possibility of expanding the fluxional structure of bullvalenes.[20] In 2022, by synthesis of dialkenyl-bullvalenes **61**, [5,5]-sigmatropic rearrangement was achieved and gave rise to tetrahydro-1,8-ethenoheptalenes **61'**, the first example of this tricyclic scaffold. DFT calculations proved that the thermodynamics of the bullvalene/tetrahydro-1,8-ethenoheptalene systems could be tuned or brought into balance by varying alkene substitution. This work has explored the possibility of more complex, extended systems of Cope rearrangements. (Scheme 1.13)

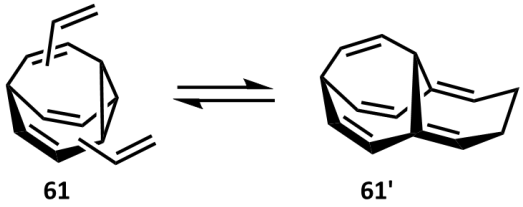

Scheme 1.13. The dialkenyl-bullvalene/tetrahydro-1,8-ethenoheptalene system **61**/**61'**.

1.5 Application of Fluxional Carbon Cages

The first attempt to use bullvalene derivatives as adaptive shapeshifting mixtures was reported by Schröder and co-workers in 1979.[21] Inspired by the bullvalene principle conceived by Doering, they came up with the idea of 'fluctuating or breathing rings'. They synthesised two crown ether-type compounds with bullvalene as the linkage (**62**) to investigate their association with metal-ion guests, which they expected to see the crown ether group to change ring size as

the bullvalene interconverts via Cope rearrangements and lead to the selective binding different metal ions depending. However, only very weak associations were observed and the effect of metal ions on their equilibrium distribution could not be determined. (Scheme 1.14)

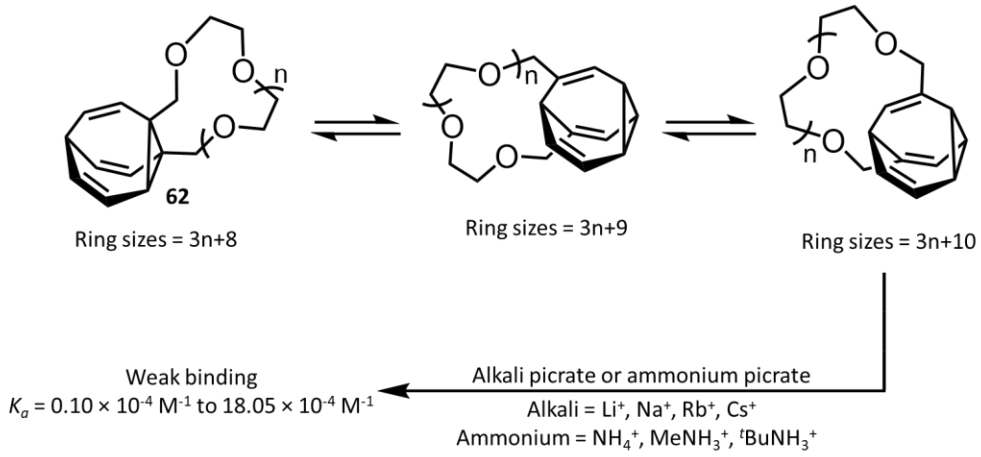

Scheme 1.14. Application of a crown-ether substituted bullvalene (**62**) with the binding of metal cations.

Bullvalene's potential for application in the chemical sensing has been investigated by Bode over the last decade.[22] In 2009, based on the high-affinity π–π interactions of porphyrin with C_{60}, Bode's group synthesized the bisporphyrin bullvalene and established the binding ability of a synthetic, shapeshifting molecular system.[22a] The results showed that the addition of C_{60} shifts the equilibrium of bisporphyrin bullvalene towards isomers that more tightly bind with C_{60}, which demonstrated the possibility to spontaneously discover high-affinity binding complexes when interacted with a suitable guest (Scheme 1.15).

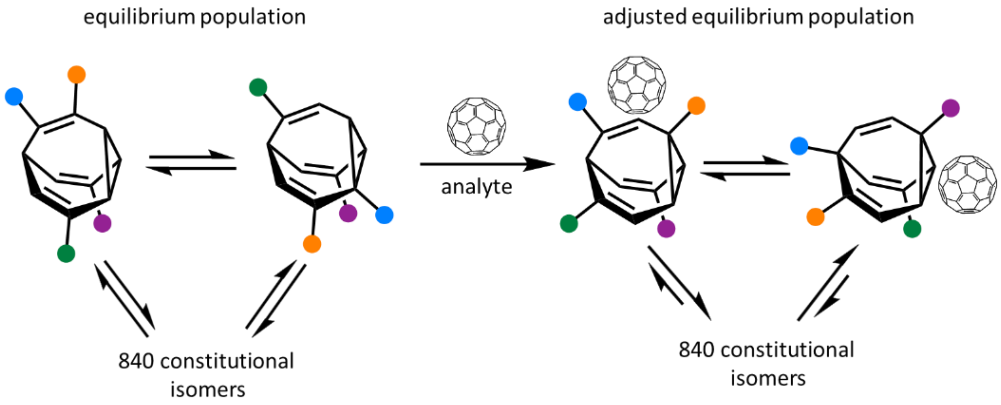

Scheme 1.15. The addition of a fullerene analyte alters the isomer distribution of the oligo-substituted bullvalene.

The ^{13}C-labelled bisporphyrin-bullvalene was then prepared in 2012 to further investigate its application in chemical sensing.[22b] By comparing the ^{13}C-NMR spectra of fullerene derivatives without analytes and those treated with fullerene C_{60}, the bullvalene core was able to easily distinguish highly similar analytes. (Figure 1.9)

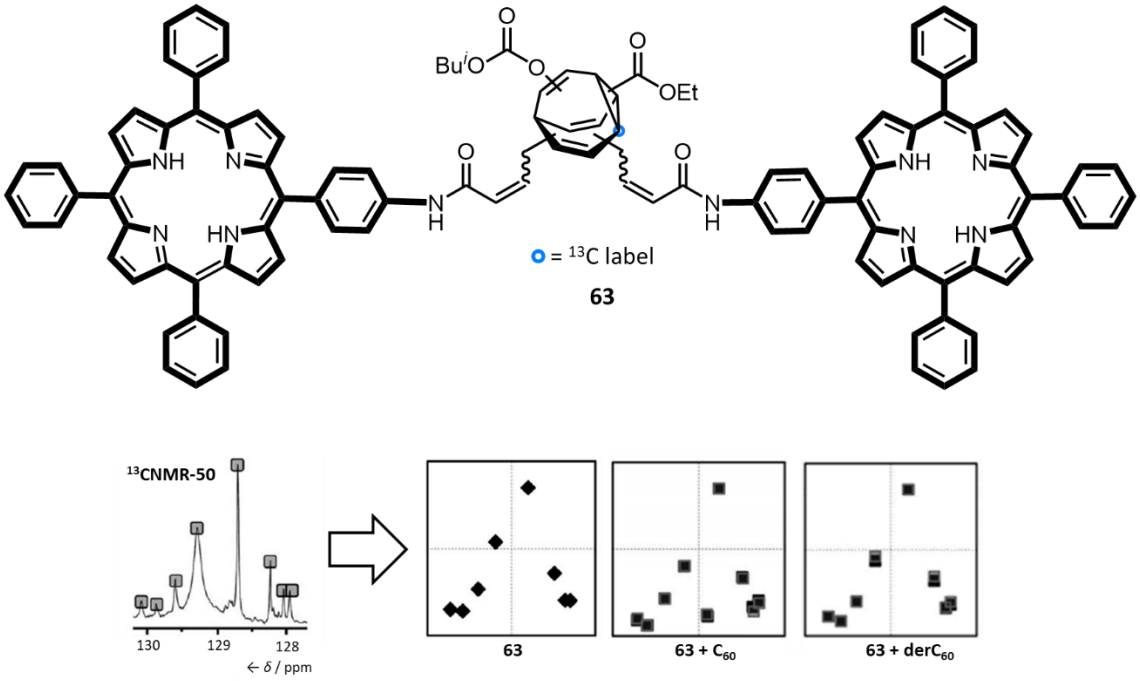

Figure 1.9. ^{13}C-labelled bisporphyrin-bullvalene **63** and a graphical representation of its ^{13}C NMR spectrum converted to its corresponding peak pattern showing the equilibrium population.

The first case of analyte binding through covalent bonding was then reported in 2013, in which the synthesised bullvalene derivatives could interact with and sense polyols through dynamic covalent condensation reactions, a dynamic bis-boronic acid-based sensor array which could detect different polyols was developed, and the ^{13}C-NMR signals were transformed into easy-to-read barcodes.[22c] The results showed that the barcode in the presence of every different polyol was distinctive, which demonstrated that the bullvalene sensor is readily able to distinguish different polyols with closely related structures. One of its significant advantages over classic sensor arrays is that the selectivity of a specific scope would not be reduced due to the dominance of the strongest binding analyte. (Figure 1.10)

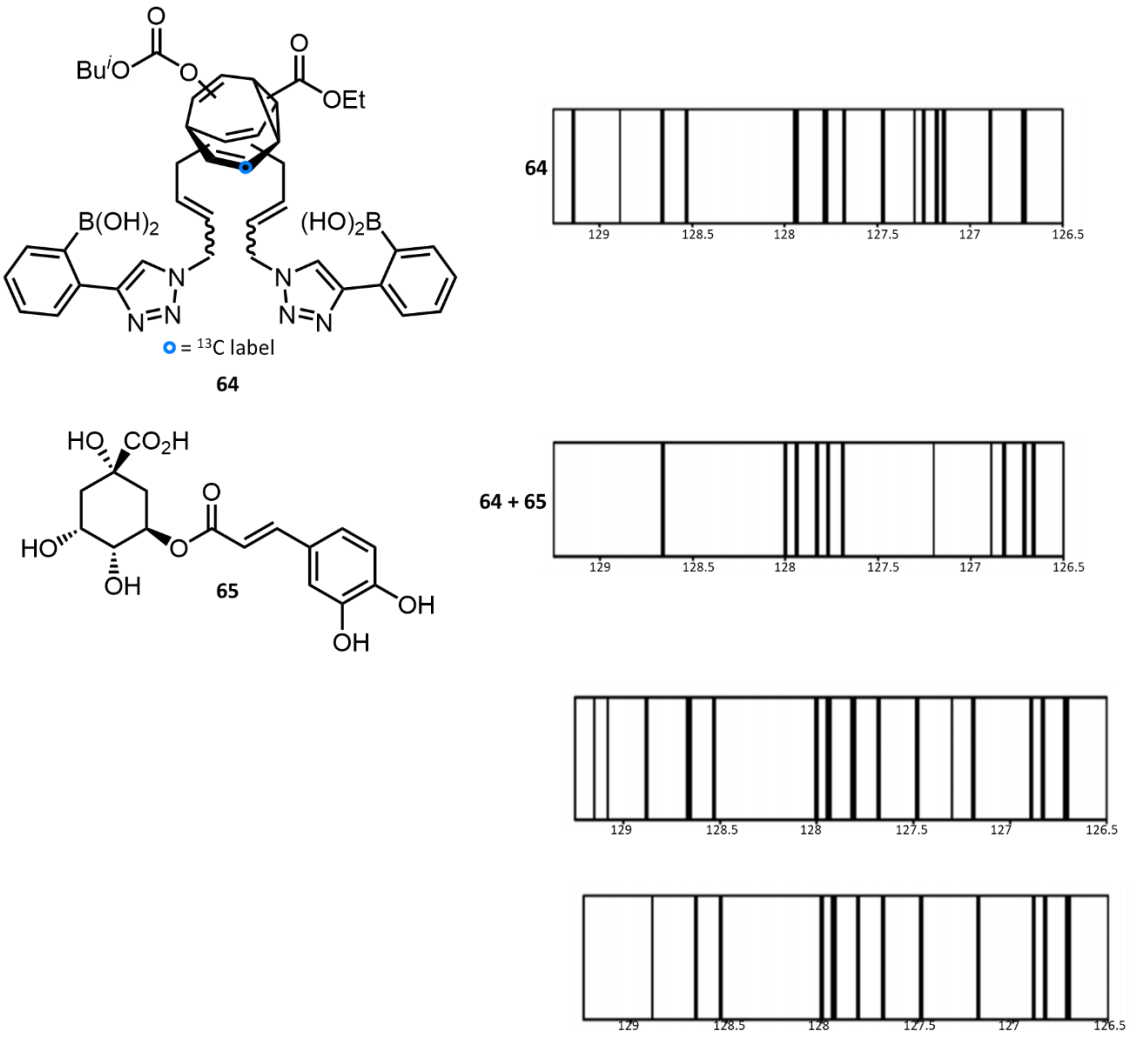

Figure 1.10. ^{13}C-labelled bis-boronic acid bullvalene **64** and its barcode compared to the barcode of a mixture of **64** and polyol **65**.

The dynamic isomerism of bullvalenes can be shifted via coordination with metal ions. In 2021, Fallon reported bullvalenes working as the building blocks of coordination cages.[23a] The bis-3-pyridyl bullvalene **66** self-assembles with Pd^{2+} or Pt^{2+} to produce a highly complex ensemble of permanently fluxional coordination cages, and anion exchange with Cl^- and I^- led to a dramatic convergence to a well-defined all-βγ isomer cage complex. (Figure 1.11)

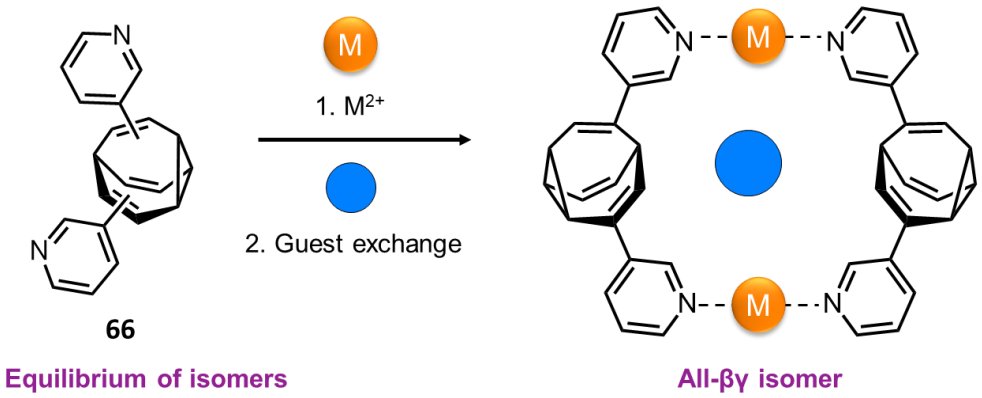

Figure 1.11. Metal-mediated and guest-induced self-assembly of bis-3-pyridyl bullvalene cage reported by Fallon.

Similar to Fallon's coordination cage, the chelate complex of bullvalene and Ag^+ was reported by Ihmels.[23b] Disubstituted bullvalene-harmane conjugate **67** was prepared and low-temperature NMR spectroscopy proved that the isomeric distribution of **67** is occupied by two major isomers (ββ and βγ), and via the complexation with Ag^+, the dynamic isomerization of the bullvalene was controlled and led to only one predominant valence isomer (ββ). By adding hexacyclene that displaces the Ag^+, the forming and removing of chelation became reversible, converting between the distributions of one and two isomers. (Figure 1.12) This control of valence isomerism is achieved by straightforward chemical stimuli, which could lead to the application in self-sorting systems or molecular machines.

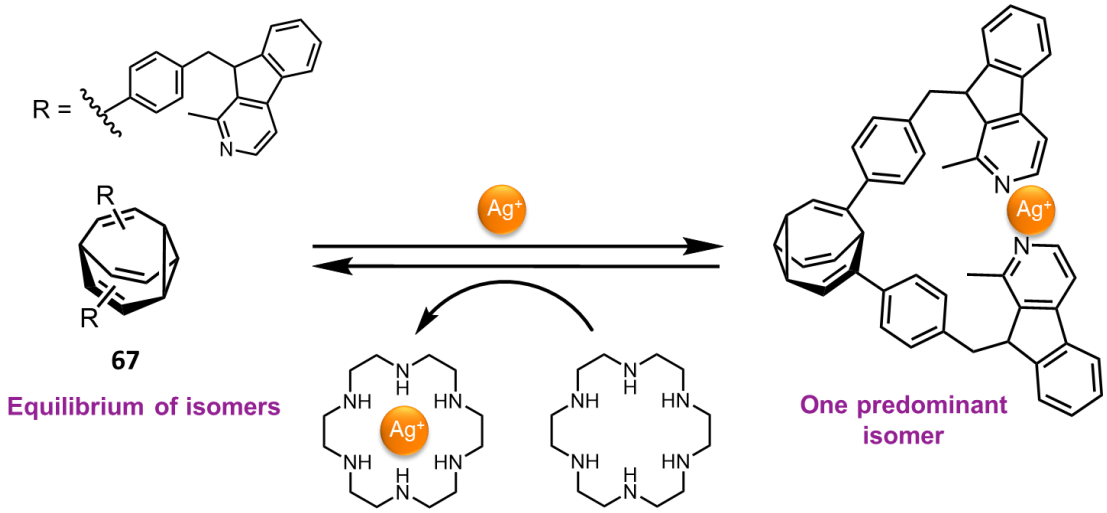

Figure 1.12. The reversible system of bullvalene chelate complex by Ihmels.

The incorporation of bullvalenes into polymers was first reported by Golder.[24] A series of bullvalene co-polymers were prepared using Suzuki-Miyuara polycondensation, and the bullvalene units were shown to decrease structural rigidity within π-rich materials, owing to the fact that the self-contained library of valence isomers could provide an ensemble of structural kinks to modulate chain architecture. (Figure 1.13) The incorporated bullvalene polymers exhibit high thermal stability and tuneable thermal properties, which provides the potential to work as internal plasticizer to modulate the properties of π-rich polymers.

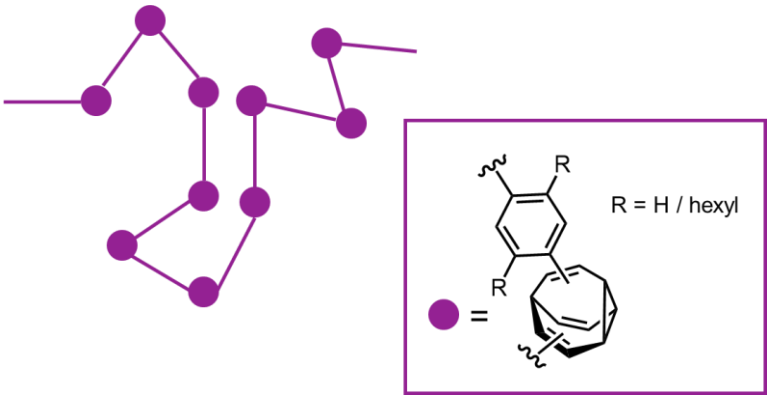

Figure 1.13. The structure of poly(bullvalene-co-phenylene)s.

Bullvalenes have been introduced into physical chemistry and electrics applications in recent years by utilising their ability to convert between different shapes.[25] Ihmels reported dinaphthoylmethyl-substituted bullvalene derivative **68** that exhibits excimer fluorescence[25a], which is due to the fluxional bullvalene core supporting the excimer formation of the aroyl substituents and offering the opportunity to monitor externally induced structural changes by fluorescence spectroscopy. (Figure 1.14a) Fallon made di-substituted bullvalenes into single-molecule NEMS piezoresistor by utilising their constitutional and conformational isomerisations.[25b] (Figure 1.14b)

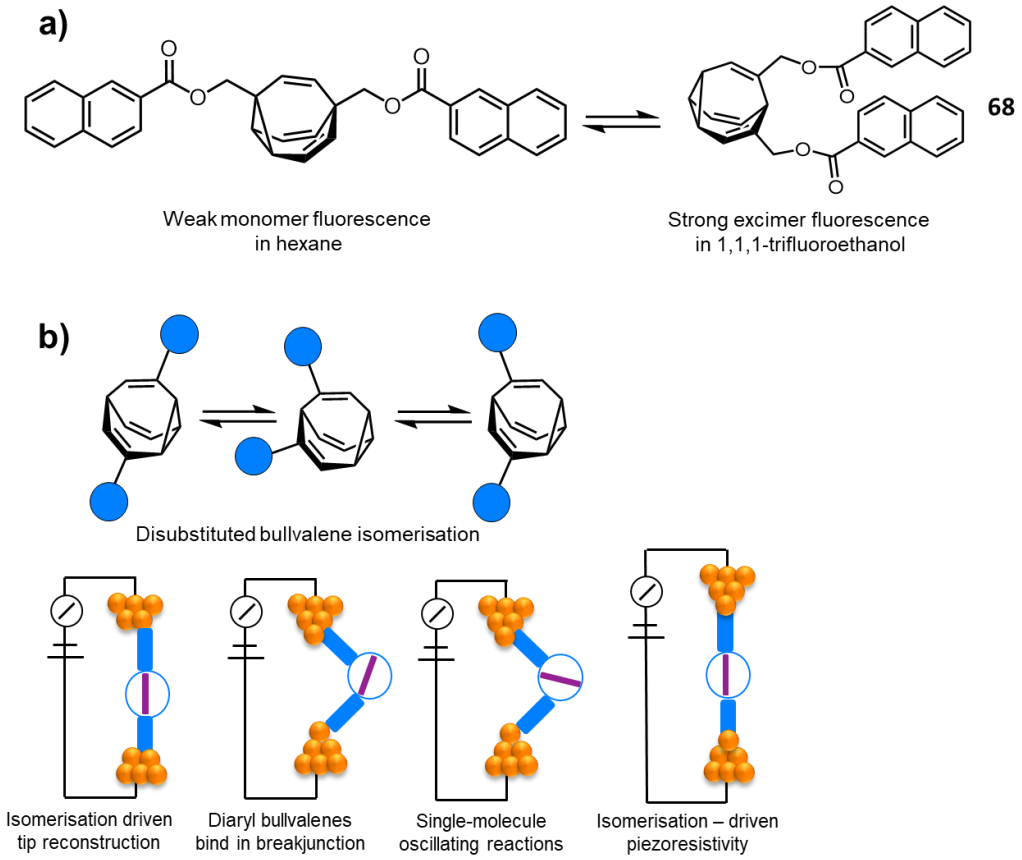

Figure 1.14. a) The fluorescent dinaphthoylmethyl-substituted bullvalene **68**; b) Molecular and interfacial structural changes of bullvalenes in solution and in NEMS devices.

The first example of bullvalene in biological applications was reported by Fallon and co-workers in 2023, in which bullvalene is di-substituted with vancomycin (Figure 1.15).[26] The obtained bullvalene vancomycin dimers **69** show strong antimicrobial activity not prone to rapidly acquired clinical resistance, which could be due to the dynamic adaptive binding interactions of the bullvalene core, as well as the destabilisation of the complex formed between the flippase MurJ and lipid-linked peptidoglycan precursor Lipid II in the cell wall of bacteria.

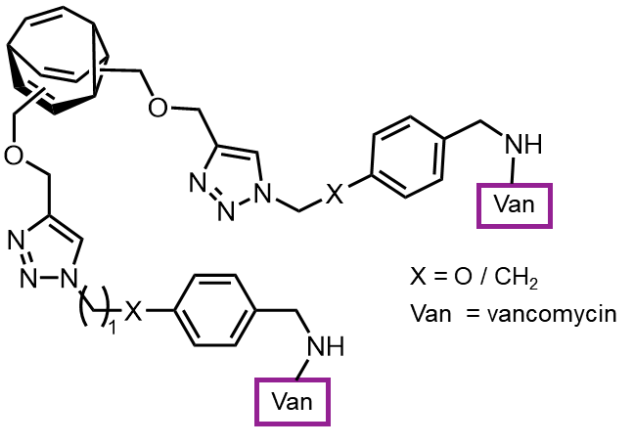

69

Figure 1.15. The chemical structures of bullvalene vancomycin dimers reported by Fallon and co-workers.

1.6 Overview

In summary, fluxional carbon cages are unique molecules with 'shapeshifting' abilities due to rapid and reversible Cope rearrangements, and this rare phenomenon is crucial to the concept of valence isomerisation, illustrating that a single rigid molecule could form a dynamic structural library. The fundamental and application studies on fluxional carbon cages, despite development of synthetic methods, are mainly focused on altering equilibrium populations and isomer distributions through specific noncovalent bonding interactions or dynamic covalent bonds with different guests. Since their discovery in the 1960s, fluxional carbon cages still remain of significant interest because of their potential for exploring complex biological systems and creating new functional materials.

As illustrated in this chapter, the fundamental aspects of bullvalenes and barbaralanes have been intensively studied, i.e. concise synthetic routes have been developed to obtain oligosubstituted bullvalenes, and the dynamic chirality of barbaralanes have been halted via covalent bonding. Low-temperature NMR spectroscopy and computational modelling have played an important role in analysis and predictions of their dynamic behaviour. The applications of fluxional carbon cages remain relatively unexplored, although examples of bullvalenes being used in sensing, fluorescence and even antibiotics have been reported, these applications are still in the initial stage and have not been systematically proved and amplified.

Based on the experience of previous studies, we continue to explore both fundamental studies and applications of fluxional carbon cages, including the noncovalent control of dynamic enantiomerism, crystallisation behaviour of barbaralane oligomers and the potential of bullvalenes being used in functional materials. We intend to fully understand and control the fluxional behaviour of these molecules in in both solution and solid state, which will clear the path towards precise determination and predictions of their properties, leading to more accurate and systematic investigations on their innovative applications.

1.7 References

1. A. C. Cope and E. M. Hardy, *J. Am. Chem. Soc.* 1940, **62**, 441.

2. (a) W. von E. Doering and W. R. Roth, *Tetrahedron.* 1963, **19**, 175; (b) G. Schröder, *Angew. Chem.* 1963, **75**, 722; *Angew. Chem. Int. Ed. Eng.* 1963, **2**, 481; (c) A. Adult, *J. Chem. Educ.* 2001, **78**, 924; (d) H. G. Viehe, *Angew. Chem. Int. Ed. Eng.* 1965, **4**, 746.

3. (a) P. Ahlberg, D. L. Harris and S. Winstein, *J. Am. Chem. Soc.* 1970, **92**, 5545; (b) D. Cremer, P. Svensson, E. Kraka and P. Ahlberg, *J. Am. Chem. Soc.* 1993, **115**, 7445; (c) P. Ahlberg, J. B. Grutzner, D. L. Harris and S. Winstein, *J. Am. Chem. Soc.* 1970, **92**, 3478; (d) B. Grutzner and S. Winstein, *J. Am. Chem. Soc.* 1970, **92**, 3186; (e) P. Ahlberg, D. L. Harris and S. Winstein, *J. Am. Chem. Soc.* 1970, **92**, 2146

4. (a) J. G. Henkel and J. T. Hane, *J. Org. Chem.* 1983, **48**, 3858; (b) C. Engdahl and P. Ahlberg, *J. Am. Chem. Soc.* 1979, **101**, 3940; (c) L. G. Greifenstein, J. B. Lambert, M. J. Broadhurst, L. A. Paquette, *J. Org. Chem.* 1973, **38**, 1210; (d) G. G. Cristoph, S. Hardwick, U. Jacobsson Y.-B. Koh, R. Moerck and L. A. Paquette, *Tetrahedron. Lett.* 1977, **14**, 1249.

5. H. E. Zimmerman and G. L. Grunwald, *J. Am. Chem. Soc.* 1996, **88**, 183.

6. (a) W. von E. Doering and J. W. Rosenthal, *J. Am. Chem. Soc.* 1966, **88**, 2078; (b) M. Jones and L. T. Scott, *J. Am. Chem. Soc.* 1967, **89**, 150; (c) J. Font, F. Löpez and F. Serratosa, *Tetrahedron. Lett.* 1972, **13**, 2589; (d) J. F. M. Oth, R. Merényi, J. Nielsen and G. Schröder, *Chem. Ber.* 1965, **98**, 3358.

7. (a) Rebsamen, K.; Schröder, G. Chem. Ber.1993, 126, 1425−1427; (b) Rebsamen, K.; Schröder, G. Chem. Ber.1993, 126, 1419−1423; (c) A. R. Lippert. J. Kawobamrung and J. W. Bode, *J. Am. Chem. Soc.* 2006, **128**, 14738.

8. P. R. McGonigal, C. de León, Y. H. Wang, A. Homs, C. R. Solorio-Alvarado and A. M. Echavarren, *Angew. Chem. Int. Ed.* 2012, **51**, 13093.

9. O. Yahiaoui, L. F. Pašteka, B. Judeel and T. Fallon, *Angew. Chem. Int. Ed.* 2018, **57**, 2570.

10. (a) H. D. Patel, T. H. Tran, C. J. Sumby, L. F. Pasteka and T. Fallon, *J. Am. Chem. Soc.* 2020, **142**, 3680–3685; (b) O. Yahiaoui, L. F. Pašteka, C. J. Blake, C. G. Newton and T. Fallon, *Org. Lett.* 2019, **21**, 9574–9578.

11. (a) A. R. Lippert, A. Naganawa, V. L. Keleshian and J. W. Bode, *J. Am. Chem. Soc.* 2010, **132**, 15790;

(b) M. He, J. W. Bode, *Org. Biomol. Chem.* 2013, **11**, 1306; (c) B. A. Hussein, W. Maturi, M. K.Rylands, A. N. Bismillah, Y. Wen, J. A. Aguilar, R. Ayub, C. Rankine and P. R. McGonigal, *Chem. Sci.* 2024, **15**, 14618-14624.

12. W. von E. Doering and W. R. Roth, *Angew. Chem. Int. Ed. Engl.* 1963, **2**, 115.

13. H. Quast, M. Witzel, E. –M. Peters, K. Peters and H. G. von Schnering, *Leibigs. Ann.* 1995, 725.

14. S. Ferrer and A. M. Echavarren, *Angew. Chem. Int. Ed.* 2016, **55**, 11178.

15. A. N. Bismillah, J. Sturala, B. M. Chapin, D. S. Yufit, P. Hodgkinson and P. R. McGonigal, *Chem. Sci.* 2018, **9**, 8631–8636.

16. A. N. Bismillah, T. G. Johnson, B. A. Hussein, A. T. Turley, P. K. Saha, H. C. Wong, J. A. Aguilar, D. S. Yufit and P. R. McGonigal, *Nature Chem.* 2023, **15**, 615–624.

17. J. Siegwarth, J. Bornhöft, C. Näther and Rainer Herges, *Org. Lett.* 2009, **11**, 15, 3450–3452.

18. M. He, J. W. Bode, Proc. *Natl. Acad. Sci.* 2011, **108**, 14752

19. Z. Shadfar, O. Yahiaoui, T. A. Collier, T. Fallon and J. R. Allison, *J. Chem. Phys.* 2021, **154**, 154105.

20. H. D. Patel, S. Gaggl, L. F. Pašteka and T. Fallon, *Org. Lett.* 2022, **24**, 319-323.

21. (a) G. Schröder and W. Witt, *Angew. Chem. Int. Ed.* 1979, **18**, 311; (b) K. Sarama, W. Witt and G. Schröder, *Chem. Ber.* 1983, **116**, 3800.

22. (a) A. R. Lippert, V. L. Keleshian and J. W. Bode, *Org. Biomol. Chem.* 2009, **7**, 1529; (b) K. K. Larson, M. He, J. F. Teichert, A. Naganawa and J. W. Bode, *Chem. Sci.* 2012, **3**, 1825; (c) J. F. Teichert, D. Mazunin and J. W. Bode, *J. Am. Chem. Soc.* 2013, **135**, 11314.7

23. (a) A. P. Birvé, H. D. Patel, J. R. Price, W. M. Bloch and T. Fallon, *Angew. Chem. Int. Ed.* 2021, **9**, e202115468; (b) C. Dohmen, T. Paululat and H. Ihmels, *Chem. Eur. J.* 2024, e202304311

24. M. N. Pomfret, P. B. Sun, Z. Huang, A. C. Freund, T. Miyoshi and M. R. Golder, *Angew. Chem. Int. Ed.* 2023, **19**, e202301695

25. (a) C. Dohmen, H. Ihmels and T. Paululat, *Eur. J. Org. Chem.* 2022, **45**, e202201172; (b) J. R. Reimers, T. Li, A. P. Birvé, L. Yang, A. C. Aragonès, T. Fallon, D. S. Kosov and N. Darwish, *Nat. Commun.* 2023, **14**, 6089.

26. A. Ottonello, J. A. Wyllie, O. Yahiaoui, S. Sun, R. A. Koelln, J. A. Homer, R. M. Johnson, E. Murray, P. Williams, J. R. Bolla, C. V. Robinson, T. Fallon, T. P. Soares da Costa and J. E. Moses, Proc. *Natl. Acad. Sci.* 2023, **120**, e22087371

CHAPTER 2 | NONCOVALENT CONTROL OVER DYNAMIC sp^3–CARBON STEREOCHEMISTRY

Synopsis

This Chapter discusses the unique synthesis of novel 9-substituted barbaralanes which interconvert between stereoisomers in the solution state through dynamic chirality. The dynamic enantiomerism of 9-substituted barbaralanes was halted through noncovalent interactions of chiral macrocycles in both solid and solution states. This was confirmed through X-ray diffraction, NMR spectroscopy and binding constant measurements, demonstrating the potential of barbaralanes to undergo covalent induced-fit binding.

Contribution statements

The author conducted: the synthesis and spectroscopic characterisations of all compounds; ^{1}H-NMR titrations of β-CD dimer **8** with barbaralanes **2** in Section 2.2.2 and 2.2.3; all the work in Section 2.2.4.

Acknowledgements

The following people are gratefully acknowledged for their contribution to this chapter: Postdoc Aisha N. Bismillah grew co-crystals of β-CD with barbaralanes **1**-**4**, and conducted ^{1}H-NMR titrations of β-CD dimer **8** with barbaralanes **1** and **3**. Dr Dimitry S. Yufit solved all the X-ray crystal structures. We are grateful to Dr Juan A. Aguilar for assistance with NMR measurements.

2.1 Introduction

Dynamic chirality refers to a phenomenon where a low-energy barrier to racemisation allows for the mutual conversion of enantiomers.[1] In supramolecular chemistry, dynamic chirality is present in rotaxanes,[1a] information ratchets,[2] disulfides[3], macrocycles,[4] etc. This occurs either through supramolecular interactions with chiral inducers or through an intramolecular chiral conformation maintained by steric hindrance, which prevents racemisation.

Dynamic chirality at atomic stereogenic centres is primarily dominated by phosphorous[5] and nitrogen species[6] owing to their ability to process pyramidal inversion at room temperature. Spontaneous (reagent-free) enantiomerisations of sp^3 carbon atoms are relatively rare as the configurations of carbon centres are stable without first breaking and reforming bonds at the stereogenic centre. Miller and co-workers[7] have reported dynamic stereogenic centres through redox interconversion (Figure 2.1a). However, the redox interconversion cannot be well controlled and remains dynamic in the solid state.

Barbaralanes possess rapid Cope rearrangements within their carbon skeleton, which leads to dynamic sp^3 stereochemistry by changing the relative positions of neighbouring atoms without breaking the stereogenic center.[8] The covalent control of sp^3 stereochemistry of barbaralanes has been demonstrated by McGonigal.[9] The enantiomerisation distribution of barbaralanes can be biased through a covalent ligand backbone or ion pairing, allowing the dynamic enantiomerizations to be stopped and restarted (Figure 2.1b).

This chapter explores a new method for the control of dynamic sp^3 stereochemistry of barbaralanes via noncovalent bonding.[10] Through the host-guest interactions between barbaralanes and chiral macrocycles (i.e. cyclodextrins), the equilibrium distribution of the barbaralanes stereoisomers are expected to be shifted in both solution and solid state (Figure 2.1c). A series of 9-substituted barbaralanes were prepared and encapsulated by β-cyclodextrin, and the effect of noncovalent binding was analysed in two aspects: In the solid state, the host-guest complex of barbaralanes with β-cyclodextrin was analysed *via* XRD and solid-state NMR spectroscopy to observe the shift of stereoisomerism, assisted by NMR titrations to determine the binding constants. In the solution state, the Cope rearrangement of barbaralol was stopped via a radical reaction in the presence of β-cyclodextrin, and various methods (NMR shift

reagent, optical rotation, circular dichroism, etc.) were utilised to investigate the potential enantioenrichment of the product. In some cases, self-sorting dimers were observed in the co-crystal complexes, and β-cyclodextrin and barbaralane dimers were synthesised for further investigations of the host-guest systems.

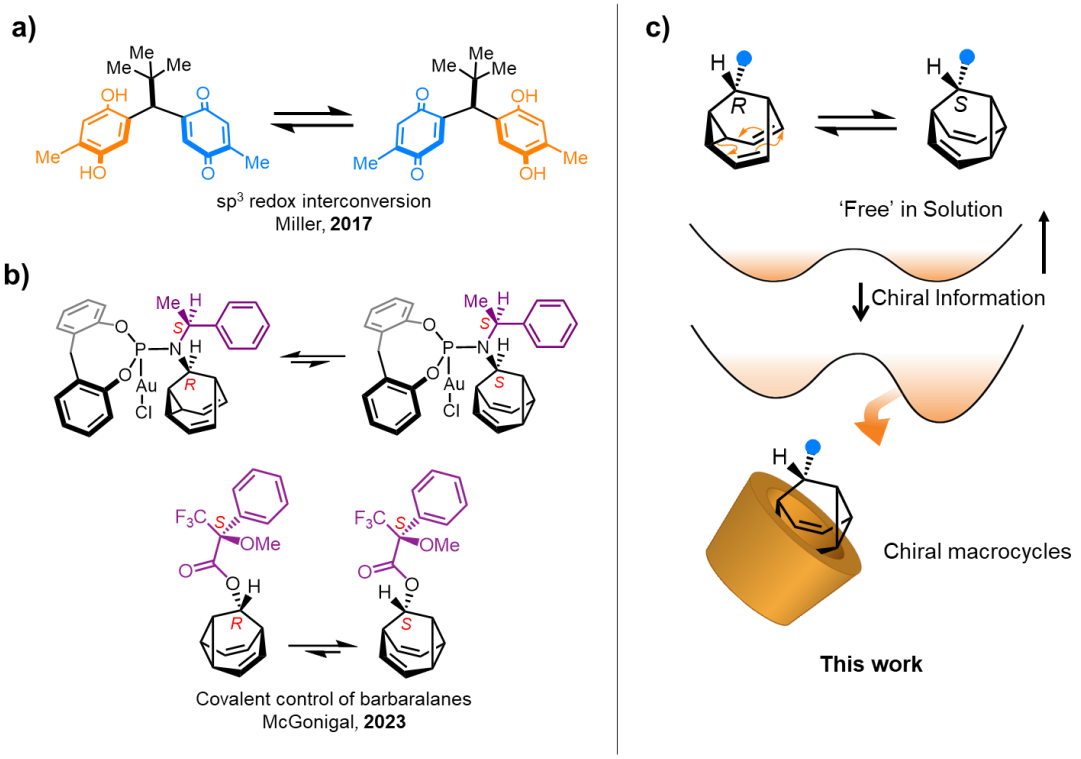

Figure 2.1. a) Redox interconversion of sp^3-C stereochemistry demonstrated by Miller and co-workers; b) Covalent control of stereochemistry of barbaralanes reported by McGonigal; c) Noncovalent control of stereochemistry of barbaralanes via chiral macrocycles.

2.2 Results and Discussion

2.2.1 Synthesis and Characterisations of 9-Substituted Barbaralanes

The synthetic routes of target 9-substituted barbaralanes **1**, **2**, **3** and **4** all started with the formation of intermediate barbaralone **6** and then breaking symmetry through further modifications of the carbonyl group: parent barbaralol **1** was obtained by reduction of the carbonyl into a hydroxyl group, fluorobenzyl barbarlol **2** and tolyl barbarlol **3** were synthesised via Grignard reactions, and the amine barbaralane dimer **4** was obtained by reductive amination which attached two barbaralyl to form a secondary amine (Scheme 2.1). All four target

molecules could be soluble in water due to the presence of hydroxyl and amine moieties, which benefited to the studies of their binding behaviour in aqueous solution. Single crystals of synthesised barbaralanes **1**, **2**, and **4** were obtained and analysed via XRD (Full details see section 2.5.2), and all of the crystals were found to be racemic: the monomer **1** and **2** exhibit a 1:1 ratio of *R*- and *S*-enantiomers, while the dimer **4** crystallises as its *meso* diastereoisomer (*R*,*S*).

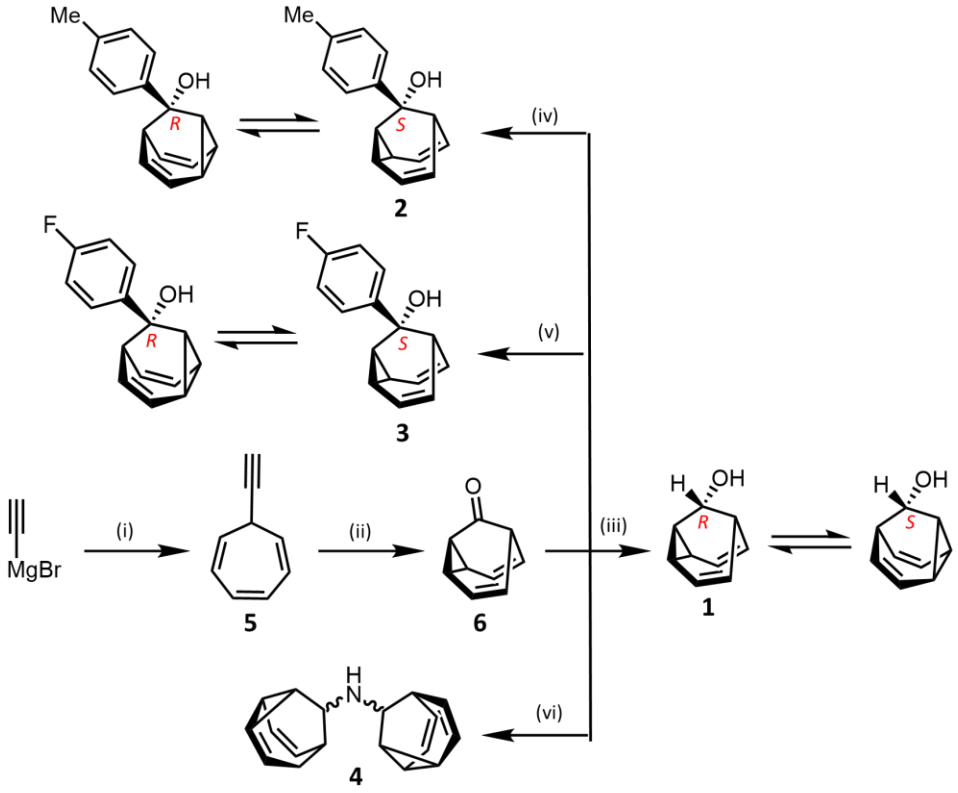

Scheme 2.1. Synthesis of 9-substituted barbaralanes **1**-**3** and barbaralane dimer **4**. Reagents and conditions: (i) 1. LiCl / THF / –78 °C / 10 min, 2. Tropylium tetrafluoroborate / –78 °C to rt, 83% (ii) IPrAu(MeCN)BF_4 (5 mol%) / Ph_2SO / CH_2Cl_2 / rt / 16 h, 60%. (iii) $LiAlH_4$ / Et_2O / 0 °C / 3 h, 78%. (iv) *p*-Tolylmagnesium bromide / THF / 0 °C to rt / 16 h, 80%. (v) *p*-Fluoro magnesium bromide / THF / 0 °C to rt / 16 h, 67%. (vi) NH_3 / MeOH / glacial AcOH / $NaBH_3CN$ / 100 °C / 24 h, 53%.

The chemical structures of all target molecules were confirmed by ^{1}H- and ^{13}C-NMR spectroscopy. In the ^{1}H-NMR spectra of barbaralanes **1**-**4** and barbaralone **6**, the signals of 1/5, 2/4 and 6/8 positions coalesce due to their rapid interconversions in solution. Barbaralone **6** only shows three broad peaks because of the symmetry of the sp^2 carbon, and when the 9-

position is turned into a nonsymmetric sp^3 stereocentre (i.e. reduced into a hydroxyl group), the 3&7 position will be resolved into two peaks respectively due to different environments on each side of the stereocentre (Figure 2.2). To simplify the assignments of peaks and determination of configuration, we stipulate the 2, 3 and 4 positions to be on the same side of less prioritised substituent on the sp^3 stereocentre, while the 6, 7 and 8 on the side of more prioritised one. i.e. in the case of barbaralol **1**, the 2, 3 and 4 positions are on the same side with the H atom, while the 6, 7 and 8 are on the same face with the hydroxyl group.

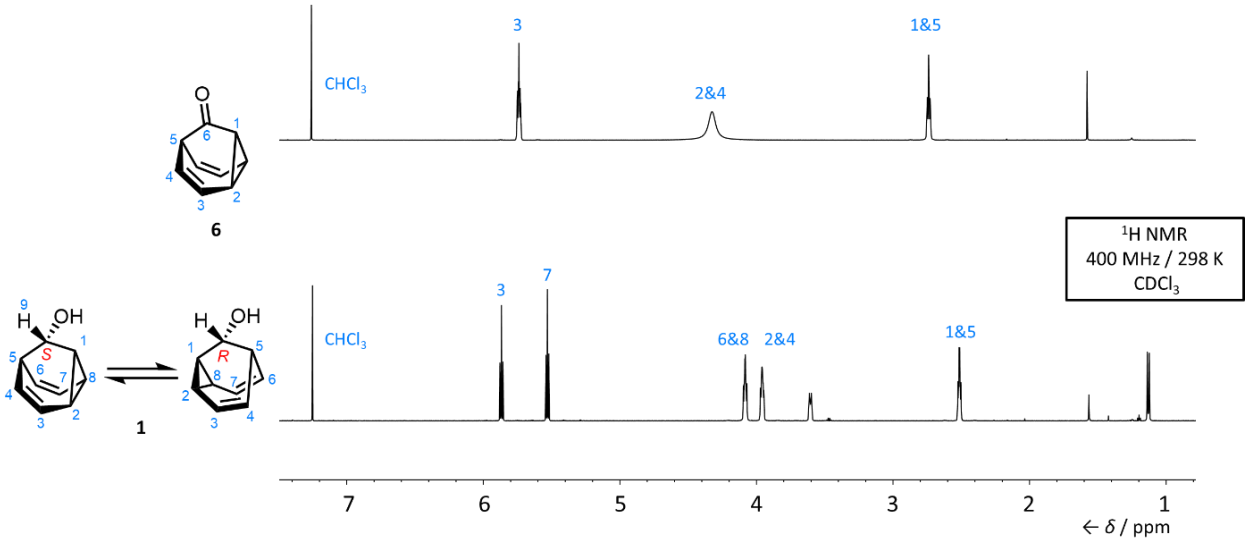

Figure 2.1. Comparison of partial ^{1}H NMR spectra of barbaralone **6** and barbaralol **1** demonstrating the formation of sp^3 stereocentre.

2.2.2 Host-Guest Studies of Barbaralane and Cyclodextrin Monomers

It has been reported that cyclodextrins form 1:1 inclusion complexes with adamantane derivatives[11] which have similar structures to barbaralone **6**. Initial ^{1}H-NMR spectroscopic binding tests of barbaralol **1** and barbaralone **6** with α-, β- and γ-cyclodextrins respectively[12] have demonstrated that β-cyclodextrin has the strongest binding with barbaralanes and led to significant shift of ^{1}H-NMR peaks. As a result, β-cyclodextrin was chosen as the host molecule throughout this project.

To investigate the effect of noncovalent bonding on the dynamic sp^3-C stereochemistry, β-CD was used to encapsulate barbaralanes **1**, **2**, and **3** which possess a sp^3 stereocentre. The co-

crystals of β-CD with three barbaralanes were all obtained and analysed via XRD. In the crystal structure of β-CD⊃**1**, the parent barbaralol **1** and β-CD form a 1:1 complex where a single enantiomer (*S*-) of **1** is observed inside the β-CD cavity, which indicates that the chiral information of β-CD has successfully halted the dynamic enantiomerism via host-guest interactions (Figure 2.2) with the macrocycle, along with interactions with neighbouring 1:1 complexes in the crystal lattice. The XRD structure exhibit some degree of disorder, but the relatively low R-factor (R_1 = 0.0499) indicates a reliable conclusion.

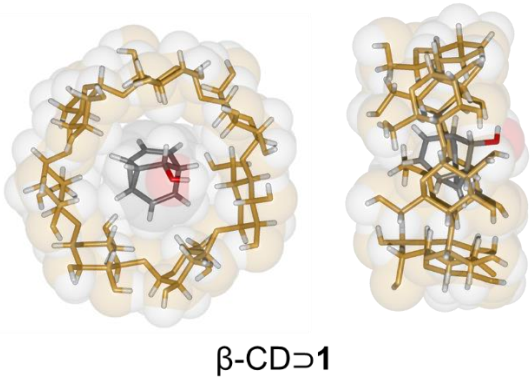

Figure 2.2. The front and side view of the 1:1 co-crystal of β-CD⊃**1**

When β-CD encapsulates tolyl barbaralol **2** or fluorobenzyl barbaralol **3**, their co-crystal structures are more complicated as a pair of β-CD form a head-to-head dimer, and each CD cavity holds one barbaralol molecule with one having *R*- and the other *S*- stereochemistry, which presents a self-sorting behaviour.[13] The two diastereoisomer complexes are both paired with the larger opening of CD cavity facing each other, the tolyl barbaralol **2** are paired as 'tail-to-tail' (with two barbaralyl cages facing each other) while the fluorobenzyl barbaralol are 'head-to-head' (with two fluorobenzyl substituents stacked together). The different orientations of **2** and **3** could be due to the strong electronic repulsion of fluorine atoms on **2**, which push them to the larger opening of the cavity, stabilising the complex through π-π stacking of aromatic rings. These racemic dimers seem to be simply resolved by dynamic preferential crystallisation[14] for closer packing, however, from the perspective of forming a 2:2 complex in the solid state, the spatial information is passed on to the adapted guests where the best fit is achieved by selectively resolving a pair of opposing barbaralane stereoisomers.

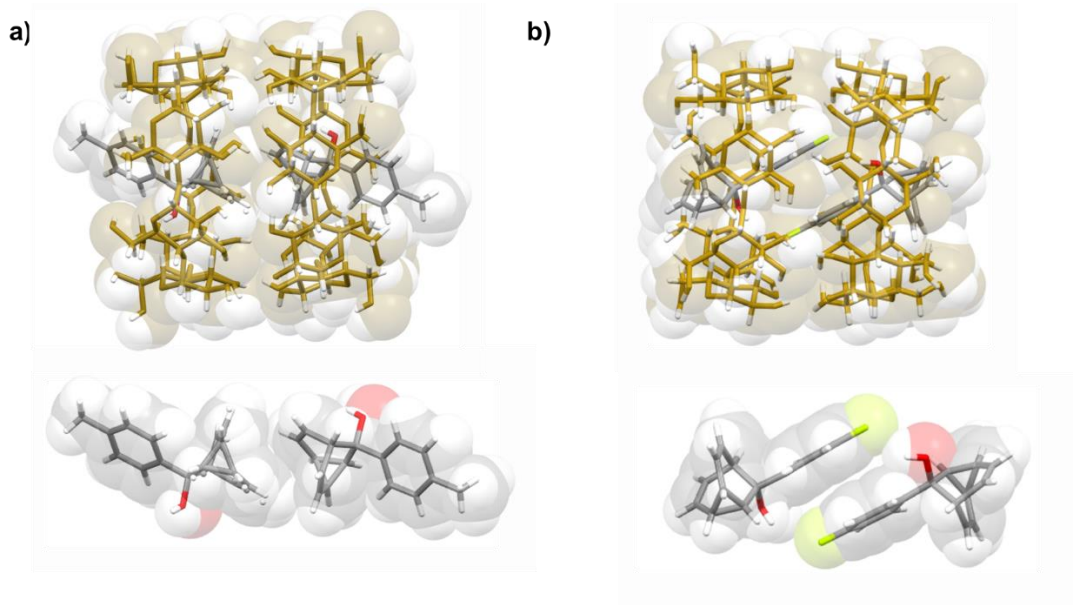

Figure 2.3. a) Side view of the 2:2 co-crystal of β-CD⊃**2** and the packing of **2** with β-CD hidden.; b) Side view of the 2:2 co-crystal of β-CD⊃**3** and the packing of **3** with β-CD hidden.

^{1}H-NMR spectroscopic titrations between β-CD and barbaralane **1**-**3** were carried out to quantify the stoichiometry and binding strength of the complex.[12] The titrations were performed using both high and low concentrations of the same host-guest complex and each concentration was conducted twice and taken the average data. Consistent binding constants were obtained across the same one-to-one stoichiometry model, enabling the determination of both the host-guest interaction stoichiometry and the association constant (K_a). Figure 2.4 shows a summary of the titration between β-CD and parent barbaralol **1**: D_2O solution of β-CD (12.33 mM) was titrated into **1** (1.23 mM) and a ^{1}H NMR spectrum was acquired after each addition of β-CD. The shift changes of peak 3, 7 and 1/5 were recorded and the data was fit using Bindfit[15] with two different optimisation algorithms (Nelder-Mead[16] and L-BFGS-B[17]) to determine the stoichiometry[18] and binding constant (K_a). Titration with lower concentrations (6.16 mM of β-CD and 0.62 mM of **1**) was also conducted and the same results were obtained. Similarly, the titrations between β-CD and two other synthesised barbaralanes were conducted and analysed using the same method. Both complexes fit a one-to-one binding isotherm as expected, and the calculated binding constants showed that the fluorobenzyl barbaralol **2** has a similar binding strength with **1** (9.0×10^2 M^{-1}±2.87%) while the tolyl barbaralol binds significantly stronger

(5.5×10^3 M^{-1}±2.81%).[9] The error values (standard deviation of the calculated binding curves) are all low, indicating a high-quality data collection and suitable fitting model.

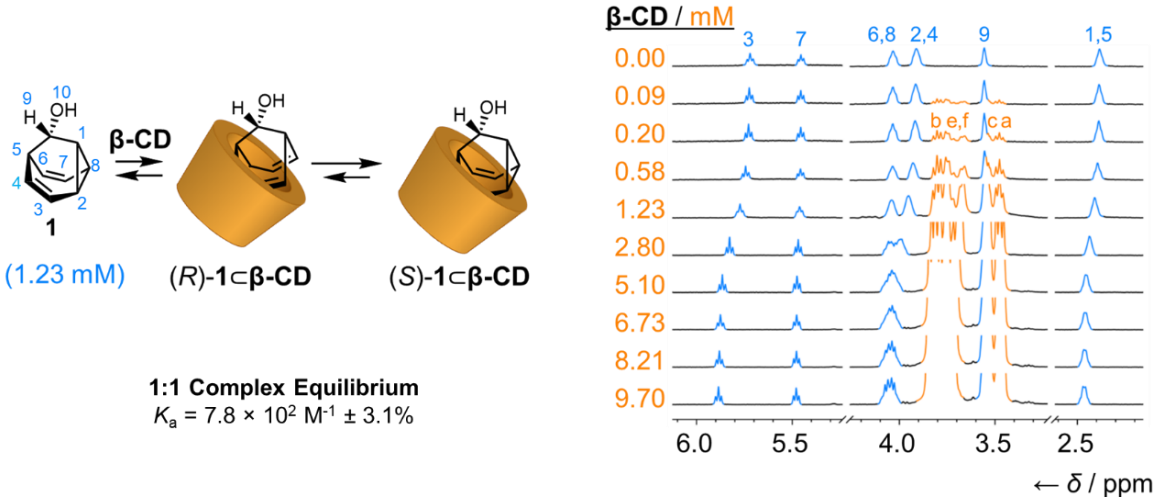

Figure 2.4. Summary of previous ^{1}H-NMR titrations between β-CD and parent barbaralol **1**.

2.2.3 Host—Guest Studies of Barbaralane and Cyclodextrin Dimers

The host—guest studies in section 2.2.2 proved that the dynamic enantiomerism of barbaralanes could be affected by the chiral β-CD. However, in the co-crystal structures of β-CD⊃**2** and β-CD⊃**3**, the 2:2 complex is not expected. To further investigate the driving force of forming the racemic dimer, a β-CD dimer **8** was prepared and taken into further host-guest studies with barbaralanes. The synthesis of **8** followed the methods developed by Williams and co-workers[19]: a nitrophenol dimer **7** was first prepared via Swern oxidation of 3-nitrophenol with oxalyl chloride, and then it was taken into a nucleophilic reaction with two equivalents of amino-substituted cyclodextrin, linking the two CD units together to obtain the desired β-CD dimer **8** (Scheme 2.2).

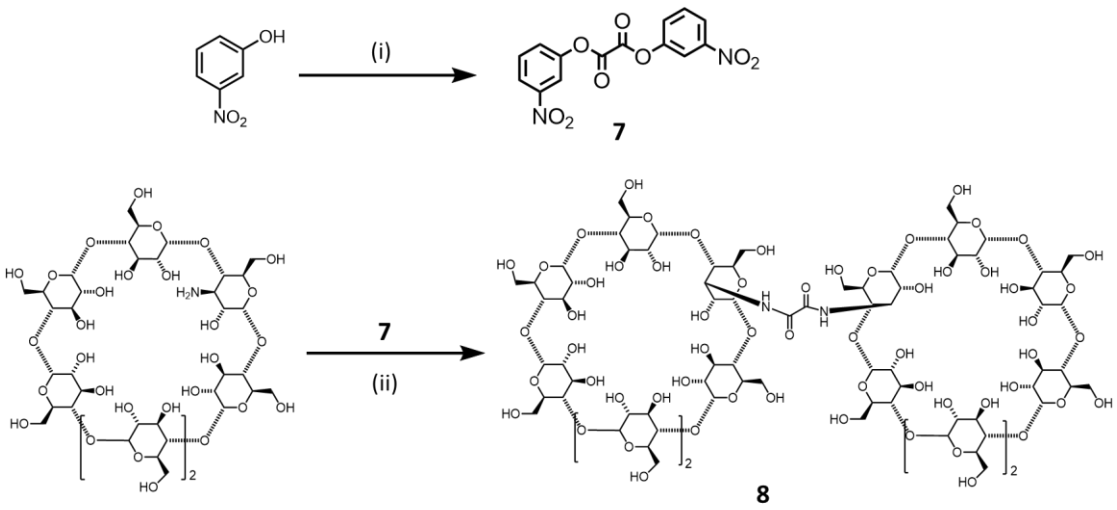

Scheme 2.2. Synthetic route of the target β-CD dimer **8**. (i) Triethylamine / oxalyl chloride / N_2 / 0 °C / 2 h, (ii) DMF / rt / 36 h.

The synthesised β-CD dimer **8** was used to encapsulate barbaralanes **1**-**3**. Unfortunately, the broken symmetry of substituted β-CD brought great difficulty to crystal growth, thus no crystal structure of **8** or its complex with barbaralane was obtained. ^{1}H-NMR titrations between **8** and tolyl barbaralol **2** were first conducted and analysed using the same methods in section 2.2.2, and assuming the dimer host will form a 1:2 complex with the guest molecules, the concentration of D_2O solution of the host **8** was adjusted to 6.16 mM corresponding to 1.23 mM of tolyl barbaralol **2**. Figure 2.5 shows the obtained stacked partial ^{1}H-NMR spectra. The obtained data was first fit with a 1:2 binding isotherm, and K_1, the association constant of one guest molecule (**2**) binding to the host (**8**), as well as K_2, the constant of the second guest molecule binding to the complex of guest⊂host were calculated to be 3.5×10^3 M^{-1} ± 8.2% and 8.7×10^2 M^{-1} ± 23%, respectively. The obtained association constants orientated the 1:2 binding model of β-CD dimer **8** with tolyl barbaralol **2** to be non-cooperative[20] as K_1 equals to $4K_2$, which indicated that the binding of the first and second guest molecule are completely independent. However, the significantly large error of the calculated K_2 (23%) made the conclusion less reliable, which indicated either a low-quality data or a wrong fitting model, and more accurate conduction of the experiments is needed.

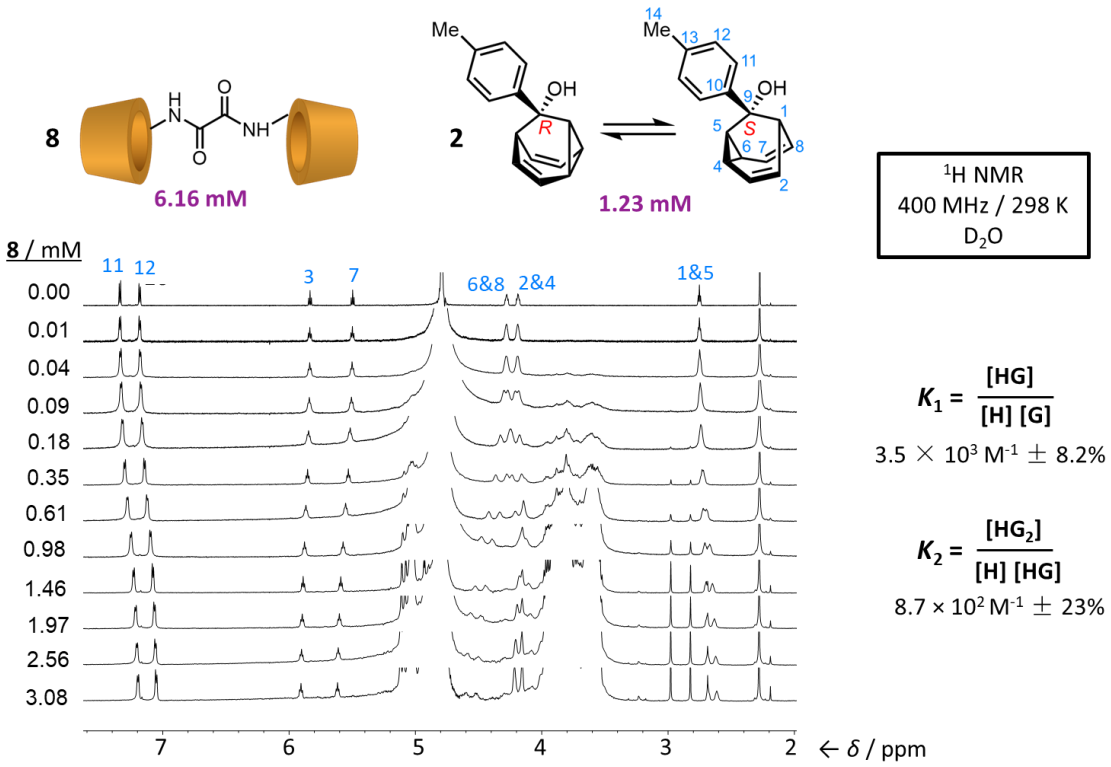

Figure 2.5. Illustration of initial ^{1}H-NMR titrations between β-CD dimer **8** and tolyl barbaralol **2**.

The ^{1}H-NMR titration of **8** and **2** was then repeated with the same concentrations, and the large D_2O signal was suppressed using Robust-5 and PROJECT pulse sequences for higher accuracy. The new results were fit with a 1:1 binding model, and the new K_a was calculated to be 4.3 × 10^3 M^{-1} ± 5.81%. Considering the significantly different deviations in binding curves, and a non-cooperative binding model for the restrained CD dimer **8** is highly unlikely, the 1:1 model is more reasonable. The ^{1}H-NMR titrations of **8** with parent barbaralol **1** and fluorophenyl barbaralol **3** were then conducted and analysed with the same concentrations (full details see section 2.5.3), and all three barbaralanes showed more reasonable association constants using the 1:1 binding model (Figure 2.6). Similar to the results with β-CD monomer, the tolyl barbaralol **2** also shows significantly higher binding strength with the β-CD dimer comparing to the other two barbaralanes (Table 2.2). These results demonstrated that all three barbaralanes form a 1:1 complex with the β-CD dimer, violating from our initial assumption of 1:2. A possible explanation is that the linker of the dimer has restrained the movement of two CD cavities, making them difficult to encapsulate two barbaralanes at the same time.

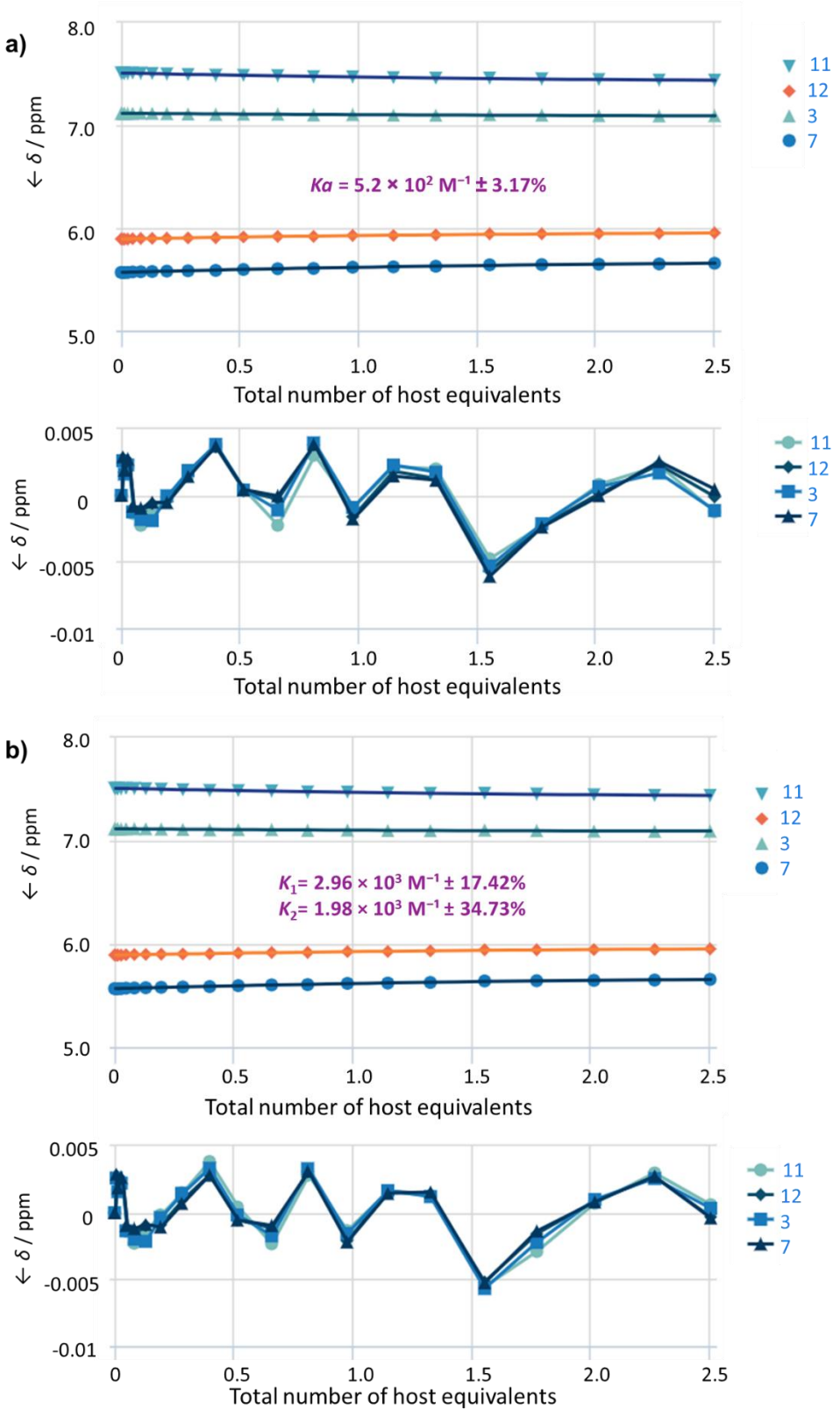

Figure 2.6. Comparison of binding curves of the host-guest complex of **3** and **8** obtained using 1:1 and 1:2 model (Nelder-Mead).

Guest molecule	Association Constant (*Ka*) / M^{-1} with 1:1 model	Association Constant (*Ka*) / M^{-1} with 1:2 model
1	1.6×10^2 $M^{-1} \pm 8.23$	K_1=4.22×10^4 $M^{-1} \pm 584\%$ K_2=25.69 $M^{-1} \pm 12.27\%$
2	4.3×10^3 $M^{-1} \pm 5.81\%$	K_1=69.6 $M^{-1} \pm 4.09\%$ K_2=9.29×10^3 $M^{-1} \pm 7.29\%$
3	5.2×10^2 $M^{-1} \pm 3.17\%$	K_1= 2.96×10^3 $M^{-1} \pm 17.42\%$ K_2= 1.98×10^3 $M^{-1} \pm 34.73\%$

Table 2.1. The calculated binding constants of all three host-guest complex with both 1:1 and 1:2 model. All association constants are the average numbers of Nelder-Mead and L-BFGS-B model.

Apart from using a dimer host, a dimer guest, the synthesised barbaralane dimer **4** was also taken into further host-guest studies. Co-crystal of **4** and β-CD was successfully obtained, and its initial XRD result demonstrated that barbaralane dimer **4** and β-CD form a 3:4 complex similar to a self-assembly tube (Figure 2.6). Notably, the two β-CD molecules in the middle of the unit cell encapsulated two barbaralyl units of **4**, forming a head-to-head dimer. Different from the structures of β-CD⊃**2** and β-CD⊃**3**, the captured barbaralane dimer **4** was observed to be the (*S*,*S*)-diastereoisomer, violating from the racemic (*R*,*S*)-diastereoisomer present in the individual crystal structure of **4**.

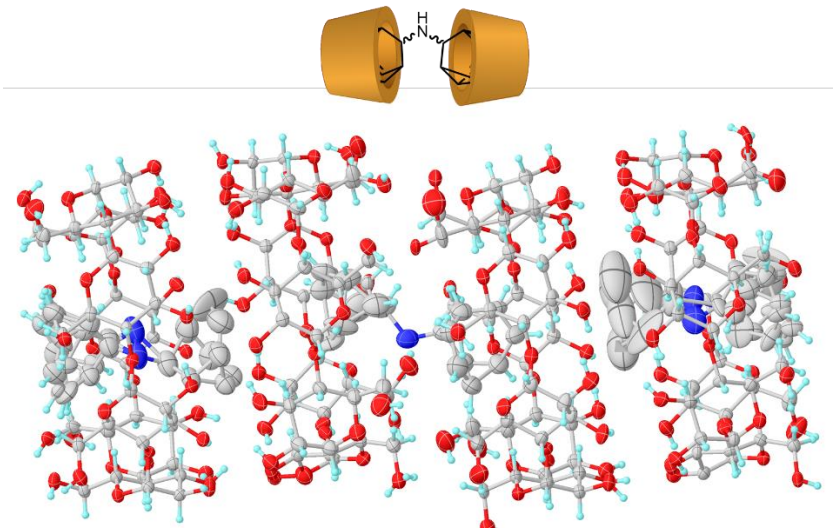

Figure 2.6. Initial co-crystal structure of barbaralane dimer **4** with β-CD. Different elements are distinguished by colours: H = light blue, C = grey, N = dark blue, O = red. Thermal ellipsoids shown with 50% probability.

2.2.4 The 'freezing' reaction of barbaralane and enantiorichment analysis

The studies in section 2.2.2 and 2.2.3 showed that the dynamic enantiomerism of barbaralanes could be controlled by a chiral macrocycle (β-CD). However, these results are mainly demonstrated in the solid state (co-crystal), while the ^{1}H-NMR titrations only work as the method of determining the binding strength and model, but not directly proving the control of dynamic stereochemistry in the solution state. We also cannot simply observe the barbaralane—CD complex by low-temperature NMR spectroscopy as it requires −90 °C to freeze the dynamic enantiomerism,[9] which is far below the melting point of D_2O. To fulfil the blank of solution state studies, a 'freezing' reaction was developed to stop the Cope rearrangements of barbaralanes and trap the dynamic enantiomerism in aqueous solution, and when the reaction process happens in the presence of β-CD, the obtained 'frozen' product should have an enantioenrichment due to the chiral information of the β-CD (Figure 2.7). By analysing the *ee* value of the 'frozen' product, the noncovalent control of dynamic stereochemistry in the solution state can be detected.

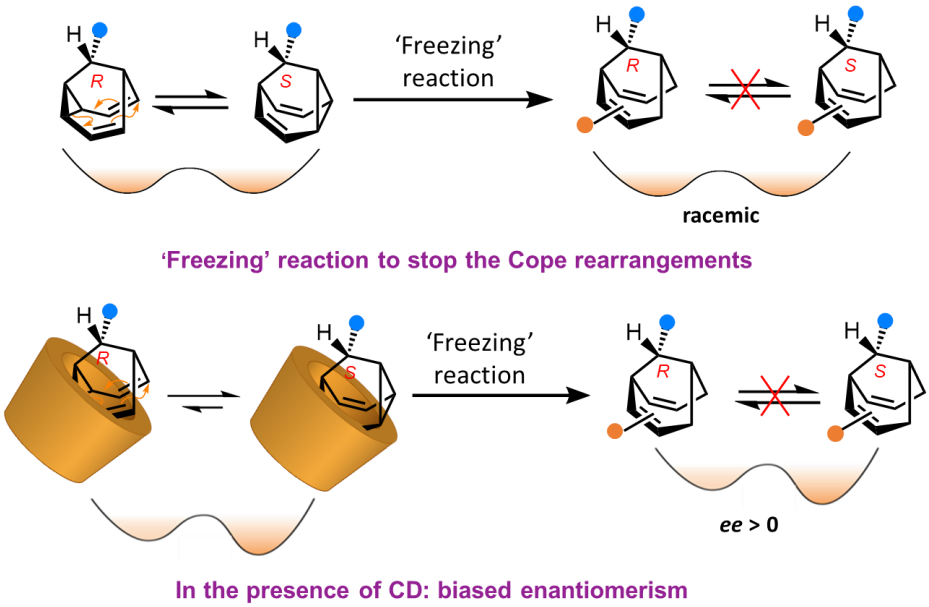

Figure 2.7. Illustration of the 'frozen' reaction and *ee* value determination.

The 'frozen' barbaralane **9** with non-dynamic enantiomerism was synthesised via a radical reaction on parent barbaralol **1**: a radical of mercaptoethanol was generated by benzophenol under 365 nm irradiation before it was attached to the olefin bridge of the barbaralyl core. The

reaction was conducted both in the presence and in the absence of two equivalents of β-CD dissolved in H_2O. The obtained samples of barbaralane **9** were characterised by ^{1}H- and ^{13}C-NMR spectroscopy. The two batches were labelled as **etr-9** (enantioenriched) and **rac-9** (racemic) respectively. Notably, apart from the 10 position (stereocentre), the 4 position with attached mercaptoethanol is also a sp^3 stereocentre, giving rise to diastereoisomerism. Correlations observed in NOESY NMR spectroscopy (full details see section 2.5.1) showed that the 10 and 4 positions have the same stereochemical descriptors, narrowing down the possible diastereoisomers to be only (*R*, *R*) and (*S*, *S*).

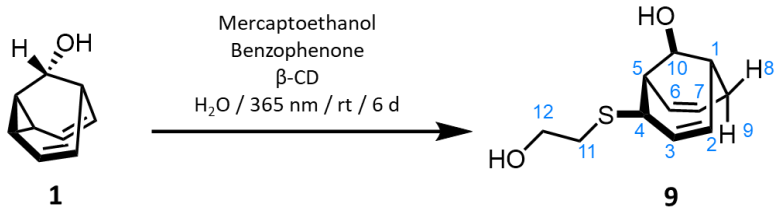

1 **9**

Scheme 2.3. Synthetic route of the 'frozen' barbaralane **9**.

Optical rotation experiments were first conducted as the simplest way to investigate the possible enantioenrichment of **etr-9**. Two sets of optical rotations were carried at 25 °C for both **etr-9** and **rac-9** in $CHCl_3$. The α-D value was recorded ten times on each sample. However, the obtained data was unreliable as the numbers were relatively low, and **rac-9** had even higher absolute value of α-D values than **etr-9**. As the optical rotations could not quantify the *ee* value, more advanced methods were needed.

Set	α-D value (**rac-9**)	α-D value (**etr-9**)
1	9.1	−2.23
2	4.46	−3.00
3	2.57	−2.75
4	2.57	−3.35
5	2.40	−1.37
6	2.40	−0.34
7	3.60	−3.18
8	2.57	−1.72

9	2.57	−2.15
10	3.09	−1.80

Table 2.2. Optical rotation results of **9**. All experiments are conducted using 30 mg of **9** in 2 mL of $CHCl_3$ (0.07 M).

Chiral shift reagents were then used, aiming to determine the *ee* value through separation of NMR peaks via their non-covalent interactions with different enantiomers to induce shifts in the NMR signals of enantiomers and allow their differentiation based on their distinct chemical environments. Pirkle's alcohol was first chosen as it is a common chiral shift reagent with both *R*- and *S*- enantiomer commercially available.[21] Six NMR samples in $CDCl_3$ were prepared: 30 mM of pure **etr-9/rac-9**, 30 mM of **etr-9/rac-9** + 300 mM of *R*-Pirkle's alcohol, and 30 mM of **etr-9/rac-9** + 300 mM of *S*-Pirkle's alcohol. The ^{1}H-NMR of all six samples were recorded on the same instrument at 25 °C, and the obtained spectra were referenced and stacked to observe the shift changes (Figure 2.8). The stacked data showed that addition of Pirkle's alcohol led to observable shift changes of the H_{10} on the stereocentre, and a small split was observed on the top of the peak. However, the four spectra of **etr-9/rac-9** + *R*/*S*-Pirkle's alcohol only had slight differences with one another, and the split of peak 9 is too insignificant to determine the ratio of the two enantiomers. The results indicated that Pirkle's alcohol might not interact strongly enough with **9**, or the *ee* value of **etr-9** might be too small to be observed.

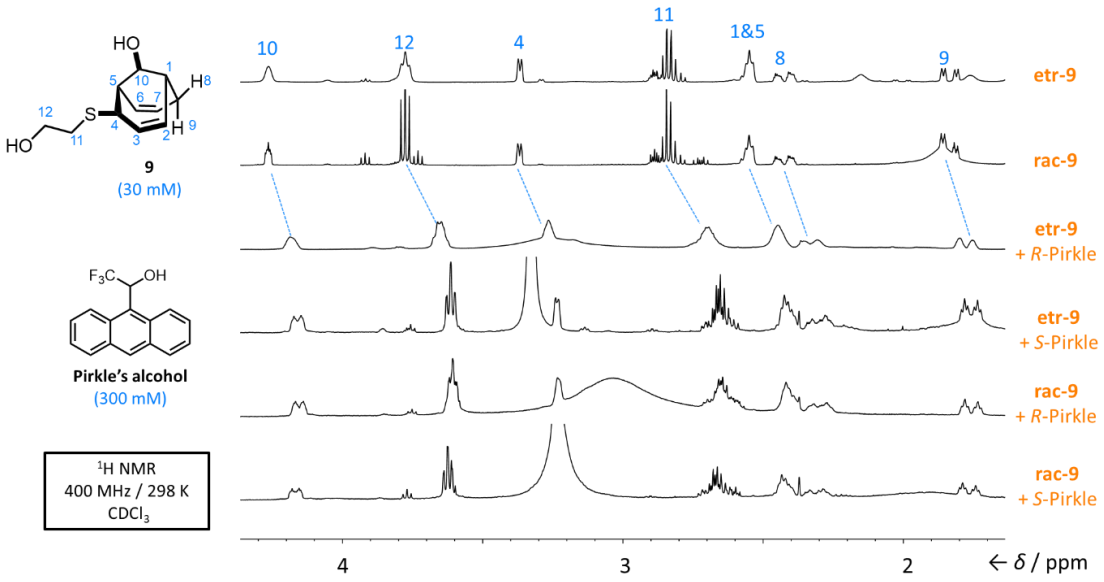

Figure 2.8. Stacked partial ^{1}H-NMR spectra of chiral shift tests on **9** using Pirkle's alcohol.

Similar to Pirkle's alcohol, $Eu(tfc)_3$ was the second option of chiral shift reagent as it is commonly used in determination of the enantioenrichment of alcohols.[17] ^{1}H-NMR spectra of 30 mM of **etr-9/rac-9** + 1.5 mM of $Eu(tfc)_3$ in $CDCl_3$ and pure **9** in $CDCl_3$ were recorded and stacked. Broad peaks and significant shift changes were observed due to the paramagnetic property of the lanthanide element. Similar to the results of using Pirkle's alcohol, the spectra of **etr-9** and **rac-9** after adding $Eu(tfc)_3$ had only slight difference in shifts, and the peak of 1/5 was resolved into two peaks with approximate 1:1 intensity (Figure 2.9), indicating that either the **etr-9** only has a negligible *ee* value, or the $Eu(tfc)_3$ is also not an ideal chiral shift reagent on **9**.

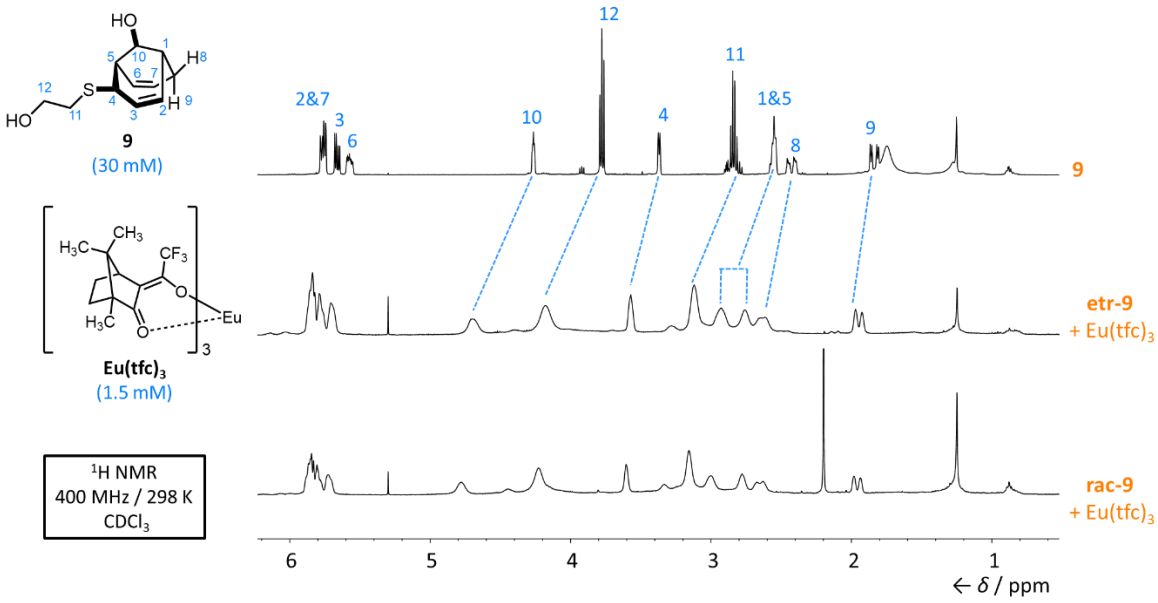

Figure 2.9. Stacked partial ^{1}H-NMR spectra of chiral shift tests on **9** using $Eu(tfc)_3$.

β-CD was also used to work as a chiral shift reagent as the previous results had already shown that it has a strong binding strength with barbaralanes. ^{1}H-NMR spectra of 16.5 mM of **etr-9/rac-9** + 16.5 mM of β-CD in D_2O and pure **9** in D_2O were recorded and stacked. Significant shift changes were observed upon addition of β-CD as expected. However, the spectra of **rac-9** + β-CD and **etr-9** + β-CD showed almost identical NMR shifts, and only peak of 1/5 was resolved into two with approximate 1:1 intensity, thus we still cannot differentiate the **rac-9** and **etr-9**.

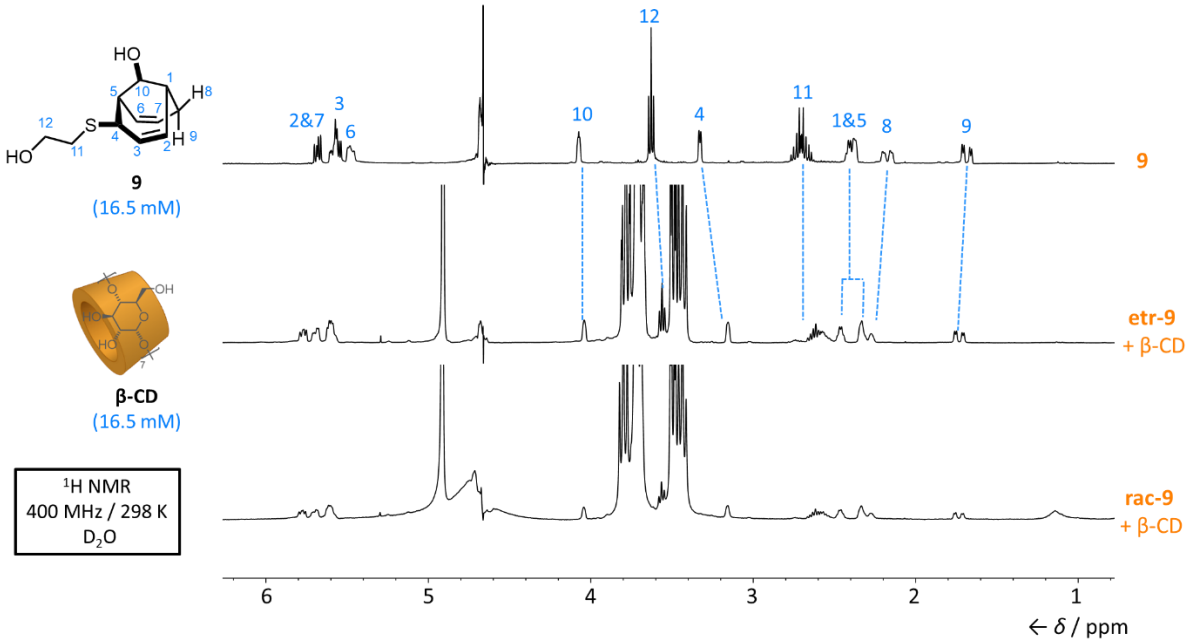

Figure 2.10. Stacked partial ^{1}H-NMR spectra of chiral shift tests on **9** using β-CD. D_2O signal was suppressed using watersupp.

Previous studies on covalent control of barbaralane stereochemistry[9] has demonstrated that Mosher's acid,[23] the chiral derivatizing agent could covalently form esters with barbaralanes and split the 1/5 peak into two in the ^{1}H-NMR spectra via sequential broken of symmetry on the barbaralyl core. Excess amount of *S*-Mosher's acid (10 eq.) was activated as the acid chloride and taken onto an esterification reaction with **etr-9** to form Mosher-**9**. Column chromatography was conducted to obtain semi-crude product with remaining **9**. According to the integrations in the ^{1}H-NMR spectra, only about 50% of the starting material **9** reacted with Mosher's acid, and one equivalent of Mosher's acid was attached to **9**. Significantly large shift change of the 12 position was observed (0.7 ppm) while the 10 position remained at similar shift, and no split of peaks were observed (Figure 2.11). These results suggested that the Mosher's acid only attached to the hydroxyl group on the 12 position instead of the target 10 position due to higher steric hindrance, and the chiral information at the 12 position was not able to transmit to the stereocentre and resolve observable NMR peaks.

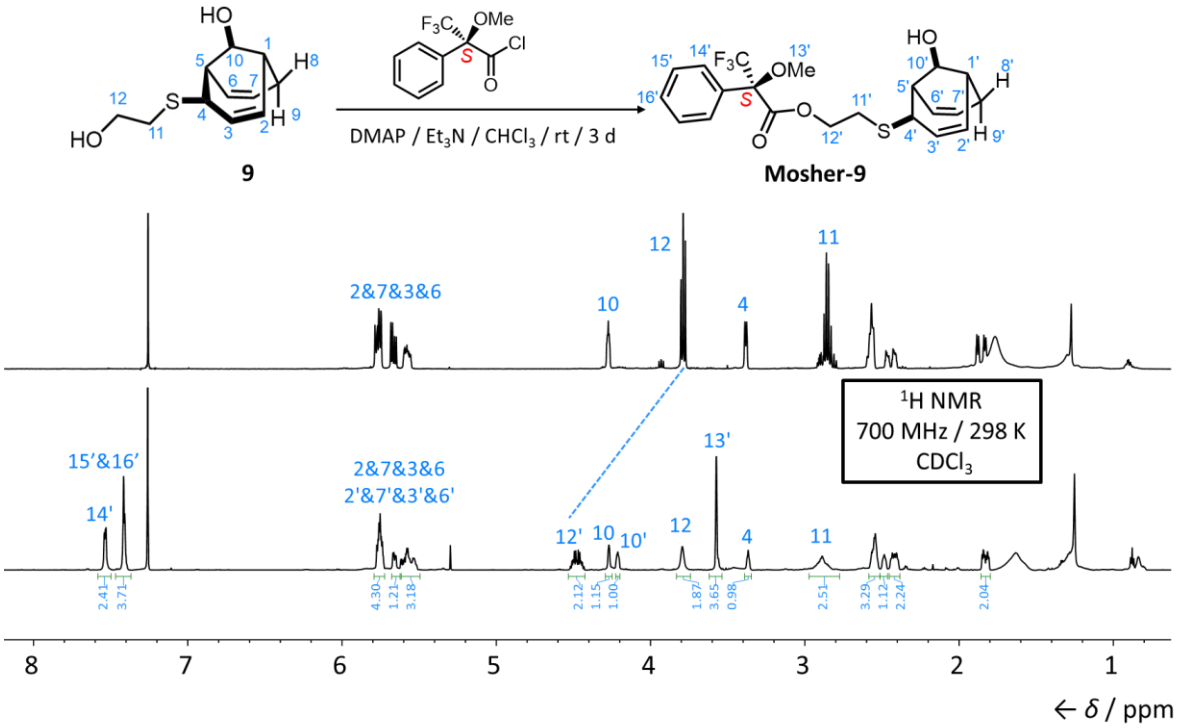

Figure 2.11. Synthetic route of Mosher-**9** and stacked partial ^{1}H-NMR spectra of **9** and semi-crude Mosher-**9**.

2.3 Conclusions and Future Work

In summary, by investigating the dynamic chirality of barbaralane molecules which contain a fluxional sp^{3}–carbon stereocentre, we have proved that the dynamic stereochemistry could be controlled through noncovalent interactions of chiral macrocycles to a certain extent. ^{1}H-NMR titrations between β-CD and synthesised barbaralanes have determined a 1:1 binding stoichiometry and association constants. The co-crystal of β-CD with barbaralol **1** has convincingly demonstrated that the enatiomerisation equilibrium could be biased completely to one side in the solid state. The co-crystals of β-CD with tolyl barbaralol **2** and fluorobenzyl barbaralol **3** present the more complicated, self-sorted racemic dimers which led to further investigations using synthesised β-CD and barbaralane dimers. ^{1}H-NMR titrations between β-CD dimer and barbaralanes gave 1:1 binding stoichiometry instead of the expected 1:2, and no co-crystal structures were obtained, making it difficult to determine more specific binding behaviour of β-CD dimer and barbaralanes. The co-crystal of barbaralane dimer **4** with β-CD was successfully obtained, and initial XRD results showed a self-assembled, tube-like complex

in which a molecule of **4** is encapsulated by two β-CD units, which is similar to the head-to-head dimer of β-CD⊃**2** and β-CD⊃**3** but not racemic as the encapsulated **4** possesses (*S*,*S*)-diastereoisomerism. Comparing the four co-crystal structures obtained, the parent barbaralol **1** and barbaralane dimer **4** have relatively small substituents, and they both exhibit single enantiomer (*S*) when encapsulated by β-CD, while tolyl barbaralol **2** and fluorobenzyl barbaralol **3** have relatively large sizes and both form racemic dimers with the host. However, the tolyl barbaralol **2** is confirmed to have much stronger binding strength with the host than the other two guest molecules, thus it cannot be stated that the racemic dimers are due to incomplete capture and inefficient control of large-sized guests. It is reasonable to deduce that the formation of the racemic dimers is a consequence of closer packings of barbaralane **2** and **3** inside the β-CD cavity, which implies that the packings in the solid state might override the halt of stereochemistry. Further XRD analysis and ^{1}H-NMR titrations are ongoing and will help to draw the conclusion.

The 'freezing reaction' has been developed as an efficient and stable method to stop the Cope rearrangement and trap the dynamic chirality of barbaralanes. Determination of the enantioenrichment of the 'frozen' product **9** obtained in the presence of β-CD could prove the noncovalent effect over enantiomerism equilibrium in the solution state. Various methods of *ee* value determination have been used but no significant difference between **etr-9** and **rac-9** were observed. In future experiments, chiral HPLC will be utilised as it is the most straightforward way to obtain the *ee* value without further interpretation of crude data, and considering the molecule **9** does not have great chromophores, mass-detection might be added. However, the results of chiral shift reagents indicated that the **etr-9** could possibly be racemic (or with very low *ee* value). If so, the 'freezing' reaction will be conducted again on the tolyl barbaralol **2**, as it is less soluble in water and binds more strongly with β-CD, which will increase the noncovalent interactions.

To conclude, we have demonstrated the noncovalent control over dynamic sp^3 stereochemistry via encapsulation with chiral macrocycles. Convincing results have been obtained via NMR spectroscopy, binding model and XRD, with more experiments in the solution state needed to complete the story. ^{1}H-NMR titrations using lower concentrations of host and guest molecules

(3.08 mM:0.62 mM) will be conducted as supplementary experiments. The behaviour of barbaralanes changing their chirality in response to macrocycles could mimic the conformational induced-to-fit model in nature[24] through a dynamic covalent process, providing these molecules potential to be developed in the field of catalysis or molecular devices.

2.4 Experimental Details

2.4.1 Specific Experimental Methods

For general experimental details see page *xv*. Solution-state ^{1}H NMR spectra for barbaralanes **1**-**3** with β-CD dimer **8** were acquired on a Varian Inova-500 (^{1}H 500.130 MHz and ^{13}C 125.758) MHz spectrometer with either presaturation or a pulse sequence combining Robust-5 and PROJECT pulse sequences.[25] The X-ray single-crystal diffraction data were collected at 120.0(2) K using λMoKα radiation (λ = 0.71073 Å) on a Bruker D8Venture (Photon100 CMOS detector, IμS-microsource, focusing mirrors) diffractometer for barbaralanes **1**-**4** and the host-gust complex of β-CD and barbaralol **1**. Diffractometers were equipped with Cryostream (Oxford Cryosystems) open-flow nitrogen cryostats. All structures were solved by direct method and refined by full-matrix least squares on F2 for all data using Olex2[26] and SHELXT[27] software. All non-hydrogen atoms were refined anisotropically and hydrogen atoms were placed in the calculated positions and refined in riding mode.

2.4.2 Synthesis of guest barbaralanes 1-4

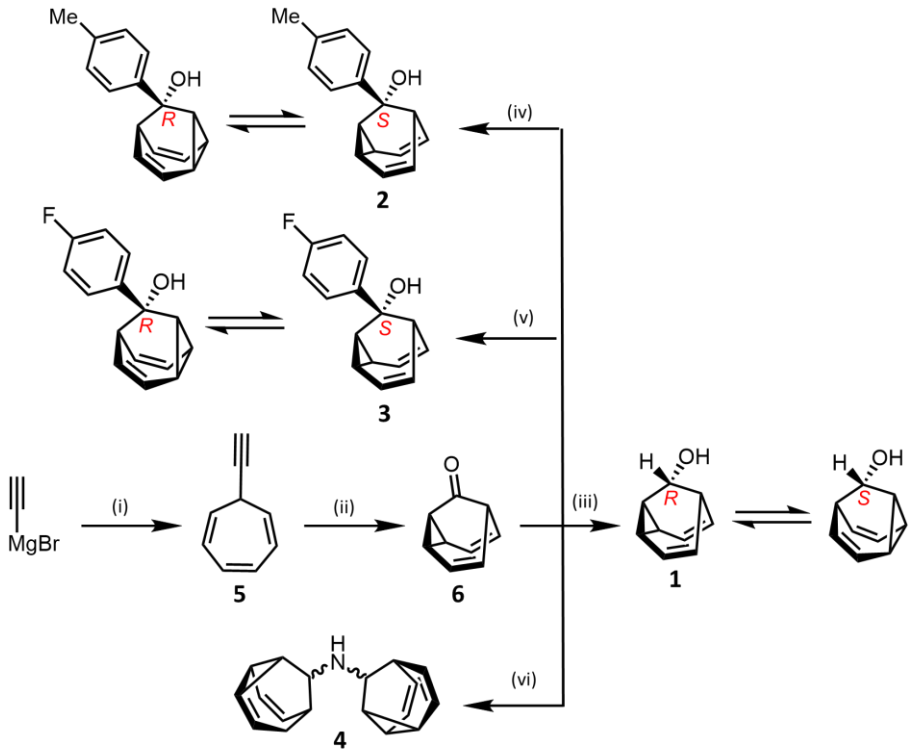

Scheme 2.4. Synthesis of compounds **5** and **6**, barbaralane monomers **1-3** and barbaralane dimer **4**. Reagents and conditions: (i) 1. LiCl / THF / –78 °C / 10 min. 2. Tropylium tetrafluoroborate / –78 °C to rt. (ii) IPrAu(MeCN)BF_4 (5 mol%) / Ph_2SO / CH_2Cl_2 / rt / 16 h. (iii) $LiAlH_4$ / Et_2O / 0 °C / 3 h. (iv) *p*-Tolylmagnesium bromide / THF / 0 °C to rt / 16 h. (v) *p*-Fluoromagnesium bromide / THF / 0 °C to rt / 16 h. (vi) NH_3 / MeOH / glacial AcOH / $NaBH_3CN$ / 100 °C / 24 h.

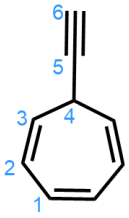

7-Ethynylcyclohepta-1,3,5-triene (5): Anhydrous LiCl (0.524 g, 12.4 mmol) was placed in an oven-dried round-bottomed flask fitted with a septum under an N_2 atmosphere. Anhydrous THF was added (38 mL) and the resulting solution was cooled to –78 °C before addition of a solution of ethynyl magnesium bromide (22.5 mL, 12.2 mmol, 0.5 M in THF) and stirring for 10 min at this temperature. Tropylium tetrafluoroborate (1.00 g, 5.62 mmol) was added to the reaction mixture and the reaction mixture was stirred for 16 h, where the temperature was allowed to warm to rt, following removal of the ice bath. The reaction was quenched with a saturated aqueous solution of NH_4Cl (20 mL), then extracted with Et_2O (3 × 30 mL). The combined organic extracts were then dried

over $MgSO_4$, filtered and the solvent removed under reduced pressure (rotary evaporator bath at 16 °C, ≥ 100 mbar). The crude residue was purified by column chromatography (Teledyne Isco CombiFlash Rf+ system, 24 g SiO_2, n-pentane) to give the title compound as a colouress oil (539 mg, 4.60 mmol, 83%). **^{1}H NMR** (600 MHz, $CDCl_3$) δ 6.66 (dd, *J* = 3.7, 2.7 Hz, 2H, H_1), 6.33 – 6.07 (m, 2H, H_2), 5.40 – 5.16 (m, 2H, H_3), 2.73 – 2.43 (m, 1H, H_4), 2.17 (s, 1H, H_6). **^{13}C NMR** (151 MHz, $CDCl_3$) δ 131.2 (C_1), 125.1 (C_2), 123.0 (C_3), 85.8 (C_5), 68.5 (C_6), 31.5 (C_4). **HRMS-ASAP** m/z = 117.0701 $[M+H]^+$, calculated for C_9H_9 = 117.0704.

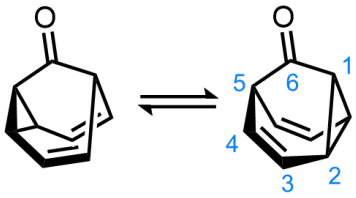

Tricyclo[3.3.1.0^{2,8}]nona-3,6-dien-9-one ((Barbaralone 6): 7-Ethynylcyclohepta-1,3,5-triene **5** (1.00 g, 8.68 mmol) and diphenyl sulphoxide (3.51 g, 17.0 mmol) were charged in a flask and dissolved in anhydrous CH_2Cl_2 (15 mL) at rt. (Acetonitrile)[1,3-bis(2,6-diisopropylphenyl)-imidazol-2-ylidene]gold(I) tetrafluoroborate (309 mg, 0.43 mmol) was added in one portion at the same temperature and the reaction mixture was stirred for 16 h. The reaction was quenched with 10 drops of Et_3N and the solvent was removed under reduced pressure. The crude residue was purified by column chromatography (Teledyne Isco CombiFlash Rf+ system, 24 g SiO_2, hexanes−EtOAc, gradient elution from 0 to 100%) to give the title compound as a light yellow solid (685 mg, 5.18 mmol, 60%). **M.P.** 55 – 57 °C. **^{1}H NMR** (700 MHz, $CDCl_3$) δ 5.97 – 5.51 (m, 2H, H_3), 4.32 (br s, 4H, $H_{2/4}$), 2.90 – 2.55 (m, 2H, $H_{1/5}$). **^{13}C NMR** (176 MHz, $CDCl_3$) δ 211.0 (C_6), 121.7 ($C_{2/4}$ or C_3), 121.5 ($C_{2/4}$ or C_3), 38.3 ($C_{1/5}$). **HRMS-ASAP** m/z = 133.0648 $[M+H]^+$, calculated for $C_9H_9O^+$ = 133.0653.

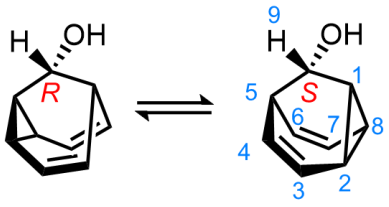

(±)-Tricyclo[3.3.1.0^{2,8}]nona-3,6-dien-9-ol (Barbaralol 1): $LiAlH_4$ (120 mg, 3.16 mmol) was placed in an oven-dried round-bottomed flask fitted with a septum under a N_2 atmosphere and suspended in anhydrous Et_2O (5 mL). The mixture was cooled to 0 °C and then a solution of barbaralone **6** (200 mg, 1.51 mmol) in anhydrous Et_2O (5 mL) was added dropwise. The reaction mixture was stirred at this temperature for 3 h. The reaction was quenched with a saturated aqueous solution of potassium

sodium tartrate (25 mL) and allowed to warm to rt before being extracted with Et_2O (3 × 30 mL). The combined organic extracts were dried over $MgSO_4$ and the solvent was removed under reduced pressure (rotary evaporator bath at 16 °C, ≥ 100 mbar). The crude residue was purified by column chromatography (Teledyne Isco CombiFlash Rf+ system, 24 g SiO_2, *n*-pentane–Et_2O, gradient elution from 0 to 100%) to give the title compound as a white solid (159 mg, 1.18 mmol, 78%). **M. P.** 82 – 84 °C. **^{1}H NMR** (400 MHz, $CDCl_3$) δ 5.88 (t, J = 7.9 Hz, 1H, H_3), 5.54 (t, J = 7.6 Hz, 1H, H_7), 4.16 – 4.04 (m, 2H, H_6 and H_8), 4.02 – 3.92 (m, 2H, H_2 and H_4), 3.61 (d, J = 3.3 Hz, 1H, H_9), 2.59 – 2.47 (m, 2H, H_1 and H_5), 1.14 (s, 1H, H_{10}). **^{13}C NMR** (151 MHz, $CDCl_3$) δ 123.3 (C_3), 120.9 (C_7), 76.4 (C_6 and C_8), 72.4 (C_2 and C_4), 62.5 (C_9), 31.8 (C_1 and C_5). **HRMS-ASAP** *m/z* = 117.0699 $[M\text{-}OH]^+$, calculated for $C_9H_9^+$: 117.0704.

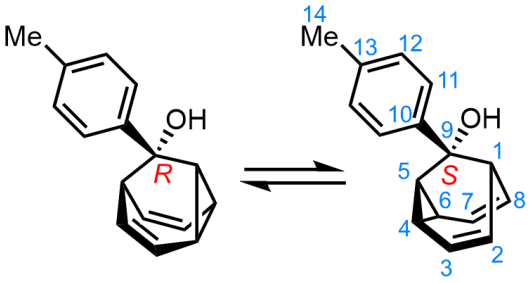

(±)-6-(4-Tolyl)bicyclo[3.2.2]nona-3,8-dien-6-ol (Tolyl barbaralol 2): Magnesium turnings (100 mg, 4.54 mmol) and I_2 (57 mg, 0.23 mmol, 5 mol%) were placed in an oven-dried two-necked round-bottomed flask fitted with a condenser and a septum under a N_2 atmosphere. The flask was gently heated with a heat gun until the I_2 started to sublime for activation of Mg. The flask was cooled down to rt. A quarter of a solution of 4-bromotoluene (760 mg, 4.5 mmol) in anhydrous THF (10 mL) was added to the reaction mixture, which was heated until it reached reflux. Upon gentle reflux, the remaining solution of 4-bromotoluene in anhydrous THF was added dropwise over 30 min. The reaction mixture was heated at reflux for 30 min before cooling to rt. Barbaralone **6** (111 mg, 0.84 mmol) was transferred to an oven-dried round-bottomed flask, and the flask was purged with N_2. Anhydrous THF (10 mL) was added and the solution was cooled to 0 °C. The Grignard solution (prepared above) was added dropwise over 30 min to the barbaralone solution. The reaction mixture was stirred for 16 h, and the temperature was raised from 0 °C to rt, following removal of the ice bath. The reaction was quenched with a saturated aqueous solution of NH_4Cl (10 mL), then extracted with EtOAc (3 × 20 mL). The combined organic extracts were dried over $MgSO_4$, filtered and the solvent

removed under reduced pressure. The crude residue was purified by column chromatography (Teledyne Isco CombiFlash Rf+ system, 24 g SiO_2, hexanes–CH_2Cl_2, gradient elution from 0 to 100% including 0.5% Et_3N in the elution) to yield the title compound as a cream-coloured solid (136 mg, 0.61 mmol, 80%). **M.P.** 59 – 61°C. **^{1}H NMR** (700 MHz, $CDCl_3$) δ 7.33 (d, J = 8.2 Hz, 2H, H_{11}), 7.12 (d, J = 7.9 Hz, 2H, H_{12}), 5.91 (t, J = 7.7 Hz, 1H, H_7), 5.58 (t, J = 7.6 Hz, 1H, H_3), 4.28 – 4.24 (m, 2H, $H_{6/8}$), 4.24 – 4.21 (m, 2H, $H_{2/4}$), 2.83 – 2.57 (m, 2H, $H_{1/5}$), 2.33 (d, J = 0.7 Hz, 3H, H_{14}), 1.98 (s, 1H, H_{15}). **^{13}C NMR** (176 MHz, $CDCl_3$) δ 140.4 (C_{10}), 136.8 (C_{13}), 128.6 (C_{12}), 126.4 (C_{11}), 123.2 (C_7), 120.9 (C_3), 77.8 ($C_{2/4}$), 75.5 ($C_{6/8}$), 68.6 (C_9), 38.2 ($C_{1/5}$), 21.2 (C_{14}). **HRMS-ASAP** m/z = 207.1154 $[M\text{-}OH]^+$, calculated for $C_{16}H_{15}$: 207.1174.

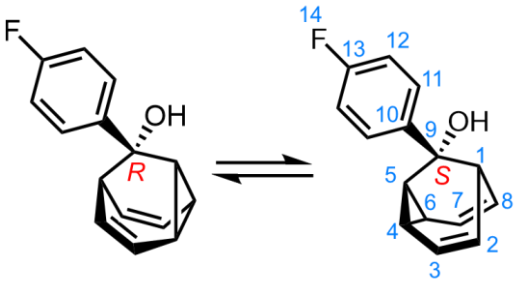

(±)-6-(4-Fluorophenyl)bicyclo[3.2.2]nona-3,8-dien-6-ol (Fluorobenzyl barbaralol 3): Magnesium turnings (120 mg, 5.04 mmol) and I_2 (64 mg, 0.25 mmol, 5 mol%) were placed in an oven-dried two-necked round-bottomed flask fitted with a condenser and a septum under a N_2 atmosphere. The flask was gently heated with a heat gun until the I_2 started to sublime. The flask was cooled down to rt. A quarter of a solution of 1-bromo-4-fluorobenzene (875 mg, 5.00 mmol) in anhydrous THF (10 mL) was added to the reaction mixture, which was heated until it reached reflux. Upon gentle reflux, the remaining solution of 1-bromo-4-fluorobenzene in anhydrous THF was added dropwise over 30 min. The reaction mixture was heated at reflux for 30 min before cooling to rt. Barbaralone **6** (111 mg, 0.84 mmol) was transferred to an oven-dried round-bottomed flask, and the flask was purged with N_2. Anhydrous THF (10 mL) was added and the solution was cooled to 0 °C. The Grignard solution (prepared above) was added dropwise over 30 min to the barbaralone solution. The reaction mixture was stirred for 16 h, and the temperature was raised from 0 °C to rt, following removal of the ice bath. The reaction was quenched with a saturated aqueous solution of NH_4Cl (10 mL), then extracted with EtOAc (3 × 20 mL). The combined organic extracts were dried over $MgSO_4$, filtered and the solvent removed under reduced pressure. The crude residue was purified by column chromatography

(Teledyne Isco CombiFlash Rf+ system, 24 g SiO_2, hexanes−CH_2Cl_2, gradient elution from 0 to 100% including 0.5% Et_3N in the elution) to yield the title compound as a white solid (129 mg, 0.84 mmol, 67%). **M.P.** 60 – 62 °C. **^{1}H NMR** (700 MHz, $CDCl_3$) δ 7.48 – 7.19 (m, 2H, H_{11}), 7.07 – 6.75 (m, 2H, H_{12}), 5.92 (t, J = 7.7 Hz, 1H, H_7), 5.59 (t, J = 7.7 Hz, 1H, H_3), 4.29 – 4.24 (m, 2H, $H_{6/8}$), 4.24 – 4.17 (m, 2H, $H_{2/4}$), 2.68 – 2.61 (m, 1H, $H_{1/5}$), 2.04 (s, 1H, H_{15}). **^{13}C NMR** (176 MHz, $CDCl_3$) δ 162.7 (d, J_{CF} = 245.2, C_{13}), 139.20 (C_{10}), 128.20 (d, J_{CF} = 8.0, C_{11}) 123.3 (C_7), 121.0 (C_3), 114.67 (d, J_{CF} = 21.1, C_{12}), 77.8 ($C_{2/4}$), 75.4 ($C_{6/8}$), 68.5 (C_9), 38.3 (C_1 and C_5). **^{19}F NMR** (376 MHz, $CDCl_3$) δ –119.30 (m, F_{14}). **HRMS-ASAP** m/z = 211.0923 $[M\text{-}OH]^+$, calculated for $C_{15}H_{12}F$: 211.0911.

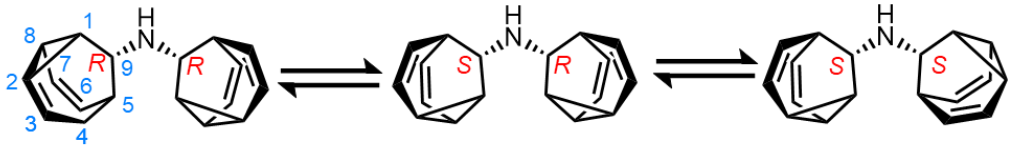

Di(9-barbaralyl) amine (Barbaralane dimer 4): Barbaralone **6** (80 mg, 0.61 mmol) and ammonia (0.15 mL, 2.0 M in MeOH, 0.30 mmol) was dissolved in dry MeOH (0.8 mL) in a microwave vial. Glacial acetic acid (12 µL, 0.21 mmol) was added and the solution was stirred at rt for 30 min. $NaBH_3CN$ (46 mg, 0.73 mmol) was added and the reaction mixture was stirred at 100 °C to reflux for 24 h. The reaction was quenched with 5 drops of Et_3N, washed with a saturated solution of aqueous $NaHCO_3$ (10 mL), extracted with CH_2Cl_2 (3 × 20 mL), dried over $MgSO_4$ and purified by column chromatography (Teledyne Isco CombiFlash Rf+ system, 12 g SiO_2, CH_2Cl_2−15% MeOH, 1% Et_3N) to give the title compound as a brown solid. (39 mg, 0.16 mmol, 53% yield) **M. P.** 78 – 81 °C. **^{1}H NMR** (600 MHz, $CDCl_3$) δ 5.78 (t, J = 7.8 Hz, 2H, H_3), 5.56 (t, J = 7.7 Hz, 2H, H_7), 4.07 – 3.99 (m, 4H, $H_{6/8}$), 3.91 (m, 4H, $H_{2/4}$), 2.47 (t, J = 2.8 Hz, 2H, H_9), 2.38 (m, 4H, $H_{1/5}$). **^{13}C NMR** (167 MHz, $CDCl_3$) δ 121.2 ($C_{3/7}$), 75.8 ($C_{6/8}$), 72.2 ($C_{2/4}$), 45.7 (C_9), 29.7 ($C_{1/5}$). **HRMS-ASAP** m/z = 250.1588 $[M+H]^+$, calculated for $C_{18}H_{20}N^+$ = 250.1590.

2.4.3 Synthesis of β-CD dimer 8

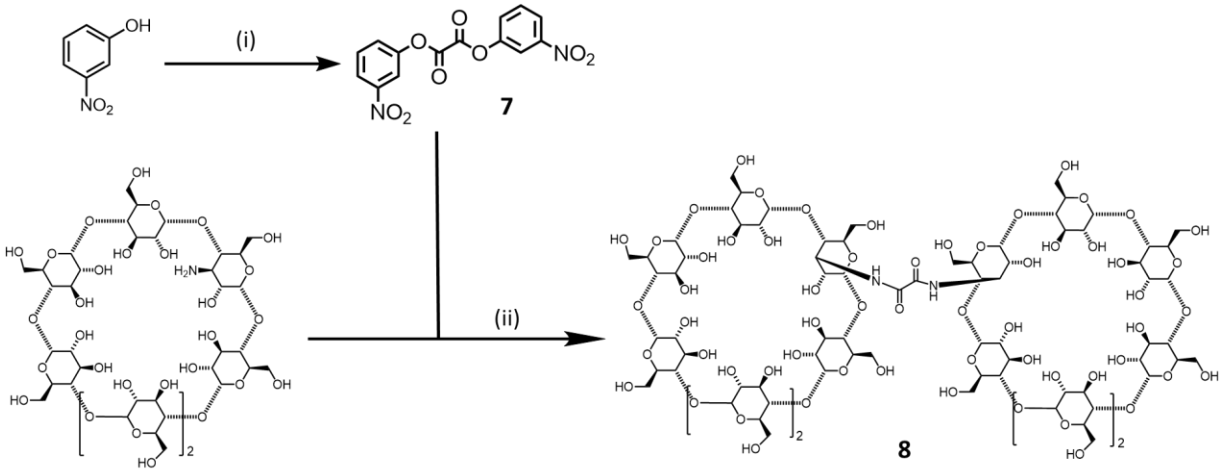

Scheme 2.4. Synthesis of compound **7** and β-CD dimer **8**. Reagents and conditions: (i) Oxalyl chloride / Et_3N / PhMe / 0 °C / 2 h. (ii) DMF / rt / 36 h.

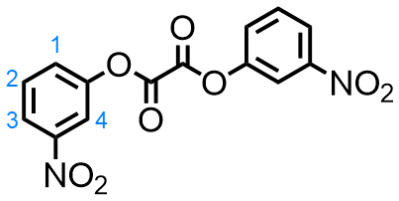

Bis(3-nitrophenyl) oxalate (7): A solution of 3-nitrophenol (2.13 g, 15.3 mmol) in 40 mL of toluene was dried by azeotropic distillation. The solution was cooled to 0 °C under an N_2 atmosphere. Et_3N (2.1 g, 15.1 mmol) and oxalyl chloride (0.64 mL, 7.5 mmol) was added with stirring. The temperature was kept below 10 °C using an ice bath. After stirring for 2 h, a precipitate formed and was collected using Buchner filtration, and dried under reduced pressure. The product was washed with anhydrous chloroform (2 × 10 mL) and dried under vacuum. Recrystallisation from MeCN afforded the title compound as pale-yellow platelets (94.7 mg, 0.285 mmol, 4% yield). **^{1}H NMR** (400 MHz, $CDCl_3$) δ 8.26 (d, J = 7.9 Hz, 1H, H_3), 8.22 (s, 1H, H_4), 7.70 (m, 1H, H_1), 7.67 (dd, J = 4.2, 2.4 Hz, 2H, H_2). Characterisation data are consistent with those reported previously: *Aust. J. Chem.* 1997, **50**, 9-12.

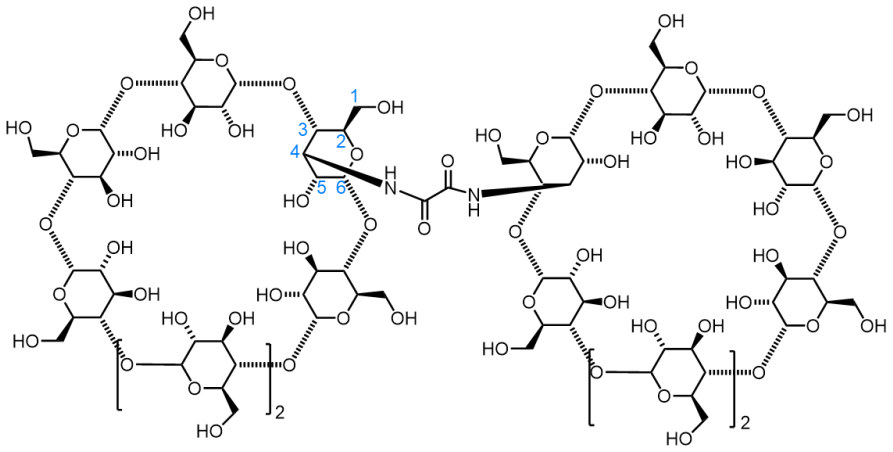

***N*,*N*-Bis((2AS,3AS)-3A-deoxy-β-cyclodextrin-3A-yl)oxalamide (β-CD dimer 8):** Amino-substituted cyclodextrin (200 mg, 0.176 mmol) and bis(3-nitrophenyl) oxalate **7** (29.0 mg, 0.0867 mmol) was dissolved in DMF (4 mL) and the solution was stirred at rt for 36 h. The solvent was removed under reduced pressure, and the crude residue was purified *via* column chromatography (Teledyne Isco CombiFlash Rf+ system, C18, H_2O—MeOH gradient elution from 0 to 100%) to give the title compound as colorless crystals (92.9 mg, 0.0404 mmol, 46% yield). **^{1}H NMR** (600 MHz, D_2O): δ 3.60 (m, 28H, H_1), 3.85 (m, 56H, $H_{2/3/4/5}$), 5.05 (m, 14H, H_6). Characterisation data are consistent with those reported previously: *Aust. J. Chem.* 1997, **50**, 9-12.

2.4.4 Synthesis of 'frozen' barbaralane 9

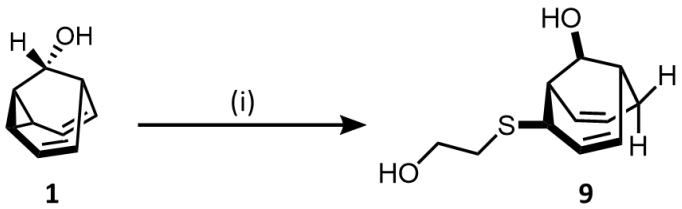

Scheme 2.5. Synthesis of barbaralane **9**. Reagents and conditions: (i) Mercaptoethanol / benzophenone / β-CD / 365 nm / H_2O / 6 d.

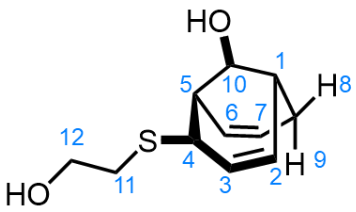

4-((2-hydroxyethyl)thio)bicyclo[3.3.1]nona-2,6-dien-9-ol (9): Barbaralol **1** (190 mg, 1.42 mmol), β-cyclodextrin (3.36 g, 2.96 mmol), and mercaptoethanol (570 mg, 7.12 mmol) were dissolved in degassed H_2O (100 mL). Benzophenone

(100 mg, 1.04 mmol) was added and the reaction mixture was irradiated using a 365 nm UV lamp at rt for 6 d. The aqueous mixture was extracted with $CHCl_3$/iPrOH (7:3, 3 × 50 mL), purified via column chromatography (Teledyne Isco CombiFlash Rf+ system, 12 g SiO_2, DCM – 15% MeOH gradient elution), and washed with H_2O (20 mL) to give the title compound as a yellow oil (40 mg, 0.188 mmol, 15% yield). **^{1}H NMR** (400 MHz, $CDCl_3$) δ 5.76 (m, *J* = 9.8, 5.9 Hz, 2H, $H_{2/7}$), 5.66 (dd, *J* = 9.9, 4.6 Hz, 1H, H_3), 5.58 (ddd, *J* = 9.5, 5.5, 2.9 Hz, 1H, H_6), 4.30 – 4.24 (m, 1H, H_{10}), 3.78 (t, *J* = 5.8 Hz, 2H, H_{12}), 3.37 (d, *J* = 4.7 Hz, 1H, H_4), 2.85 (t, *J* = 5.7 Hz, 2H, H_{11}), 2.55 (m, *J* = 4.8 Hz, 2H, $H_{1/5}$), 2.43 (ddd, *J* = 18.6, 5.5, 2.6 Hz, 1H, H_8), 1.84 (dd, J = 18.4, 4.8 Hz, 1H, H_9). **^{13}C NMR** (101 MHz, $CDCl_3$) δ 132.3 (C_6), 127.1 (C_2), 126.0 (C_3), 125.1 (C_7), 64.8 (C_{10}), 61.0 (C_{12}), 46.7 (C_5), 42.1 (C_1), 35.9 (C_4), 34.9 (C_{11}), 25.0 (C_8). **HRMS-ESI**: m/z = 235.0760 $[M+Na]^+$, calculated for $C_{11}H_{16}NaO_2S^+$ = 235.0763

2.5 Appendix of Supplementary Data and Discussion

2.5.1 Structural Assignment by 2D NMR

The relative stereochemistry of the 10 and 4 positions of synthesised barbaralane **9** was determined by 2D NMR. The broad ^{1}H peak at 1.74 ppm was confirmed to be the signal of the hydroxyl group at 10 position (OH_{10}) as it does not correlate to any other ^{1}H in COSY or any ^{13}C signal in HSQC and HMBC spectra, and the NOESY spectrum showed that the broad OH peak only corelates to H_{12} and H_7 but not H_{11} (Figure 2.11). As no correlation of H_7 with H_{12} or H_{11} was observed, the OH_{10} was determined to be on the same side of the mercaptoethanol moiety, which suggested that the substituents on 10 and 4 positions are on the same face.

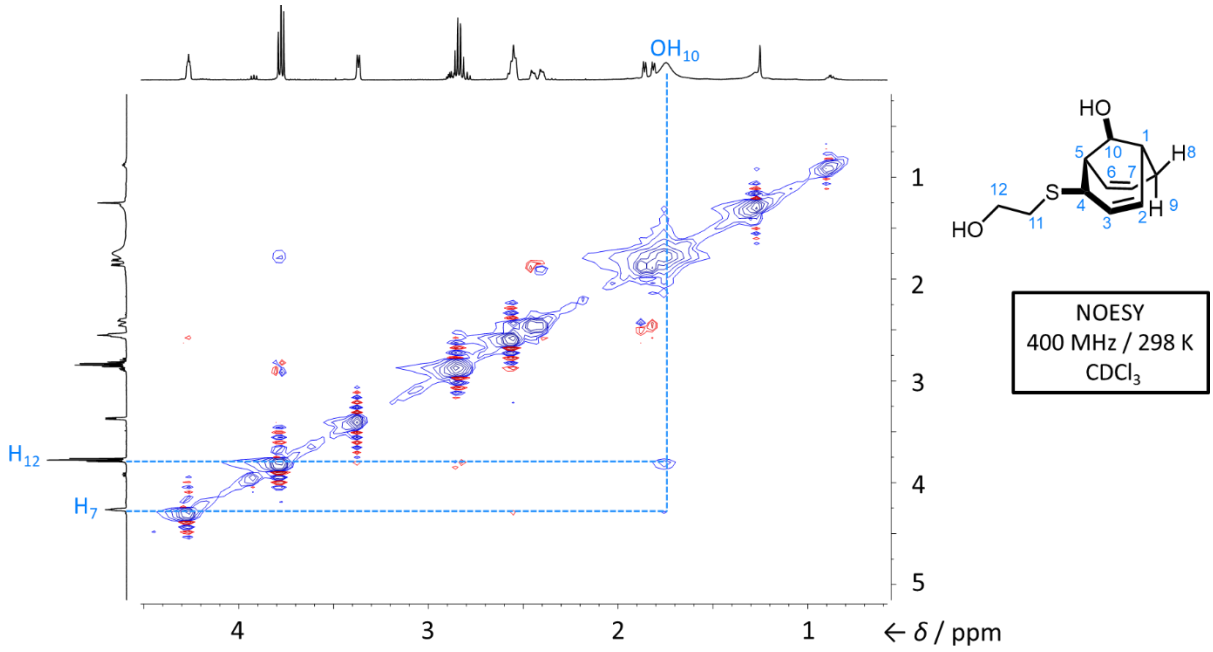

Figure 2.11. Partial NOESY spectrum of **9**.

2.5.2 X-ray Crystallographic Analysis

(±)-Tricyclo[3.3.1.02,8]nona-3,6-dien-9-ol (Barbaralol 1)

Crystals of **1** suitable for X-ray diffraction were grown by slow evaporation of a saturated MeCN solution.

Figure 2.12. Solid-state structure of **1** including probability ellipsoids at 50%.

Crystal data: $C_9H_{10}O$, M = 134.17, crystal system = monoclinic, space group = C2/c, a = 21.0930(5), b = 12.8259(3), c = 20.9409(5) Å, , α = 90°, β = 104.257(1)°, γ = 90°, U = 5490.8(2) $Å^3$, F(000) = 2304.0, Z = 32, Dc = 1.298 $g \cdot cm^{-3}$, μ = 0.653 mm^{-1} (Mo-Kα, λ = 0.71073 Å), T = 120(1) K. Final $wR_2(F^2)$ = 0.0945 for all data, conventional $R_1(F)$ = 0.0360 for reflections with I ≥ 2σ, GOF = 1.037.

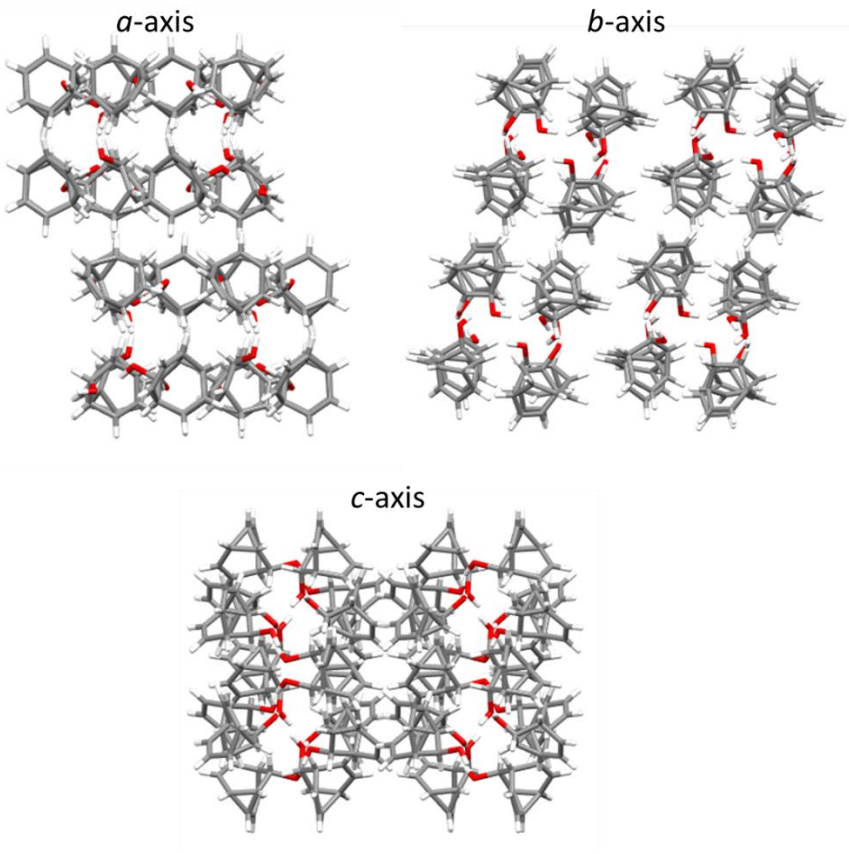

Figure 2.13. Solid-state superstructure of **1** viewed along the three unit cell axes.

(±)-6-(4-Tolyl)bicyclo[3.2.2]nona-3,8-dien-6-ol (Tolyl barbaralol 2)

Crystals of **2** suitable for X-ray diffraction were grown by slow evaporation of a saturated CH_2Cl_2 solution.

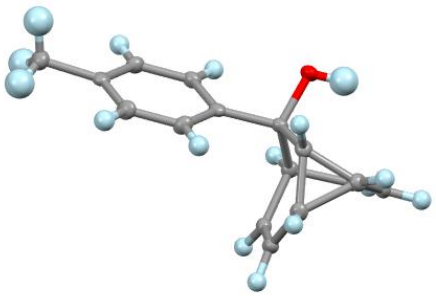

Figure 2.14. Solid-state structure of **2** including probability ellipsoids at 50%.

Crystal data: $C_{16}H_{16}O$, M = 224.29, crystal system =monoclinic, space group = $P2_1/n$, a = 10.2068(4) Å, b = 11.9926(4) Å, c =19.6537(7) Å, α = 90 °, β = 103.9617(14) °, γ = 90 °, U =2334.66(15) $Å^3$, F(000) = 960.0, Z =8, Dc = 1.276 $g \cdot cm^{-3}$, μ = 0.078 (MoKα, λ = 0.71073),

T =120.0 K. Final $wR_2(F^2)$ = 0.0945 for all data, conventional $R_1(F)$ = 0.0372 for reflections with $I \geq 2\sigma$, GOF = 1.027.

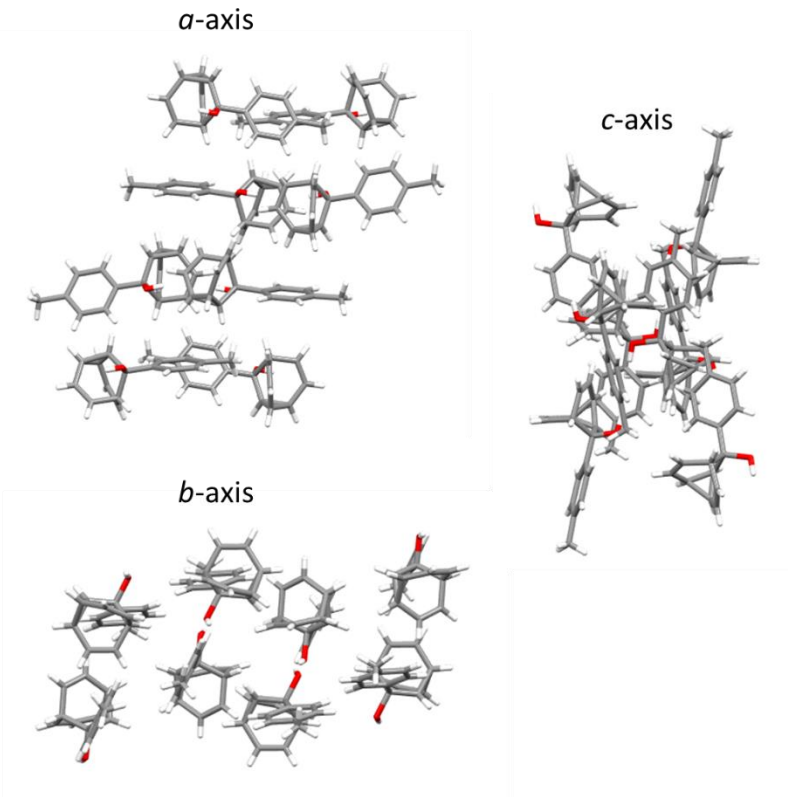

Figure 2.15. Solid-state superstructure of **2** viewed along the three unit cell axes.

Di(9-barbaralyl) amine (Barbaralane dimer 4)

Crystals of **4** suitable for X-ray diffraction were grown by slow evaporation of a hexanes solution at room temperature.

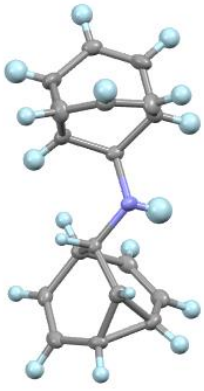

Figure 2.16. Solid-state structure of **4** including probability ellipsoids at 50%.

Crystal data: C_{18} H_{19} N, M = 249.35, crystal system = monoclinic, space group = P2/n, a = 13.0743(15) Å, b = 6.3413(7) Å, c = 15.7485(18) Å, α = 90 °, β = 97.325(4) °, γ = 90 °, U = 1295.02 Å^3, Z = 4, Dc = 1.277 g·cm^{-3}.

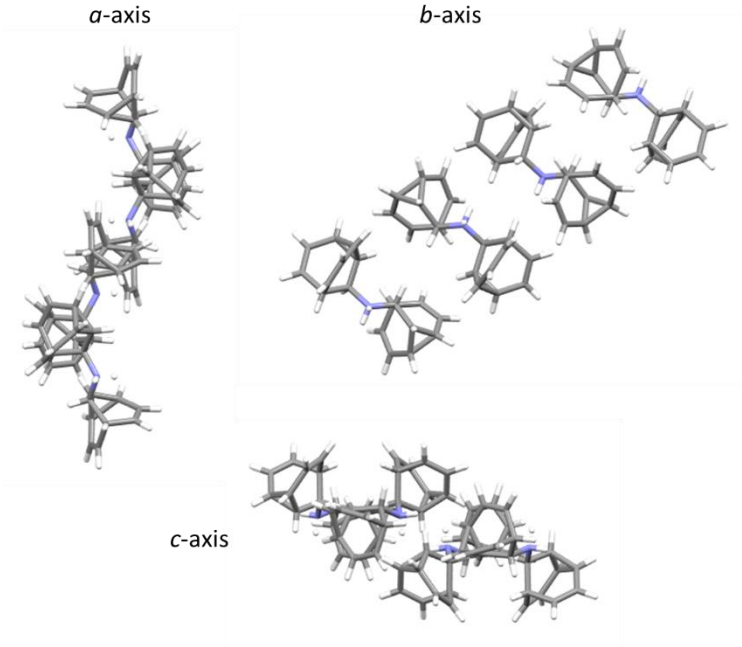

Figure 2.17. Solid-state superstructure of **2** viewed along the three unit cell axes.

Host–Guest Complex: β-CD–Tricyclo[3.3.1.02,8]nona-3,6-dien-9-ol (1)

Crystals of the host–guest complex suitable for X-ray diffraction were grown by the slow cooling of an aqueous H_2O solution of the two compounds in a one-to-one ratio from 100 °C to room temperature over the course of two weeks in a crystallisation oven which was followed by slow evaporation of the solution.

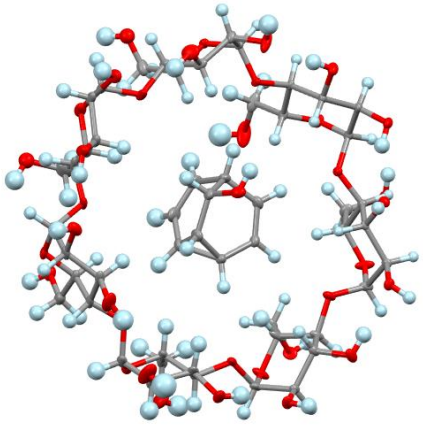

Figure 2.18. Solid-state structure of the host–guest complex including probability ellipsoids at 50%.

Crystal data: $C_{51}H_{92}O_{42}$, M = 1377.24, crystal system = monoclinic, space group = $P2_1$, a = 15.0368(9) Å, b = 10.3400(6) Å, c = 20.0143(12) Å, α = 90 °, β =102.729(2) °, γ = 90 °, U = 3035.4(3) Å^3, F(000) = 1468.0, Z =2, Dc = 1.507 g·cm^{-3}, μ = 0.132 (MoKα, λ = 0.71073), T =120.0 K. Final $wR_2(F^2)$ = 0.1340 for all data, conventional $R_1(F)$ = 0.0499 for reflections with I ≥ 2σ, GOF = 1.036.

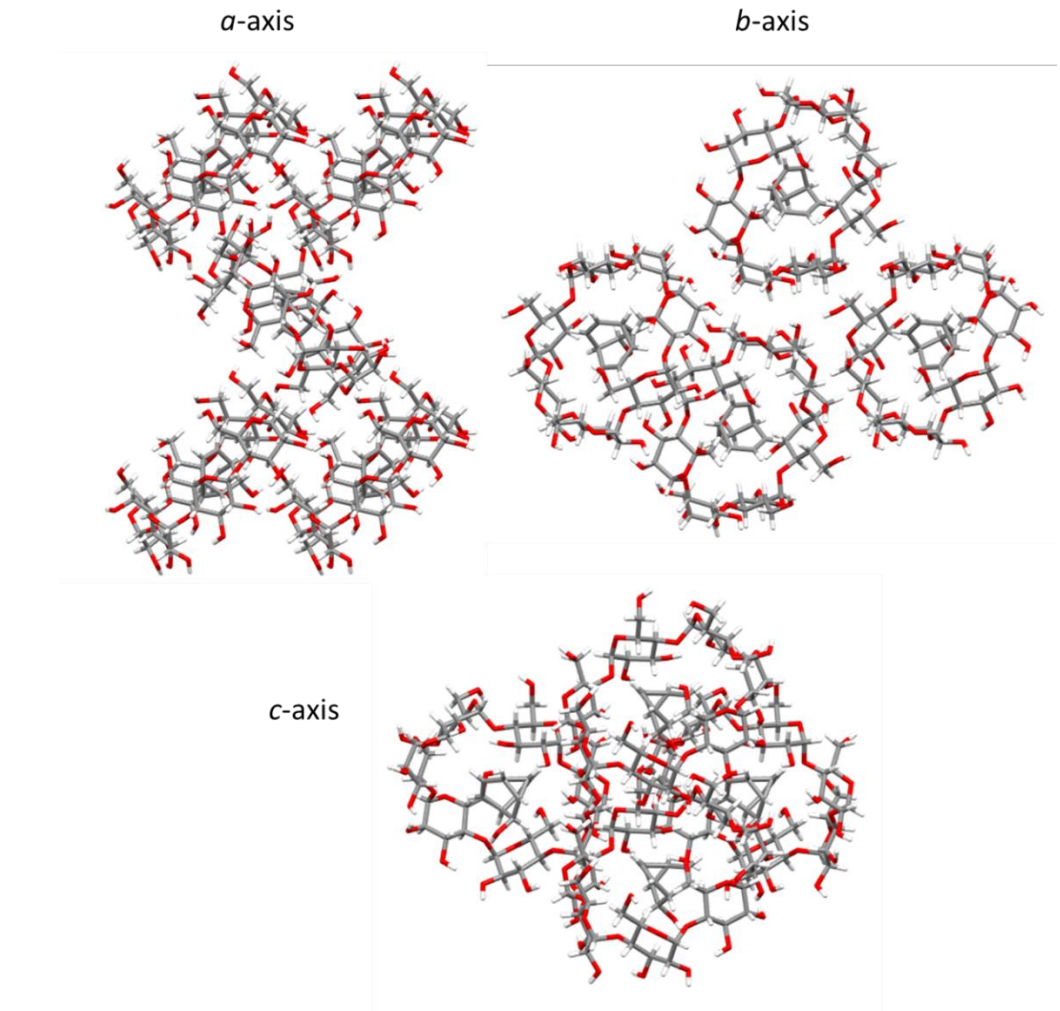

Figure 2.19. Solid-state superstructure of the host–guest complex viewed along the three unit cell axes.

Host–Guest Complex: β-CD–(±)-6-(4-Tolyl)bicyclo[3.2.2]nona-3,8-dien-6-ol (2)

Crystals of the host–guest complex suitable for X-ray diffraction were grown by the slow cooling of an aqueous H_2O solution of the two compounds in a one-to-one ratio from 100 °C to room temperature over the course of two weeks in a crystallisation oven which was followed by slow evaporation of the solution.

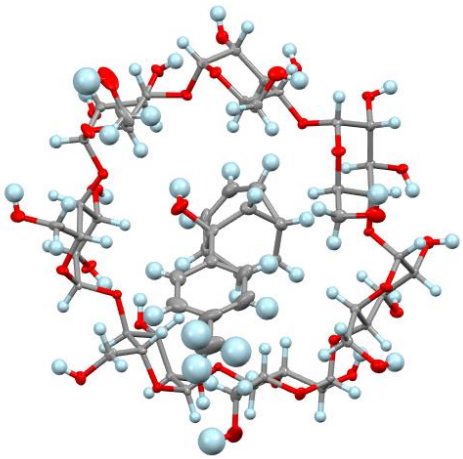

Figure 2.19. Solid-state structure of the host–guest complex including probability ellipsoids at 50%.

Crystal data: $C_{58}H_{106.5}O_{46.5}$, M = 1547.93, crystal system = monoclinic, space group = $P2_1$, a = 15.2430(13) Å, b = 32.258(3) Å, c = 15.4685(13) Å, α = 90 °, β = 102.522(3) °, γ = 90 °, U = 7425.2(11) Å^3, F(000) = 3306.0, Z = 4, Dc = 1.385 g·cm^{-3}, μ = 0.121 (MoKα, λ = 0.71073), T = 120.0 K. Final $wR_2(F^2)$ = 0.1408 for all data, conventional $R_1(F)$ = 0.0551 for reflections with I ≥ 2σ, GOF = 1.043.

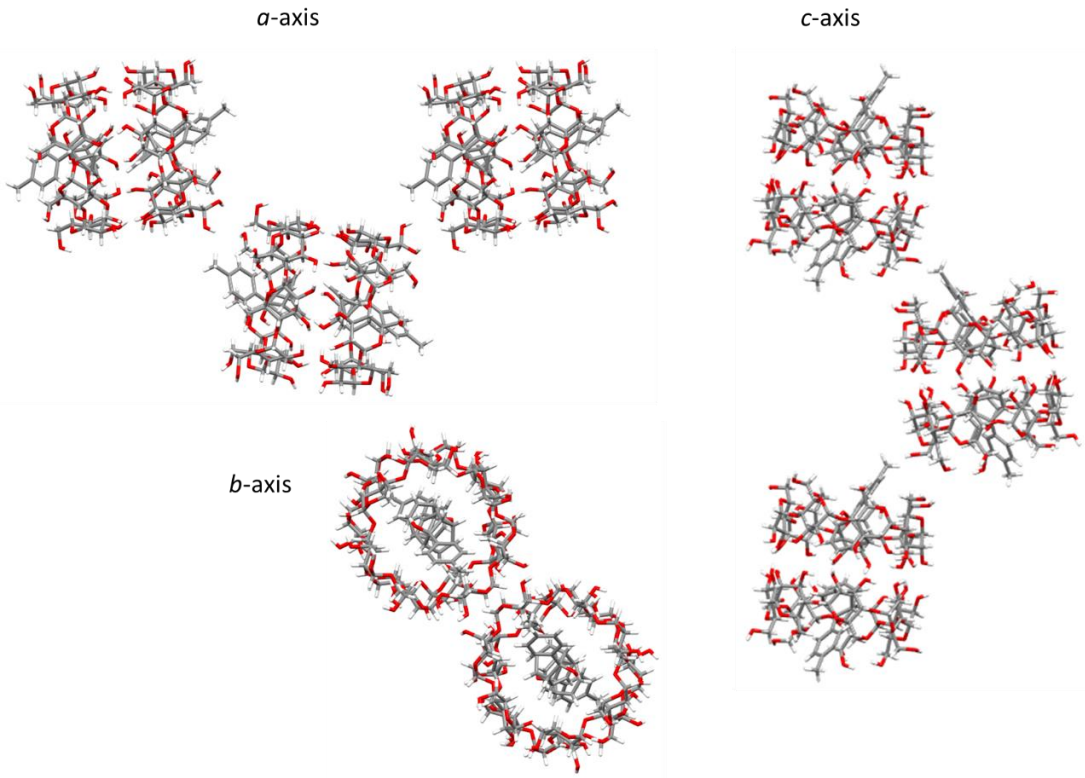

Figure 2.20. Solid-state superstructure of the host–guest complex viewed along the three unit cell axes.

Host–Guest Complex: β-CD–(±)-6-(4-Fluorophenyl)bicyclo[3.2.2]nona-3,8-dien-6-ol (3)

Crystals of the host–guest complex suitable for X-ray diffraction were grown by the slow cooling of an aqueous H_2O solution of the two compounds in a one-to-one ratio from 100 °C to room temperature over the course of two weeks in a crystallisation oven which was followed by slow evaporation of the solution.

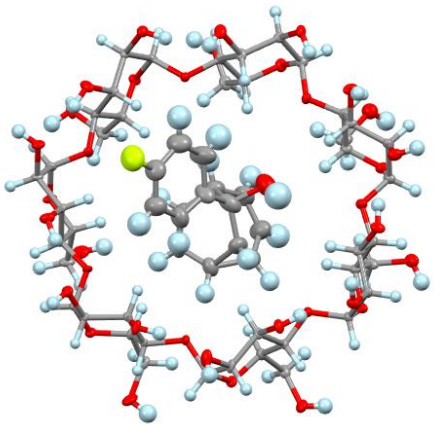

Figure 2.21. Solid-state structure of the host–guest complex including probability ellipsoids at 50%.

Crystal data: $C_{57}H_{107}FO_{48}$, M = 1579.42, crystal system = triclinic, space group = P1, a = 15.2430(13) Å, b = 32.258(3) Å, c = 15.4685(13) Å, α = 90 °, β = 102.522(3) °, γ = 90 °, U = 7425.2(11) $Å^3$, F(000) = 1684.0, Z = 4, Dc = 1.470 $g \cdot cm^{-3}$, μ = 0.131 (MoKα, λ = 0.71073), T = 120.0 K. Final $wR_2(F^2)$ = 0.2044 for all data, conventional $R_1(F)$ = 0.0735 for reflections with $I \geq 2\sigma$, GOF = 0.980.

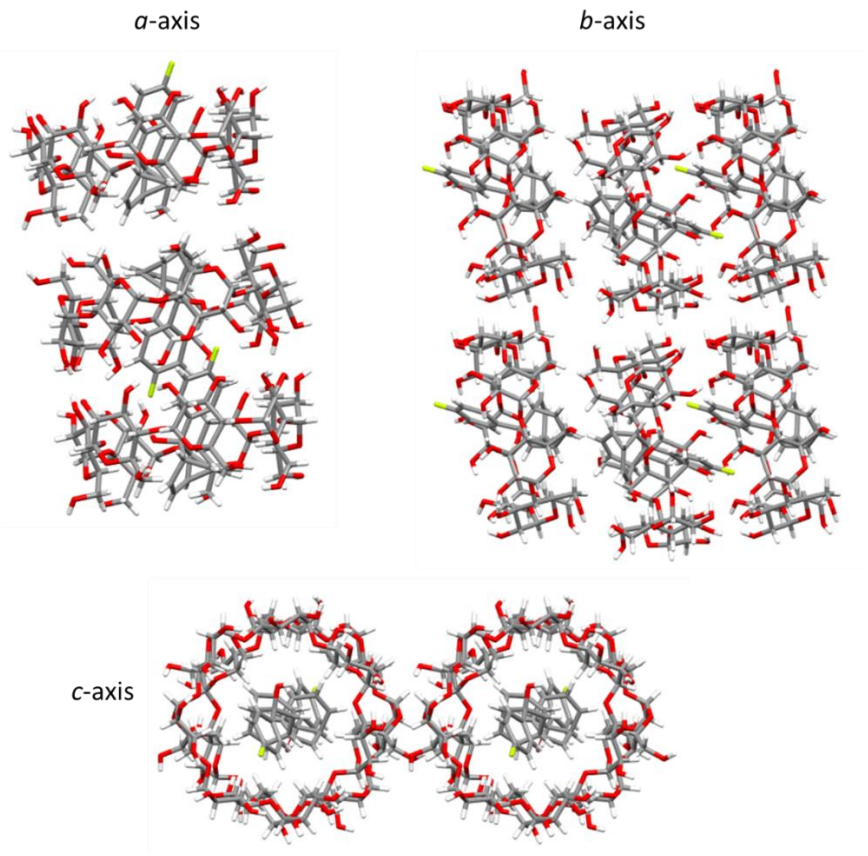

Figure 2.17. Solid-state superstructure of the host–guest complex viewed along the three unit cell axes.

2.5.3 ^{1}H NMR Titrations

In order to determine the stoichiometry and the association constant between the guest molecules (**1**, **2**, **3**, **4**) and the host (β-CD, **8**), ^{1}H NMR titrations were conducted. For each guest molecule, an NMR titration was completed at two different concentrations. The concentrations for guest–host (bararlane–β-CD dimer) are 1.23 mM:6.16 mM. The preparation of samples includes making a solution of the guest (1 equiv.) in D_2O (1.0 mL). 0.5 mL of the guest solution was transferred to a clean NMR tube and a ^{1}H NMR spectrum was acquired. To the remaining 0.5 mL of the guest solution, β-CD dimer **8** (2.5 equiv.) was added to obtain the solution about to titrate into the guest NMR tube. After each addition of the host–guest solution, the NMR tube was shaken thoroughly and a ^{1}H NMR spectrum was recorded. Each set of host and guest titrations are repeated once.

Bindfit analysis was conducted using specific ^{1}H signals selected based on their chemical shifts and relevance to the binding interactions: in the case of barbaralanes **2** and **3**, both aromatic (11

and 12) and aliphatic protons (3 and 7) were selected as they represent different binding sites of the guest molecules and all exhibit relatively significant changes during the titration. H atoms 3, 7 and 1&5 in barbaralol **1** were selected for the same criteria. The NMR spectroscopic shifts of all the selected peaks upon each addition were plotted against the concentration of host and fit choosing the 1:1 NMR model and Nelder-Mead / L-BFGS-B methods in Bindfit.

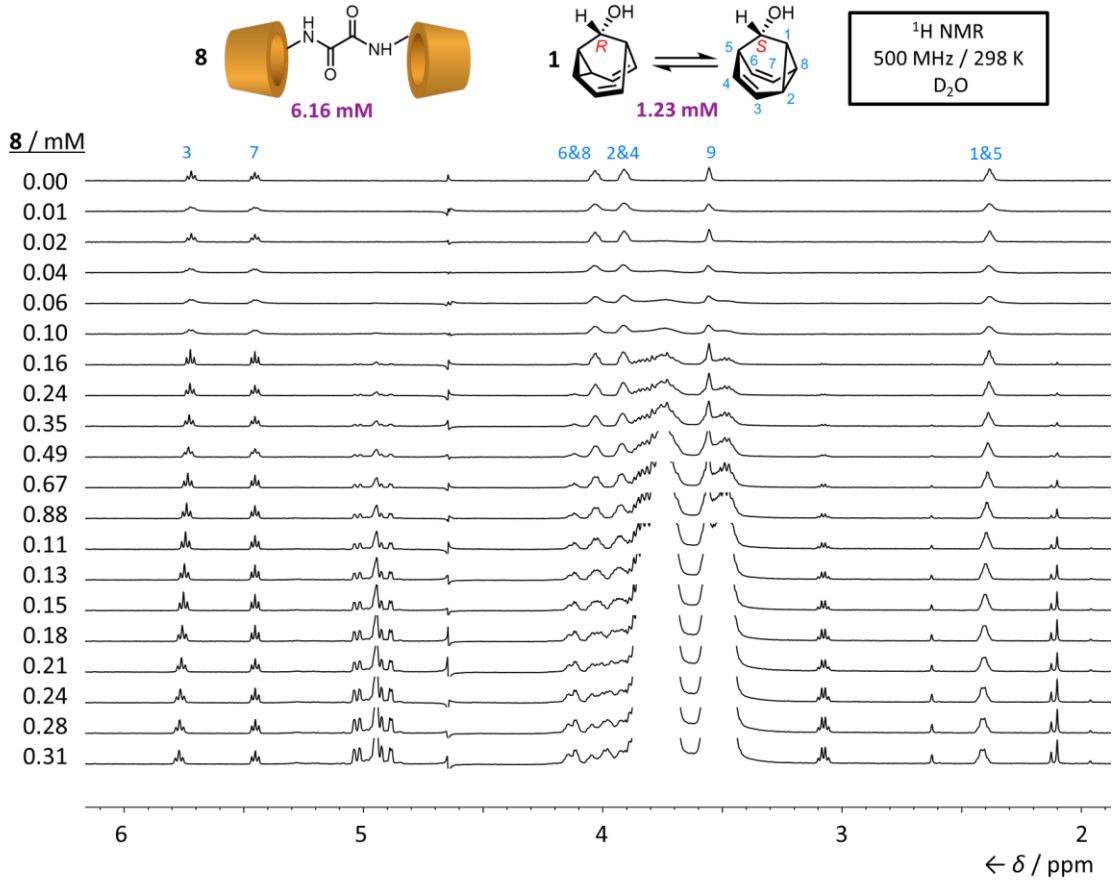

Figure 2.18. Partial ^{1}H NMR spectra of parent barbaralol **1** (1.23 mM) solutions containing different concentrations of **8**. All spectra have been acquired using presaturation with Robust-5 and PROJECT pulse sequences to suppress the water signal

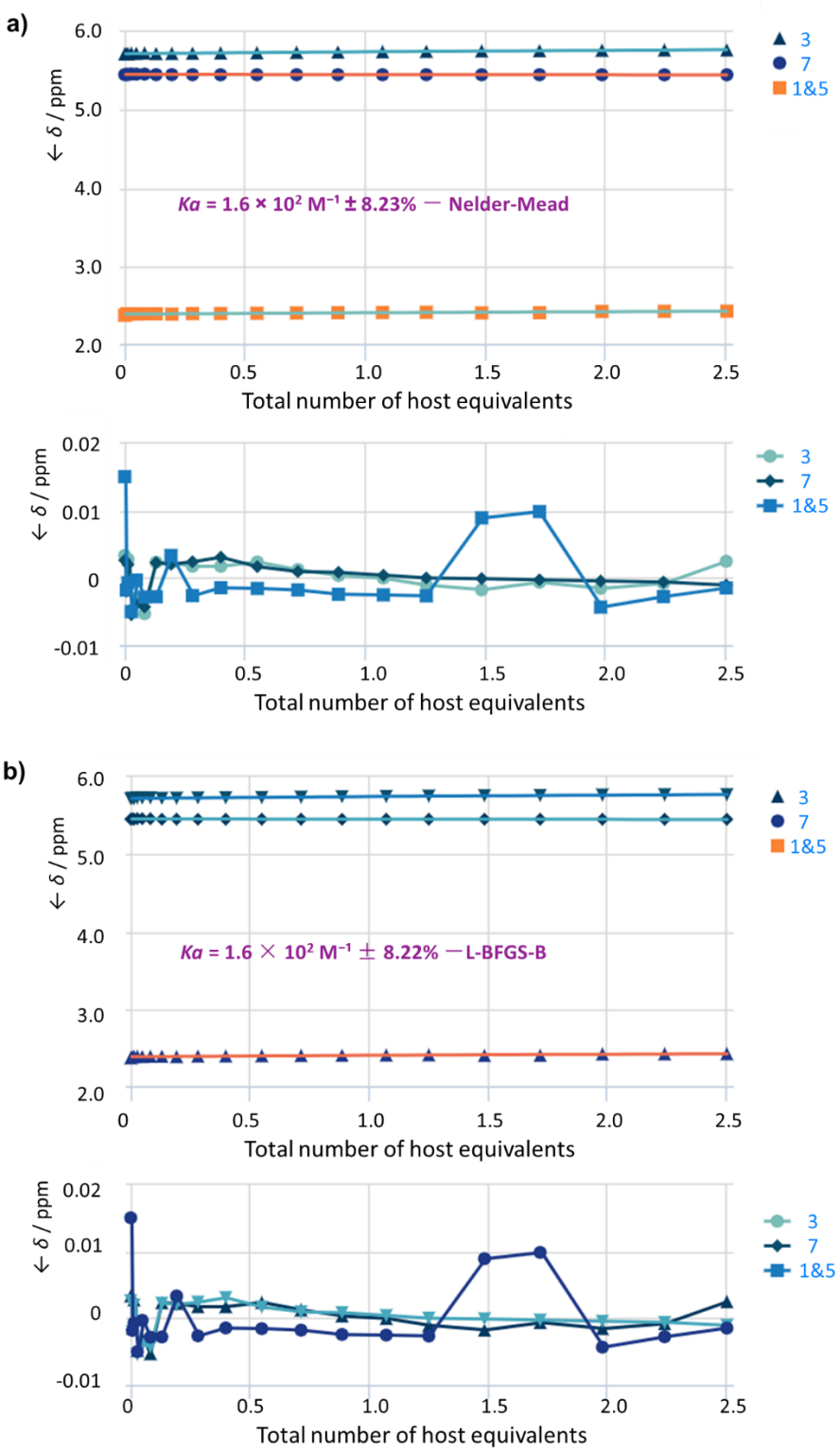

Figure 2.19. Chemical shift and shift changes (ppm) plotted against number of β-CD equivalents and fit to a one-to-one binding curve using the (a) Nelder-Mead algorithm or the (b) L-BFGS-B algorithm. Association constants are given with their respective errors. Proton labels correspond to those shown in Figure 2.18.

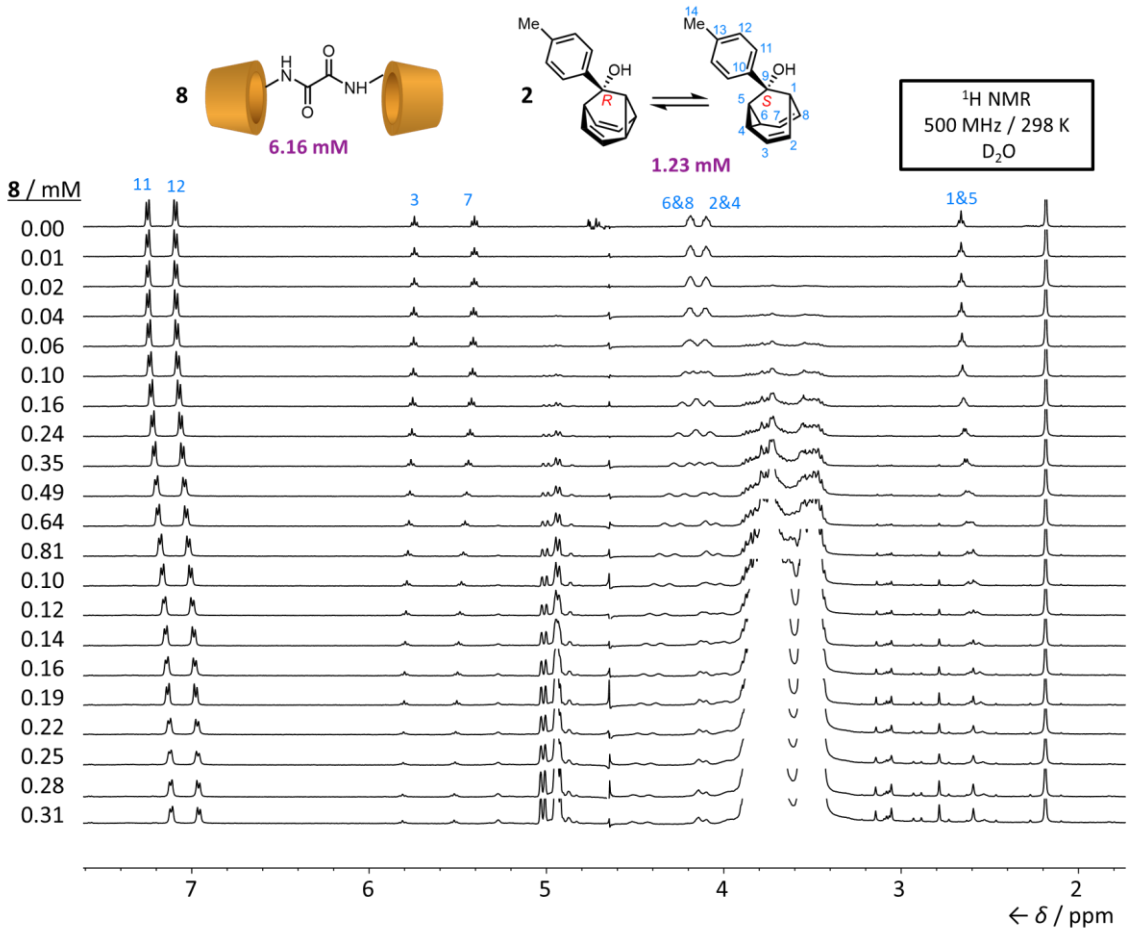

Figure 2.20. Partial ^{1}H NMR spectra of tolyl barbaralol **2** (1.23 mM) solutions containing different concentrations of **8**. All spectra have been acquired using presaturation with Robust-5 and PROJECT pulse sequences to suppress the water signal

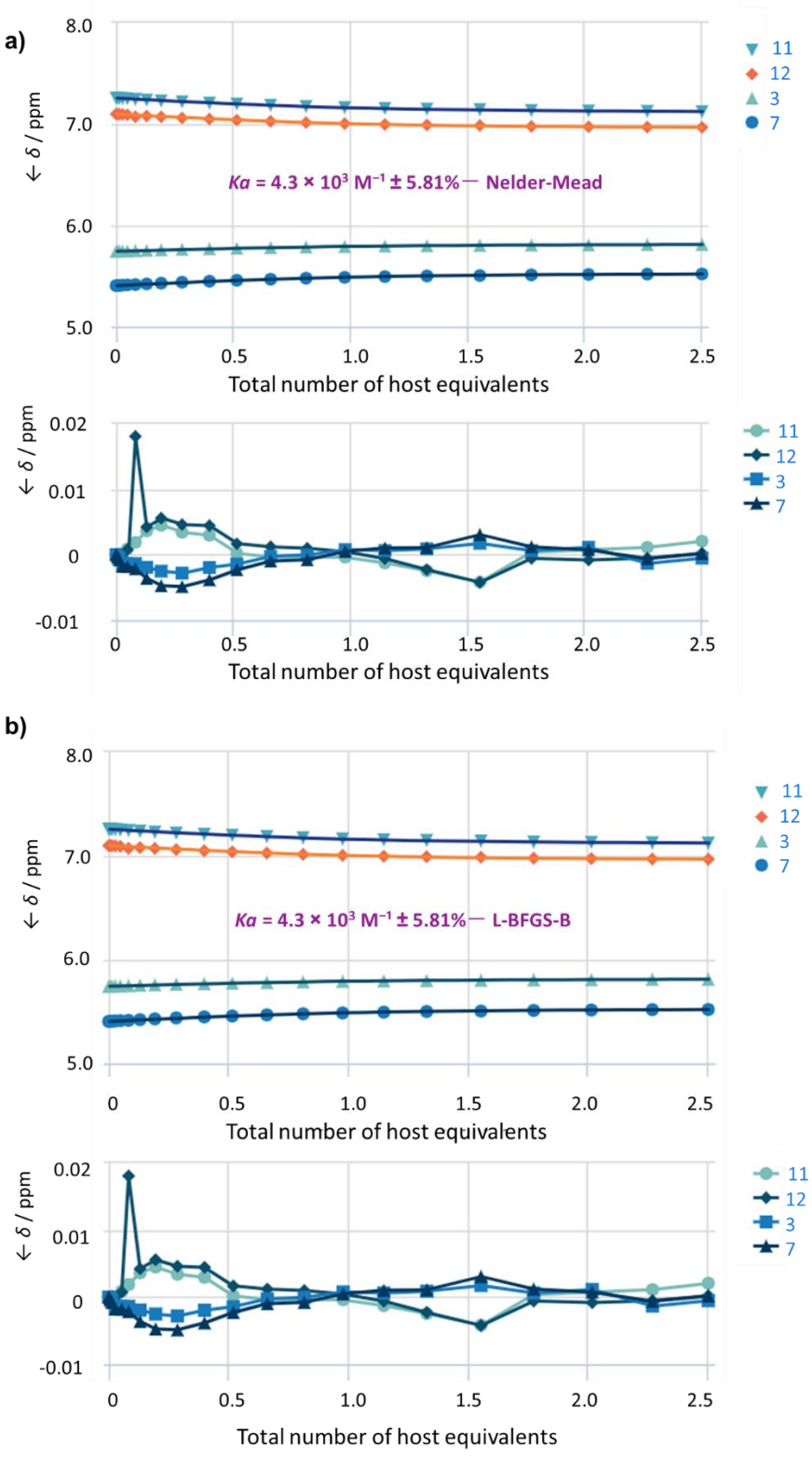

Figure 2.21. Chemical shift and shift changes (ppm) plotted against number of β-CD equivalents and fit to a one-to-one binding curve using the (a) Nelder-Mead algorithm or the (b) L-BFGS-B algorithm. Association constants are given with their respective errors. Proton labels correspond to those shown in Figure 2.20.

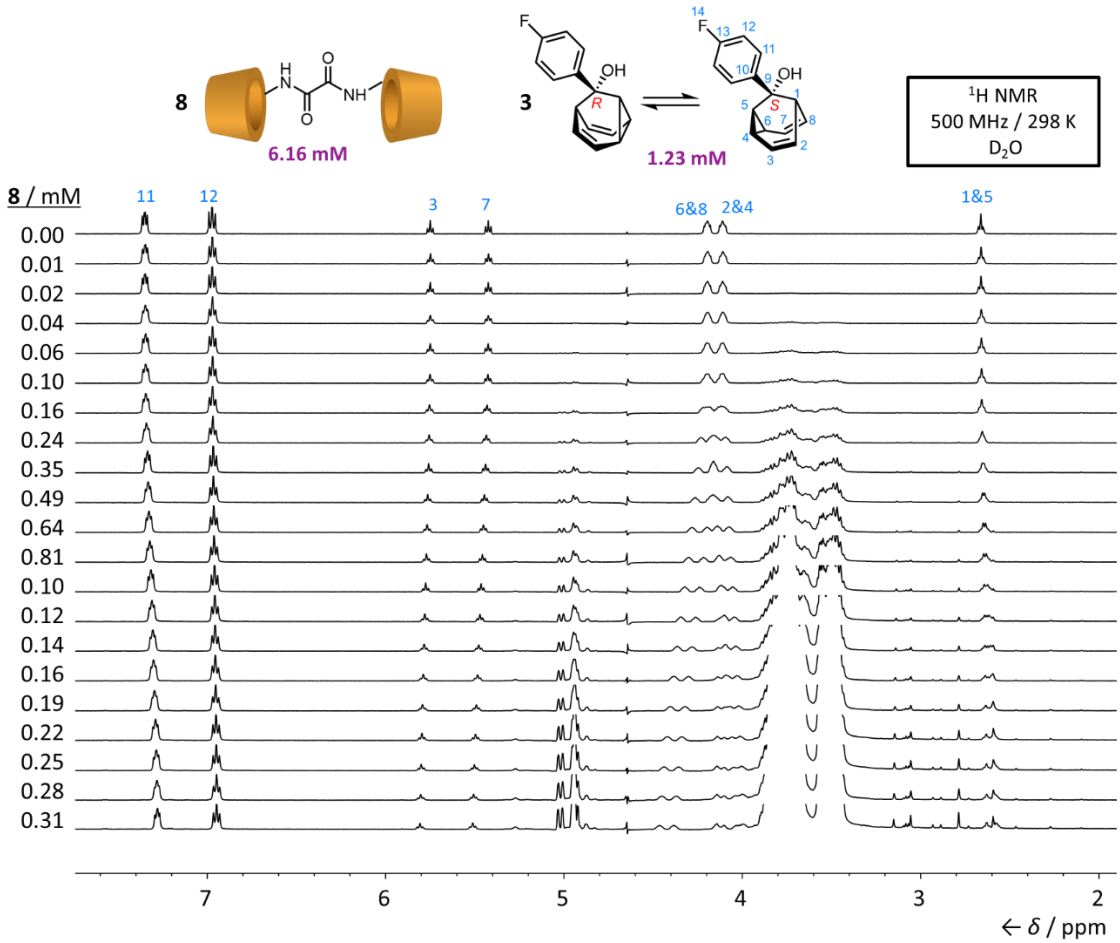

Figure 2.22. Partial ^{1}H NMR spectra of fluoro barbaralol **3** (1.23 mM) solutions containing different concentrations of **8**. All spectra have been acquired using presaturation with Robust-5 and PROJECT pulse sequences to suppress the water signal

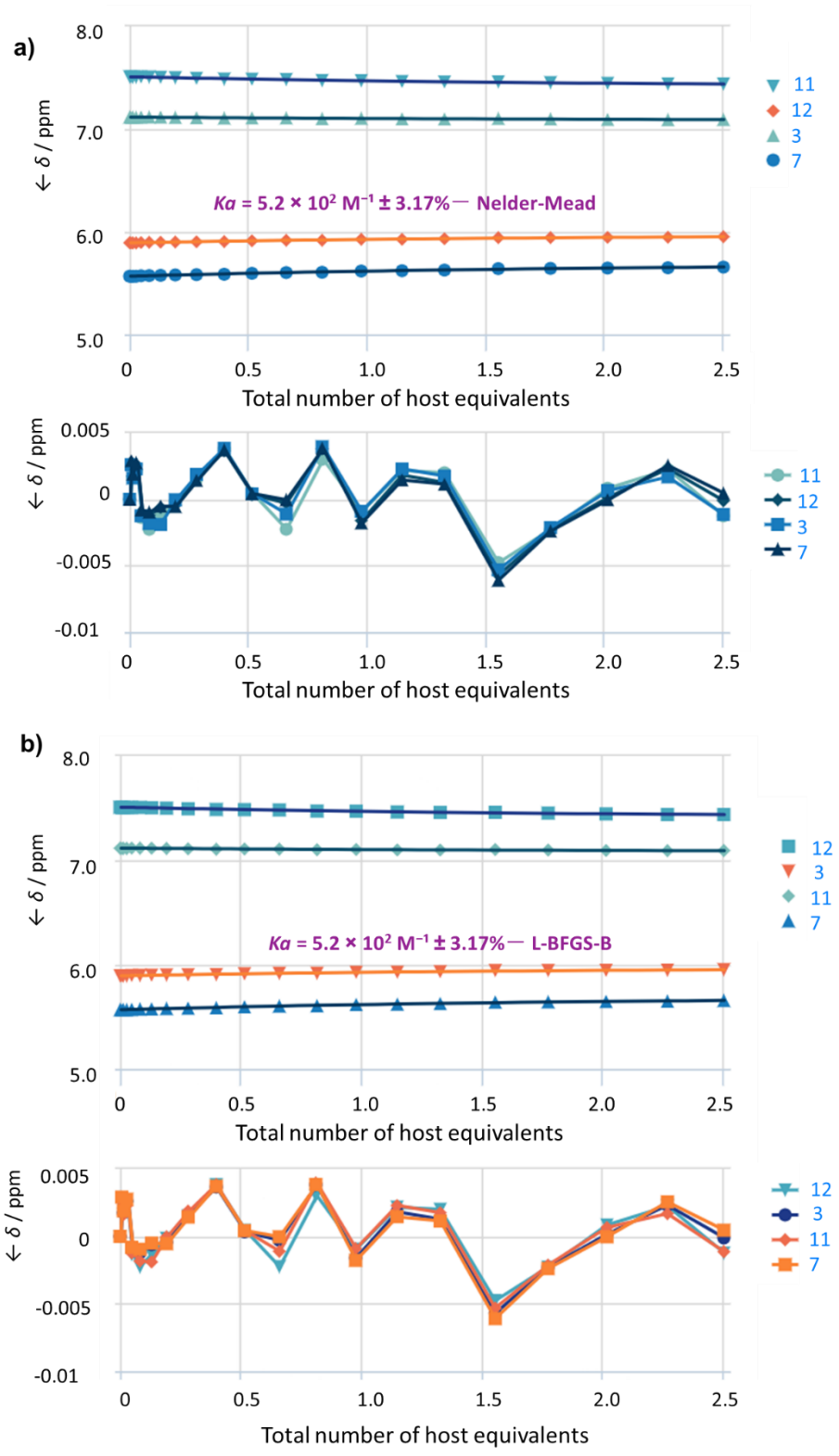

Figure 2.23. Chemical shift and shift changes (ppm) plotted against number of β-CD equivalents and fit to a one-to-one binding curve using the (a) Nelder-Mead algorithm or the (b) L-BFGS-B algorithm. Association constants are given with their respective errors. Proton labels correspond to those shown in Figure 2.22.

The stacked ^{1}H NMR spectra showed that upon addition of the host (β-CD dimer), the 2/4/6/8 positions (cyclopropane and olefinic) split into four peaks, and 1&5 changes from triplet to broad multiplet due to overlapping inequivalent resonances. For tolyl barbaralol **2** and fluoro barbaralol **3**, the chemical shift for positions 11, 12, 3 and 7 are plotted against the number of equivalents of host to determine the association constants, and for parent barbaralol 3, 7 and 1&5 positions are used.

The results for the ^{1}H NMR titrations are summarised in Table 2.3. The calculated association constants using Nelder-Mead and L-BFGS-B gave almost the same data. The obtained results demonstrate that tolyl barbaralane **2** has the strongest association constant (4.3×10^3 M^{-1} ± 5.81%) with β-CD dimer **8** while barbaralol **1** has the lowest (1.6×10^2 M^{-1} ± 8.23%). All guest molecules are shown to form one-to-one inclusion complexes.

Host–Guest Complex	Nelder-Mead Association Constant (*Ka*) / M^{-1}	L-BFGS-B Association Constant (*Ka*) / M^{-1}
8–**1**	1.6×10^2 M^{-1} ± 8.23%	1.6×10^2 M^{-1} ± 8.22%
8–**2**	4.3×10^3 M^{-1} ± 5.81%	4.3×10^3 M^{-1} ± 5.81%
8–**3**	5.2×10^2 M^{-1} ± 3.17%	5.2×10^2 M^{-1} ± 3.17%

Table 2.3. Comparison of association constants and their respective errors between β-CD dimer **8** and barbaralanes **1**-**3**.

2.6 References

1. (a) N. H. Evans, Chem. Eur. J. 2018, 24, 3101; M. Dommaschk, J. Echavarren, D. A. Leigh, V. Marcos and T. A. Singleton, *Angew. Chem. Int. Ed.* 2019, **58**, 14955-14958; (b) J. –C. Chambrom, C. Dietrich-Buchecker and J. -P. Sauvage, *Top. Curr. Chem.* 1993, **165**, 131.

2. (a) M. Alvarez-Pérez, S. M. Goldup, D. A. Leigh and A. M. Z. Slawin, *J. Am. Chem. Soc.* 2008, **130**, 1836; (b) A. de Juan, D. Lozano, A. W. Heard, M. A. Jinks, J. M. Suarez, G. J. Tizzard and S. M. Goldup, *Nat. Chem.* 2022, **14**, 179–187; (c) S. M. Goldup, *Acc. Chem. Res.* 2024, **57**, 12, 1696–1708.

3. (a) Q. Zhang, R. Toyoda, L. Pfeifer and B. L. Feringa, *J. Am. Chem. Soc.* 2023, **145**, 6976-6985; (b) Q. Zhang, S. Crespi, R. Toyoda, R. Costil, W. R. Browne, D.-H. Qu, H. Tian and B. L. Feringa, *J. Am. Chem. Soc.* 2022, **144**, 4376-4382.

4. (a) H. Wang, W. Yang, K. K. Baldridge, C.-H. Zhan, T. U. Thikekar and A. C.-H. Sue, *Chem. Sci.*, 2021, **12**, 10985-10989; (b) Y. Wang, H. Wu and J. F. Stoddart, *Acc. Chem. Res.* 2021, **54**, 2027-2039; (c) G. E. Arnott, *Chem. Eur. J.* 2018, **24**, 1744; (d) K. Kato, S. Fa and T. Ogoshi, *Angew. Chem. Int. Ed.* 2023, **62**, e202308316.

5. M. W. Gillick-Healy, E. V. Jennings, H. Meller-Bunz, Y. Ortin, K. Nikitin and D. G. Gilheany, *Chem. Eur. J.* 2017, **23**, 2332.

6. A. Forni, I. Moretti and G. Torre, *J. Chem. Soc. Chem. Commun.* 1977, 731

7. B. Kim, G. Storch, G. Banerjee, B. Q. Mercado, J. Castillo-Lora, G. W. Brudvig, J. M. Mayer and S. J. Miller, *J. Am. Chem. Soc.* 2017, **139**, 15239

8. (a) A. N. Bismillah, B. M. Chapin, B. A. Hussein and P. R. McGonigal, *Chem. Sci.* 2020, **11**, 324; (b) C. Engdahl and P. Ahlberg, *J. Am. Chem. Soc.* 1979, **101**, 3940; (c) L. G. Greifenstein, J. B. Lambert, M. J. Broadhurst, L. A. Paquette, *J. Org. Chem.* 1973, **38**, 1210.

9. A. N. Bismillah, T. G. Johnson, B. A. Hussein, A. T. Turley, P. K. Saha, H. C. Wong, J. A. Aguilar, D. S. Yufit and P. R. McGonigal, *Nature Chem.* 2023, **15**, 615–624.

10. (a) M. V. Rekharsky, H. Yamamura, C. Inoue, M. Kawai, I. Osaka, R. Arakawa, K. Shiba, A. Sato, Y. H. Ko, N. Selvapalam, K. Kim, and Y. Inoue, *J. Am. Chem. Soc.* 2006, **128**, 14871-14880; (b) X. X. Zhang, J. S. Bradshaw and R. M. Izatt, *Chem. Rev.* 1997, **97**, 3313-3362.

11. D. Grandero, J. Bordello, M. J. Pérez-Alvite, M. Novo and W. Al-Soufi, *Int. J. Mol. Sci.* 2010, **11**,

173.

12. A. N. Bismillah, PhD Thesis, Durham University, 2019.

13. M. M. S.-Sempere, G. Fernández and F. Würthner, *Chem. Rev.* 2011, **111**, 5784–5814.

14. (a) A. N. Bismillah, J. Sturala, B. M. Chapin, D. S. Yufit, P. Hodgkinson and P. R. McGonigal, *Chem. Sci.*, 2018,9, 8631-8636; (b) R. O. Gould , C. L. Jones , T. A. Stephenson and D. A. Tocher , *J. Organomet. Chem.* 1984, **264**, 365-378; (c) K. M. J. Brands and A. J. Davies, *Chem. Rev.* 2006, **106**, 2711-2733; (d) Y. Kitamoto, K. Suzuki, N. Morohashi, K. Sakai and T. Hattori, *J. Org. Chem.* 2013, **78**, 597-605; (e) K. S. MacFarlane, S. J. Rettig, Z. Liu and B. R. James, *J. Organomet. Chem.* 1998, 2, 213-219;

15. http://app.supramolecular.org/bindfit/

16. J. A. Nelder and R. Mead, *The Computer Journal*. 1965, **7**, 308.

17. C. Zhu, R. H. Byrd, P. Lu, and J. Nocedal, *ACM Transitions on Mathematical Software.* 1997, **23**, 550.

18. (a) P. Thordarson, *Chem. Soc. Rev.* 2011, **40**, 1305; (b) D. Brynn Hibbert and P. Thordarson, *Chem. Commun.* 2016, **52**, 12792.

19. C. J. Easton, S. J. van Eyk, S. F. Lincoln, B. L. May, J. Papageorgiou and M. L. Williams, *Aust. J. Chem.* 1997, **50**, 9-12.

20. M. I. Stefan and N. Le Novère, *PLoS Comput. Biol.* 2013, **9**, e1003106.

21. (a) Y. Tian, Y. Guo, X. Dong, X. Wan, K.-H. Cheng, R. Chang, S. Li, X. Cao, Y.-T. Chan and A. C.-H. Sue, *Nat. Synth.* 2023, **2**, 395–402; (b) W.H. Pirkle and P.L. Rinaldi, *J. Org. Chem.* 1977, **42**, 3217-3219

22. (a) M. Kagawa, Y. Machida, H. Nishi and J. Haginaka, *J. Pharm. Biomed. Anal.* 2005, **38**, 918-923; (b) H. Taji, Y. Kasai, A. Sugio, S. Kuwahara, M. Watanabe, N. Harada and A. Ichikawa, *Chirality*, 2002, **14**, 81-84

23. (a) J.A. Dale and H.S. Mosher, *J. Am. Chem. Soc.* 1973, **95**, 512-519; (b) D. A. Allen, A. E. Tomaso Jr., O. P. Priest, D. F. Hindson and J. L. Hurlburt, *J. Chem. Educ.* 2008, **85**, 698.

24. (a) C.-S. Goh, D. Milburn and M. Gerstein, *Curr. Opin. Struct. Biol.* 2004, **14**, 104-109; (b) D. E. Koshland Jr., *Angew. Chem. Int. Ed.* 1995, **33**, 2375-2378.

25. (a) J. A. Aguilar and A. M. Kenwright, *Analyst.* 2016, **141**, 236; (b) J. A. Aguilar, M. Nilsson, G. Bodenhausen and G. A. Morris, *Chem. Commun.* 2012, **48**, 811.

26. O. V. Dolomanov, L. J. Bourhis, R. J. Gildea, J. A. K. Howard, H. J. Puschmann, *Appl. Crystallogr.* 2009, **42**, 339.

27. G. M. Sheldrick. *Acta. Crystallogr. Sect. A Found. Crystallogr.* 2008, **64**, 112.

CHAPTER 3 | DYNAMIC PREFERENTIAL CRYSTALLISATION OF RAPIDLY INTERCONVERTING DIASTEREOISOMERS

Synopsis

This Chapter discusses the novel synthesis of a series of barbaralane oligomers and studies on their diastereoisomerisation in the solid state. The diastereoisomers of synthesised barbaralane dimers interconvert freely in solution, but resolve as various combinations in single crystals. Computational modelling confirms that the preferential crystallisation is not dictated by their inherent (solution phase) energy differences or specific noncovalent interactions. The diastereoisomers found in the solid state are favoured by efficient packing and complementary enantiomerism of individual barbarlyl units.

Contribution statements

The author conducted: the synthesis, spectroscopic characterisations, and crystal growth of all compounds except **4** and **5**; all the DFT calculations, Hirshfeld surfaces and interaction energies.

Acknowledgements

The following people are gratefully acknowledged for their contribution to this chapter: The synthesis and crystal growth of barbaralane **4** and **5** are finished by postdoc Aisha N. Bismillah and former MChem student Toby G. Johnson. Dr Dimitry S. Yufit solved all the X-ray crystal structures. Professor Graeme M. Day in Southampton conducted the initial CSP calculations.

3.1 Introduction

Kinetic resolution (KR) and dynamic kinetic resolution (DKR) are powerful strategies in asymmetric synthesis for obtaining enantiomerically pure compounds. Compared to the partial conversion of KR via selection of a specific enantiomer (Figure 3.1a), DKR allows replenishment of the racemic pool and continuously converts one enantiomer into the desired product, leading to maximum yields (Figure 3.1b).[1]

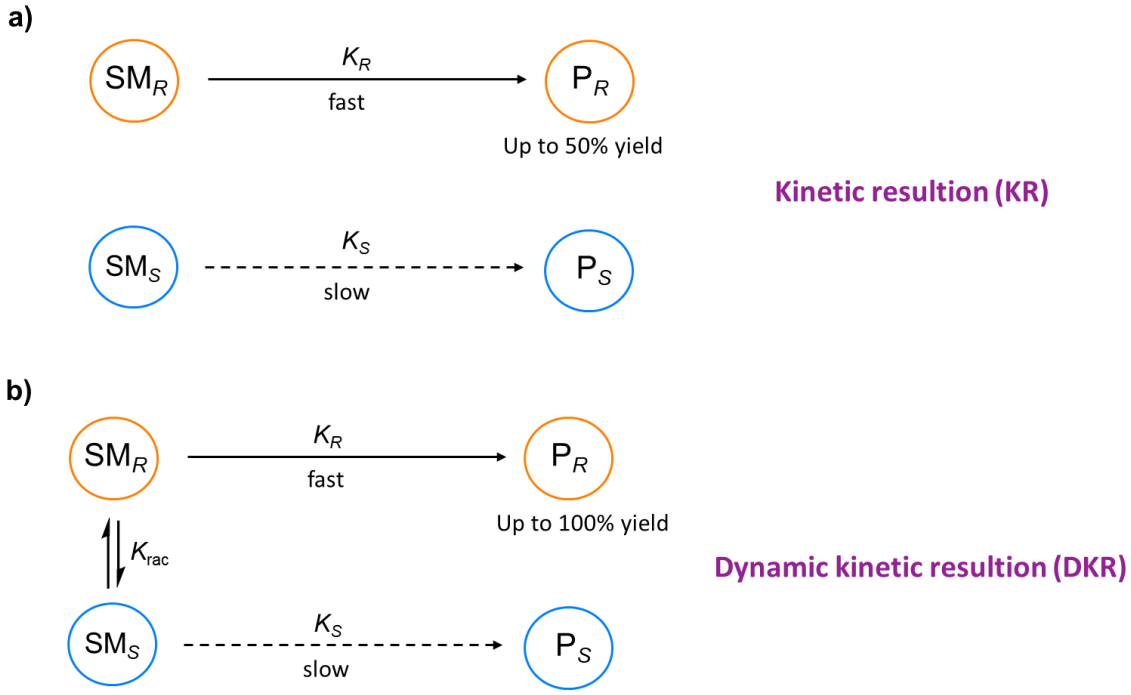

Figure 3.1. Kinetic resolution (KR) and dynamic kinetic resolution. SM_R and SM_S = the two enantiomers of the starting material; P_R and P_S = the two enantiomers of the product; K = rate constant for reaction of each isomer; Krac = rate constant for racemization.

KR and DKR are also present in crystallisation process and resolve to specific isomers in the solid state. Molecules exhibiting dynamic chirality could undergo dynamic preferential crystallisation which converts the racemic mixture to be one or more specific isomers via DKR,[3] i.e. for conglomerate molecules[2] exhibiting spontaneous resolution, Viedma ripening can selectively convert their crystals with one single chirality to the other,[3a] and pillararenes could possess single isomerism in the solid state by either spontaneous or induced resolution.[3d] Dynamic preferential crystallisation could be utilised as an effective and environmentally

friendly method in the synthesis of chiral drugs[4] and chiral materials with unique optical or electronic properties.[5]

Fluxional carbon cages such as bullvalenes and barbaralanes have dynamic structures due to their rapid and reversible Cope rearrangements[6]. Barbaralane fluctuates between only two degenerate isomers, and when substituted at the 9 position and exhibits dynamic sp^3-carbon stereochemistry that rapidly interconverts between two enantiomers[7]. It has been demonstrated that the enantiomerisation equilibrium of 9-substituted barbaralanes could be shifted by either dynamic covalent bonds or specific noncovalent interactions. Dynamic preferential crystallisations on fluxional carbon cages have been observed, i.e. homotropylidene bullvalene is found to be a conglomerate, as the single crystals precipitating from its racemic solution contain only one enantiomer.[8] Additionally, when di-substituted barbaralanes possess dynamic regioisomerisation, they could undergo shape-selective crystallisations, resolving into single valence isomers dictated by their size and shape (Figure 3.2).[9]

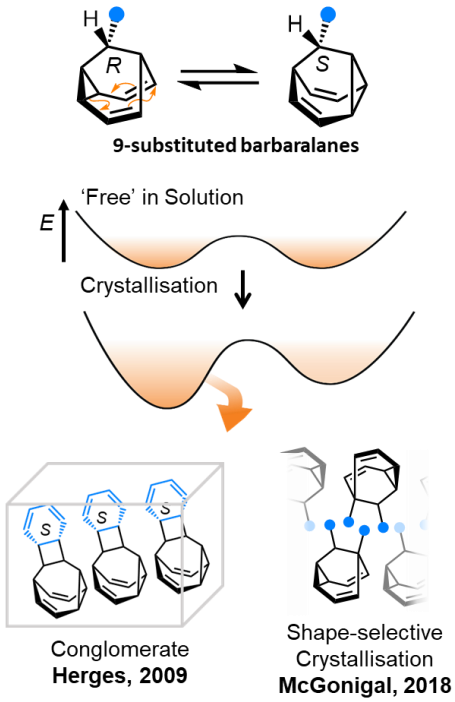

Figure 3.2. The dynamic chirality of 9-substituted barbaralanes and the effect on their enantiomerism equilibrium by crystallisation.

This chapter explores the dynamic preferential crystallisation of barbaralane dimers. 9-Substituted barbaralane monomers without added chiral information have a 1:1 enantiomerism

equilibrium in the solution state,[7] and their interconversion are trapped in the solid state, giving racemic crystals with 1:1 ratio of *R*- and *S*-enantiomers (Figure 3.3a). When two barbaralane molecules are linked via the 9-position to form a dimer, their dynamic enantiomerisation will evolve into dynamic diastereoisomerisation (Figure 3.3b). DFT calculations indicated that all the diastereoisomers could convert freely in solution. The diastereoisomers have small energy differences between them (see Section 3.2.3), giving equilibrium mixtures that are close to the statistical 1:1:2 ratio of (*R*,*R*), (*S*,*S*) and *meso* diastereoisomer. Interestingly, when the fluxional mixtures undergo dynamic preferential crystallisation, various combinations of diastereoisomers could be resolved, and their distributions are not related to this statistical equilibrium. Hirshfeld surfaces and intermolecular energies indicated that no specific noncovalent interactions have influenced the crystal packing. The superstructures of dimer crystals show that they exhibit self-sorting and high *Z*' behaviour, suggesting that their diastereoisomerisation in the solid state generally adheres to the tendency of forming racemic pairs, thereby achieving more efficient molecular packing.

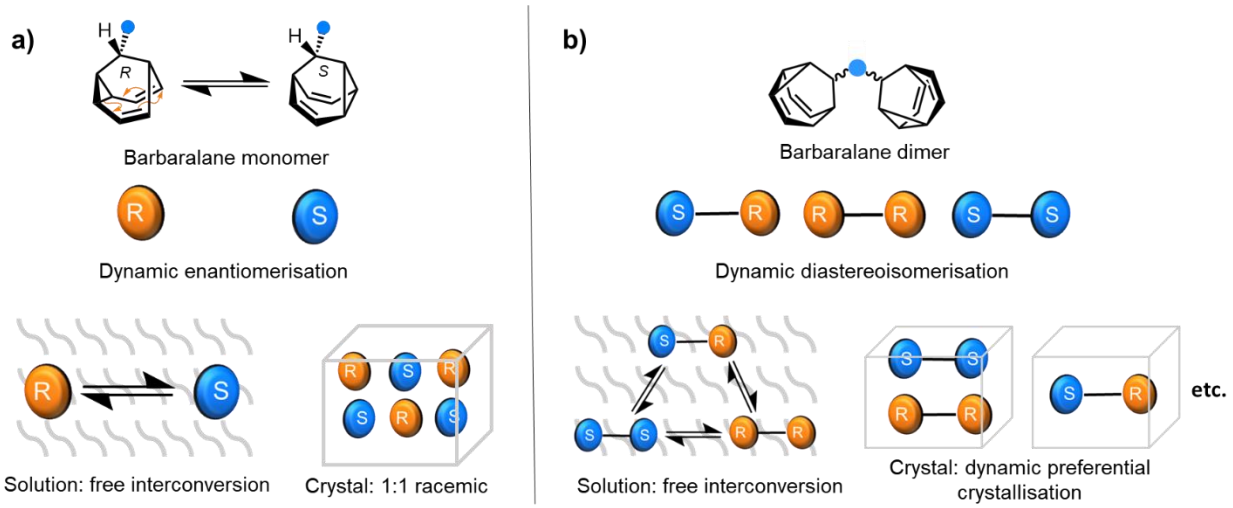

Figure 3.3. a) Dynamic enantiomerisation of barbaralane monomer; b) Dynamic diastereoisomerisation of barbaralane dimer

3.2 Results and Discussion

3.2.1 Synthesis and Characterisations of Barbaralane Dimers

Seven barbaralane oligomers were synthesised (Scheme 3.1) in 1–2 steps from precursor barbaralone **9**. The dimers **1**, **2**, **3**, **6** and tetramer **7** were prepared via reductive amination of barbaralone **9** with three different amines. The trithiolane dimer **5** was obtained through oxygen-sulfur exchange of barbaralone **9** with Lawesson's reagent. For the diester dimer **4**, the barbaralone **9** was reduced into barbaralol **10** by $LiAlH_4$, followed by the addition of terephthaloyl chloride to give the esterificated product **4**, together with its mono-substitued by-product, **4'**. All the dynamic stereocenters are labelled with wiggy bonds.

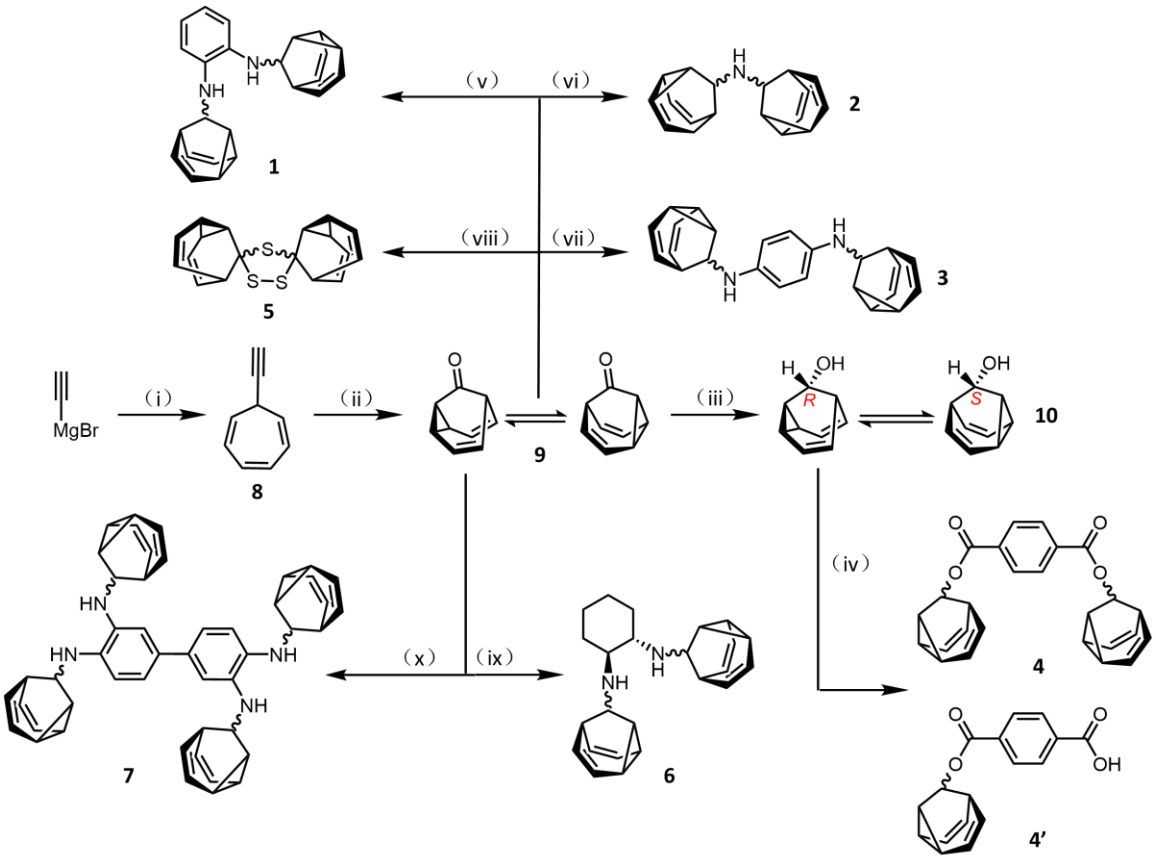

Scheme 3.1 Synthesis of compounds **8**, **9**, **10** and barbaralane oligomers **1**-**7**. Reagents and conditions: (i) 1. LiCl / THF / –78 °C / 10 min. 2. Tropylium tetrafluoroborate / –78 °C to rt, 83%. (ii) IPrAu(MeCN)BF_4 (5 mol%) / Ph_2SO / CH_2Cl_2 / rt / 16 h, 60%. (iii) $LiAlH_4$ / Et_2O / 0 °C / 3 h, 78%. (iv) Terephthaloyl chloride / $CHCl_3$ / DMAP / Et_3N / rt / 3 d, 27% and 25%. (v) 1,2-Diaminobenzene / MeOH / glacial AcOH / $NaBH_3CN$ / 100 °C / 16 h, 40%. (vi) NH_3 / MeOH / glacial AcOH / $NaBH_3CN$ / 100 °C

/ 24 h, 53%. (vii) 1,4-Diaminobenzene / MeOH / glacial AcOH / $NaBH_3CN$ / 100 °C / 16 h, 67%. (viii) Lawesson's Reagent / PhMe / 110 °C / 18 h, 13%. (ix) (1*S*,2*S*)-diaminocyclohexane / MeOH / glacial AcOH / $NaBH_3CN$ / 100 °C / 16 h, 26%. (x) 3,3′-diaminobenzidine / MeOH / THF / glacial AcOH / $NaBH_3CN$ / 130 °C / 24 h, 8%.

The structures of all products were characterised by ^1H, ^{13}C NMR spectroscopy and mass spectroscopy. Notably, when the barbaralane units are oligomerised *via* a non-chiral linkage (**1**, **2**, **3**, **4**, **5** and **7**), the ^1H-NMR peaks of their 6&8/2&4 positions could not be resolved due to identical environments. However, in the dimer **6** where the two barbaralanes are linked via the chiral (1*S*,2*S*)-diaminocyclohexane, the 6&8/2&4 peaks are resolved in the ^1H-NMR spectrum due to the reduced symmetry (Figure 3.4).

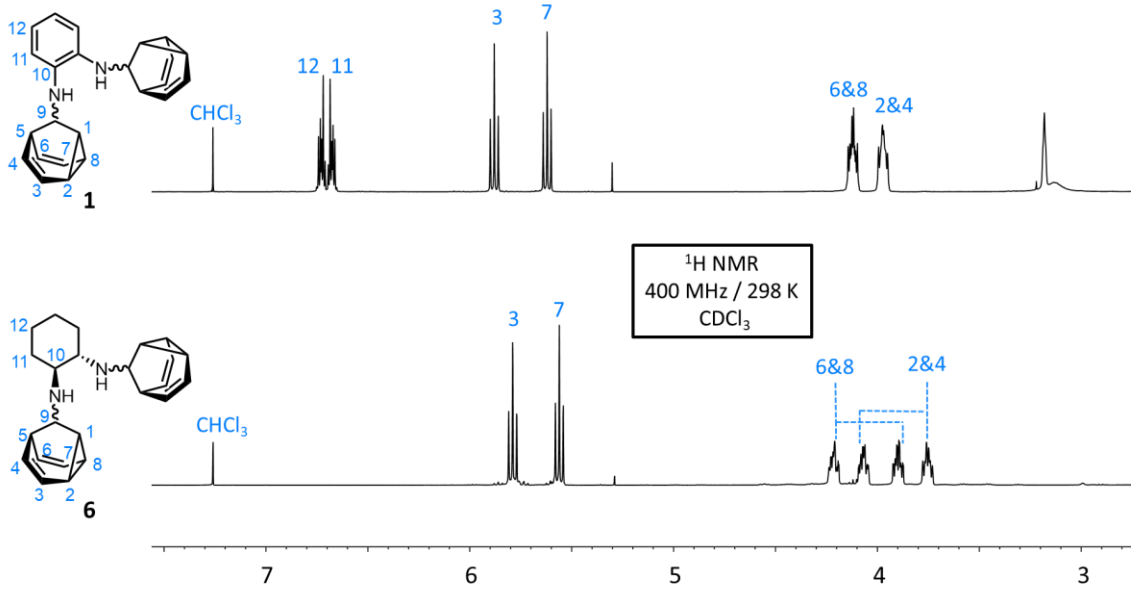

Figure 3.4. Comparison of partial ^1H-NMR spectra of **1** and **6**.

3.2.2 X-Ray Diffraction Results

Five out of seven barbaralane oligomers form crystalline solids, allowing to analyse their solid-state structures by single-crystal X-ray diffraction (Full details see section 3.4.4). All five dimers showed specific dynamic preferential crystallisation, where **1**, **2** and **4** only gave the *meso* isomer, the trithiolane dimer **5** gave the (*R*,*R*)- and (*S*,*S*)-isomers with a 1:1 ratio, and the aniline dimer **3** surprisingly adopts all three isomers with a 1:1:1 ratio in the solid state (Figure

3.5a). None of these results match the statistical equilibrium (1:2:1), consistent with them undergoing a resolution process upon crystallisation. In all cases, the crystals are racemic, i.e., they contain an overall 1:1 ratio of *R*- and *S*-barbaralyl units, albeit while exhibiting various diastereomer combinations. The *meso* diastereoisomer is the most common isomer found in the structures investigated, appearing in four of the five soild state superstructures. The trithiolane dimer **5** is the exception as it resolves 1:1 ratio of (*R*,*R*)- and (*S*,*S*)-diastereoisomers, which could be influenced by the stereogenity of its disulfide moiety: the conformational flexibility of disulfide bond can generate *P*- and *M*-stereoisomerism,[3c] providing the molecule with more complicated forms of stereodivergency (Figure 3.5b). In the unit cell of dimer **5**, it is evident that all the (*S*,*S*)-diastereoisomers exhibit *P*-disulfide linkers, and all the (*R*,*R*)-diastereoisomers exhibit *M*-ones, and the overall structure are not only racemic in the case of sp^3 chirality, but also conformational chirality. The observed resolution of dimer **5** indicated the stereodivergent chirality from disulfide bonds is transferred to the barbaralyl cores through covalent bonding.

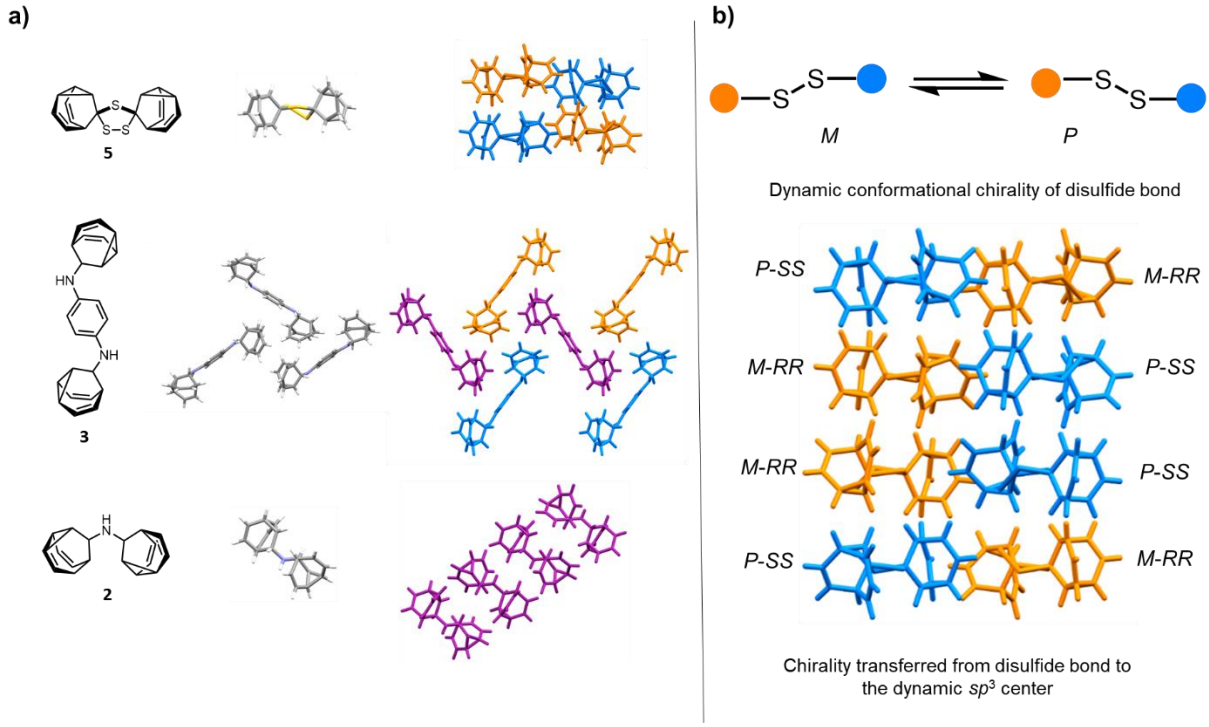

Figure 3.5. (a) Comparison of the crystal structures of barbaralane dimers **2**, **3** and **5**. Diastereoisomers in the packing diagram are distinguished by colours: orange = (*R*,*R*), blue = (*S*,*S*), purple = *meso*. (b) Illustration of dynamic chirality of disulfide bond and its chirality transfer to dimer **5**.

The superstructures of all dimer crystals possess 'zigzag' sheets along a certain axis. The observed zigzag superstructures are similar to some reported 'Z-bond' behaviour of ionic liquids,[10] or the self-assembled supramolecular helices[3c,11] where the dynamic stereoisomers are orderly arranged and stabilized in the solid state as a result of social self-sorting.[11,12] The skeleton of the zigzag sheets is built by the dimers overlapping across each other to form head-to-tail superstructures, i.e. in the trithiolane dimer **5**, one zigzag motif contains four molecules in a (*S*,*S*)-(*R*,*R*)-(*R*,*R*)-(*S*,*S*) sequence, (Figure 3.6a), and in dimer **2** the zigzag motif is composed of four of the sole *meso* diastereoisomer (Figure 3.6b). For both dimers, each point where two motifs overlap is a complementary pair of *R*- and *S*-barbaralyl units.

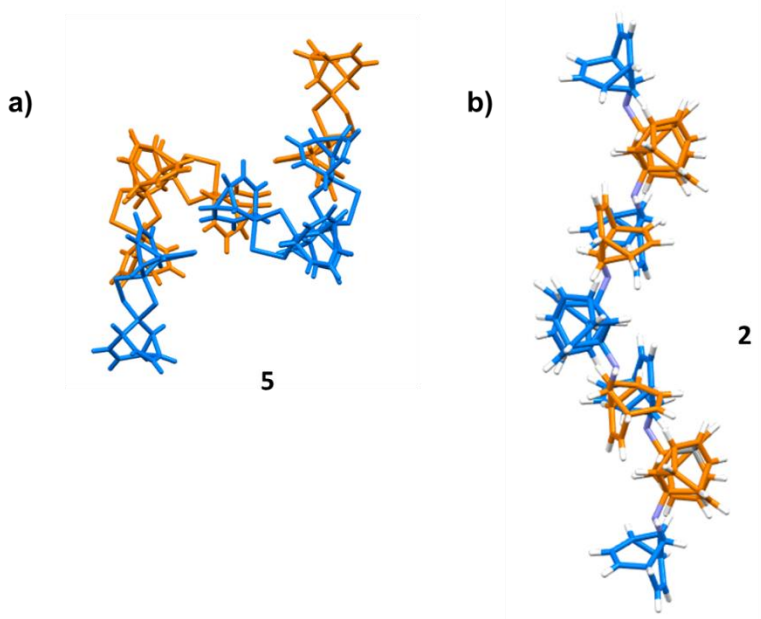

Figure 3.6. The superstructures of barbaralane dimers with barbaralyl enantiomerism distinguished by colours: organge = *R*, blue = *S*. (a) Trithiolane dimer **5**. (b) Amino dimer **2**.

All obtained dimer crystals exhibit high *Z* (number of molecules in the unit cell) values, and the majority of them also exhibit high *Z*′ (number of asymmetric units in the unit cell) values (Table 3.2), indicating that they either resolve different diastereoisomers or identical isomers occupying distinct, independent positions in the unit cell.[13] The trithiolane dimer **5** has a particularly high *Z*′ value (> 4), which is an extremely rare phenomenon in general (< 0.1% in CSD).[14] The unusual *Z* and *Z*′ values of barbaralane crystals are likely to be an outcome of awkward shape and high constraints,[15] as the barbaralyl units are rigid non-planar, cage-like

moieties, making it difficult to optimize packing and minimize voids in the solid state. Dimers with longer linkers (**1**, **3** and **4**) tend to exhibit lower *Z* values as they gain higher conformational flexibility which allows for various shapes, i.e. in the crystal structures of **3** and **4**, the individual molecules are aligned perpendicularly to form T-shaped configurations (Figure 3.7). The comparison of **3** and **4** also explains their different diastereoisomerisations: in dimer **4**, the linker length (~10 Å) is such that when one *meso*-**4** molecule is oriented vertically, it spans a distance that could accommodate two *meso*-**4** oriented horizontally, allowing for efficient packing with the sole *meso* diastereoisomer (Figure 3.7a), while in dimer **3**, the linker length is slightly shorter (~7.6 Å), and the U-shape of (*R*,*R*)/(*S*,*S*)-isomer could accommodate one barbaralyl unit like a inclusion complex (Figure 3.7b). Overall, the crystalline behaviours of barbaralane dimers are mainly dictated by the tendency of forming racemic units and packing closely, and resolution of multiple diastereoisomers indicated that they could spontaneously form co-crystals.

Compound	***Z***	***Z′***	**Resolved diastereoisomer(s)**
1	2	1	*meso*
2	4	1	*meso*
3	3	1.5	*meso*/(*R*,*R*)/(*S*,*S*)
4	2	1	*meso*
5	64	8	(*R*,*R*)/(*S*,*S*)

Table 3.2 *Z′* values of synthesised barbaralane dimers **1**-**5**.

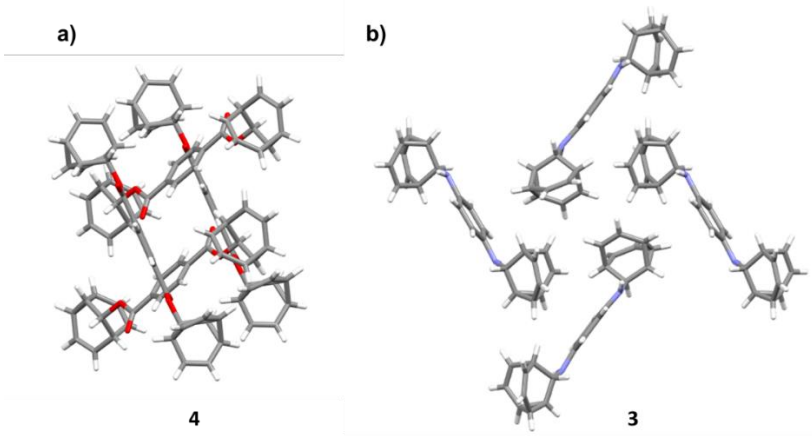

Figure 3.7. Configurations of barbaralane dimers in the unit cell. (a) dimer **4**, (b) dimer **3**.

The crystal structures of synthesised barbaralane monomers **10** and **4'** are also obtained and analysed. Both monomers exhibit a 1:1 ratio of *R*- and *S*- enantiomer to form racemic crystals, and their orientations in the superstructures are influenced by noncovalent interactions: a pair of *R*- and *S*-enantiomers of barbaralane **4'** form a cyclic structure through hydrogen bonding of the carboxylic moieties (Figure 3.8a), which is common behaviour for carboxylic acids.[16] In the case of barbaralol **10**, consecutive molecules forming (-*R*-*R*-*S*-*S*-) sequences are held together by the hydrogen bonding between their hydroxyl substituents to give a chiral supramolecular helix[3c,17], and the overall crystal structure exhibit achirality due to the presence of both enantiomorphs (*P*- and *M*-) of the supramolecular spirals (Figure 3.8b). The compared results show that oligomerised barbaralanes exhibit significantly fewer noncovalent bonding interactions than the monomers directing the packings in the solid state, which could be due to the extra barbaralyl unit having hindered the linker moieties and inhibited their interactions with each other.

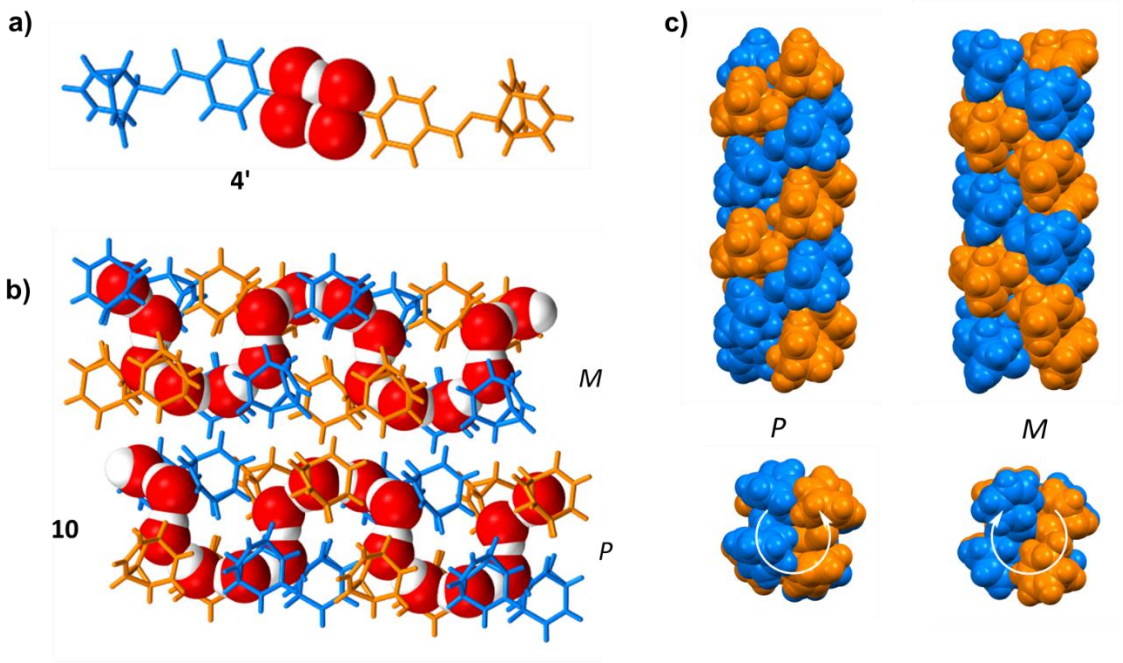

Figure 3.8. Superstructures of barbaralane monomers, enantiomers are distinguished by colours: orange = *R*, blue = *S*. (a) Cyclic structure of **4'** with the space-filling structure of the carboxylic terminals; (b) Partial complementary *P*/*M* chiral helix pair of **10** with the space-filling structure of the hydroxyl groups. (c) Space filling structures of *P*/*M* helices of **10**.

3.2.3 In Silico Modelling

DFT calculations (ωB97XD 6-31++G(d,p)) were carried out to model the Δ*G* between the diastereoisomers of the dimers in solution. All the calculations are carried out under implicit conformational control. The results show that barbaralane dimers **1–5** all have very low energy difference between their *meso* and (*R,R*)/(*S,S*) isomers (Table 3.2), indicating that they will be present in solution in populations relatively close to the statistical ratio of 2:1:1. The results of *ortho*-aniline dimer **1** and diester dimer **4** show that in the solution state, their energetically-favoured major isomers are (*R,R*) and (*S,S*), which is opposite to the crystalline state (*meso*). The resolution of minor isomers in the solid state confirms that the preferential crystallisation of barbaralane diastereoisomers does not relate to the degree of energies in the solution state.

Compounds	**Major Isomer**	**ΔG_{calc} kJ·mol^{-1}**	**Crystal**
(*S,S*)/*meso*/(*R,R*)**1**	*S,S*/*R,R*	1.2	*meso*
(*S,S*)/*meso*/(*R,R*)**2**	*meso*	1.9	*meso*
(*S,S*)/*meso*/(*R,R*)**3**	*S,S*/*R,R*	0.6	(*S,S*)/(*R,R*)/ *meso*
(*S,S*)/*meso*/(*R,R*)**4**	*S,S*/*R,R*	2.2	*meso*
(*S,S*)/*meso*/(*R,R*)**5**	*S,S*/*R,R*	0.2	(*S,S*)/(*R,R*)

Table 3.2 Calculated Δ*G* values of six synthesised barbaralane dimers and the comparison of energetically favoured isomers in solution vs the resolved isomers in solid state.

Hirshfeld surfaces of each crystal structure were generated, representing the spatial distribution of electron density around a molecule in order to search for specific noncovalent bonding interactions (Full details see section 3.4.6). The Hirshfeld surfaces of all the dimers show that no interatomic distances are significantly closer than the sum of the respective Van der Waals radii in all dimer crystals.[18] For example, in compound **1** and **2**, the most prominent close contacts present are weak H···H–C and H···H–N interactions, which remain within ~0.5 Å of the sum of the Van der Waals radii (Figure 3.9). Conversely, significant hydrogen bonding interactions are observed in both monomers **4'** and **10** involving their hydroxyl and carboxylic

terminal groups, which correspond to their cyclic and helix behaviours in the superstructures.

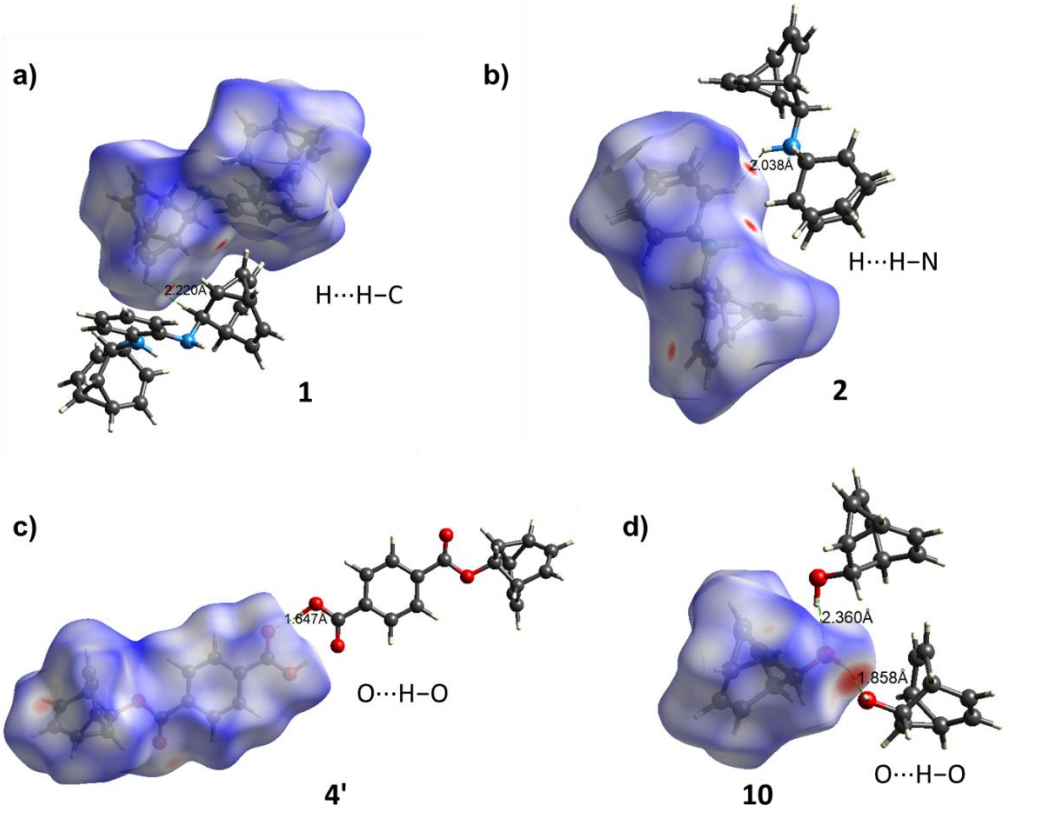

Figure 3.9. Calculated Hirshfeld surfaces for the X-ray crystal structures of (a) **1**, (b) **2**, (c) **4'** and (d) **10**, showing the most significant close contacts with neighbouring molecules.

The intermolecular interactions in the solid state were determined by DFT modelling (Full details see Section 3.4.6), in which the total interaction energies (E_{tot}) between neighbouring molecules based on the individual energetic components of electrostatics (E_{ele}), polarisation (E_{pol}), dispersion forces (E_{dis}) and repulsion (E_{rep}) were calculated respectively. These results further confirmed the lack of significant noncovalent bonding interactions of barbaralane dimers. For example, a cluster of the amino dimer **2** was generated with a central molecule surrounded by 14 neighbouring ones within its 3.8 Å radius (Figure 3.10). The strongest pairings with the central molecule are at positions G and I which have interaction energies of $E_{tot} = -52.5$ and -49.1 kJ mol^{-1}, respectively. The dispersion forces contributed to the majority of E_{tot} at all positions, suggesting that the packing of the molecules is not affected by any specific noncovalent bonding (Table 3.2).

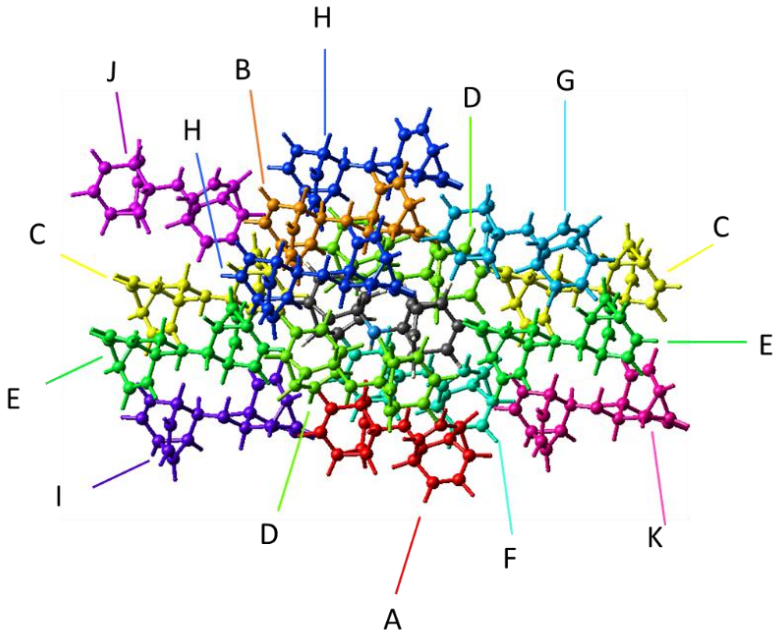

Figure 3.10. A section of the solid-state superstructure of **2** in which a central molecule (coloured by element) is surrounded by its 14 nearest neighbours (labelled A–I, distinguished by different colours). Labels and colours are duplicated for molecules that reside at symmetry-related coordinates relative to the central molecule.

Neighbouring molecule	R/Å	E_{ele}	E_{pol}	E_{dis}	E_{rep}	E_{tot}
A	6.07	-10.1	-1.0	-46.0	34.9	-29.9
B	5.45	-11.6	-1.5	-56.6	37.4	-39.5
C	10.23	-2.7	-0.5	-16.1	9.7	-11.2
D	6.34	-7.0	-2.1	-34.4	16.4	-28.8
E	9.95	-6.6	-1.2	-24.0	16.6	-18.4
F	6.51	-6.0	-0.4	-29.9	21.8	-19.2
G	10.22	-1.3	-0.2	-9.0	2.2	-8.0
H	8.36	-2.1	-0.2	-12.5	6.5	-9.2
I	10.33	-0.4	-0.1	-7.7	1.9	-6.0
J	12.60	-1.2	-0.0	-3.0	0.0	-3.8
K	11.62	-0.2	-0.0	-4.9	1.3	-3.7

Table 3.2 Calculated intermolecular interaction energies (kJ mol^{-1}) for pairs of molecules in the solid-state structure of **1**.

Crystal structure predictions (CSP) were conducted to predict the most energetically favoured crystallisation behaviour of barbaralanes,[19] in which the lattice energies of different combinations of isomers are calculated and ranked to find out the most stable ones (with highest crystal density). The initial CSP results of the trithiolane dimer **5** have compared the calculated lattice energy of three combinations: racemic crystal of a 1:1 (*R*,*R*)/(*S*,*S*), conglomerate of only (*R*,*R*), and racemic of only *meso* (Figure 3.11). The obtained results showed that the crystal which only contains the *meso* isomer has the lowest lattice energy and highest crystal density in theory (red dots at the bottom right), while the 1:1 mixture of (*R*,*R*)/(*S*,*S*) isomers have higher lattice energy of ~3 kJ·mol^{-1} (pointed out by arrow). The difference between CSP and XRD results indicated that either lattice energies are not dominant in affecting the crystallisation behaviour of **5**, or the specific calculation methods are not suitable for molecules exhibiting complicated dynamic chirality.

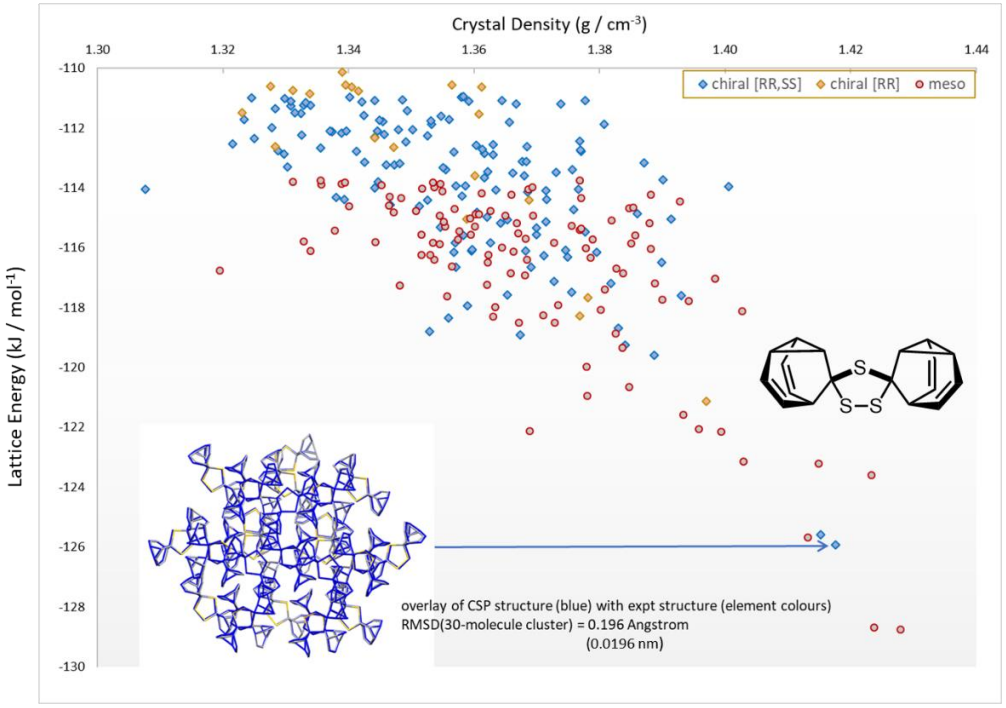

Figure 3.11. Initial CSP result of trithiolane dimer **5**.

3.3 Conclusions and Future Work

In summary, a series of barbaralane oligomers have been synthesised and studied their dynamic preferential crystallisations. The obtained barbaralane dimers all form racemic crystals, but resolved various combinations of diastereoisomers. The crystalline behaviour of the dimers

seem to follow the tendency of forming racemic crystals with the simplest combinations: for those without any added chiral or pro-chiral information, the *meso* diastereoisomer dominates the majority of the solid states, and for the trithiolane dimer **5** with a stereogenic disulfide bond, only the (*R*,*R*) and (*S*,*S*) isomers are resolved to avoid the rise of *P*- and *M*-chirality. The most interesting case is the aniline dimer **3** which resolves all three diastereoisomers in a 1:1:1 ratio as it is neither the simplest combination nor the mathematical ratio of the solution state. Analysis of superstructures and Z/Z' values reveal that the diastereoisomerisation of **3** is actually dictated by efficient packing as the 1:1:1 ratio of three isomers could utilise their differences of shapes like building blocks to form compact superstructures. Various *in silico* modelling studies have been conducted: DFT calculations indicate that all the diastereoisomers have very low ΔG differences and could interconvert freely in solution, Hirshfeld surfaces show that no significant interactions influence the crystal packings, and CSP on the energetically-favoured crystallisation behaviour of dimer **5** gives the opposite conclusion to the experimental result. The computational results suggest that the dynamic preferential crystallisation of barbaralane dimers is not related to energy differences or noncovalent interactions, but dictated by packing and geometry. The XRD results of two barbaralane monomers were also obtained and analysed, the monomers tend to form 1:1 *R*- and *S*-enantiomers and their packings are more influenced by noncovalent interactions. We can conclude the following trends in crystallisation behaviour of barbaralane oligomers (without external chiral information):

1) Racemic, 1:1 ratios of *R*- and *S*- barbarlyl units occur in all cases investigated so far.
2) In most cases barbaralane dimers resolve the *meso*-diastereoisomer, and exceptions are listed in 3) and 4).
3) The stereogenicity of substituents could transfer to the barbarlyl cores and lead to specific isomers.
4) For dimers with relatively longer linkers, the different shape between diastereoisomers could lead to various diastereoisomers allowing for closer packings with each other. Conversely, dimers with short linkers do not exhibit significantly different shapes between diastereoisomers, decreasing the possibility of resolving non-*meso* isomer.
5) The most prioritised factor dictating the dynamic resolution in the solid state is forming a

racemic crystal, then efficient packing and single (or minimum) diastereoisomer.

It cannot be denied that the above guidelines could only be applied in non-conglomerate crystals, however, as conglomerates only takes up ~10% of the chiral pool and their mechanism of forming still remains unclear,[20] the conclusion could help to predict the crystalline behaviours of not only barbaralanes but also other molecules possessing dynamic chirality. Notably, computational modelling in this study only plays a supporting role, as they are either proved to be nonrelevant or give opposite results to the experiments. The observed high Z/Z' values of obtained molecules correspond to their awkward shape and complex packing arrangements, and their occurrence among the barbaralane library has highlighted an exceptional regularity on the relatively rare high Z' crystals.

To conclude, the preferential crystallisations of dynamically chiral barbaralanes are generally a geometrical consequence involving packings and racemisations instead of chemical interactions. Currently the XRD results of the synthesised dimer **6** with a chiral linker have not been obtained, and tetramer **7** which can access ten different diastereoisomers, and their crystalline behaviour will further validate our conclusions.

3.4 Experimental Details

3.4.1 Specific Experimental Methods

For general experimental details see page *xv*. The X-ray single-crystal diffraction data were collected at 120.0(2) K using λMoKα radiation (λ = 0.71073 Å) on a Bruker D8Venture (Photon100 CMOS detector, IμS-microsource, focusing mirrors) diffractometer for barbaralane dimers **1**-**5**. Diffractometers were equipped with Cryostream (Oxford Cryosystems) open-flow nitrogen cryostats. All structures were solved by direct method and refined by full-matrix least squares on F2 for all data using Olex2 and SHELXT software. All non-hydrogen atoms were refined anisotropically and hydrogen atoms were placed in the calculated positions and refined in riding mode.

3.4.2 Synthesis of Barbaralane Oligomers 1-7

7-Ethynylcyclohepta-1,3,5-triene (8): The synthetic and spectroscopic data has been presented in Section 2.4.2 and will not be reproduced here to avoid redundancy.

Barbaralone (9): The synthetic and spectroscopic data has been presented in Section 2.4.2 and will not be reproduced here to avoid redundancy.

Barbaralol (10): The synthetic and spectroscopic data has been presented in Section 2.4.2 and will not be reproduced here to avoid redundancy.

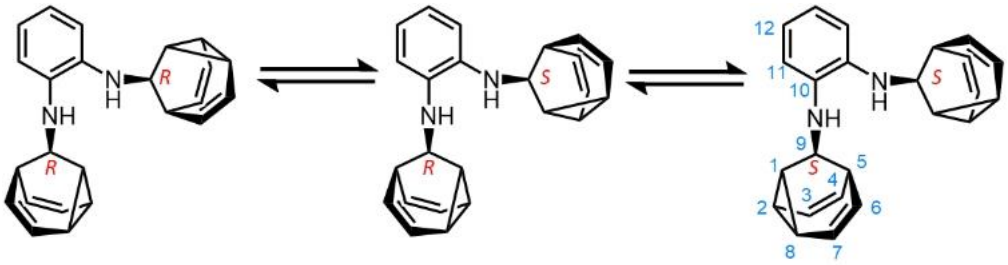

1,2-Di(9-barbaralyl)-diaminobenzene (1): Barbaralone **9** (80 mg, 0.61 mmol) and 1,2-diaminobenzene (32 mg, 0.30 mmol) were dissolved in dry MeOH (0.8 mL). Glacial acetic acid (12 µL, 0.21 mmol) was added and the solution was stirred at rt for 30 min. $NaBH_3CN$ (46 mg, 0.73 mmol) was added and the reaction mixture was stirred at 100 °C for reflux for 16 h. The reaction was quenched with 5 drops of Et_3N, washed with a saturated aqueous solution of $NaHCO_3$ (10 mL), extracted with CH_2Cl_2 (3 × 20 mL), dried over $MgSO_4$ and purified by column chromatography (Teledyne Isco CombiFlash Rf+ system, 12 g SiO_2, hexanes−EtOAc, gradient elution from 0 to 100%, 1% Et_3N) to give the title compound as a colorless oil (41 mg, 0.12 mmol, 40%). **^{1}H NMR** (400 MHz, $CDCl_3$) δ 6.74 – 6.70 (m, 2H, H_{12}), 6.68 – 6.63 (m, 2H, H_{11}), 5.87 (t, J = 7.9 Hz, 2H, H_3), 5.61 (t, J = 7.7 Hz, 2H, H_7), 4.15 – 4.06 (m, 4H, $H_{6/8}$), 4.01 – 3.91 (m, 4H, $H_{2/4}$), 3.23 – 3.14 (m, 2H, H_9), 2.58 – 2.49 (m, 4H, $H_{1/5}$). **^{13}C NMR** (151 MHz, $CDCl_3$) δ 37.0 (C_{10}), 122.8 (C_3), 121.2 (C_7), 119.6 (C_{12}), 115.8 (C_{11}), 76.1 ($C_{6/8}$), 72.4 ($C_{2/4}$), 43.9 (C_9), 29.2 ($C_{1/5}$). **HRMS-ESI** m/z = 341.2005 $[M+H]^+$, calculated for $C_{24}H_{25}N_2^+$ = 341.2012.

Di(9-barbaralyl) amine (2): The synthetic and spectroscopic data has been presented in Section 2.4.2 and will not be reproduced here to avoid redundancy.

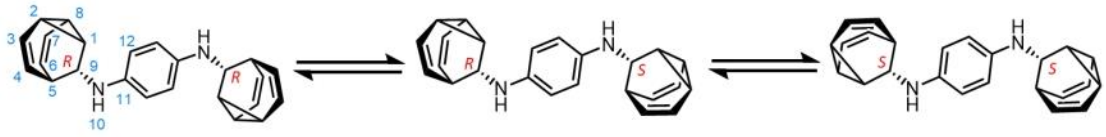

***N*, *N*'-di(9-barbaralyl)benzene-1,4-diamine (3):** Barbaralone **9** (80 mg, 0.61 mmol) and 1,4-diaminobenzene (32 mg, 0.30 mmol) were dissolved in dry MeOH (0.8 mL). Glacial acetic acid (12 µL, 0.21 mmol) was added and the solution was stirred at rt for 30 min. $NaBH_3CN$ (46 mg, 0.73 mmol) was added and the reaction mixture was stirred at 100 °C for reflux for 16 h. The reaction was quenched with 5 drops of Et_3N, washed with a saturated aqueous solution of $NaHCO_3$ (10 mL), extracted with CH_2Cl_2 (3 × 20 mL), dried over $MgSO_4$ and purified by column chromatography (Teledyne Isco CombiFlash Rf+ system, 12 g SiO_2, hexanes−EtOAc, gradient elution, 1% Et_3N) to give the title compound as a red solid (68 mg, 0.20 mmol, 67%). **M. P.** 196 – 198 °C. **^{1}H NMR** (400 MHz, $CDCl_3$) δ 6.51 (s, 4H, H_{12}), 5.83 (t, J = 7.9 Hz, 2H, H_3), 5.61 (m, 2H, H_7), 4.10 (m, 4H, $H_{6/8}$), 3.92 (m, 4H, $H_{2/4}$), 3.20 (m, 2H, H_9), 2.53 (m, 4H, $H_{1/5}$). **^{13}C NMR** (151 MHz, $CDCl_3$) δ 122.9 (C_3), 121.3 (C_7), 116.7 (C_{12}), 75.8 ($C_{6/8}$), 72.2 ($C_{2/4}$), 44.8 (C_9), 28.7 ($C_{1/5}$). [C_{11} not observed due slow relaxation of quaternary environment]. **HRMS-ASAP** m/z = 341.2018 $[M+H]^+$, calculated for $C_{24}H_{25}N_2^+$ = 341.2012.

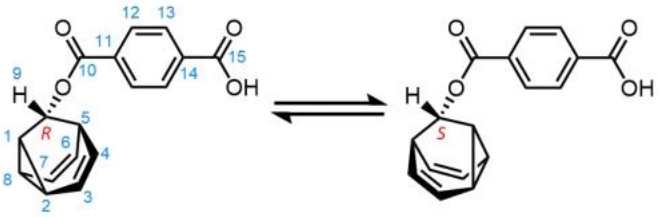

4-(9-barbaraloxy)carbonyl benzoic acid (4'): To an oven-dried round-bottomed flask, under a N_2 atmosphere was added terephthaloyl chloride (90 mg, 0.44 mmol) in anhydrous $CHCl_3$ (4.2 mL). Barbaralol **10** (50 mg, 0.37 mmol), DMAP (37 mg, 0.30 mmol) and Et_3N (0.15 mL, 1.09 mmol) were then added to the mixture. The reaction was left to stir at rt for 3 d. The reaction was quenched with an aqueous solution of NH_4Cl (25 mL, saturated) then extracted with $CHCl_3$ (3 × 20 mL). The combined organic extracts were dried over $MgSO_4$ and the solvent was removed under reduced pressure. The crude residue was purified by column chromatography (Teledyne Isco

CombiFlash Rf+ system, 12 g SiO_2, hexanes−EtOAc, gradient elution from 0 to 100% including 0.1% Et_3N in the elution) to give the title compound as a colorless solid (26 mg, 0.1 mmol, 25%). **M.P.** 224 – 226 °C. **^{1}H NMR** (600 MHz, $CDCl_3$) δ 8.14 (d, *J* = 8.6 Hz, 2H, H_{12} or H_{13}), 8.07 (d, *J* = 8.6 Hz, 2H, H_{12} or H_{13}), 5.87 (t, *J* = 7.9 Hz, 1H, H_7), 5.60 (t, *J* = 7.7 Hz, 1H, H_3), 4.98 (t, *J* = 3.3 Hz, 1H, H_9), 4.36 – 4.11 (m, 2H, H_2 and H_4), 4.11 – 4.03 (m, 2H, H_8 and H_6), 2.72 (td, *J* = 6.1, 3.2 Hz, 1H, H_5 and H_1). **^{13}C NMR** (151 MHz, $CDCl_3$) δ 170.5 (C_{10} or C_{15}), 165.6 (C_{10} or C_{15}), 135.4 (C_{14} or C_{11}), 132.9 (C_{11} or C_{14}), 130.2 (C_{12} or C_{13}), 129.8 (C_{12} or C_{13}), 122.0 (C_7), 121.3 (C_3), 75.1 (C_2 and C_4), 72.7 (C_8 and C_6) 67.9 (C_9), 28.5 (C_5 and C_1). **HRMS-ASAP** *m/z* = 283.0971 $[M+H]^+$, calculated for $C_{17}H_{15}O_4^+$ = 283.0970.

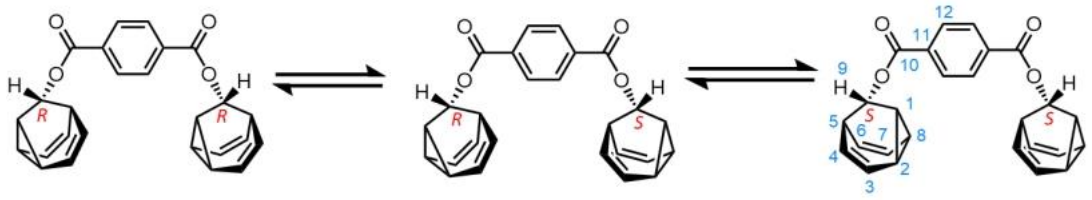

Di(9-barbaraloxy)-1,4-benzoate (4): During the above procedure, the title compound was also isolated as a white solid (40 mg, 0.10 mmol, 27% yield). **M. P.** 215 – 217 °C. **^{1}H NMR** (600 MHz, $CDCl_3$) δ 8.01 (s, 4H, H_{12}), 5.86 (t, *J* = 7.9 Hz, 2H, H_3), 5.61 (t, *J* = 7.6 Hz, 2H, H_7), 4.96 (t, *J* = 3.3 Hz, 2H, H_9), 4.20 – 4.10 (m, 4H, $H_{6/8}$), 4.08 – 4.01 (m, 4H, $H_{2/4}$), 2.81 – 2.64 (m, 4H, $H_{1/5}$). **^{13}C NMR** (151 MHz, $CDCl_3$) δ 165.8 (C_{10}), 134.5 (C_{11}), 129.6 (C_{12}), 122.0 (C_7), 121.3 (C_3), 75.2 ($C_{6/8}$), 72.8 ($C_{2/4}$), 67.7 (C_9), 28.5 ($C_{1/5}$). **HRMS-ASAP** m/z = 299.1608 $[M+H]^+$, calculated for $C_{26}H_{23}O4^+$ = 299.2048.

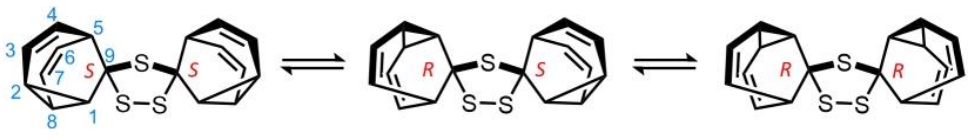

Dispiro(1,2,4-trithiolane-3,2':5,2''-dibarbaralane) (5): Barbaralone **9** (50 mg, 0.38 mmol) was dissolved in anhydrous PhMe (2 mL, 0.2 M) and 2,4-bis(4-methoxyphenyl)-2,4-dithioxo-1,3,2,4-dithiadiphosphetane (Lawesson's reagent, 100 mg, 0.25 mmol) was added to the stirred reaction mixture under an N_2 atmosphere. The reaction mixture was then heated to 110 °C to reflux and left to stir for 18 h. After cooling to rt, the solvent was removed under reduced

pressure. The crude residue was purified by preparative TLC, eluting with hexanes−EtOAc (4:1) to give the title compound as a colourless solid (15 mg, 0.05 mmol, 13% yield). The material was further purified by recrystallisation, preparing a saturated MeCN solution at 80 °C for reflux and slowly cooling to rt over 2 d in a crystallisation oven. **M. P.** 208 – 210 °C. **^{1}H NMR** (600 MHz, $CDCl_3$) δ 5.72 – 5.70 (m, 4H, $H_{3/7}$), 4.37 – 4.24 (m, 4H, $H_{2/4}$), 4.24 – 4.17 (m, 4H, $H_{6/8}$), 3.33 – 2.79 (m, 4H, $H_{1/5}$). **^{13}C NMR** (151 MHz, $CDCl_3$) δ 122.4 (C_3), 121.1 (C_7), 77.4 ($C_{2/4}$), 77.3 ($C_{6/8}$), 37.0 ($C_{1/5}$) [C_9 not observed due to slow relaxation of quaternary environment]. **HRMS-ASAP** m/z = 329.0495 $[M+H]^+$, calculated for $C_{18}H_{17}S_3^+$ = 329.0492.

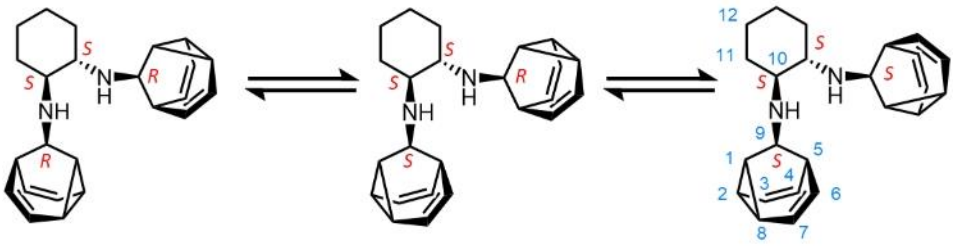

1,2-Di(9-barbaralyl)-(1*S*,2*S*)-diaminocyclohexane (6): Barbaralone **9** (80 mg, 0.61 mmol) and (1*S*,2*S*)-diaminocyclohexane (34 mg, 0.30 mmol) was dissolved in dry MeOH (0.8 mL). Glacial acetic acid (12 µL, 0.21 mmol) was added and the solution was stirred at rt for 30 min. $NaBH_3CN$ (46 mg, 0.73 mmol) was added and the reaction mixture was stirred at 100 °C to reflux for 16 h. The reaction was quenched with 5 drops of Et_3N, washed with a saturated aqueous solution of $NaHCO_3$ (10 mL), extracted with CH_2Cl_2 (3 × 20 mL), dried over $MgSO_4$ and purified by column chromatography (Teledyne Isco CombiFlash Rf+ system, 12 g SiO_2, hexanes−EtOAc, gradient elution from 0 to 100%) to give the title compound as a yellow oil. (27 mg, 0.078 mmol, 26% yield). **^{1}H NMR** (400 MHz, $CDCl_3$) δ 5.77 (t, *J* = 7.8 Hz, 2H, H_3), 5.54 (t, *J* = 7.7 Hz, 2H, H_7), 4.24 – 4.14 (m, 2H, H_6 or H_8), 4.05 (td, *J* = 7.6, 3.4 Hz, 2H, H_2 or H_4), 3.96 – 3.80 (m, 2H, H_6 or H_8), 3.74 (td, *J* = 7.3, 4.0 Hz, 2H, H_2 or H_4), 2.53 – 2.39 (m, 4H, $H_{1/9}$ or $H_{5/9}$), 2.30 (tt, *J* = 6.9, 2.7 Hz, 2H, H_1 or H_5), 2.12 – 2.00 (m, 2H, H_{10}), 1.88 (dt, *J* = 13.1, 2.5 Hz, 2H, H_{11E}), 1.62 (dq, *J* = 8.7, 3.0 Hz, 2H, H_{12E}), 1.17 – 1.06 (m, 2H, H_{12A}), 1.04 – 0.89 (m, 2H, H_{11A}). **^{13}C NMR** (151 MHz, $CDCl_3$) δ 122.6 (C_3), 121.1 (C_7), 80.6 (C_6 or C_8), 71.8 (C_6 or C_8), 67.7 (C_2 or C_4), 59.4 (C_{10}), 45.1 (C_9), 32.8 (C_{11}), 30.4 (C_1 or C_5), 29.3 (C_1 or C_5), 25.1 (C_{12}). **HRMS-ESI** m/z = 347.2475 $[M+H]^+$, calculated for $C_{24}H_{31}N_2^+$ = 347.2482. E and A

symbols were used to present the equatorial and axial H atoms on the 11 and 12 positions.

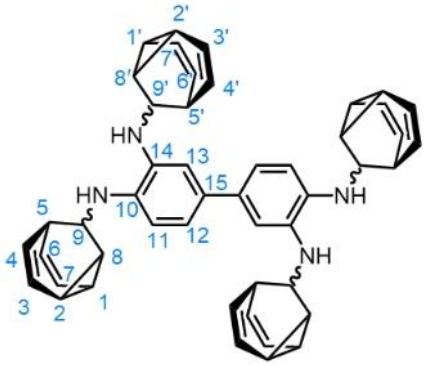

***N*³,*N*³',*N*⁴,*N*⁴'-tetra-9-barbaralyl-[1,1'-biphenyl]-3,3',4,4'-tetraamine (7)**: Barbaralone **9** (80 mg, 0.61 mmol) and 3,3′-diaminobenzidine (32 mg, 0.15 mmol) was dissolved in dry MeOH (0.4 mL) and dry THF (0.4 mL). Glacial acetic acid (12 µL, 0.21 mmol) was added and the solution was stirred at rt for 30 min. $NaBH_3CN$ (46 mg, 0.72 mmol) was added and the reaction mixture was stirred at 130 °C for reflux for 24 h. The reaction was quenched with 5 drops of Et_3N, washed with aqueous $NaHCO_3$ (10 mL), extracted with CH_2Cl_2 (3 × 20 mL), dried over $MgSO_4$ and purified *via* column chromatography (Teledyne Isco CombiFlash Rf+ system, 24 g HP SiO_2, pentane*−EtOAc, gradient elution from 0 to 100%) to give the title compound as a yellow oil. (8 mg, 11.8 µmol, 8% yield) **^{1}H NMR** (400 MHz, $CDCl_3$) δ 6.90 (dd, *J* = 8.0, 2.0 Hz, 2H, H_{11}), 6.84 (d, *J* = 2.0 Hz, 2H, H_{13}), 6.71 (d, *J* = 8.1 Hz, 2H, H_{12}), 5.91 (t, *J* = 7.9 Hz, 4H, $H_{3/3'}$), 5.64 (td, *J* = 7.7, 1.7 Hz, 4H, $H_{7/7'}$), 4.15 (td, *J* = 7.2, 3.7 Hz, 8H, $H_{6/6'/8/8'}$), 4.01 (d, *J* = 8.2 Hz, 8H, $H_{2/2'/4/4'}$), 3.27 (s, 2H, H_9 or $H_{9'}$), 3.21 (s, 2H, H_9 or $H_{9'}$), 2.63 – 2.55 (m, 8H, $H_{1/1'/5/5'}$). **^{13}C NMR** (151 MHz, $CDCl_3$) δ 135.27 (C_{10} or C_{14}), 134.86 (C_{10} or C_{14}), 132.54 (C_{15}), 122.81 ($C_{3/3'}$), 121.21 ($C_{7/7'}$), 118.69 (C_{11}), 116.12 (C_{13}), 114.33 (C_{12}), 76.15 ($C_{6/6'/8/8'}$), 72.44 ($C_{2/2'/4/4'}$), 44.13 (C_9 or $C_{9'}$), 43.93 (C_9 or $C_{9'}$), 29.29 ($C_{1/1'/5/5'}$). **HRMS-ASAP** m/z = 679.3802 $[M+H]^+$, calculated for $C_{48}H_{47}N_4^+$ = 679.3795.

* Pentane was used as hexane will be trapped into the target compound.

3.4.3 Structural Assignment by 2D NMR

In order to distinguish the 10-12 positions, especially the axial and equatorial H atoms with respect to each other on the cyclohexane ring of the barbaralane dimer **6**, 2D NMR spectroscopy (COSY, HSQC, etc.) was acquired for the assignment of each peak. The 10 position was first distinguished as the C_{10} peak only correlates with one ^{1}H peak in the HSQC spectrum, while the 11 and 12 both correlate with two separate ^{1}H signals (Figure 3.12).

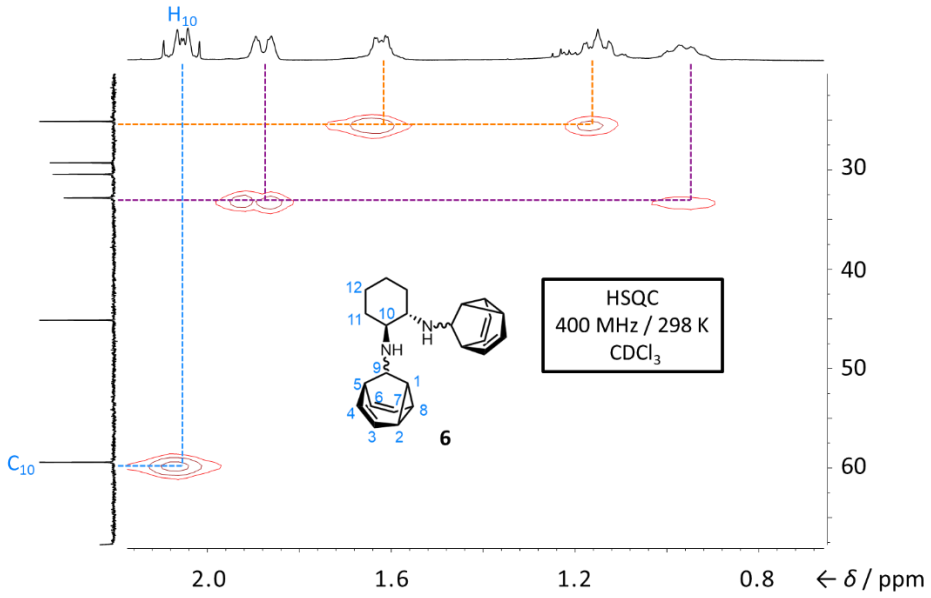

Figure 3.12. Partial HSQC spectrum of **6**.

The axial H atom on the 11 position (H_{11A}) was then distinguished as it is observed to be correlated with H_{10} in the COSY spectrum (Figure 3.13). Upon finding H_{11A}, H_{12A} was then distinguished due to its correlation with H_{11A}. The remaining equatorial H atoms were determined via HSQC correlations in Figure 3.12.

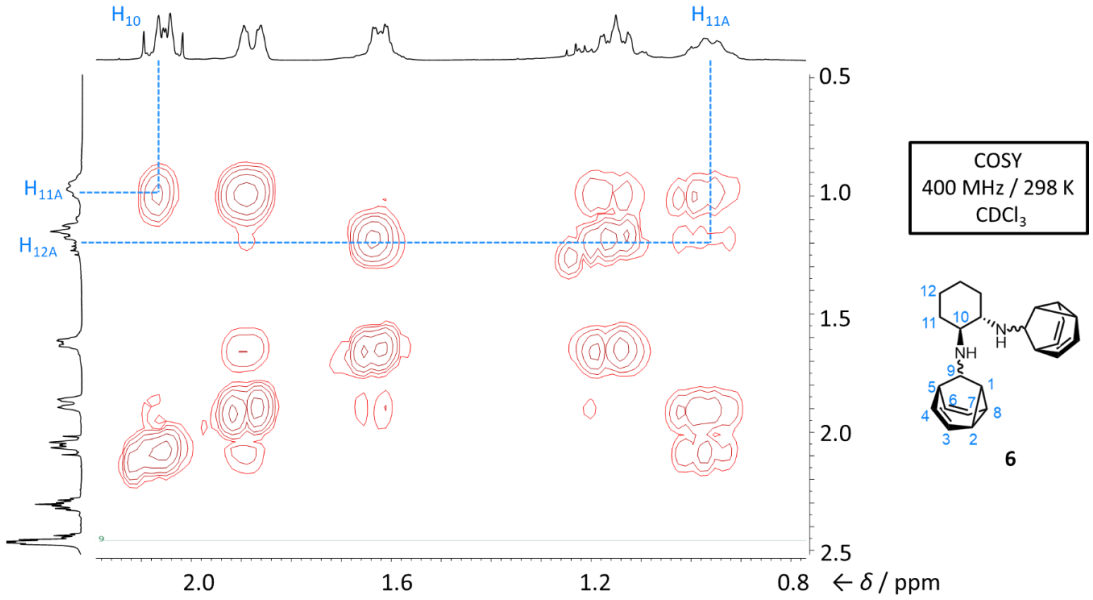

Figure 3.13. Partial COSY spectrum of **6**.

3.4.4 X-ray Crystallographic Analysis

_N_, _N_'-di(9-barbaralyl)benzene-1,2-diamine (1)

Crystals of **1** suitable for X-ray diffraction were grown by slow evaporation of a hexanes / DCM solution at −20 °C.

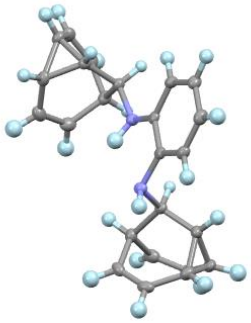

Figure 3.14. Solid-state structure of **1** including probability ellipsoids at 50%.

Crystal data: $C_{24}H_{24}N_2$, M = 340.45, crystal system = triclinic, space group = P-1, a = 10.0864(5), b = 10.5107(5), c = 10.7405(5) Å, α = 62.838(5) °, β = 71.717(4) °, γ = 61.472(5), U = 883.38(9) $Å^3$, F(000) = 364.0, Z = 1, Dc = 1.280 $g \cdot cm^{-3}$, μ = 0.570 (Cu Kα, λ = 1.54184), T =110.00(10) K. Final $wR_2(F^2)$ = 0.0846 for all data, conventional $R_1(F)$ = 0.0343 for reflections with $I \geq 2\sigma$, GOF = 1.031.

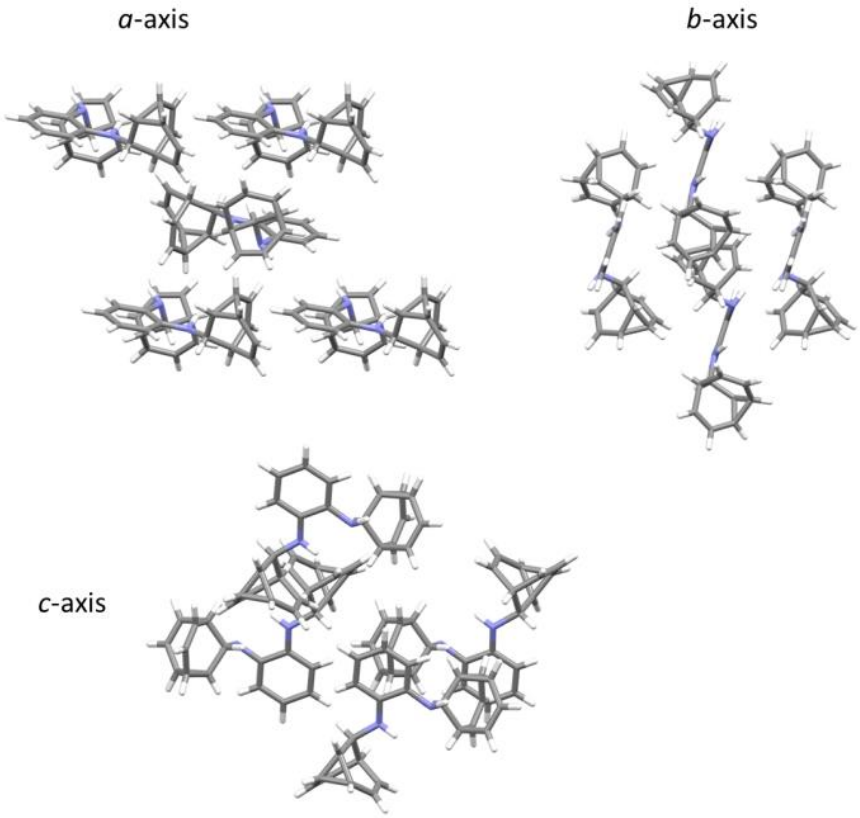

Figure 3.15. Solid-state superstructure of **1** viewed along the three unit cell axes.

Di(9-barbaralyl) amine (2):

The X-ray diffraction data has been presented in Section 2.5.2 and will not be reproduced here to avoid redundancy.

***N*, *N*'-di(9-barbaralyl)benzene-1,4-diamine (3)**

Crystals of **3** suitable for X-ray diffraction were grown by slow evaporation of a hexanes solution at room temperature.

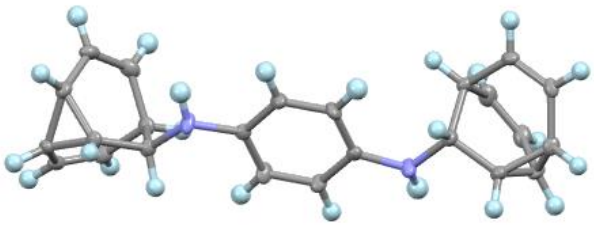

Figure 3.16. Solid-state structure of **3** including probability ellipsoids at 50%.

Crystal data: $C_{24}H_{24}N_2$, M = 340.45, crystal system = triclinic, space group = P-1, a = 6.2803(13), b = 13.913(2), c = 15.421(3) Å, α = α = 80.458(5)°, β = 80.869(6)°, γ = 77.475(7)°, U = 1286.6(4) $Å^3$, F(000) = 546.0, Z = 3, Dc = 1.318 $g \cdot cm^{-3}$, μ = 0.077 mm^{-1}(Mo-Kα, λ = 0.71073 Å), T =120.00 K. Final $wR_2(F^2)$ = 0.1484 for all data, conventional $R_1(F)$ = 0.0766 for reflections with I ≥ 2σ, GOF = 1.024.

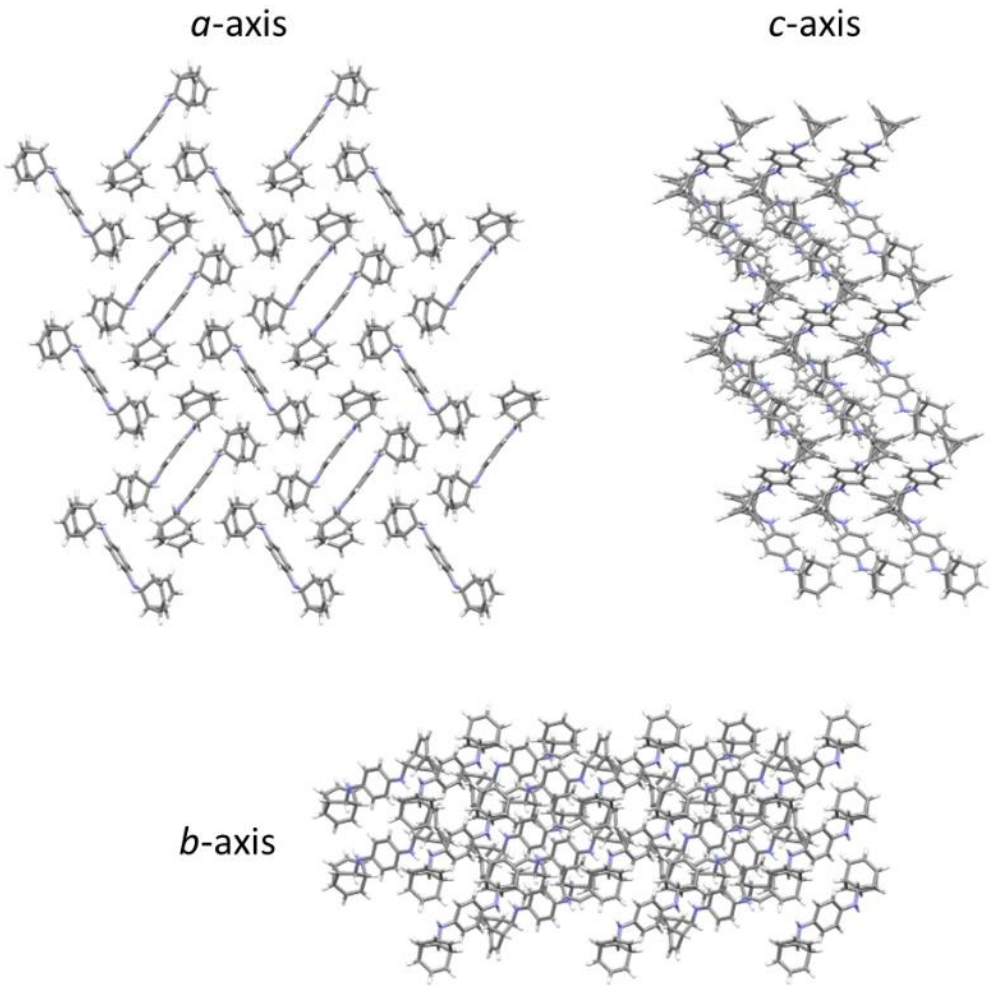

Figure 3.17. Solid-state superstructure of **3** viewed along the three unit cell axes.

Di(9-barbaraloxy)-1,4-benzoate (4):

Crystals of **4** suitable for X-ray diffraction were grown by slow evaporation of a saturated MeCN solution.

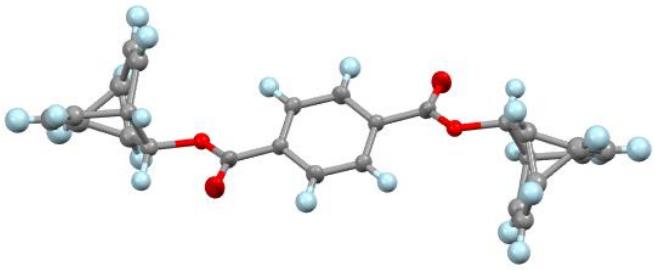

Figure 3.18. Solid-state structure of **4** including probability ellipsoids at 50%.

Crystal data: $C_{26}H_{22}O_4$, M = 398.43, crystal system = triclinic, space group = P-1, a = 6.4905(12) Å, b = 10.678(2) Å, c = 13.900(3) Å, α = 90.748(5)°, β = 96.640(5)°, γ = 91.764(5)°, U = 956.2(3) $Å^3$, F(000) = 420.0, Z = 2, Dc = 1.384 $g \cdot cm^{-3}$, F(000) = 420.0, μ = 0.093, T =120.0 K. Final $wR_2(F^2)$ = 0.2360 for all data, conventional $R_1(F)$ = 0.0884 for reflections with $I \geq 2\sigma$, GOF = 1.035.

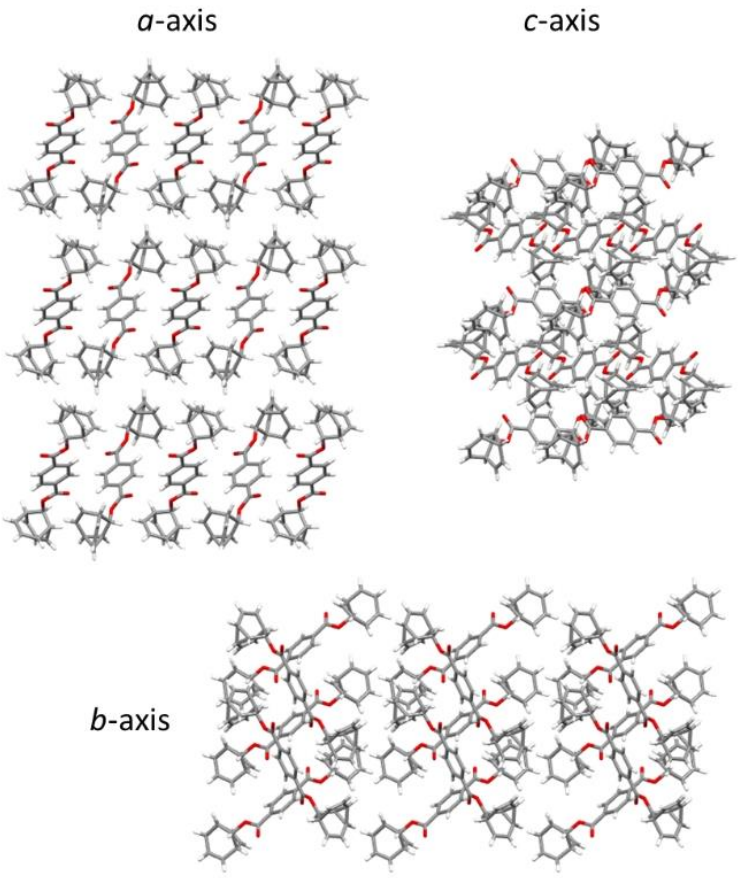

Figure 3.19. Solid-state superstructure of **4** viewed along the three unit cell axes.

4-(9-barbaraloxy)carbonyl benzoic acid (4'):

Crystals of **4'** suitable for X-ray diffraction were grown by slow evaporation of a saturated MeCN solution.

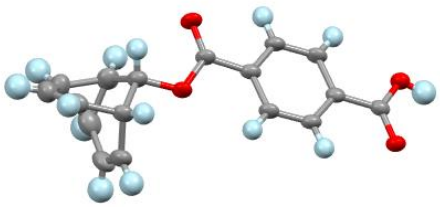

Figure 3.20. Solid-state structure of **4'** including probability ellipsoids at 50%.

Crystal data: $C_{17}H_{14}O_4 \times 0.5\ CHCl_3$, M = 341.97, crystal system = monoclinic, space group = C2/c, a = 11.439(3) Å, b = 6.3633(15) Å, c = 42.650(10) Å, α = 90°, β = 95.091(5)°, γ = 90°, U = 3092.3(13) $Å^3$, F(000) = 1416.0, Z = 8, Dc = 1.469 $g \cdot cm^{-3}$, μ = 0.325, T =100.0 K. Final $wR_2(F^2)$ = 0.2939 for all data, conventional $R_1(F)$ = 0.0957 for reflections with $I \geq 2\sigma$, GOF = 1.081.

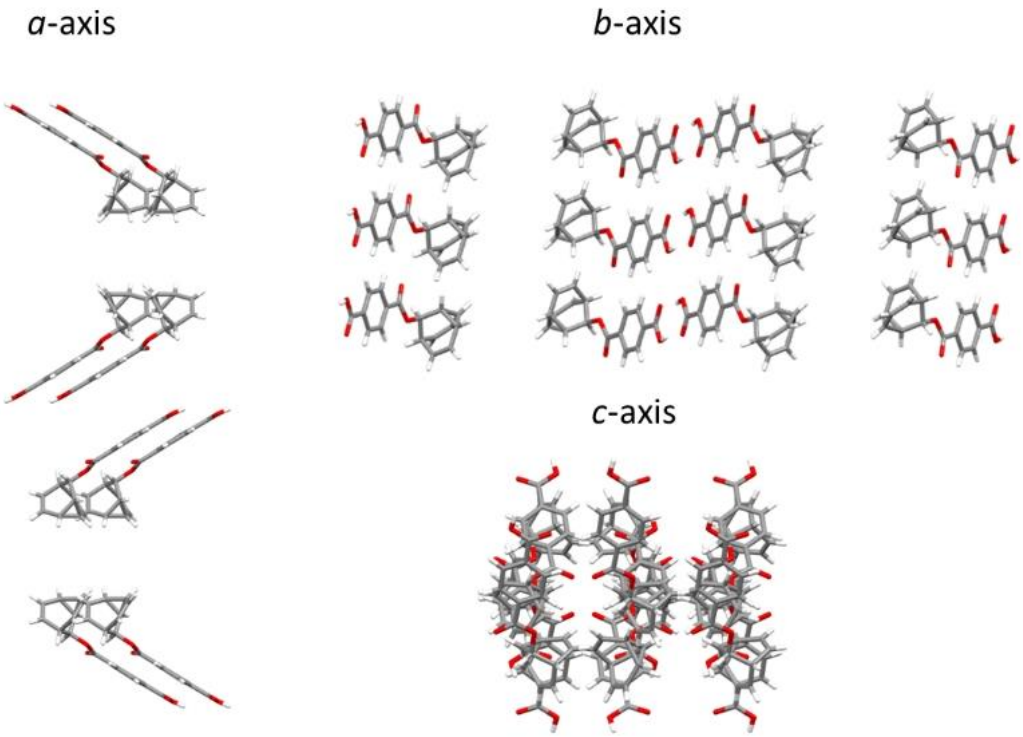

Figure 3.21. Solid-state superstructure of **4'** viewed along the three unit cell axes.

Dispiro(1,2,4-trithiolane-3,2':5,2''-dibarbaralane) (5):

Crystals of **5** suitable for X-ray diffraction were grown by slow cooling of a hot and saturated MeCN solution.

Figure 3.22. Solid-state structure of **5** including probability ellipsoids at 50%.

Crystal data: $C_{18}H_{16}S_3$, M = 328.49, crystal system = orthorhombic, space group = Pbcn, a = 20.4767(4), b = 9.3487(2), c = 15.5799(3) Å, α = 90°, β = 90°, γ = 90°, U = 2982.5(1) $Å^3$, F(000) = 1376.0, Z = 8, Dc = 1.463 mg m^{-3}, F(000) = 1376.0, Z = 8, μ = 0.486 mm^{-1}(Mo-Kα, λ = 0.71073 Å), T =120(1) K. Final $wR_2(F^2)$ = 0.1187 for all data, conventional $R_1(F)$ = 0.0432 for reflections with I ≥ 2σ, GOF = 1.038.

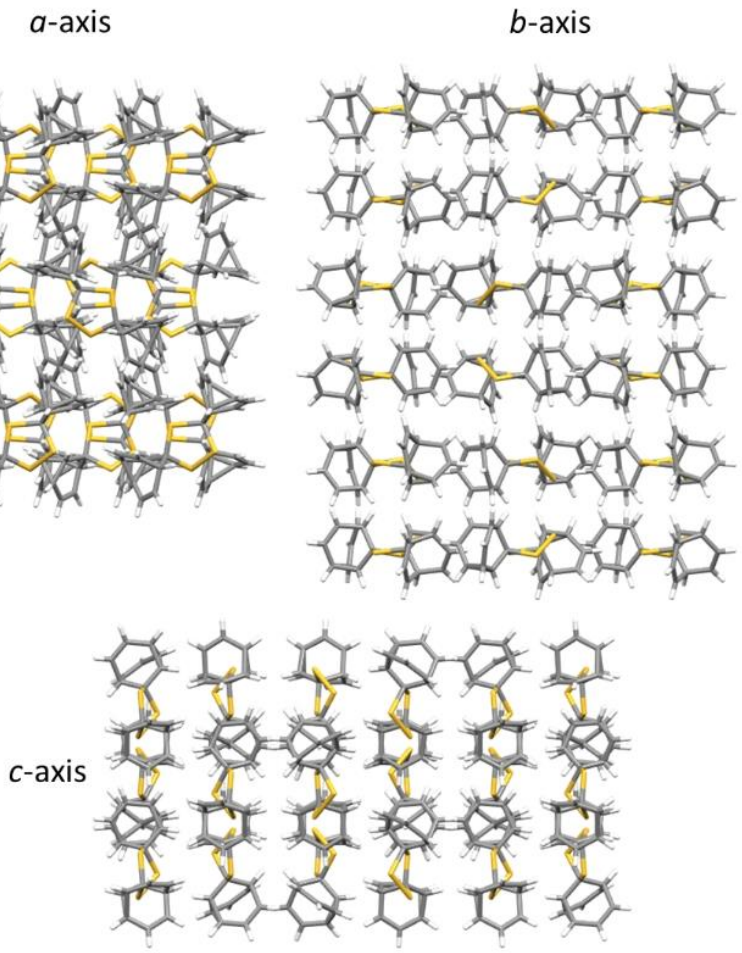

Figure 3.19. Solid-state superstructure of **5** viewed along the three unit cell axes.

Barbaralol (10)

The X-ray diffraction data has been presented in Section 2.5.2 and will not be reproduced here to avoid redundancy.

3.4.5 Calculated Solution-State Equilibiria

DFT calculations were carried out in Gaussian 16. The minimum energy ground state (GS) geometries of the barbaralanes were optimised using the range-separated hybrid (RSH) general gradient approximation GGA functional ωB97XD. Calculations were performed using the 6-31++G(d,p) basis set for H, C, N, O, and S atoms. For compounds with rotatable single bonds that lead to several accessible conformers, a molecular mechanics conformational search was performed to identify conformers that were then taken on to DFT optimisation. Conformational

searches were performed using confab implemented in Open Babel, identifying all conformers predicted to be within 15 kcal·mol^{-1} of the lowest energy structure and with a root mean square deviation of 1.0 Å or more. The Gibbs energy gaps (ΔG_{calc}) reported in Table 3.3 correspond to the difference in energy between the lowest energy conformers of the relevant diastereoisomers. The equilibrium constants (K) of diastereoisomers are calculated via the equation:

$$K = e^{-\Delta G/RT}$$

Compounds	**Major Isomer**	**ΔG_{calc} kJ·mol^{-1}**	**Equilibirum Constant (K)**
*(S,S)/meso/(R,R)***1**	*S,S/R,R*	1.2	0.62
*(S,S)/meso/(R,R)***2**	*meso*	1.9	0.46
*(S,S)/meso/(R,R)***3**	*S,S/R,R*	0.6	0.78
*(S,S)/meso/(R,R)***4**	*S,S/R,R*	2.2	0.41
*(S,S)/meso/(R,R)***5**	*S,S/R,R*	0.2	0.92
*(S,S)/meso/(R,R)***6**	*meso*	2.5	0.36

Table 3.3. Energetics and equilibrium constants of the dynamic sp^3-carbon equilibria.

3.4.6 Hirshfeld Surfaces and Intermolecular Energies

Hirshfeld surfaces were calculated for the crystal packing structures of **1, 2, 3,** and **4** (**5** not obtained due to disorders) in CrystalExplorer21 using an isovalue of 0.5 and mapping the normalised contact distance, d_{norm}. The surfaces highlight in red illustrate any regions in which the molecular surfaces meet at distances shorter than the sum of van der Waals radii, while white and blue illustrate regions where they meet at distances that are the sum of the van der Waals radii or longer, respectively. As a result, the Hirshfeld surfaces of **1**, **2**, **3** and **4** reveal there are only a few contacts that are slightly shorter than the sum of van der Waals radii, indicating that that there are no strong and specific noncovalent interactions in the solid state that direct the crystal packing.

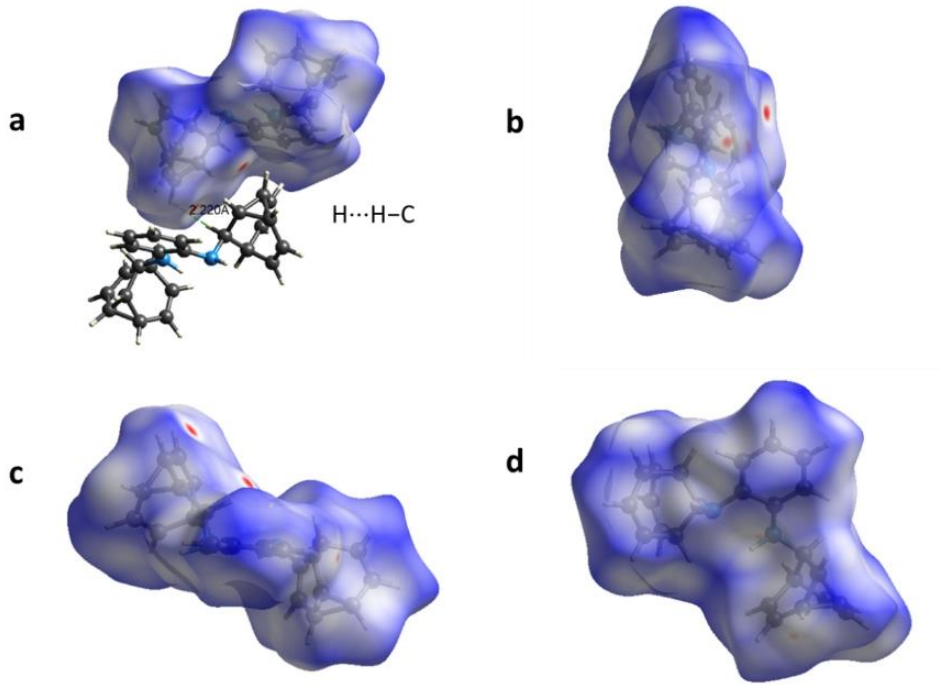

Figure 3.21. Hirshfeld surface of **1**, showing (a) the most significant close contacts, as well as views of the surface along the crystallographic (b) a-axis, (c) b-axis, and (d) c-axis.

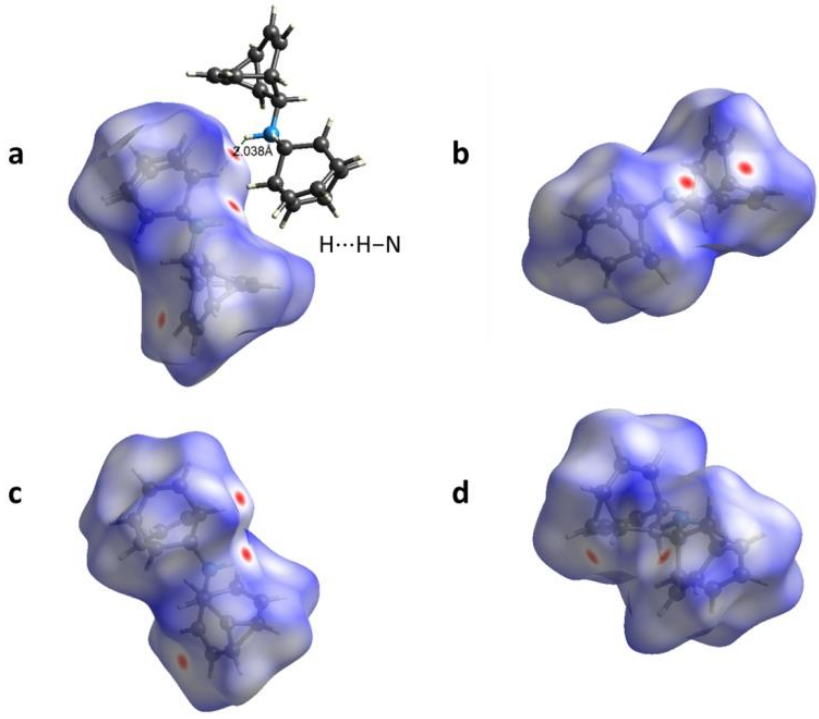

Figure 3.22. Hirshfeld surface of **2**, showing (a) the most significant close contacts, as well as views of the surface along the crystallographic (b) a-axis, (c) b-axis, and (d) c-axis.

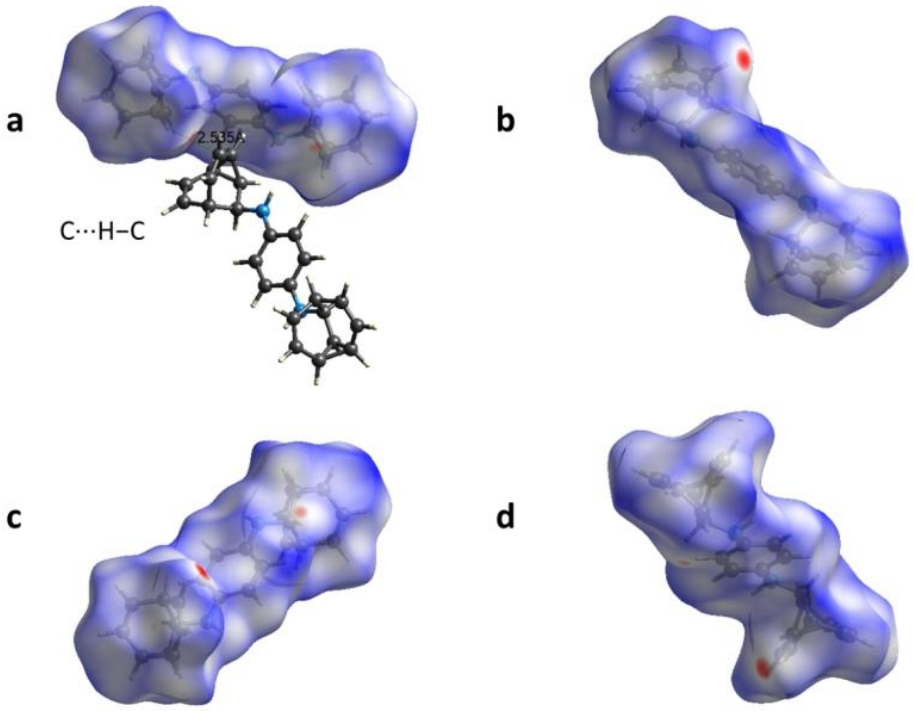

Figure 3.23. Hirshfeld surface of *meso*-**3**, showing (a) the most significant close contacts, as well as views of the surface along the crystallographic (b) a-axis, (c) b-axis, and (d) c-axis.

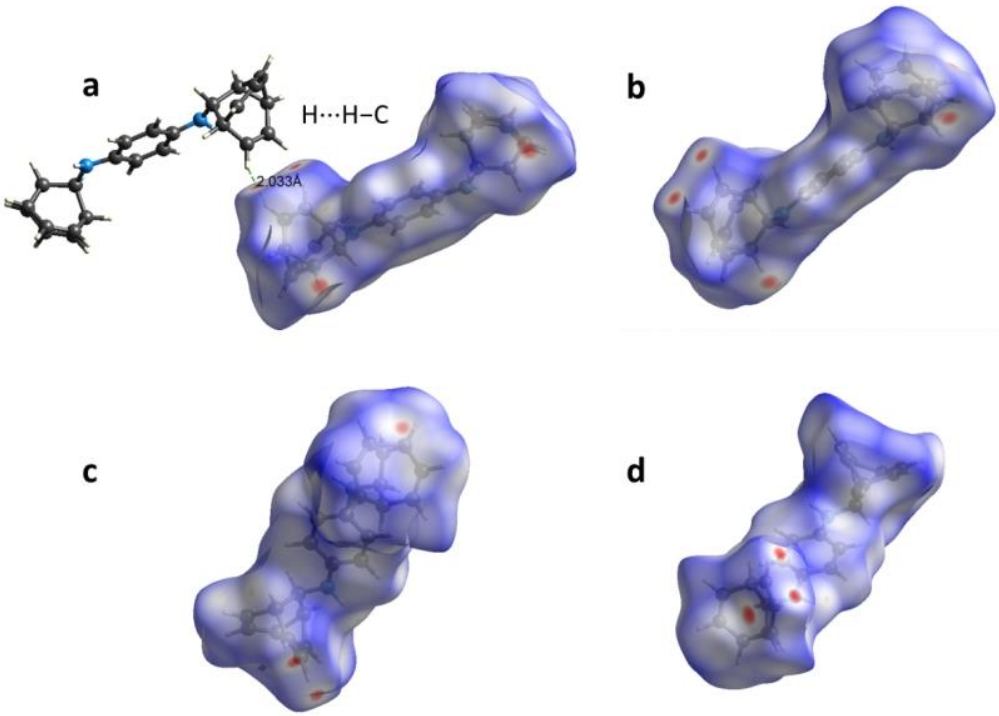

Figure 3.24. Hirshfeld surface of (*R,R*)/(*S,S*)-**3**, showing (a) the most significant close contacts, as well as views of the surface along the crystallographic (b) a-axis, (c) b-axis, and (d) c-axis.

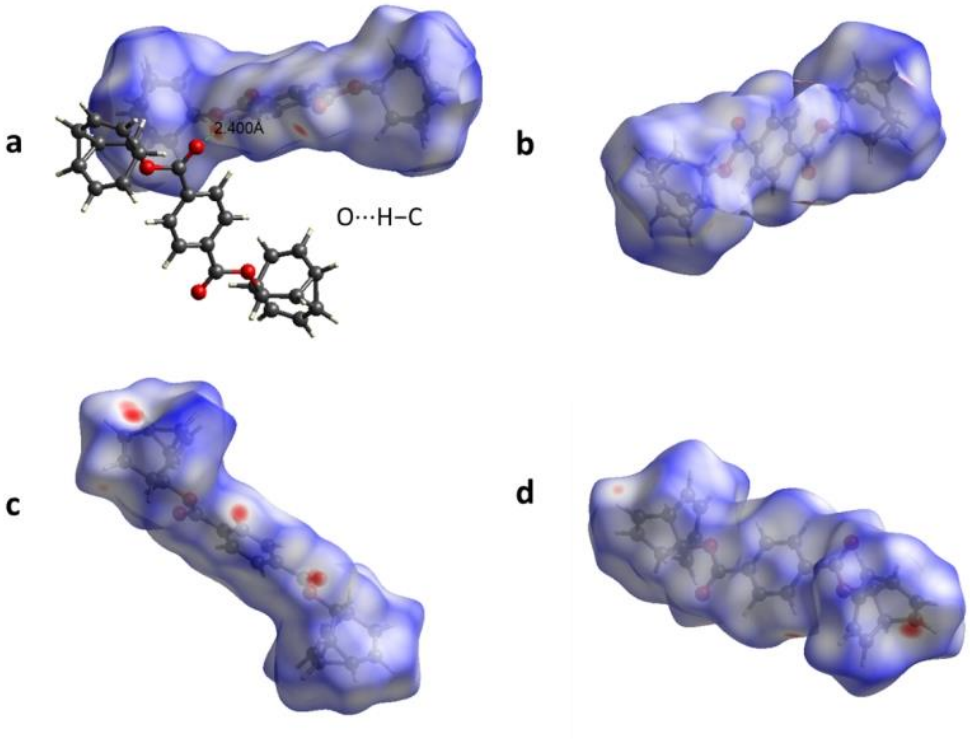

Figure3.25. Hirshfeld surface of **4**, showing (a) the most significant close contacts, as well as views of the surface along the crystallographic (b) a-axis, (c) b-axis, and (d) c-axis.

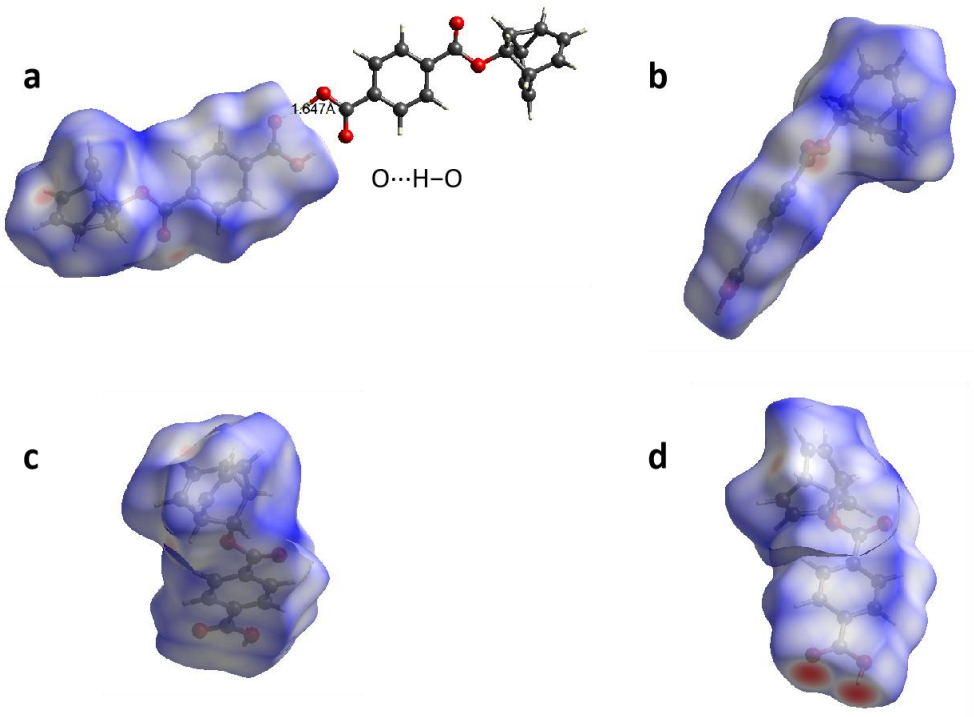

Figure 3.26. Hirshfeld surface of **4'**, showing (a) the most significant close contacts, as well as views of the surface along the crystallographic (b) a-axis, (c) b-axis, and (d) c-axis.

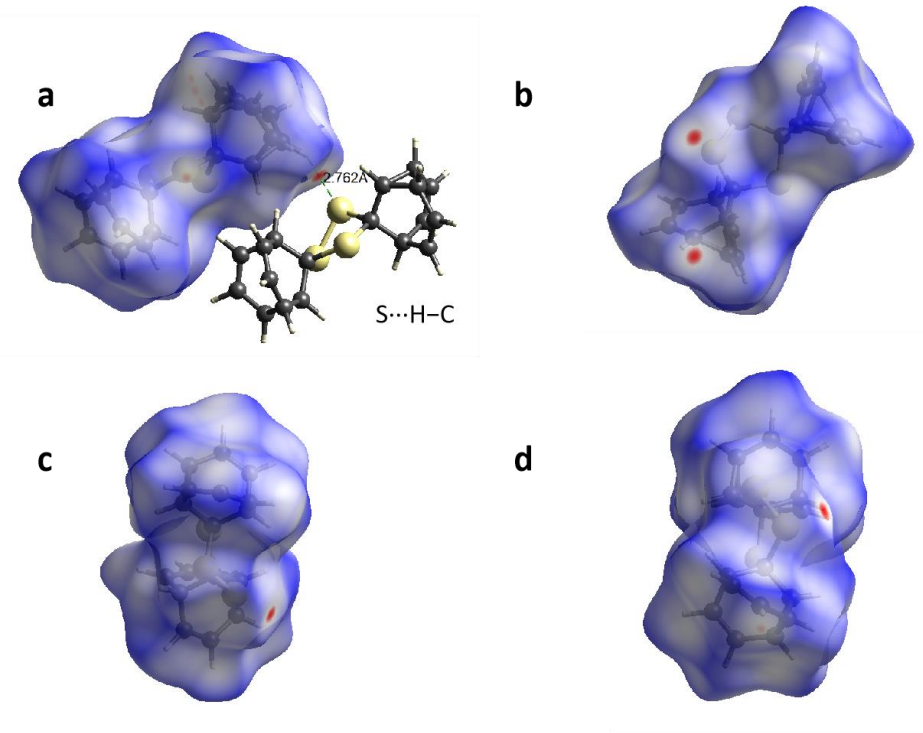

Figure 3.27. Hirshfeld surface of **5**, showing (a) the most significant close contacts, as well as views of the surface along the crystallographic (b) a-axis, (c) b-axis, and (d) c-axis.

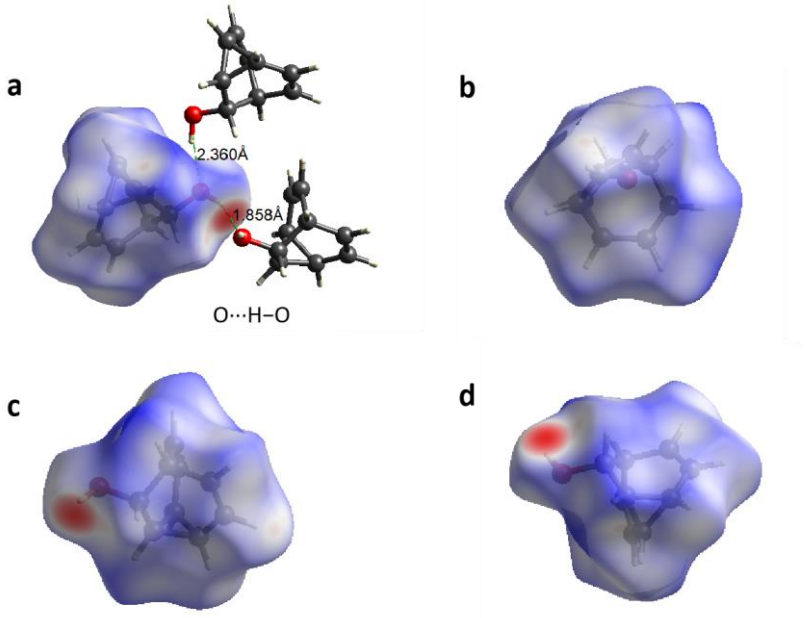

Figure 3.28. Hirshfeld surface of **10**, showing (a) the most significant close contacts, as well as views of the surface along the crystallographic (b) a-axis, (c) b-axis, and (d) c-axis.

DFT calculations were performed to quantify the interaction energies between neighbouring molecules in the solid state using the CE-B3LYP [B3LYP/6-31G(d,p)] energy model in CrystalExplorer21. Based on the X-ray crystal structure coordinates, a cluster was generated around a central molecule, extending to molecules that come within 3.8 Å of the central molecule at any point.

***N*, *N*'-di(9-barbaralyl)benzene-1,2-diamine (1)**

	N	R / Å	E_{ele}	E_{pol}	E_{dis}	E_{rep}	E_{tot}
	2	10.53	-7.3	-1.1	-31.0	21.9	-22.1
	1	7.97	-6.9	-0.7	-47.0	29.8	-30.3
	2	10.09	-7.2	-1.1	-41.0	27.6	-27.1
	1	13.47	-1.8	-0.0	-3.7	0.0	-5.2
	1	8.20	-7.6	-1.5	-35.3	21.8	-26.4
	1	7.97	-1.3	-0.7	-22.5	5.2	-18.3
	1	6.90	-18.3	-2.7	-72.0	51.1	-52.5
	2	10.51	-0.7	-0.1	-7.4	2.3	-5.8
	1	6.93	-12.7	-3.0	-61.8	32.8	-49.1
	1	8.09	-4.6	-0.5	-28.4	18.3	-18.7
	1	13.67	-0.7	-0.0	-2.7	0.0	-3.2

Table 3.4. Calculated intermolecular interaction energies (in kJ·mol^{-1}) for the solid-state structure of **1**

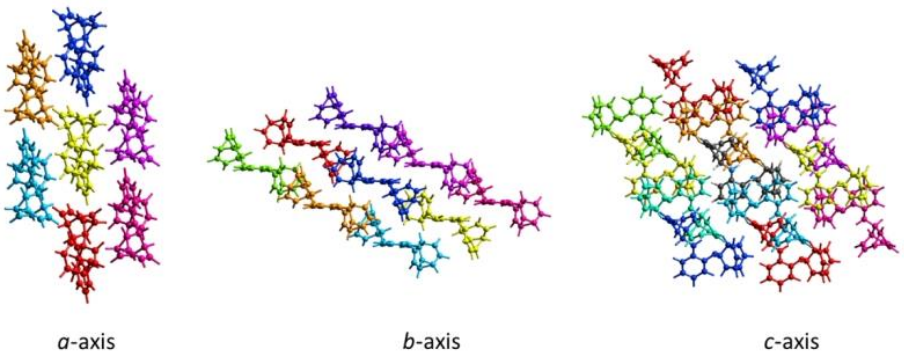

Figure 3.29. The cluster of molecules used to model intermolecular interaction energies listed in Table 3.4. The central molecule is coloured according to atom type (C, grey; H, white; N, blue) and surrounding molecules are coloured to match the colour code in Table 3.4.

Di(9-barbaralyl) amine (2)

	N	R / Å	E_{ele}	E_{pol}	E_{dis}	E_{rep}	E_{tot}
	2	10.23	-2.7	-0.5	-16.1	9.7	-11.2
	1	5.45	-11.6	-1.5	-56.6	37.4	-39.5
	2	9.95	-6.6	-1.2	-24.0	16.6	-18.4
	1	10.22	-1.3	-0.2	-9.0	2.2	-8.0
	2	6.34	-7.0	-2.1	-34.4	16.4	-28.8
	1	6.51	-6.0	-0.4	-29.9	21.8	-19.2
	2	8.36	-2.1	-0.2	-12.5	6.5	-9.2
	1	10.33	-0.4	-0.1	-7.7	1.9	-6.0
	1	12.60	-1.2	-0.0	-3.0	0.0	-3.8
	1	6.07	-10.1	-1.0	-46.0	34.9	-29.9
	1	11.62	-0.2	-0.0	-4.9	1.3	-3.7

Table 3.5. Calculated intermolecular interaction energies (in kJ·mol^{-1}) for the solid-state structure of **2.**

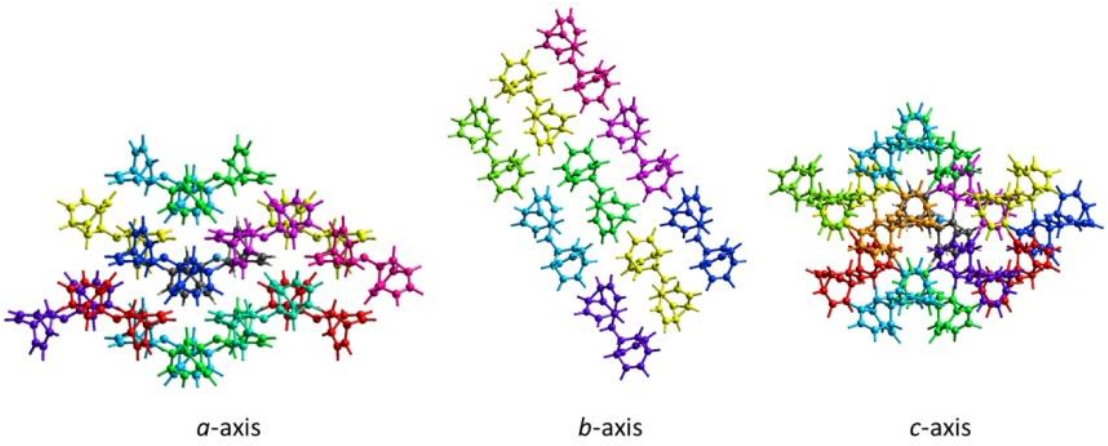

Figure 3.30. The cluster of molecules used to model intermolecular interaction energies listed in Table 3.5. The central molecule is coloured according to atom type (C, grey; H, white; N, blue) and surrounding molecules are coloured to match the colour code in Table 3.5.

***meso-N, N'*-di(9-barbaralyl)benzene-1,4-diamine (3)**

	N	R / Å	E_{ele}	E_{pol}	E_{dis}	E_{rep}	E_{tot}
	2	12.35	-0.1	-0.0	-3.1	0.0	-2.9
	2	11.29	-8.8	-1.6	-34.4	23.6	-25.8
	2	6.28	-14.8	-1.0	-63.6	44.7	-44.2

	2	9.93	-6.6	-1.5	-36.9	22.3	-26.5
	1	8.73	-5.9	-1.1	-31.3	19.5	-22.3
	2	10.52	-0.7	-0.1	-7.5	2.6	-5.7
	2	9.60	-11.2	-2.1	-40.0	28.2	-30.8
	2	10.09	-2.6	-0.7	-12.9	3.3	-12.5

Table 3.6. Calculated intermolecular interaction energies (in kJ·mol^{-1}) for the solid-state structure of *meso*-**3**

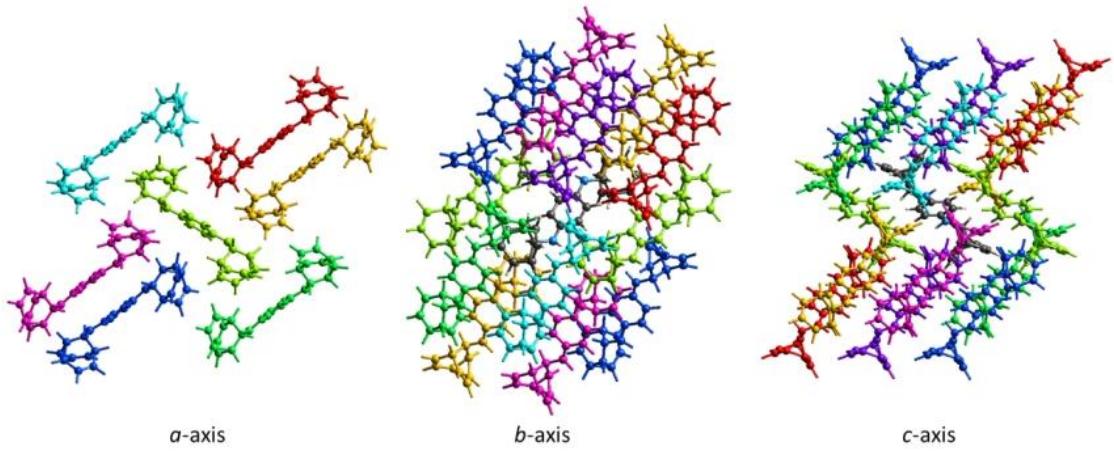

Figure 3.31. The cluster of molecules used to model intermolecular interaction energies listed in Table 3.6. The central molecule is coloured according to atom type (C, grey; H, white; N, blue) and surrounding molecules are coloured to match the colour code in Table 3.6.

(*R*,*R*)/(*S*,*S*)-*N*, *N*'-di(9-barbaralyl)benzene-1,4-diamine (3)

	N	R / Å	E_{ele}	E_{pol}	E_{dis}	E_{rep}	E_{tot}
	2	6.28	-16.6	-1.4	-65.7	48.4	-45.9
	1	13.66	2.7	-0.2	-8.2	0.0	-4.5
	1	5.28	-13.0	-5.0	-77.6	53.4	-52.0
	1	12.35	-1.4	-0.0	-3.1	0.0	-4.2
	1	9.60	-11.2	-2.1	-40.0	28.2	-30.8
	1	9.93	-6.6	-1.5	-36.9	22.3	-26.5
	1	5.72	-8.0	-3.7	-66.4	42.2	-43.0

	1	11.96	-2.8	-0.2	-12.7	15.6	-4.5
	1	10.87	-1.3	-0.1	-11.2	5.5	-7.9
	1	8.73	-5.9	-1.1	-31.3	19.5	-22.3
	1	10.52	-0.7	-0.1	-7.5	2.6	-5.7
	1	10.09	-2.6	-0.7	-12.9	3.3	-12.5
	1	11.29	-8.8	-1.6	-34.4	23.6	-25.8
	1	12.68	1.4	-0.2	-9.9	0.0	-7.3

Table 3.7. Calculated intermolecular interaction energies (in kJ·mol^{-1}) for the solid-state structure of (*R*,*R*)/(*S*,*S*)-**3.**

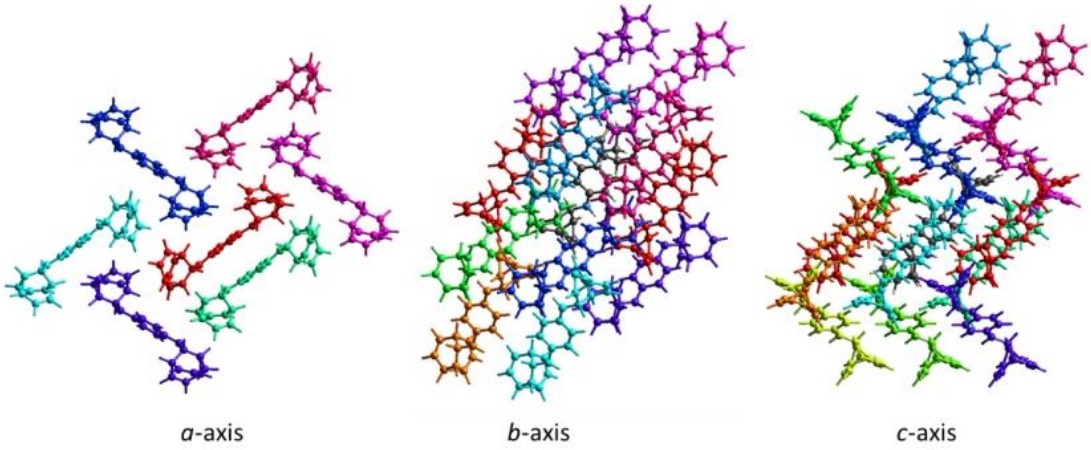

Figure 3.32. The cluster of molecules used to model intermolecular interaction energies listed in Table 3.7. The central molecule is coloured according to atom type (C, grey; H, white; N, blue) and surrounding molecules are coloured to match the colour code in Table 3.7.

Di(9-barbaraloxy)-1,4-benzoate (4)

	N	R / Å	E_{ele}	E_{pol}	E_{dis}	E_{rep}	E_{tot}
	1	6.16	-8.8	-2.5	-38.9	26.0	-29.1
	2	10.96	-5.5	-2.0	-27.6	15.2	-21.9
	2	14.99	0.2	-1.0	-27.5	0.0	-24.4
	1	6.33	-9.2	-2.1	-33.7	20.4	-27.9
	2	6.49	-9.5	-3.0	-64.1	39.3	-43.8

	2	13.90	0.4	-0.1	-2.5	0.0	-1.9
	2	11.25	-6.8	-2.3	-19.5	14.9	-16.5
	2	15.61	-2.1	-0.1	-6.2	0.0	-7.8
	2	16.01	-3.1	-0.2	-8.9	0.0	-11.2

Table 3.8. Calculated intermolecular interaction energies (in $kJ \cdot mol^{-1}$) for the solid-state structure of **4**

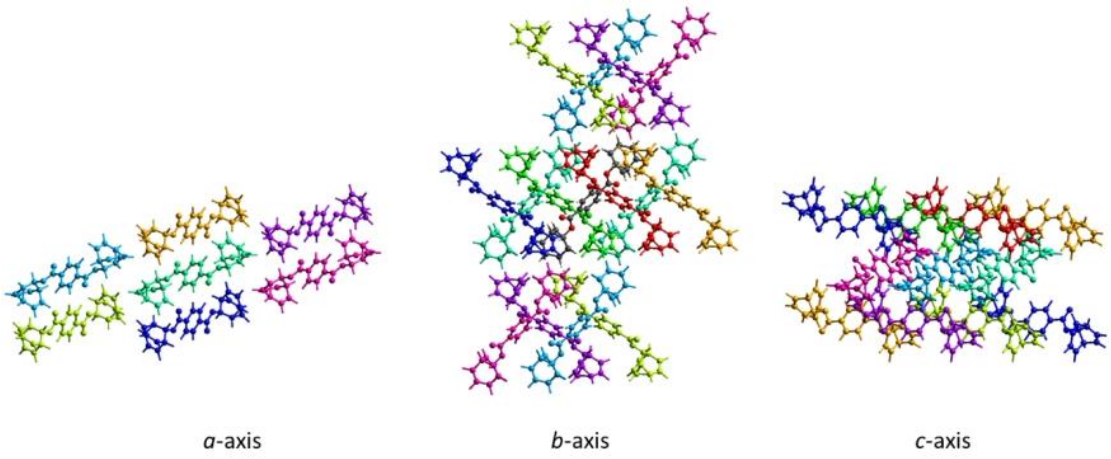

Figure 3.33. The cluster of molecules used to model intermolecular interaction energies listed in Table 3.8. The central molecule is coloured according to atom type (C, grey; H, white; O, red) and surrounding molecules are coloured to match the colour code in Table 3.8.

3.5 References

1. (a) H. Pellissier, *Tetrahedron* 2003, **59**, 8291-8327; (b) H. Pellissier, *Tetrahedron* 2011, **67**, 3769-3802.

2. (a) H. D. Flack, *Acta*. *Cryst.* 2009, **65**, 371–389; (b) J. Gal, *Chirality* 2008 **20,** 5-19; (c) J. Gal, *Chirality* 2011, **23**, 1-16; (c) G. Vantomme and J. Crassous, *Chirality* 2021, **33**, 597-601.

3. (a) L.-C. Sögütoglu, R. R. E. Steendam, H. Meekes, E. Vlieg and F. P. J. T. Rutjes, *Chem. Soc. Rev*. 2015, **44**, 6723-6732; (b) Y. Kitamoto, K. Suzuki, N. Morohashi, K. Sakai and T. Hattori, *J. Org. Chem.* 2013, **78**, 597–605; (c) Q. Zhang, R. Toyoda, L. Pfeifer and B. L. Feringa, *J. Am. Chem. Soc.* 2023, **145**, 6976-6985; Q. Zhang, S. Crespi, R. Toyoda, R. Costil, W. R. Browne, D.-H. Qu, H. Tian and B. L. Feringa, *J. Am. Chem. Soc.* 2022, **144**, 4376-4382; (d) H. Wang, W. Yang, K. K. Baldridge, C.-H. Zhan, T. U. Thikekar and A. C.-H. Sue, *Chem. Sci.*, 2021, **12**, 10985-10989; (e) Y. Zuo, X. Liu, E. Fu and S. Zhang, *Angew. Chem. Int. Ed.* 2023, **62**, e202217225.

4. (a) L.-D. Shiau, K.-F. Liu and Y.-C. Hsu, *Chem. Eng. Res. Des.* 2017, **117**, 301-308; (b) T. Q. Trung, J. M. Kim and K. H. Kim, *Arch. Pharm. Res.* 2006, **29**, 108-111.

5. (a) X.-H. Pham, J.-M. Kim, S.-M. Chang, I.-h. Kim and W.-S. Kim, *J. Mol. Catal. B Enzym.* 2009, **60**, 87-92; (b) Y. Zhu, L. Ge, L. Chen, C. Chen, Y. Wang and K. Yang, *Sep. Purif. Technol.* 2022, **282**, 120056.

6. (a) W. von E. Doering, W. R. Roth, *Tetrahedron* 1963, **19**, 715–737; (b) G. Schröder, *Angew. Chem. Int. Ed. Eng.* 1963, **2**, 481; (c) A. N. Bismillah, B. M. Chapin, B. A. Hussein and P. R. McGonigal, *Chem. Sci.* 2020, **11**, 324

7. A. N. Bismillah, T. G. Johnson, B. A. Hussein, A. T. Turley, P. K. Saha, H. C. Wong, J. A. Aguilar, D. S. Yufit and P. R. McGonigal, *Nature Chem.* 2023, **15**, 615–624.

8. J. Siegwarth, J. Bornhöft, C. Näther and Rainer Herges, *Org. Lett.* 2009, **11**, 15, 3450–3452.

9. A. N. Bismillah, J. Sturala, B. M. Chapin, D. S. Yufit, P. Hodgkinson and P. R. McGonigal, *Chem. Sci.* 2018, **9**, 8631–8636.

10. (a) Y. Wang, H. He, C. Wang, Y. Lu, K. Dong, F. Huo and S. Zhang, *JACS Au* 2022, **2**, 543–561; (b) K. Dong, S. Zhang, and Q. Wang, *Sci. China Chem*. 2015, **58**, 495–500.

11. A. Samanta, Z. Liu, S. K. M. Nalluri, Y. Zhang, Ge. C. Schatz and J. F. Stoddart, *J. Am. Chem. Soc.* 2016, **138**, 14469–14480.

12. (a) Z. He, W. Jiang and C. A. Schalley, *Chem. Soc. Rev.* 2015, **44**, 779-789; (b) W. M. Bloch and G.

H. Clever, *Chem. Commun.* 2017, **53**, 8506-8516; (c) H. M. Coubrough, S. C. C. van der Lubbe, K. Hetherington, A. Minard, C. Pask, M. J. Howard, C. F. Guerra and A. J. Wilson, *Chem. -Eur. J.* 2018, **25**, 785– 795; (d) Z. Ashbridge, O. M. Knapp, E. Kreidt, D. A. Leigh, L. Pirvu and F. Schaufelberger, *J. Am. Chem. Soc.* 2022, **144**, 17232–17240.

13. (a) K. M. Steed and J. W. Steed, *Chem. Rev.* 2015, **115**, 2895–2933; (b) E. M. Brás, M. S. C. Henriques, J. A. Paixão and R. Fausto, *Cryst. Growth Des.* 2018, **18**, 4167–4173.

14. (a) J. W. Steed, *Cryst. Eng. Comm.* 2003, **5**, 169; (b) G. R. Desiraju, *Cryst. Eng. Comm.* 2007, **9**, 91.

15. K. M. Anderson, M. R. Probert, A. E. Goetaa and J. W. Steed, *Cryst. Eng. Comm.* 2011,**13**, 83-87.

16. (a) K. M. Anderson, A. E. Goeta and J. W. Steed, *Cryst. Growth Des.* 2008, **8**, 2517–2524; (b) F. H. Allen, W. D. S. Motherwell, P. R. Raithby, G. P. Shields, R. Taylor, *New J. Chem.* 1999, **25**, 34.

17. (a) Toby G. Johnson, MChem Thesis, Durham University, 2019; (b) P. K. Mandal, G. W. Collie, B. Kauffmann and I. Huc, *Angew. Chem. Int. Ed.* 2014, **53**, 14424–14427; (c) P. Weng, X. Yan, Y.-B. Jiang, *Chem. Systems Chem.* 2023, **5**, e202200043; (d) H. Zeng, R. S. Miller, R. A. Flowers and B. Gong, *J. Am. Chem. Soc.* 2000, **122**, 2635; (e) J. Sánchez-Quesada, C. Seel, P. Prados, J. de Mendoza, I. Dalcol, and E. Giralt, *J. Am. Chem. Soc.* 1996, **118**, 277.

18. (a) R. S. Rowland and R. Taylor, *J. Phys. Chem.* 1996, **100**, 7384; (b) T. Steiner, *Angew. Chem. Int. Ed.* 2002, **41**, 48-76.

19. (a) M. O'Shaughnessy, J. Glover, R. Hafizi, M. Barhi, R. Clowes, S. Y. Chong, S. P. Argent, G. M. Day and A. I. Cooper, *Nature* 2024, **630**, 102–108; (b) A. M. Reilly, R. I. Cooper, C. S. Adjiman, S. Bhattacharya, A. D. Boese, J. G. Brandenburg, P. J. Bygrave, R. Bylsma, J. E. Campbell, R. Car, D. H. Case, R. Chadha, J. C. Cole, K. Cosburn, H. M. Cuppen, F. Curtis, G. M. Day, R. A. DiStasio Jr, A. Dzyabchenko, B. P. van Eijck, D. M. Elking, J. A. van den Ende, J. C. Facelli, M. B. Ferraro, L. Fusti-Molnar, C. -A. Gatsiou, T. S. Gee, R. de Gelder, L. M. Ghiringhelli, H. Goto,S. Grimme, R. Guo, D. W. M. Hofmann, J. Hoja, R. K. Hylton, L. Iuzzolino, W. Jankiewicz, D. T. de Jong, J. Kendrick, N. J. J. de Klerk, H.-Y. Ko, L. N. Kuleshova, X. Li, S. Lohani, F. J. J. Leusen, A. M. Lund, J. Lv, Y. Ma, N. Marom, A. E. Masunov, P. McCabe, D. P. McMahon, H. Meekes, M. P. Metz, A. J. Misquitta, S. Mohamed, B. Monserrat, R. J. Needs, M. A. Neumann, J. Nyman, S. Obata, H. Oberhofer, A. R. Oganov, A. M. Orendt, G. I. Pagola, C. C. Pantelides, C. J. Pickard, R. Podeszwa, L. S. Price, S. L. Price, A. Pulido, M. G. Read, K. Reuter, E. Schneider, C. Schober, G. P. Shields, P. Singh, I. J. Sugden, K. Szalewicz, C. R. Taylor, A.

Tkatchenko, M. E. Tuckerman, F. Vacarro, M. Vasileiadis, A. Vazquez-Mayagoitia, L. Vogt, Y. Wang, R. E. Watson, G. A. de Wijs, J. Yang, Q. Zhuqq and C. R. Groom, *Acta Crystallogr. B Struct. Sci. Cryst. Eng. Mater.* 2016, **72**, 439–459.

20. (a) M. P. Walsh, J. A Barclay, C. S. Begg, J. Xuan, N. T. Johnson, J. C. Cole and M. O. Kitching, *JACS Au* 2022, **2**, 2235-2250; (b) M. P. Walsh, J. A. Barclay, C. S Begg, J. Xuan and M. O. Kitching, *Cryst. Growth Des.* 2023, **23**, 2837-2844.

CHAPTER 4 |
MOLECULAR GLASS PROERTIES OF FLUXIONAL CARBON CAGES

Synopsis

This Chapter discusses the synthesis of novel di-substituted bullvalenes and their analogous, non-dynamic BDTs. The isomerism distributions of synthesised bullvalenes are determined by low-temperature NMR spectroscopy. Polarised microscopy and DSC experiments show that both bullvalene and BDT exhibit glass transitions, while the bullvalene also possesses surface fracture under cooling, indicating that it either has higher degree of crystallinity or higher coefficient of thermal expansion than its non-dynamic analogue.

Contribution statements

The author conducted: all the work in this chapter apart from low-temperature NMR experiments.

Acknowledgements

The following people are gratefully acknowledged for their contribution to this chapter: Dr Aisha N. Bismillah conducted low-temperature NMR experiments of bullvalene **1**. Dr Stephen Cowling helped obtaining the polarised microscopy and DSC data.

4.1 Introduction

Fluxional carbon cages such as bullvalenes undergo rapid Cope rearrangements that alter the positions of atoms or functional groups, creating thousands of degenerate isomers (Figure 4.1a) without breaking the carbon skeleton.[1] Substituting one or more hydrogen atoms with different groups can bias this degeneracy, imparting the molecule with 'shapeshifting' properties that enable interconversion between various constitutional isomers (Figure 4.1b). Over the last few decades, the fundamental studies of bullvalene have been intensively investigated such as synthesis[2] and network analysis[3], as well as its potential applications including chemical sensing[4], coordination cage[5], polymer[6], fluorophore[7] and antibiotics[8]. These studies have involved the characterisations on various aspects of bullvalenes including isomerism distribution, metal binding, antibacterial activity, etc. The crystalline behaviour of bullvalene and its derivatives have been studied since the 1960s.[2c,9] Unsubstituted bullvalene was observed to still possess fluxional behaviour in the solid state,[9c,9d,9e] and substituted bullvalenes tend to undergo shape-selective crystallisation, resolving only one constitutional isomer.[2c,10]

Molecular glasses, a series of non-crystalline solids composed of organic molecules lacking long-range order and exhibiting amorphous structures, have been explored in various drug-delivery[11] and organic electronics applications[12] due to their mechanical, adhesion and solubility properties. The most significant feature of molecular glasses is the glass transition temperature (T_g) which indicates the transition between a rubbery (flexible and elastic) and glassy (rigid and brittle) state. The existence of a T_g proves that crystallisation could be avoided,[13] however, molecular glasses could also crystallise in some cases: some small-sized molecules have been observed to exhibit fracture under cooling, due to the stress generated by adhering to a substrate or container with a different thermal expansion coefficient.[14] The fracture behaviour itself can represent some degree of crystallinity, as it suggests the material has relatively higher brittleness, and the internal stresses caused by cooling will create free surfaces and accelerate crystallisation[15].

The structures of organic molecular glasses tend to have rigid components, but also process dissymmetry, flexibility and conformational disorder.[16] The fluxional behaviour of substituted bullvalene provides a mixture of isomers with different constitution and shape, which could

increase the degree of disorder and disrupt the orderly packing of molecules in the solid state, enhancing the possibility of forming non-crystalline, amorphous solids.

This chapter investigates the molecular glass properties of bullvalenes. Di-substituted bullvalene **1** was synthesised, and its chemical structure and isomerism distribution were characterised by variable-temperature ^{1}H and ^{13}C-NMR spectroscopy. Significant surface fractures of **1** under cooling was observed by polarised microscopy. Presence of T_g and fracture peaks were observed in differential scanning calorimetry (DSC). For comparison, bicyclo[4.2.2]deca-2,4,7,9-tetraene (BDT) **2**, the non-dynamic analogue of **1** with a highly similar chemical structure, were synthesised and analysed with the same methods. Unexpectedly, the DSC and polarised microscopy results show that **2** also exhibits a T_g but not fracture, which indicates that the dynamic bullvalene **1** has an even higher degree of crystallinity and brittleness than the non-dynamic BDT **2**. These results violate the initial hypothesis that the dynamic feature would contribute to amorphous and non-crystalline solid, instead, the dynamic isomerism of bullvalenes might adjust the orderly packing of crystals via selective forming of specific constitutional isomers, or the fluxional behaviour has provided with the bullvalene with higher coefficient of thermal expansion (CTE).

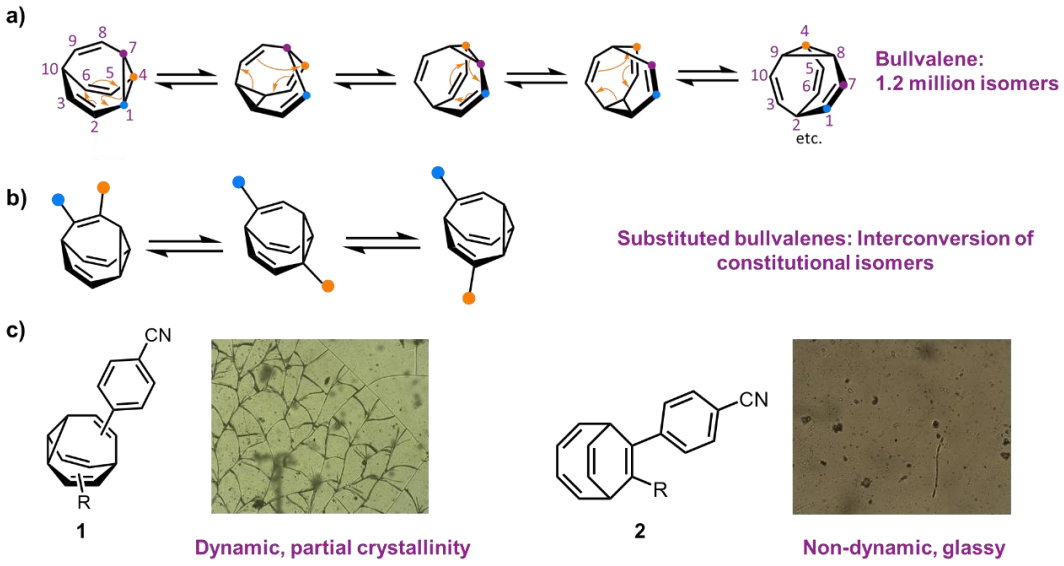

Figure 4.1 (a) The dynamic Cope rearrangement of bullvalene; (b) The interconversion of substituted bullvalene isomers; (c) Comparison of the microscopy images of dynamic bullvalene **1** and non-dynamic bicyclo[4.2.2]deca-2,4,7,9-tetraene (BDT) **2**.

4.2 Results and Discussion

4.2.1 Synthesis and Characterisations of Bullvalenes and BDTs

Di-substituted bullvalene **1** were synthesized following the route reported by Fallon, which utilizes the Co-catalyzed [6+2] cycloaddition of substituted alkyne and cyclooctatreane.[2c] The designed structures of target molecules are based on the commonly-used liquid crystal molecule 4-cyano-4'-pentylbiphenyl (5CB), as it contains both rigid (benzonitrile) and flexible (alkyl chain) components, leading to a higher possibility of forming glasses. The Bpin-substited alkyne **3** were obtained via boronation of 1-hexyne/1-heptyne, before being taken into the Co-catalysed [6+2] cycloaddition to form the Bpin-substituted BDT **4**. The intermediate **4** was first converted to bullvalene **5** via di-π-methane photoisomerisation under UV irradiation, then Suzuki-coupling to replace the Bpin substitute with bromobenzonitrile to form the target bullvalene **1**. The controlled BDT **2** was prepared with a similar synthetic route, with the BDT **4** directly taken into Suzuki coupling without photoisomerization (Scheme 4.1).

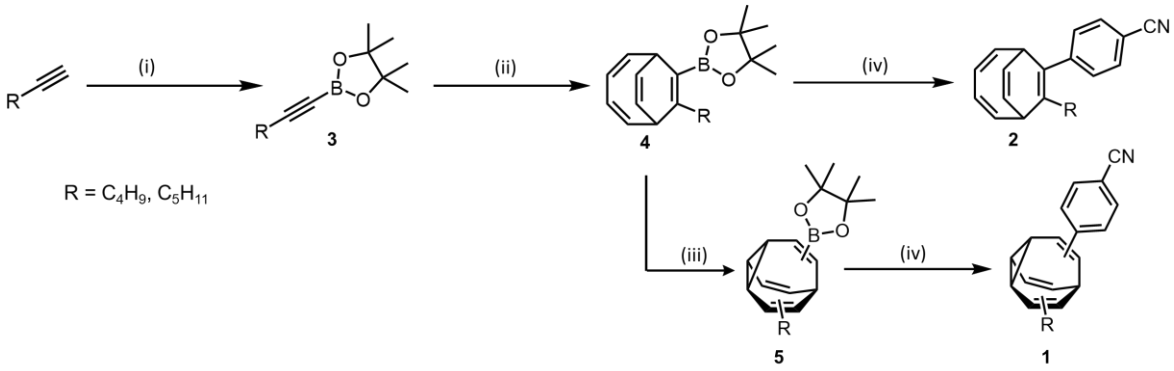

Scheme 4.1. Molecular structures and general synthetic routes of **1** and **2**. Reagents and conditions: (i) 1. n-butyllithium (2.5 M in hexane) / diethyl ether / –78 °C / 1 h, 2. 4,4,5,5-Tetramethyl-2-(1-methylethoxy)-1,3,2-dioxaborolane / rt / 4 h, 31－49%. (ii) $CoBr_2$ (dppe) / ZnI_2 / Zn / cyclooctatetraene / 1,2-dichroloethane / rt / 16 h, 29－35%. (iii) Thioxanthone / THF / 365 nm. (iv) 4-bromobenzonitrile / $Pd(PPh_3)_4$ / THF / 10% NaOH / 60 °C / 16 h, 25－85%.

The structures of obtained **1** and **2** were confirmed by ^{1}H- and ^{13}C-NMR spectroscopy. The broad peaks of bullvalenes **1** were resolved into individual peaks under low temperature due to

the freezing of dynamic Cope rearrangements[3,17] (Figure 4.2), allowing the assignment of each position and determination of the isomerisation distribution.

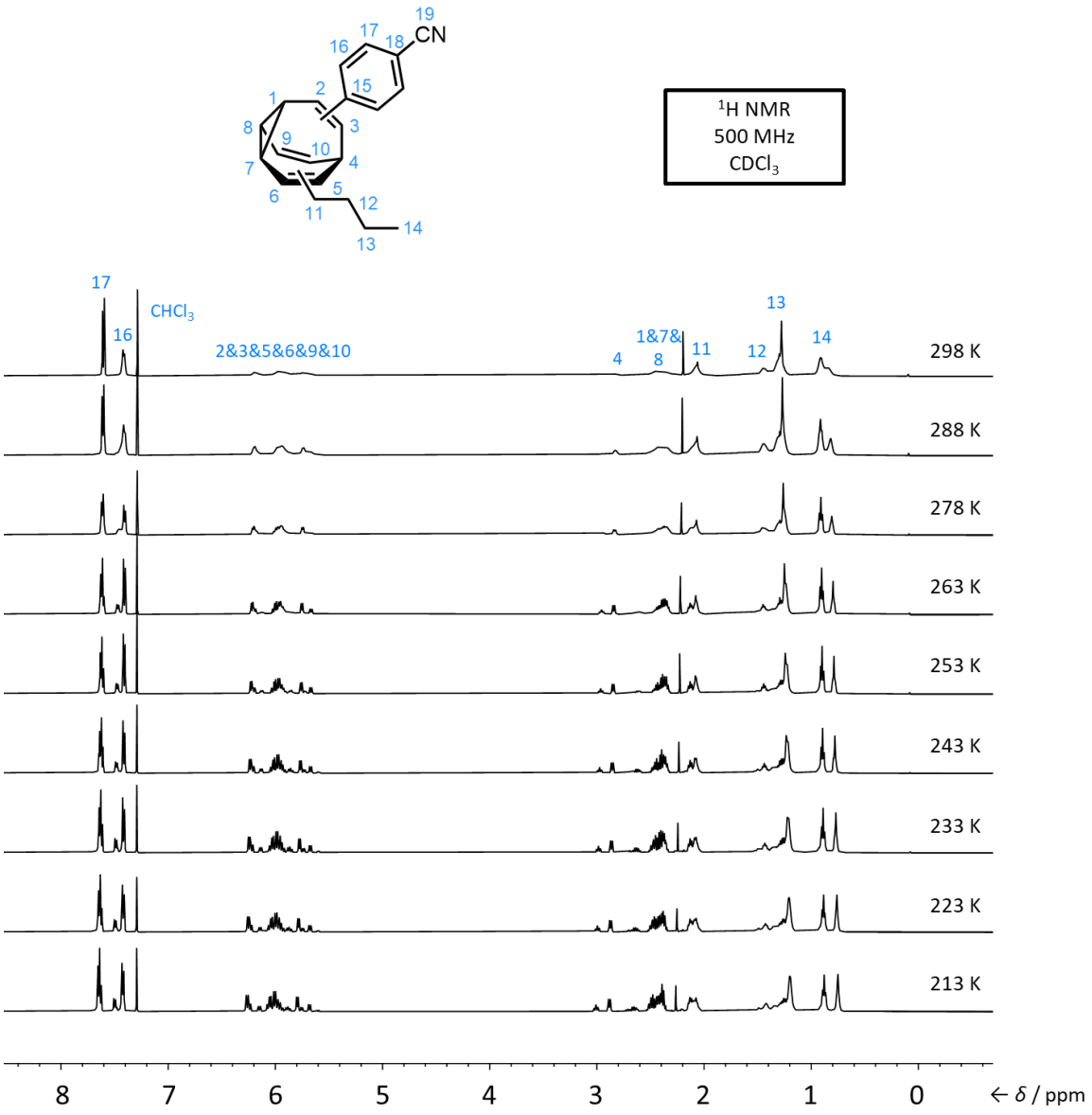

Figure 4.2. Stacked ^{1}H NMR spectra of **1b** at different temperatures.

The isomerism distribution of **1** were determined in combination with low-temperature 2D NMR spectra (Full details see section 4.4.2). In both **1a** and **1b**, there are four isomers (ββ', βγ', γβ', γγ') present in the solution state mixture with an approximate 53:25:17:5 ratio, and the ββ' isomer in which both substituents flank the bridgehead position is observed as the major isomer (Figure 3.3). The obtained isomerism distribution results closely match Fallon's previous network analysis of di-substituted bullvalenes.[2c]

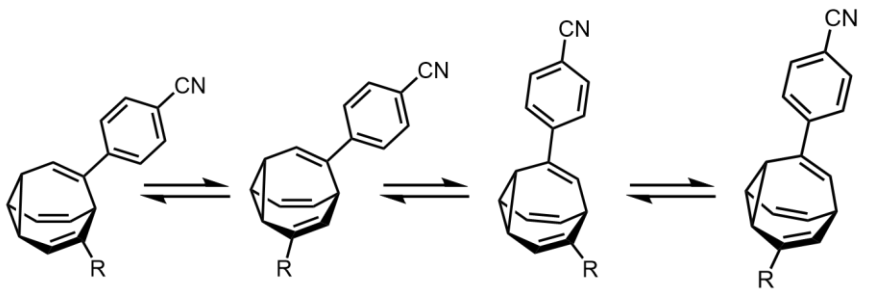

	ββ'	βγ'	γβ'	γγ'	
Isomer distribution ratio	53	25	17	5	**1a**: R = C_5H_{11}
	55	26	15	4	**1b**: R = C_4H_9

Figure 4.3. The constitutional isomerism distribution of bullvalene **1** obtained by low-temperature 2D NMR spectroscopy (213 K in $CDCl_3$).

4.2.2 Studies of Thermal Properties

Polarised microscopy with variation in temperature was first conducted to observe the possible phase transitions of bullvalene **1** and BDT **2**. All samples were sticky, oil-like liquids at room temperature and were observed while cooling from 25 °C to −80 °C and then warming up to room temperature again (full details see section 4.4.4). For bullvalene **1a**, the first fracture line appears at −36 °C, and the fractures continuously increase as the temperature decreases further. At −73 °C, the fractured pieces begin to form round-like shapes, indicating that the compound has separated from the glass surface. Upon warming, the fissures of the fractures gradually recover and completely disappear at −2 °C (Figure 4.4) as the material melts to a liquid. Bullvalene **1b** exhibited a similar fracturing phenomenon, which begins at a lower temperature (−70 °C), but the complete fracture or separation from the surface could not be seen due to the temperature limitation of the instrument. The microscopy images of **2a** and **2b**, the BDT analogues of **1a** and **1b**, are almost consistent at different temperatures, in which neither fractures nor solid-liquid transitions are observed under cooling and warming (Figure 4.5).

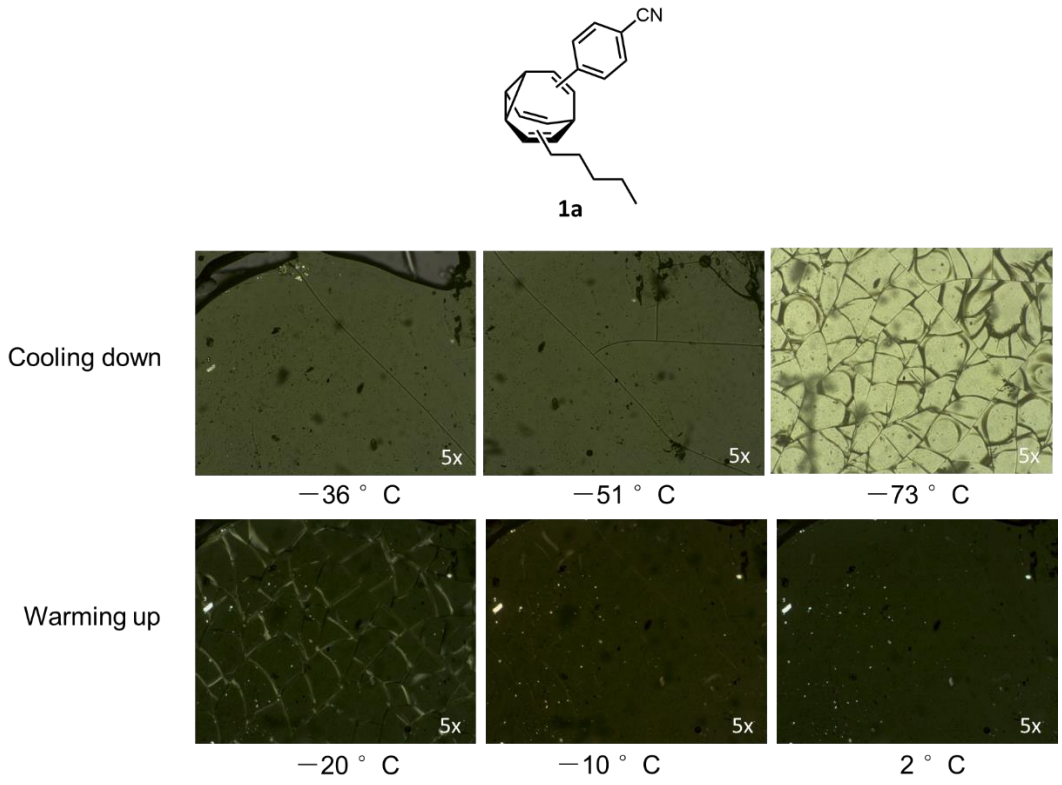

Figure 4.4. Partial polarised microscopy images of **1a** under variable temperature.

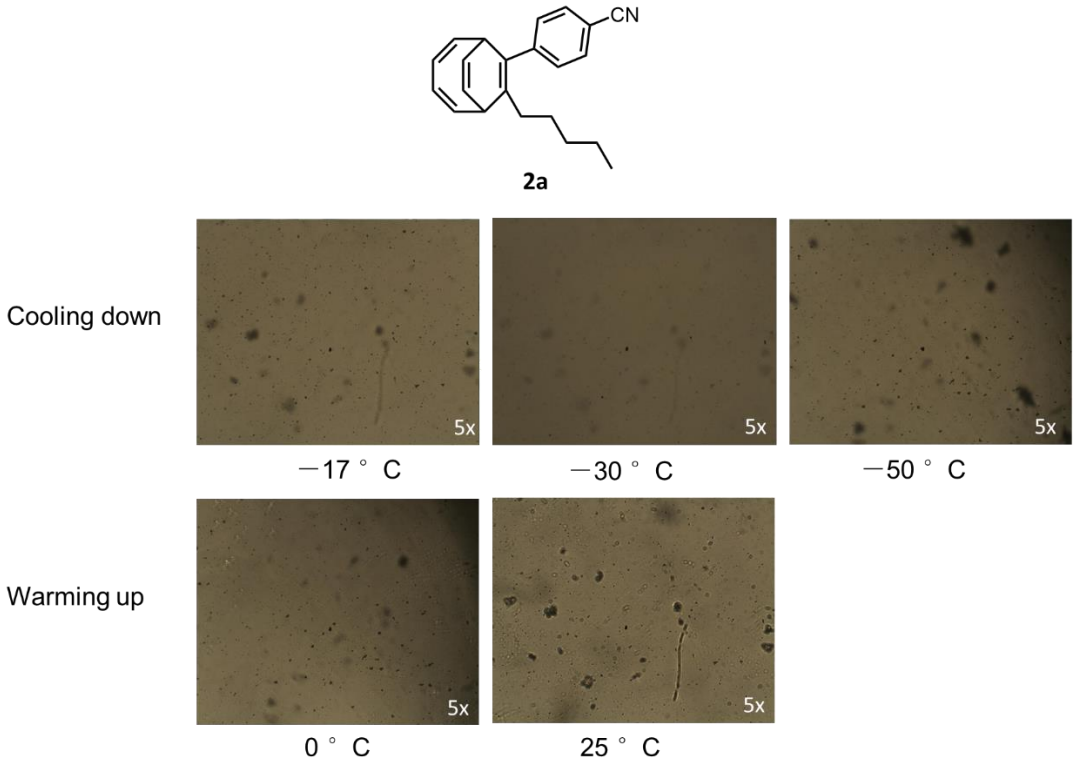

Figure 4.5. Partial polarised microscopy images of **2a** under variable temperature.

The comparison of microscopy results of **1** and **2** suggest that bullvalene **1** could exhibit both crystalline and amorphous regions, while BDT **2** could be completely amorphous, non-crystalline glasses, or crystalline solids with very low melting points that have not been observed due to instrumental limitations. To investigate the possibility of BDTs **2** being such a high-entropy solids with extremely low melting points, a search of reported molecules with melting points under −50 °C were conducted.[18] Over 700 organic molecules were found and tabulated along with their molecular formulas and melting points (full details see section 4.4.4). The searched results demonstrate that the majority of molecules with low melting points have small sizes (＜12 carbon atoms), and those which exhibit both low melting points and large sizes tend to have extremely flexible structures, i.e. trioctylaluminum has 24 carbon atoms and melts at −62 °C, but its chemical structure contains three long alkyl chains that disrupt orderly packing and decrease the melting point (Table 4.1). Although BDTs **2** are also racemic molecules containing two enantiomers which could decreases the efficiency of the packing and leads to lower melting points,[19] comparing to the searched results, BDT **2** have large sizes (> 20 carbon atoms) and rigid components, suggesting that they are highly unlikely to possess melting points lower than −80 °C. Instead, BDT **2** tend to be highly amorphous solids with a lower degree of crystallinity than bullvalene **1**.

Name of Reported Compound	**Chemical Formula**	**Chemical Structure**	**lit. M. P. (°C)**
Ethyl chloroformate	$C_3H_5ClO_2$	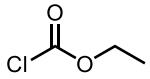	−80.6
3-Bromopentane	$C_5H_{11}Br$	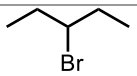	−126.2
Dibutylamine	$C_8H_{19}N$	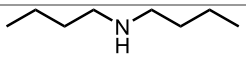	−61.8
3,7,11,15-Tetramethyl-hexadecanoic acid	$C_{20}H_{40}O_2$	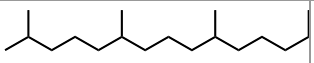	−65
Trioctylaluminum	$C_{24}H_{51}Al$	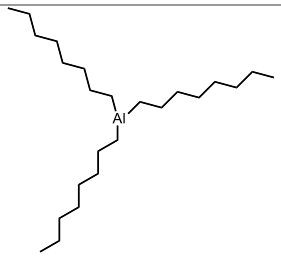	−62

Table 4.1. A set of reported molecules with low melting points.

To confirm the deduction from the results above, differential scanning calorimetry (DSC) experiments were conducted for **1** and **2**, where the heat flow of the compounds was measured under variable temperatures to capture potential phase transitions. All four compounds were first cooled down to –90 °C and warmed up to rt at a rate of 10 K / min to observe the general tendency of heat flows, and then slower rates (5 K and 1 K / min) were applied to see the potential changes of intensities or peaks.[20] The obtained DSC plots show that both **1** and **2** exhibit T_g as significant step changes on the baseline were observed for all compounds. The temperature ranges and midpoints of T_g as well as changes of heat capacity (ΔCp) were calculated in the DSC software (Full details see section 4.4.5). In the cooling process of bullvalene **1a**, the T_g ranges from –35 °C to –32 °C when being cooled down at 10 K / min, and as the cooling rate decreases, the T_g becomes shorter and insignificant, and the intensities of heat flows also decrease. A broad exothermic peak is observed at the start of the T_g, which could be related to the fracture phenomenon observed under a microscope at around –36 °C. Similarly, glass transitions with longer ranges and lower intensity peaks are also observed in the warming process (Figure 4.6a). The DSC diagrams of **1b**, **2a**, and **2b** show similar glass transition behavior to **1a**. Notably, during the 10 K/min warming process of bullvalene **1b**, a sharp endothermic peak is observed at –54.3 °C. When slower warming rates are used, the peak becomes more pronounced and shifts to a lower temperature (Figure 4.6b). This endothermic peak of **1b** likely indicates a solid-to-liquid transition. At the high warming rate of 10 K/min, thermal lag and insufficient time prevent the sample from reaching equilibrium temperature, causing the transition peak to be delayed and less pronounced. Conversely, slower warming rates provide more time to reach thermal equilibrium, resulting in a more complete and accurately detected transition. BDT **2a** and **2b** exhibit glass transitions on both cooling and warming process similar to bullvalene **1**, but no sharp peaks indicating phase transitions are observed.

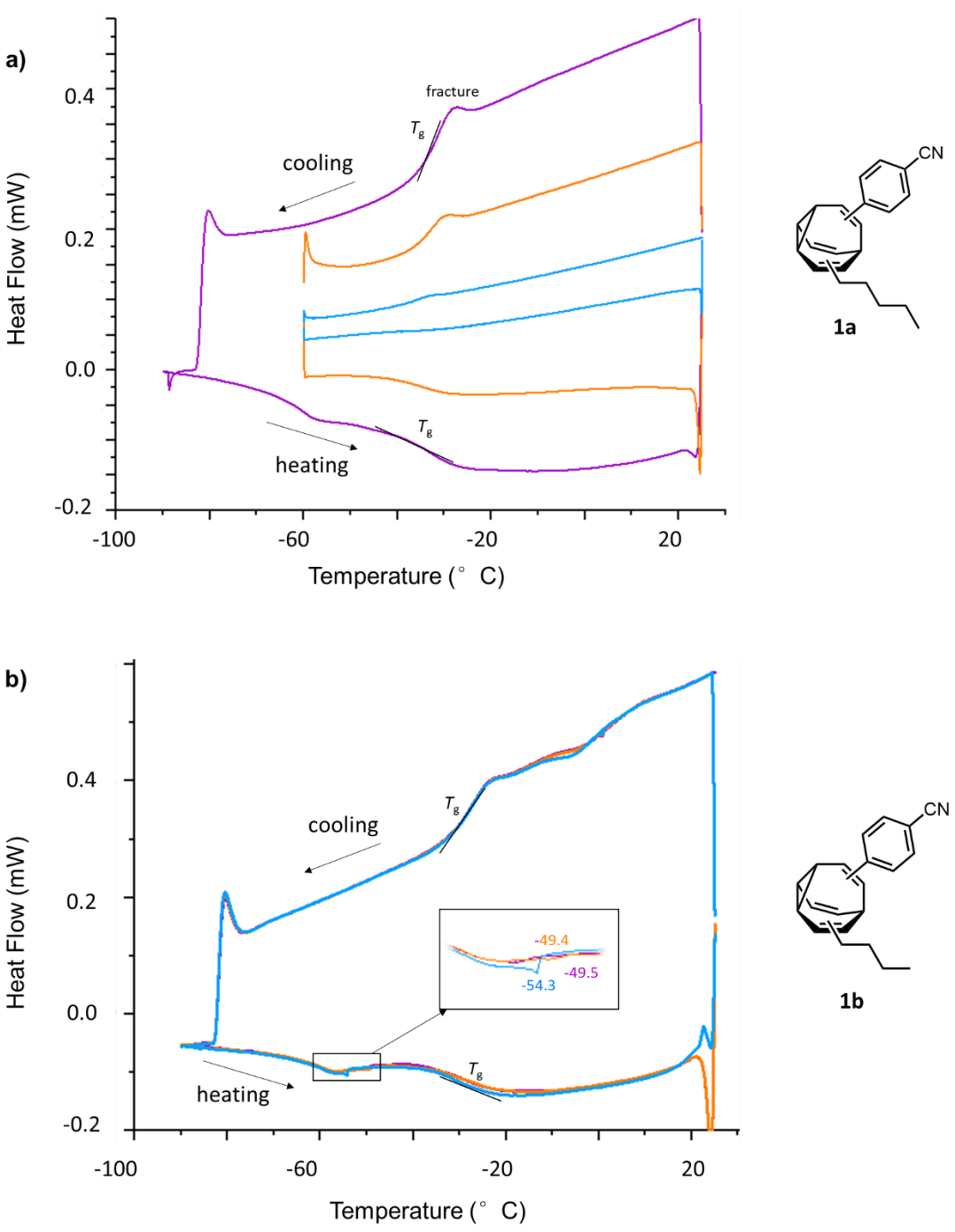

Figure 4.6. DSC diagrams of compounds **1a** and **1b**. Three cycles with different cooling and warming rates are distinguished by colours: purple = 10 K / min, orange = 5 K / min and blue = 1 K / min. The endothermic peaks upon heating are highlighted with corresponding colours.

Similar to bullvalene **1a**, BDT **2a** also exhibits heat flow intensity changes when the rate decreases from 10 K to 5 K / min, but keeps consistent when using 1 K / min (Figure 4.7). The heat flow intensity changes observed in compound **1a** and **2a** could be due to their slightly

larger sizes leading to longer times of reaching thermal equilibria. In combination of the polarised microscopy results, the dynamic bullvalene **1** tends to have a higher degree of crystallinity than their non-dynamic analogue BDT **2** by exhibiting fractures under a microscope and solid-to-liquid transitions in DSC.

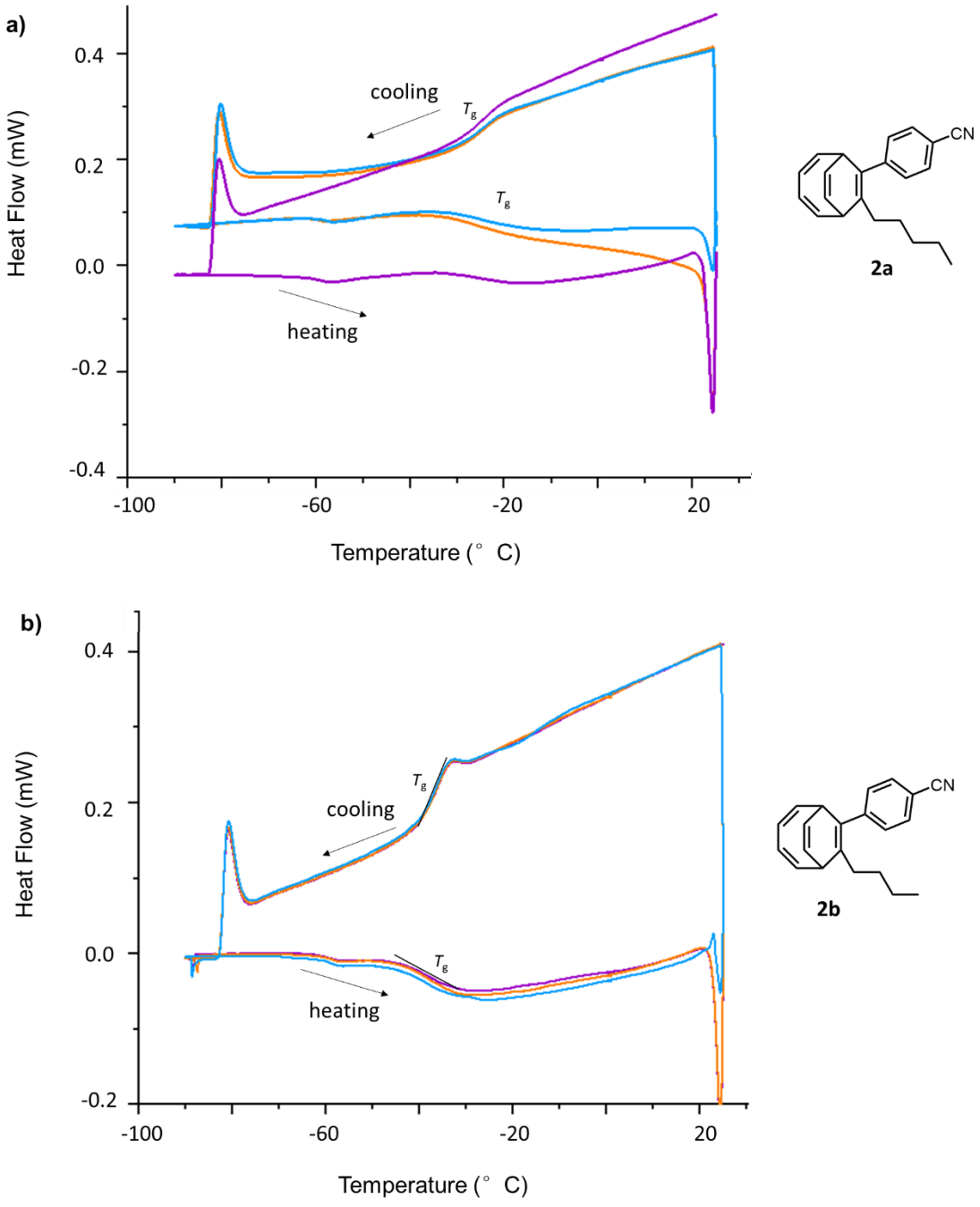

Figure 4.7. DSC diagrams of compounds **2a** and **2b**. Three cycles with different cooling and warming rates are distinguished by colours: purple = 10 K / min, orange = 5 K / min and blue = 1 K / min.

4.3 Conclusions and Future Work

In summary, the first investigation on the thermal and glass properties of bullvalenes have been conducted. Di-substituted bullvalenes **1** have been successfully synthesised and their dynamic isomerism has been fully determined by 2D NMR spectroscopy. BDTs **2** were also prepared as the non-dynamic comparison of **1**. The initial hypothesis is that the dynamic and flexible structures will contribute to glassy, non-crystalline solids, thus molecular glass properties on the dynamic bullvalene **1** and crystalline behaviour on the non-dynamic BDT **2** were expected. Unexpectedly, the polarised microscopy and DSC results show that both **1** and **2** form molecular glasses, and the dynamic bullvalene **1** tend to have even higher degrees of crystallinity.

In the polarised microscopy images on bullvalenes **1a** and **1b**, fractures are observed under cooling and recover upon warming up, while the texture of BDTs **2a** and **2b** keep almost consistent at different temperatures. The comparison of **1** and **2** suggest that bullvalene **1** has higher brittleness or thermal expansion[22] than BDT **2**. This is due to the different rates of shrinkage between crystalline and amorphous regions, indicating that although bullvalene **1** cannot form analysable crystals, it does possess at least some degree of crystallinity. The deduction is further confirmed by DSC experiments using different cooling and warming rates, where all four compounds exhibit some extents of glass transitions, but the sharp endothermic peaks observed on **1b** suggest potential solid-to-liquid transitions. Interestingly, the heat flows of **1a** and **2a** both exhibit intensity changes when using different rates, and the T_g of **1a** becomes insignificant as the rate decreases, which implies that **1a** has more amorphous regions than **1b** and is less likely to form a crystalline solid. These dynamic results suggest that the longer alkyl chains of **1a** and **2a** have not only delayed the thermal equilibria but also made the crystallinity degree less observable, making them less ideal candidates to investigate the thermal properties. In contrast, the results of **1b** and **2b** which have shorter alkyl chains have provided better evidence on higher crystallinity degrees of bullvalenes.

To conclude, the obtained results have shown that the dynamic behaviour of di-substituted bullvalenes **1** tend to create either a higher degree of crystallinity, or higher CTE than their non-dynamic analogues **2**. Both possibilities are related to the structures of **1** being highly flexible and dynamic. Currently the CTE values of synthesised bullvalenes and BDTs have not been

determined as they are challenging due to small sizes and need for precise measurement techniques. For further investigation of crystallinity, solid-state NMR spectroscopy will be conducted to compare the isomerisation distributions of bullvalene **1** in solid and solution states. Considering the structures of **1a** and **2a** have influenced the visibility of crystallinity, new sets of bullvalenes and BDTs with less flexible, simpler structures could be tested with the same methods. If fluxional carbon cages can spontaneously form ordered, crystalline solids which result in more stable solid forms and improved bioavailability, they will be potentially valuable for applications in pharmaceuticals,[23] catalysis,[24] or food additives.[25]

4.4 Experimental Details

4.4.1 Specific Experimental Methods

For general experimental details see page *xv*. DSC experiments were conducted using METTLER instrument equipped with TC100 intracooler. Samples were loaded using 20 µL aluminium light crucibles. Operations and data extractions were done using Mettler Star software V.18. The DSC diagrams are reformatted using OriginPro 2022. Polarised optical microscopy images were obtained using an Olympus BX50 Optical Microscope equipped with a Linkam Scientific LTS350 heating stage, Linkam LNP2 cooling pump, and Linkam TMS92 controller.

4.4.2 Synthesis of Bullvalene 1 and BDT 2

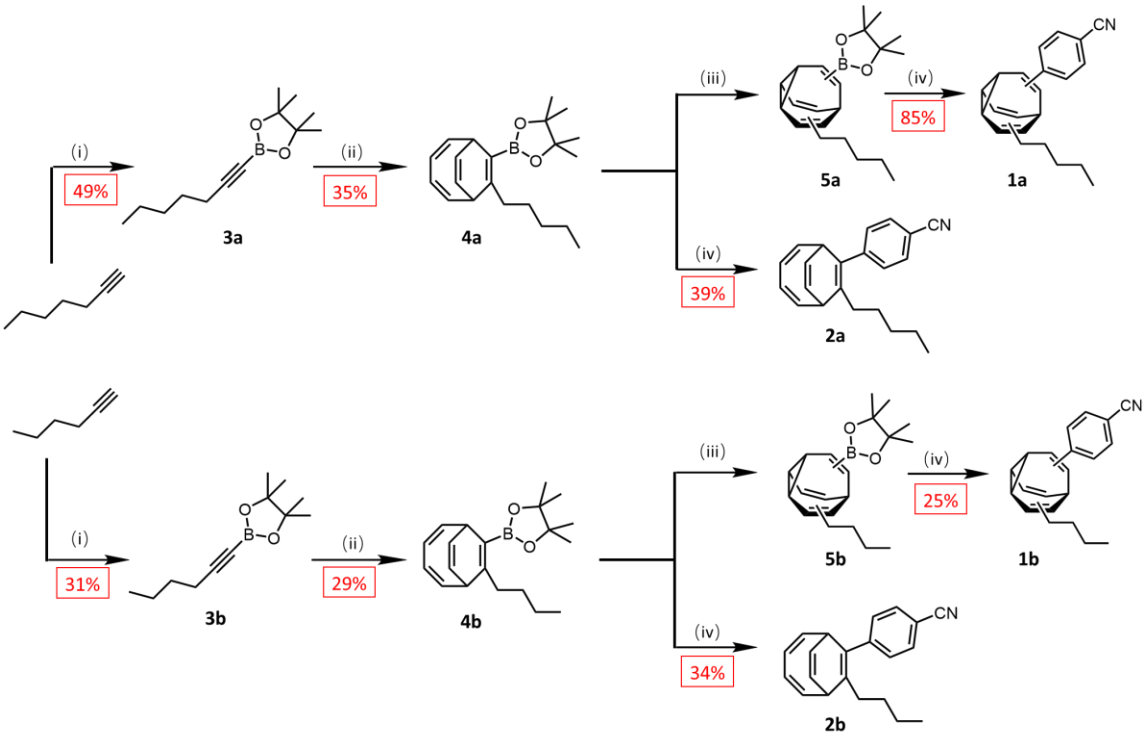

Scheme 4.1. Synthesis and yields of compounds **3**-**5**, bullvalene **1** and BDT **2**. Reagents and conditions: (i) 1. n-butyllithium (2.5 M in hexane) / diethyl ether / –78 °C / 1 h. 2. 4,4,5,5-Tetramethyl-2-(1-methylethoxy)-1,3,2-dioxaborolane / rt / 4 h. (ii) $CoBr_2$ (dppe) / ZnI_2 / Zn / cyclooctatetraene / 1,2-dichroloethane / rt / 16 h. (iii) Thioxanthone / THF / 365 nm. (iv) 4-bromobenzonitrile / $Pd(PPh_3)_4$ / THF / 10% NaOH / 60 °C / 16 h.

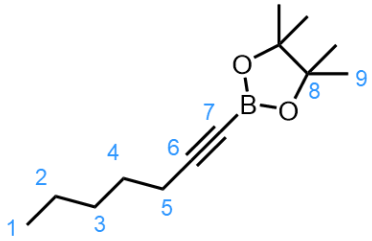

Bpin-pentyl alkyne (3a): 1-Heptyne (3.16 mL, 24 mmol) in diethyl ether (60 mL) was cooled to –78 °C under a N_2 atmosphere. n-Butyllithium (9.4 mL, 2.5 M in hexanes, 24 mmol) was added dropwise, followed by stirring at –78 °C for 1 h. 4,4,5,5-Tetramethyl-2-(1-methylethoxy)-1,3,2-dioxaborolane (4.08 mL, 20 mmol) in diethyl ether (60 mL) was then added. The reaction mixture was stirred at rt for 4 h before being cooled to –78 °C, followed by quenching with HCl (7.5 mL, 4 M in dioxane, 30 mmol) and stirring at rt for an additional 1 h. The solvent was removed under reduced pressure and the crude product was purified via column chromatography (Teledyne Isco Combi Flash Rf+ system, 80 g Al_2O_3, n-hexane – EtOAc elution from 0 to 100%) to give the title compound as a yellow oil. (1.93 g, 8.66 mmol, 49% yield) **^{1}H NMR** (400 MHz, $CDCl_3$): δ 2.23 (t, *J* = 7.2 Hz, 2H, H_5), 1.58 – 1.46 (m, 2H, H_4), 1.36 – 1.30 (m, 2H, H_3), 1.28 – 1.25 (m, 1H, H_2), 1.23 (s, 12H, H_9), 0.87 (t, *J* = 7.1 Hz, 3H, H_1). Characterisation data are consistent with those reported previously: *Eur. J. Chem.* 2020, **26**, 5360 – 5364.

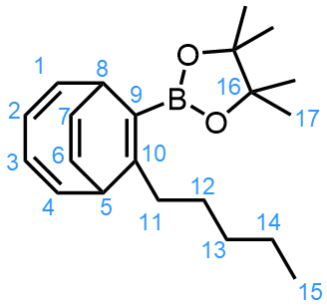

Bpin-pentyl BDT (4a): An oven-dried Schlenk tube containing ZnI_2 (256 mg, 0.8 mmol) was heated at 280 °C under high vacuum for 5 min. After cooled to rt and flushing with N_2, $CoBr_2$(dppe) (248 mg, 0.4 mmol), Zn (80 mg, 1.2 mmol), and anhydrous DCE (4 mL) were added – the reaction mixture was then degassed by three freeze-pump-thaw cycles. Cyclooctatetraene (416 mg, 4.0 mmol) was added into the reaction mixture. **3a** (904 mg, 6.0 mmol in 4 mL of anhydrous DCE, degassed) was slowly added with syringe pump over 6 h. The reaction was stirred at rt in a H_2O bath for 16 h to control the resultant exotherm. After completion, the suspension was filtered through a short pad of SiO_2 (5 g) gel eluting with Et_2O. The solvent was removed under reduced pressure, and the crude product was purified *via* column chromatography (Teledyne Isco CombiFlash Rf+ system, 12 g SiO_2, n-hexane – EtOAc elution from 0 to 100%) to give the title compound as a yellow oil (458 mg, 1.40 mmol, 35% yield). **^{1}H NMR** (400 MHz, $CDCl_3$): δ 6.28 (m, 1H,

H_2), 6.15 – 6.04 (m, 1H, H_3), 5.75 – 5.55 (m, 4H, $H_{1/4/6/7}$), 3.49 – 3.37 (m, 1H, H_8), 3.35 – 3.24 (m, 1H, H_5), 2.53 – 2.36 (m, 2H, H_{11}), 1.45 – 1.26 (m, 6H, $H_{12/13/14}$), 1.24 (d, J = 4.7 Hz, 12H, H_{17}), 0.87 (t, J = 7.1 Hz, 3H, H_{15}). **^{13}C NMR** (151 MHz, $CDCl_3$): δ 150.98 (C_{10}), 143.07 (C_2), 140.36 (C_3), 124.81 (C_7), 123.31 (C_6), 122.19 (C_1), 121.32 (C_4), 82.63 (C_{16}), 40.93 (C_5), 36.96 (C_8), 34.25 (C_{11}), 31.59 (C_{13}), 30.47 (C_{12}), 24.97 (C_{17}), 24.36 (C_{17}), 22.29 (C_{14}), 14.01 (C_{15}). **HR ASAP MS**: m/z = 302.1898 $[M+H]^+$, calculated for $C_{22}H_{24}N^+$: 302.1908.

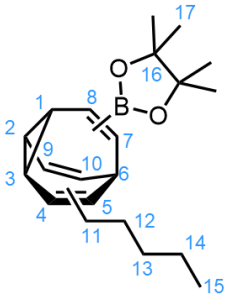

Bpin-pentyl bullvalene (5a): **4a** (281 mg, 0.86 mmol) and thioxanthone (3.60 mg, 0.019 mmol) was dissolved in anhydrous THF (4 mL). The reaction mixture was stirred under a 365 nm LED lamp with a H_2O bath for 24 h. The solvent was removed under reduced pressure and the crude product was purified *via* column chromatography (Teledyne Isco CombiFlash Rf+ system, 80 g Al_2O_3, n-hexane – DCM elution) to give the title compound as a colorless oil. The broad peaks of the ^{1}H-NMR spectrum indicated the success formation of bullvalene. The crude product was taken into the next step without further purification.

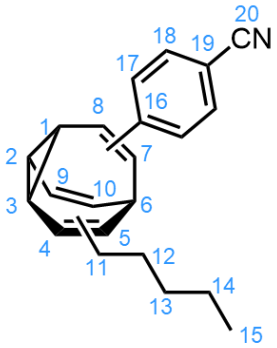

5CB bullvalene (1a): **5a** (88 mg, crude), 4-bromobenzonitrile (55 mg, 0.30 mmol), and $Pd(PPh_3)_4$ (69 mg, 0.06 mmol) was dissolved in the mixture of THF (1.5 mL) and 10% aqueous NaOH (0.6 mL). The mixture was degassed *via* three freeze-pump-thaw cycles and stirred at 60 °C for 16 h. The reaction mixture was diluted with diethyl ether and dried over $MgSO_4$. The solvent was removed under reduced pressure and the crude product was purified via column chromatography (Teledyne Isco Combi Flash Rf+ system, 24 g C18, MeOH elution) to give the title compound as a yellow oil (71 mg, 0.24 mmol, 85% yield). ^{1}H NMR (499 MHz, $CDCl_3$, 213K) δ 7.66 – 7.58 (m, 2H, H_{18}), 7.47 (m, 0.42H, H_{17}, isomer γβ'+γγ'), 7.40 (m, 1.39H, H_{17}, isomer ββ'+βγ'), 6.28 – 6.19 (m, 0.65H, H_2, isomer ββ'+βγ'), 6.13 (m, 0.16H, H_3, isomer γβ'+γγ'), 6.07 – 5.81 (m, 2H, $H_{9/10}$), 5.77 (d, J = 7.7 Hz, 0.43H, H_6, ismoer ββ'), 5.73 (d, J = 8.0 Hz, 0.13H, H_6, isomer γβ'), 5.66 (d, J = 9.0

Hz, 0.19H, H_5, isomer βγ'), 5.58 (d, *J* = 8.8 Hz, 0.04H, H_5, isomer γγ'), 2.98 (m, 0.24H, H_4, isomer βγ'), 2.86 (d, *J* = 8.7 Hz, 0.41H, H_4, isomer ββ'), 2.72 - 2.57 (m, 0.31H, H_4, isomer γβ'+γγ'), 2.53 – 2.32 (m, 3H, $H_{1/7/8}$), 2.13 – 1.99 (m, 2H, H_{11}), 1.50 – 1.01 (m, 6H, $H_{12/13/14}$), 0.84 (m, 1.92H, H_{15}, isomer ββ'), 0.77 (m, 1.28H, H_{15}, isomer βγ'+γβ'+γγ'). **^{13}C NMR** (126 MHz, $CDCl_3$, 213K) δ 149.47 (C_{20}, isomer γβ'), 147.76 (C_{20}, isomer ββ'+βγ'+γγ'), 142.32 (C_5, isomer γβ'), 141.47 (C_5, isomer ββ'), 140.28 (C_6, isomer βγ'), 139.08 (C_2, isomer βγ'), 138.63 (C_2, isomer ββ'), 137.22 (C_3, isomer γβ'), 136.82 (C_3, isomer γγ'), 132.57 (C_{18}), 128.04 (C_9), 127.92 (C_2, isomer ββ'), 127.53 (C_2, isomer βγ'), 127.17 (C_{16}, isomer γβ'+γγ'/C_{10}), 126.77 (C_3, γβ'+γγ'), 126.52 (C_{16}, isomer ββ'), 126.47 (C_{16}, isomer βγ'), 120.46 (C_6, isomer ββ'), 119.93 (C_{19}), 119.59 (C_6, isomer γβ'), 118.99 (C_5, isomer γγ'), 118.61 (C_5, isomer βγ'), 109.51 (C_{16}, isomer γβ'), 109.44 (C_{16}, isomer γγ'), 109.24 (C_{16}, isomer ββ'), 109.09 (C_{16}, isomer βγ'), 41.19 (C_{11}, isomer βγ'), 40.41 (C_{11}, isomer γβ'), 40.23 (C_{11}, isomer ββ'), 38.91 (C_4, isomer ββ'), 34.76 (C_4, isomer γβ'), 34.31 (C_4, isomer βγ'), 31.68 (C_{13}, isomer βγ'+γβ'+γγ'), 31.26 (C_{13}, isomer ββ'), 29.14 (C_{12}, isomer γβ'), 28.27 (C_{12}, isomer ββ'), 28.17 (C_{12}, isomer γβ'), 24.27 (C_1 or C_7 or C_8, isomer βγ'), 22.95 (C_{14}, isomer βγ'+γβ'+γγ'), 22.87 (C_{14}, isomer ββ'), 22.32 (C_1 or C_7 or C_8, isomer γβ'), 21.45 (C_1 or C_7 or C_8, isomer ββ'), 21.38 (C_1 or C_7 or C_8, isomer βγ'), 21.30 (C_1 or C_7 or C_8, isomer ββ'), 21.14 (C_1 or C_7 or C_8, isomer ββ'), 20.96 (C_1 or C_7 or C_8, isomer βγ'), 20.11 (C_1 or C_7 or C_8, isomer γβ'), 19.71 (C_1 or C_7 or C_8, isomer γβ'), 14.69 (C_{15}, isomer βγ'+γβ'+γγ'), 14.55 (C_{15}, isomer ββ'). **HR ASAP MS**: m/z = 302.1898 $[M+H]^+$, calculated for $C_{22}H_{24}N^+$: 302.1903.

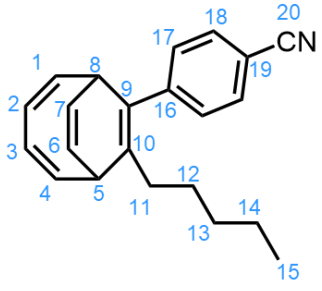

5CB BDT (2a): **4a** (140 mg, crude), 4-bromobenzonitrile (83 mg, 0.46 mmol), and $Pd(PPh_3)_4$ (23 mg, 0.02 mol) was dissolved in the mixture of THF (2 mL) and 10% aqueous NaOH (0.6 mL). The mixture was degassed *via* three freeze-pump-thaw cycles and stirred at 60 °C for 16 h. The reaction mixture was diluted with diethyl ether (10 mL) and dried over $MgSO_4$. The solvent was removed under reduced pressure and the crude product was purified *via* column chromatography (Teledyne Isco Combi Flash Rf+ system, 12 g SiO_2, hexanes-DCM elution from 0 to 100%) to give the title compound as a yellow oil (54 mg, 0.18 mmol, 39% yield). **^{1}H NMR** (400 MHz, $CDCl_3$): δ 7.61 – 7.55

(m, 2H, H_{18}), 7.29 – 7.20 (m, 2H, H_{17}), 6.33 – 6.15 (m, 2H, $H_{2/3}$), 5.88 – 5.67 (m, 4H, $H_{1/4/6/7}$), 3.33 (m, 2H, $H_{5/8}$), 2.05 (m, 1H, H_{11}), 1.88 (m, 1H, H_{11}), 1.46 – 1.28 (m, 2H, H_{12}), 1.20 – 1.05 (m, 4H, $H_{13/14}$), 0.81 (t, J = 7.1 Hz, 3H, H_{15}). **^{13}C NMR** (101 MHz, $CDCl_3$): δ 146.91 (C_{20}), 141.92 (C_2), 141.17 (C_3), 134.91 (C_9), 131.91 (C_{18}), 130.38 (C_{10}), 130.02 (C_{17}), 125.00 ($C_{6/7}$), 121.14 ($C_{1/4}$), 119.20 (C_{19}), 110.08 (C_{16}), 41.46 (C_5), 39.20 (C_8), 32.02 (C_{11}), 31.76 (C_{13}), 29.83 (C_{12}), 22.45 (C_{14}), 14.05 (C_{15}). **HR ESI MS**: m/z = 302.1903 $[M+H]^+$, calculated for $C_{22}H_{24}N^+$: 302.1909.

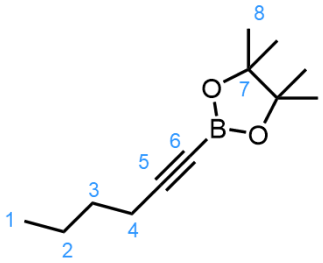

Bpin-pentyl alkyne (**3b**): 1-Hexyne (2.8 mL, 24 mmol) in diethyl ether (60 mL) was cooled to –78 °C under a N_2 atmosphere. n-Butyllithium (9.4 mL, 2.5 M in hexanes, 24 mmol) was added dropwise, followed by stirring at −78 °C for 1 h. 4,4,5,5-Tetramethyl-2-(1-methylethoxy)-1,3,2-dioxaborolane (4.08 mL, 20 mmol) in diethyl ether (60 mL) was then added. The reaction mixture was stirred at rt for 4 h before being cooled to –78 °C, followed by quenching with HCl (7.5 mL, 4 M in dioxane, 30 mmol) and stirring at rt for an additional 1 h. The solvent was removed under reduced pressure and the crude product was purified via column chromatography (Teledyne Isco Combi Flash Rf+ system, 80 g Al_2O_3, n-hexane – EtOAc elution from 0 to 100%) to give the title compound as a yellow oil. (1.30 g, 6.25 mmol, 31% yield) **^{1}H NMR** (400 MHz, $CDCl_3$): δ 2.25 (t, J = 7.1, 1.7 Hz, 2H, H_4), 1.56 – 1.46 (m, 2H, H_3), 1.46 – 1.36 (m, 2H, H_2), 1.26 (s, J = 1.7 Hz, 12H, H_8), 0.88 (t, 3H, H_1). **^{13}C NMR** (151 MHz, $CDCl_3$): δ 83.95 (C_7), 30.07 (C_3), 24.51 (C_8), 21.84 (C_2), 19.14 (C_4), 13.45 (C_1). Characterisation data are consistent with those reported previously: *J. Am. Chem. Soc.* 2020, **142**, 13867 – 13877.

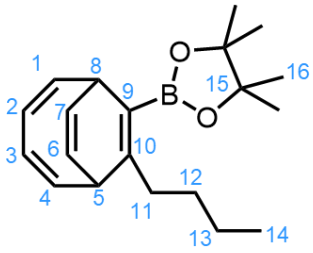

Bpin-butyl BDT (4b): An oven-dried Schlenk tube containing anhydrous ZnI_2 (128 mg, 0.4 mmol) was heated at 280 °C under high vacuum for 5 min. After cooled to rt and flushing with N_2, $CoBr_2$(dppe) (124 mg, 0.2 mmol), Zn (40 mg, 0.6 mmol), and anhydrous DCE (2 mL) were added – the reaction mixture was

then degassed by three freeze-pump-thaw cycles. Cyclooctatetraene (208 mg, 2.0 mmol) was added into the reaction mixture. **3b** (422 mg, 3.0 mmol in 2 mL of anhydrous DCE, degassed) was slowly added with syringe pump over 8 h. The reaction was stirred at rt in a H_2O bath for 16 h. After completion, the suspension was filtered through a short pad of SiO_2 (5 g) gel eluting with Et_2O. The solvent was removed under reduced pressure, and the crude product was purified via column chromatography (Teledyne Isco CombiFlash Rf+ system, 24 g SiO_2, n-hexane – EtOAc elution from 0 to 100%) to give the title compound as a colorless oil. (178 mg, 0.57 mmol, 29% yield) **^{1}H NMR** (400 MHz, $CDCl_3$): δ 6.28 (m, 1H, H_2), 6.10 (m, 1H, H_3), 5.76 – 5.48 (m, 4H, $H_{1/4/6/7}$), 3.49 – 3.37 (m, 1H, H_8), 3.35 – 3.24 (m, 1H, H_5), 2.54 – 2.38 (m, 2H, H_{11}), 1.43 – 1.28 (m, 4H, $H_{12/13}$), 1.24 (d, J = 4.4 Hz, 12H, H_{16}), 0.88 (t, J = 7.2 Hz, 3H, H_{14}). **^{13}C NMR** (151 MHz, $CDCl_3$): δ 151.07 (C_{10}), 143.18 (C_2), 140.50 (C_3), 124.86 (C_7), 123.40 (C_6), 122.29 (C_1), 121.43 (C_4), 82.73 (C_{15}), 40.99 (C_5), 37.05 (C_8), 34.11 (C_{12}), 33.16 (C_{11}), 25.08 (C_{16}), 24.59 (C_{16}), 22.53 (C_{13}), 14.05 (C_{14}). **HR ASAP MS**: m/z =313.2338 $[M+H]^+$, calculated for $C_{20}H_{30}BO_2^+$: 313.2333

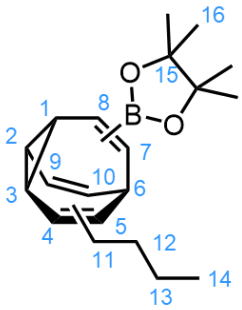

Bpin-butyl bullvalene (5b): **4b** (535 mg, crude) and thioxanthone (7.2 mg, 0.034 mmol) was dissolved in dry THF (5 mL). The reaction mixture was stirred under a 365 nm LED lamp with a H_2O bath for 24 h. The solvent was removed under reduced pressure and the crude product was purified *via* column chromatography (Teledyne Isco CombiFlash Rf+ system, 80 g Al_2O_3, n-hexane – DCM elution) to give the title compound. The broad peaks in the ^{1}H-NMR spectrum indicated the successful formation of bullvalene. The crude product was carried into the next step without further purification.

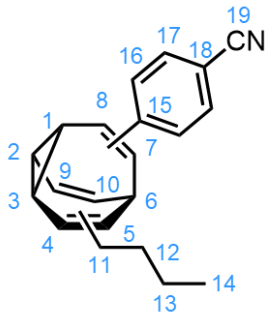

4CB bullvalene (1b): **5b** (250 mg, crude), 4-bromobenzonitrile (146 mg, 0.80 mmol), and $Pd(PPh_3)_4$ (44 mg, 0.04 mmol) was dissolved in the mixture of THF (4 mL) and 10% aqueous NaOH (1.2 mL). The mixture was degassed *via* three freeze-pump-thaw cycles and stirred at 60 °C for 16 h. The reaction mixture was diluted with diethyl ether (10 mL) and dried over $MgSO_4$. The solvent was removed under reduced pressure and the crude product was purified *via* column chromatography (Teledyne Isco Combi Flash Rf+ system, 12 g SiO_2, n-hexane-DCM elution from 0 to 100%) to give the title compound as a yellow oil (58 mg, 0.20 mmol, 25% yield). **^{1}H NMR** (500 MHz, $CDCl_3$, 213K) δ 7.68 – 7.61 (m, 2H, H_{17}), 7.49 (m, 0.36H, H_{16}, isomer γβ'+γγ'), 7.43 (m, 1.47H, H_{16}, isomer ββ'+βγ'), 6.28 – 6.22 (m, 0.72H, H_2, isomer ββ'+βγ'), 6.18 – 6.11 (m, 0.17H, H_3, γβ'+γγ'), 6.09 – 5.84 (m, 2H, $H_{9/10}$), 5.79 (d, J = 7.7 Hz, 0.44H, H_6, isomer ββ'), 5.75 (d, J = 7.9 Hz, 0.12H, H_6, isomer γβ'), 5.68 (d, J = 9.1 Hz, 0.21H, H_5, isomer βγ'), 5.60 (d, J = 8.9 Hz, 0.04H, H_5, isomer γγ'), 3.01 (m, 0.27H, H_4, isomer βγ'), 2.88 (d, J = 8.7 Hz, 0.47H, H_4, isomer ββ'), 2.74 - 2.60 (m, 0.28H, H_4, isomer γβ'+γγ'), 2.55 – 2.34 (m, 3H, $H_{1/7/8}$), 2.17 – 2.03 (m, 2H, H_{11}), 1.52 – 1.26 (m, 2H, H_{12}), 1.20 (m, 2H, H_{13}), 0.93 – 0.84 (m, 1.79H, H_{14}, isomer ββ'), 0.76 (m, 1.42H, H_{14}, isomer βγ'+γβ'+γγ'). **^{13}C NMR** (126 MHz, $CDCl_3$, 213K) δ 149.49 (C_{19}, isomer γβ'), 147.79 (C_{19}, isomer ββ'+βγ'+γγ'), 142.29 (C_5, isomer γβ'), 141.44 (C_5, isomer ββ'), 140.25 (C_6, isomer βγ'), 139.55 (C_6, isomer γγ'), 139.11 (C_2, isomer βγ'), 138.70 (C_2, isomer ββ'), 137.27 (C_3, isomer γβ'), 136.86 (C_3, isomer γγ'), 132.63 (C_{17}), 128.06 (C_9), 127.97 (C_2, isomer ββ'), 127.57 (C_2, isomer βγ'), 127.16 (C_{16}, isomer γβ'+γγ'/C_{10}), 126.84 (C_3, γβ'+γγ'), 126.57 (C_{16}, isomer ββ'+βγ'), 120.52 (C_6, isomer ββ'), 120.00 (C_{18}), 119.67 (C_6, isomer γβ'), 119.06 (C_5, isomer γγ'), 118.71 (C_5, isomer βγ'), 109.57 (C_{15}, isomer γβ'), 109.47 (C_{15}, isomer γγ'),109.29 (C_{15}, isomer ββ'), 109.12 (C_{15}, isomer βγ'), 41.57 (C_{11}, isomer γγ'), 41.02 (C_{11}, isomer βγ'), 40.20 (C_{11}, isomer γβ'), 40.04 (C_{11}, isomer ββ'), 38.96 (C_4, isomer ββ'), 34.73 (C_4, isomer γβ'), 34.32 (C_4, isomer βγ'), 31.89 (C_{12}, isomer γγ'), 31.48 (C_{12}, isomer γβ'), 30.54 (C_{12}, isomer ββ'), 30.52 (C_{12}, isomer βγ'), 30.05 (C_4, isomer γγ'), 24.26 (C_1 or C_7 or C_8, isomer βγ'), 23.19 (C_{12}, isomer γγ'), 22.89 (C_1 or C_7 or C_8, isomer γγ'), 22.67 (C13, isomer γβ'), 22.63 (C13, isomer βγ'), 22.51 (C_1 or C_7 or C_8, isomer γγ'), 22.33 (C_1 or C_7 or C_8, isomer γβ'), 22.28 (C13, isomer ββ'), 21.46

(C_1 or C_7 or C_8, isomer ββ'), 21.40 (C_1 or C_7 or C_8, isomer βγ'), 21.30 (C_1 or C_7 or C_8, isomer ββ'), 21.15 (C_1 or C_7 or C_8, isomer ββ'), 20.99 (C_1 or C_7 or C_8, isomer βγ'), 20.11 (C_1 or C_7 or C_8, isomer γβ'), 20.06 (C_1 or C_7 or C_8, isomer γγ'), 19.74 (C_1 or C_7 or C_8, isomer γβ'), 14.85 (C_{14}, isomer γγ'), 14.69 (C_{14}, isomer βγ'), 14.64 (C_{14}, isomer γβ'), 14.49 (C_{14}, isomer ββ'). **HR ESI MS**: m/z = 310.1577 $[M+Na]^+$, calculated for $C_{21}H_{21}NNa^+$: 310.1566.

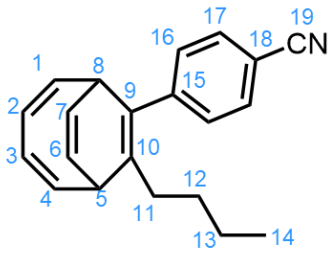

4CB BDT (2b): **4b** (183 mg, 0.59 mmol), 4-bromobenzonitrile (108 mg, 0.59 mmol), and $Pd(PPh_3)_4$ (33 mg, 0.03 mol) was dissolved in the mixture of THF (3 mL) and 10% aqueous NaOH (0.9 mL). The mixture was degassed *via* three freeze-pump-thaw cycles and stirred at 60 °C for 16 h. The reaction mixture was diluted with diethyl ether (10 mL) and dried over $MgSO_4$. The solvent was removed under reduced pressure and the crude product was purified *via* column chromatography (Teledyne Isco Combi Flash Rf+ system, 12 g SiO_2, n-hexane-DCM elution from 0 to 100%) to give the title compound as a yellow oil (56 mg, 0.20 mmol, 34% yield). **^{1}H NMR** (400 MHz, $CDCl_3$): δ 7.60 – 7.54 (m, 2H, H_{17}), 7.27 – 7.21 (m, 1H, H_{16}), 6.33 – 6.14 (m, 2H, $H_{2/3}$), 5.82 – 5.72 (m, 4H, $H_{1/4/6/7}$), 3.33 (m, 2H, $H_{5/8}$), 2.06 (ddd, J = 13.6, 9.4, 6.1 Hz, 1H, H_{11}), 1.89 (ddd, J = 13.6, 9.3, 6.4 Hz, 1H, H_{11}), 1.35 (ddd, J = 9.6, 7.5, 6.2 Hz, 2H, H_{12}), 1.16 (q, J = 7.3 Hz, 2H, H_{13}), 0.78 (t, J = 7.3 Hz, 3H, H_{14}). **^{13}C NMR** (101 MHz, $CDCl_3$): δ 146.90 (C_{19}), 141.91 (C_2), 141.16 (C_3), 134.87 (C_9), 131.91 (C_{17}), 130.40 (C_{10}), 130.03 (C_{16}), 125.00 (C_7), 124.80 (C_6), 121.14 (C_1), 121.11 (C_4), 119.19 (C_{18}), 110.08 (C_{15}), 41.47 (C_5), 39.20 (C_8), 32.37 (C_{12}), 31.81 (C_{11}), 22.68 (C_{13}), 13.95 (C_{14}). **HR ESI MS**: m/z = 310.1573 $[M+Na]^+$, calculated for $C_{21}H_{21}NNa^+$: 310.1566.

4.4.3 Structural Assignment by 2D NMR

The assignment of each peak of **1b** and analysis of isomerisation distribution were done using 2D NMR spectra obtained at 213 K. Previous studies on bullvalene isomerisation[4] have demonstrated that di-substituted bullvalenes tend to have a distribution in which ββ' > βγ' > γβ' > γγ'. In the ^{1}H and ^{13}C spectra of **1b**, multiple sets of peaks in the aromatic region are observed

to have a ratio close to 55:26:15:4 (Figure 4.1). It is assumed that the ratio represents the distribution of four isomers (ββ':βγ':γβ':γγ') in the solution mixture and the assumption will be used and proved throughout the assignment.

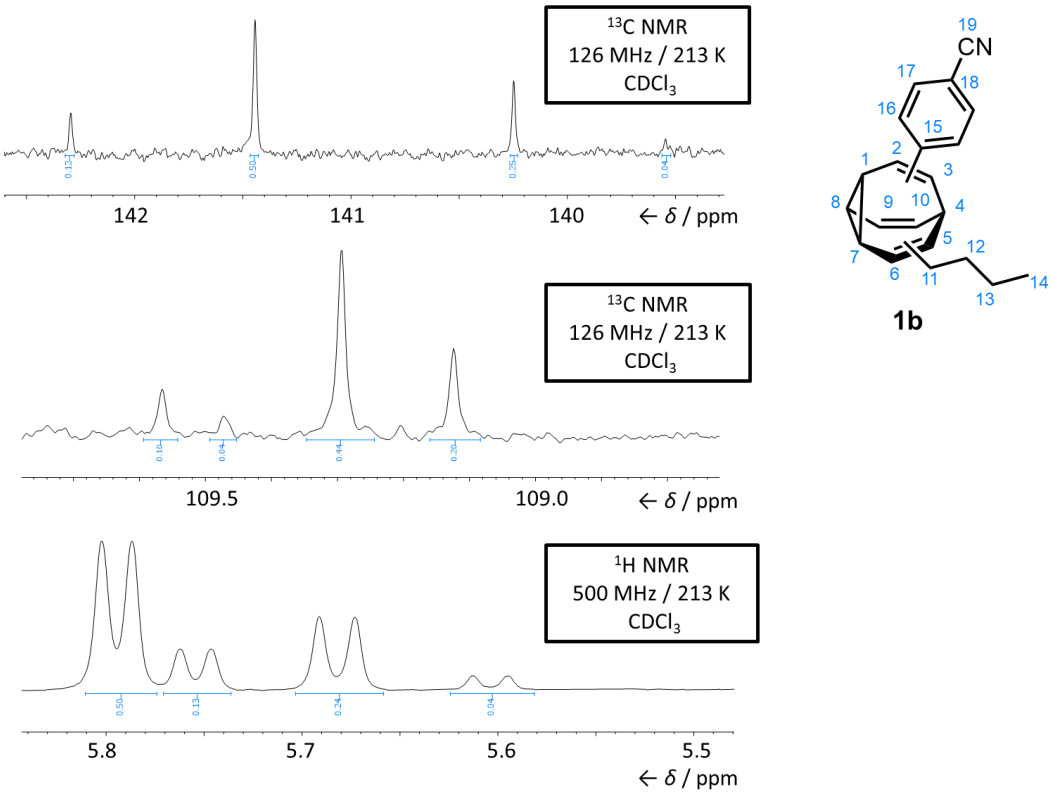

Figure 4.1. Partial ^{1}H and ^{13}C NMR spectra of **1b**.

H_{16} and H_{17} are first determined. H_{17} does not have any resolution of isomerisation, and the H_{16} isomerism is determined based on integrations. In the HMBC spectrum, C_{15} is determined via correlation with H_{16} (Figure 4.2), and the ratio of four split peaks matches up with the assumed distribution of four isomers.

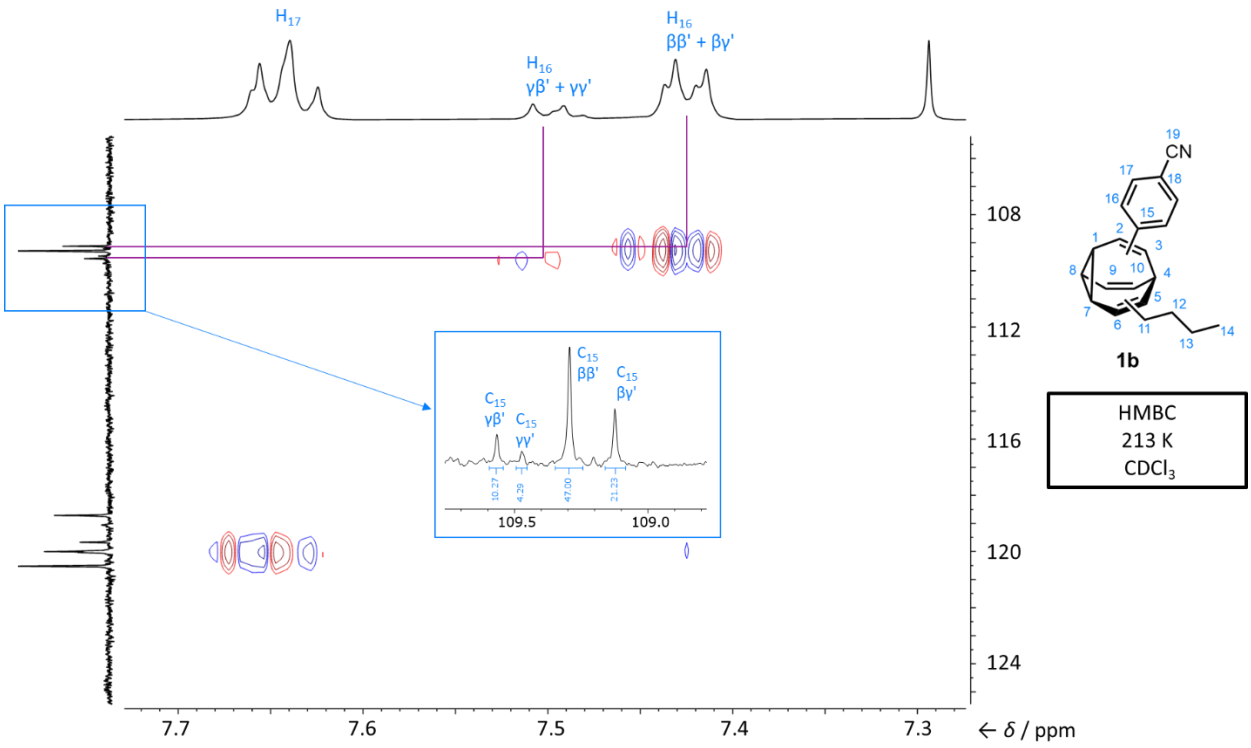

Figure 4.2. Partial HMBC spectra of **1b**.

H_{16} is also observed to correlate with the C atom attached to the benzonitrile substituent (C_3 for isomer ββ' and βγ', C_2 for isomer γβ' and γγ') in HMBC (Figure 4.3), and their neighbouring sp^2 —H atom (H_2 for isomer ββ' and βγ', H_3 for isomer γβ' and γγ') could then be determined. Note that the correlations of isomer γβ' and γγ' are sometimes not observable in 2D spectra due to low intensity, and the peaks need to be determined by the assumed ratio of integrations with isomer ββ' and βγ'.

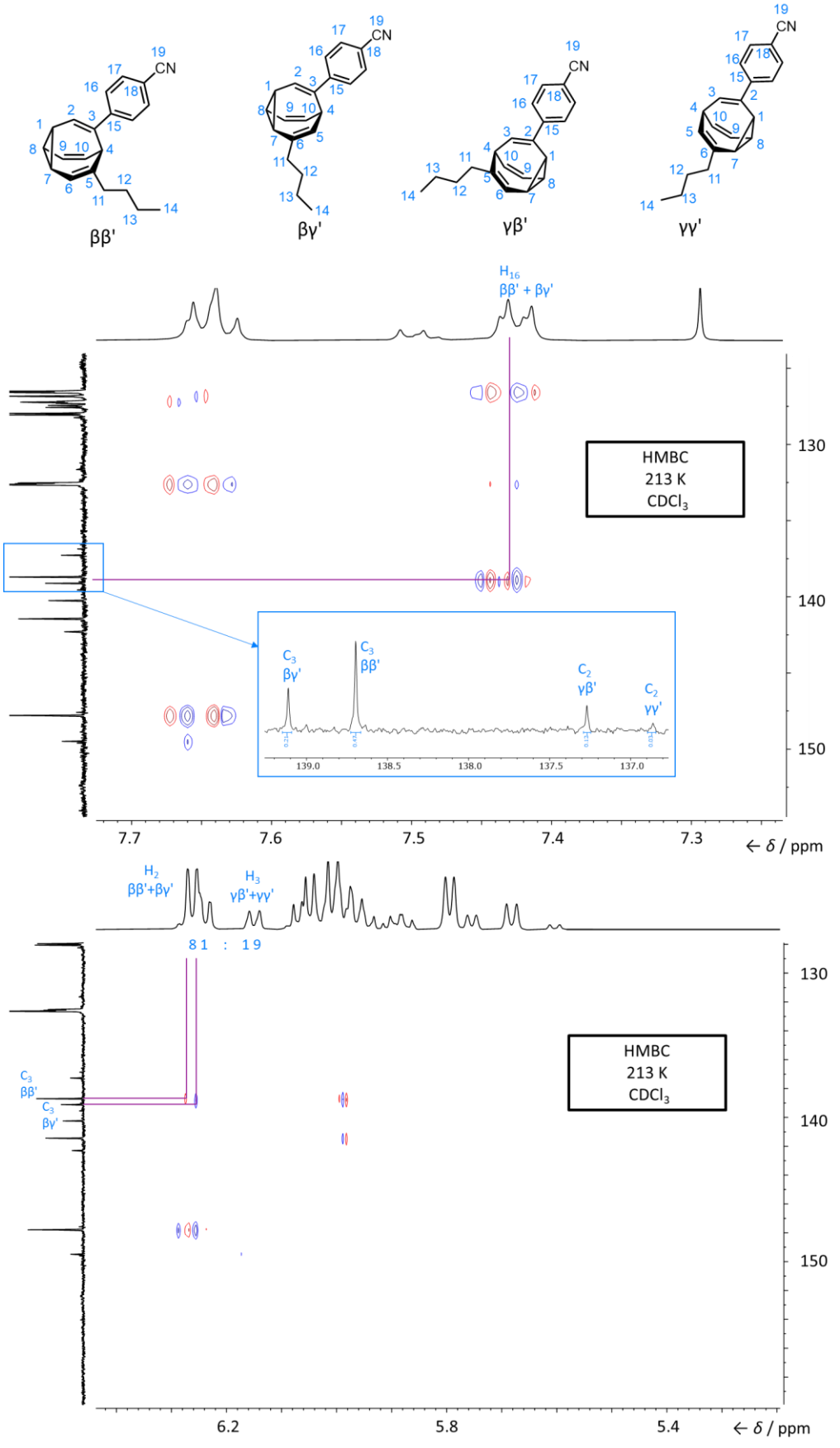

Figure 4.3. Partial HMBC spectra of **1b**.

Upon finding H_2 and H_3, the COSY spectrum allowed for the determination of their neighbouring sp^3—H atom as H_2 correlates to H_1 in isomer ββ' and βγ', and H_3 correlates to H_4 in isomer γβ' and γγ' (Figure 4.4).

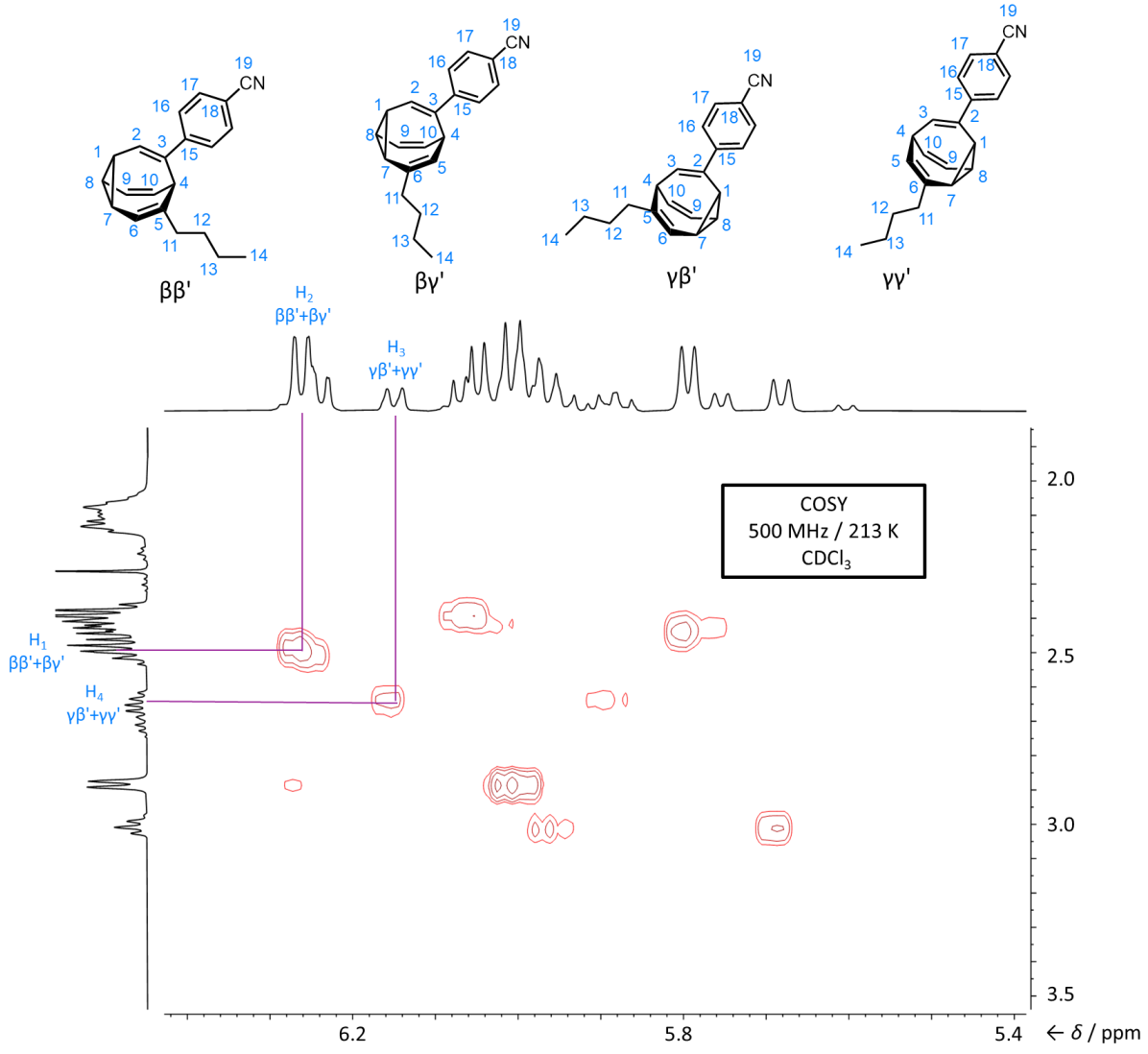

Figure 4.4. Partial COSY spectra of **1b**.

The positions on the butyl substituent are determined by the ^1H spectrum. The H_{14} split into two peaks and the isomerisation is determined via integrations (Figure 4.5).

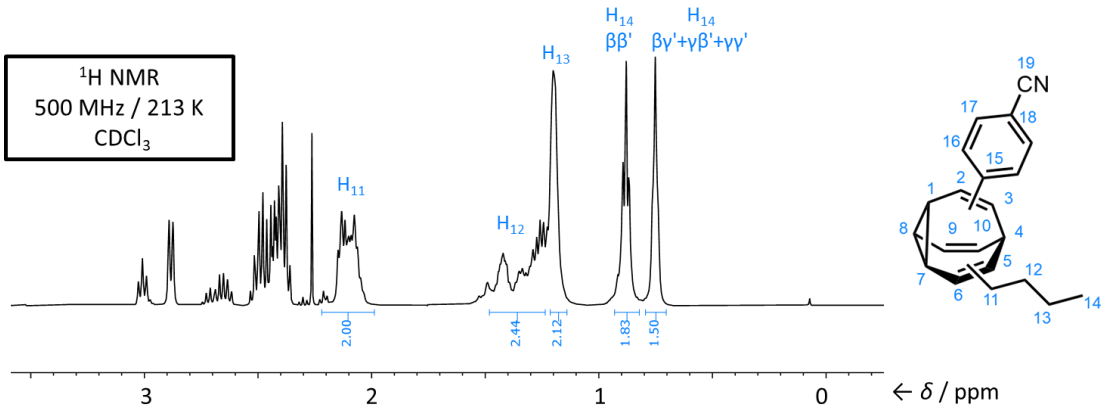

Figure 4.5. Partial ^{1}H NMR spectrum of **1b**.

The determination of H_{11} then lead to the C atom attached to the butyl substituent (C_5 for isomer ββ' and γβ', C_6 for isomer βγ' and γγ') by HMBC (Figure 4.6), as well as their neighbouring sp^2—H atom (H_6 for isomer ββ' and γβ', H_5 for isomer βγ' and γγ').

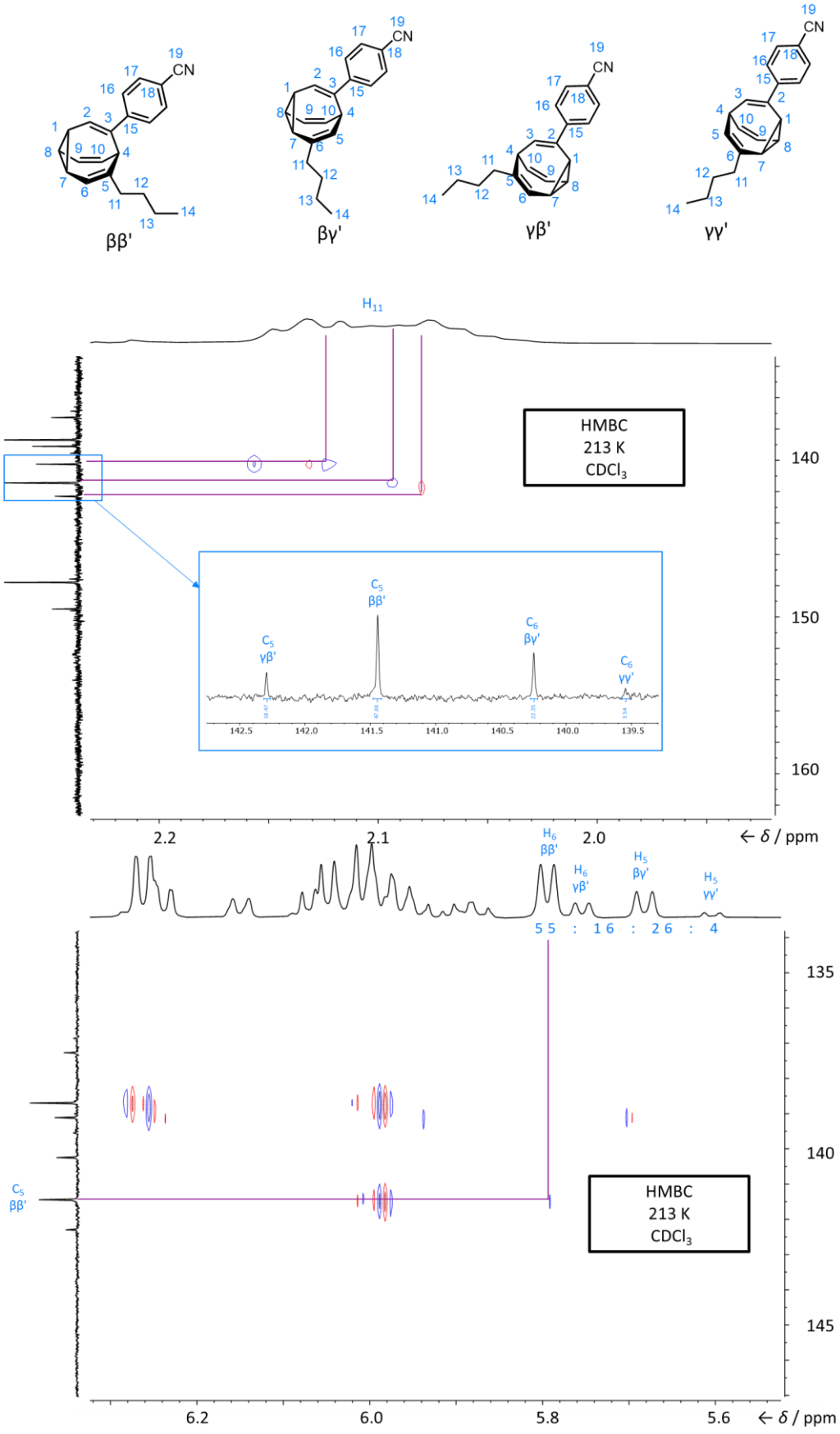

Figure 4.6. Partial HMBC spectrum of **1b**.

The H_4 of isomer ββ' is determined by HMBC as it correlates to both C_3 and C_5 (Figure 4.7). The H_4 of the other three isomers are then determined by COSY, as it correlates to H_3 in isomer γβ' and γγ' and H_5 in isomer βγ' (Figure 4.8).

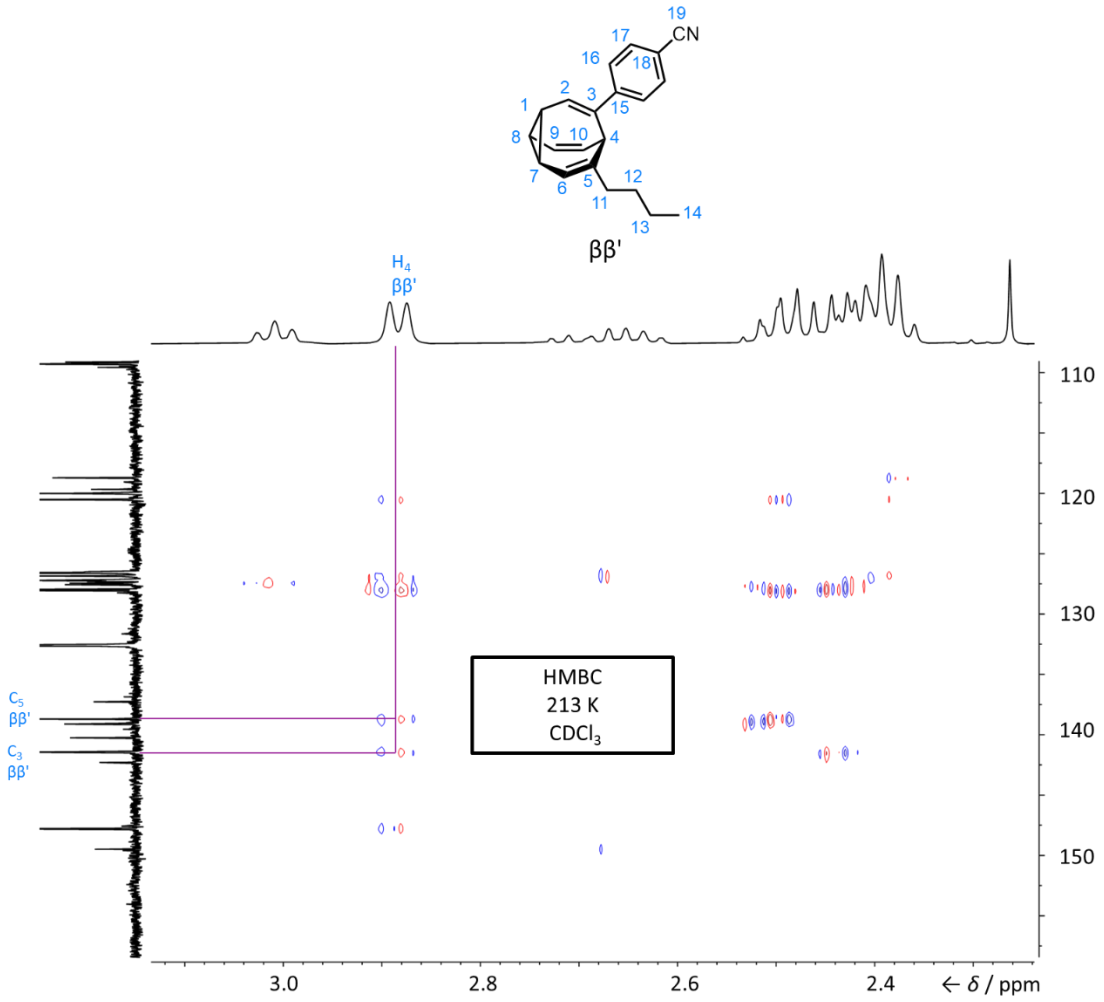

Figure 4.7. Partial HMBC spectrum of **1b**.

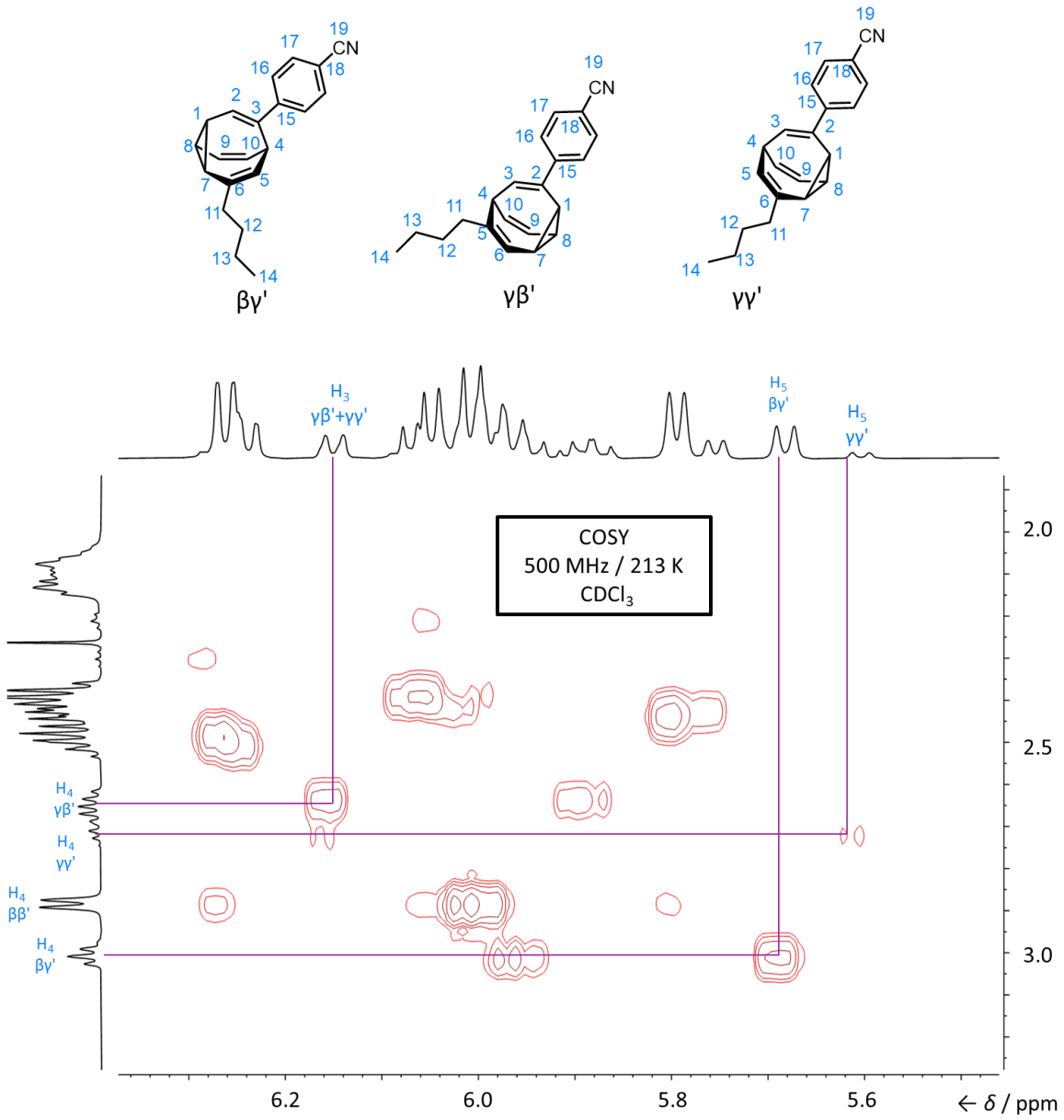

Figure 4.8 Partial HMBC spectrum of **1b**.

H_{10} of all isomers could then be determined via the correlations with H_4 in the COSY spectrum (Figure 4.9). After the determination of $H_{2/3/5/6/10}$, the remaining set of peaks in the olefin region (6.09－6.03 ppm) should only belong to H_9.

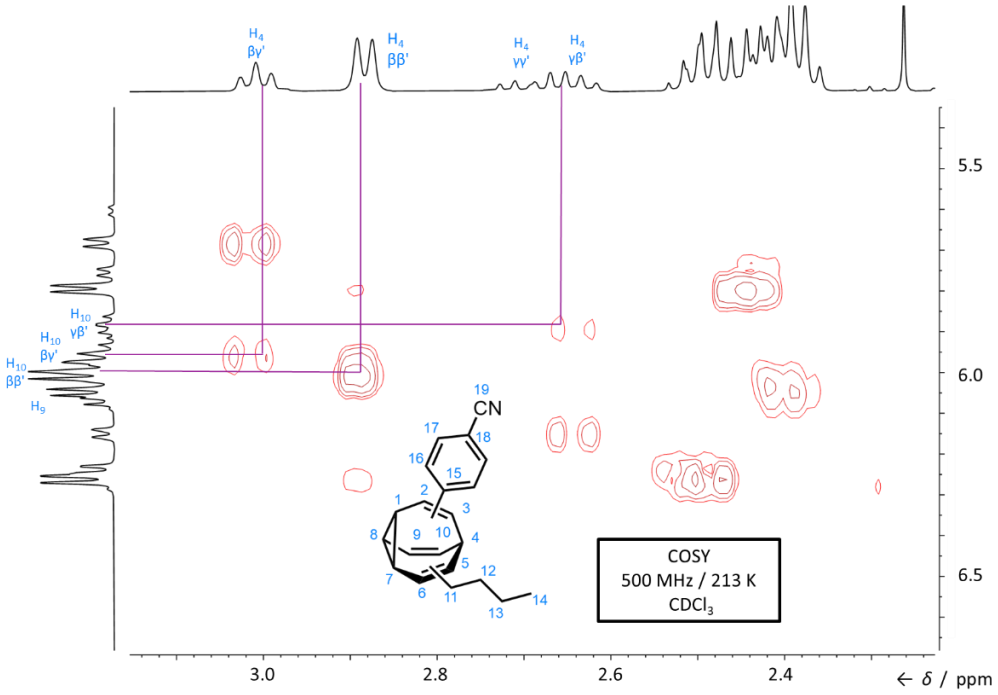

Figure 4.9. Partial COSY spectrum of **1b**.

After determination of all the other ^{1}H peaks, the remaining peaks at 2.55 – 2.34 ppm could only belong to $H_{1/7/8}$. The three positions on the cyclopropane ring could not be distinguished from each other as the correlations are overlapping in the 2D spectra.

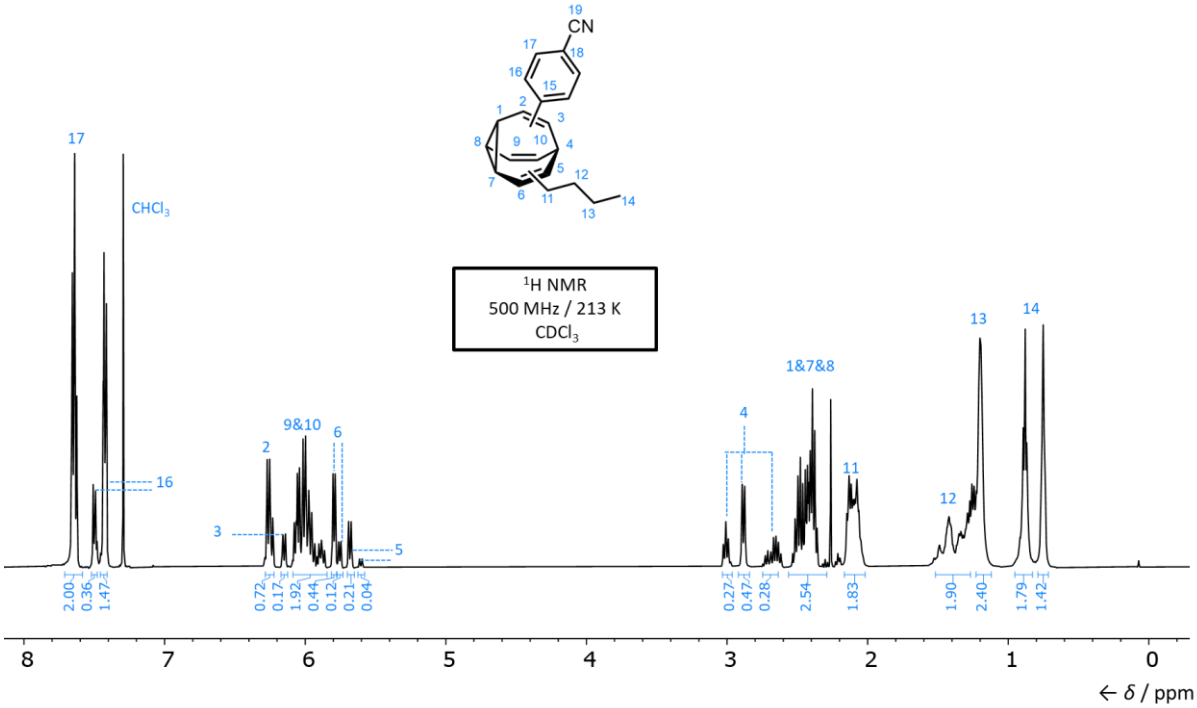

Figure 4.10. Fully assigned ^{1}H NMR spectrum of **1b**.

Finally, the C_{18} and C_{19} are distinguished from each other by HMBC, where C_{18} correlates to both H_{16} and H_{17} while C_{19} only correlates to H_{17} (Figure 4.11). C_{19} is also observed to split into two peaks upon isomerisation.

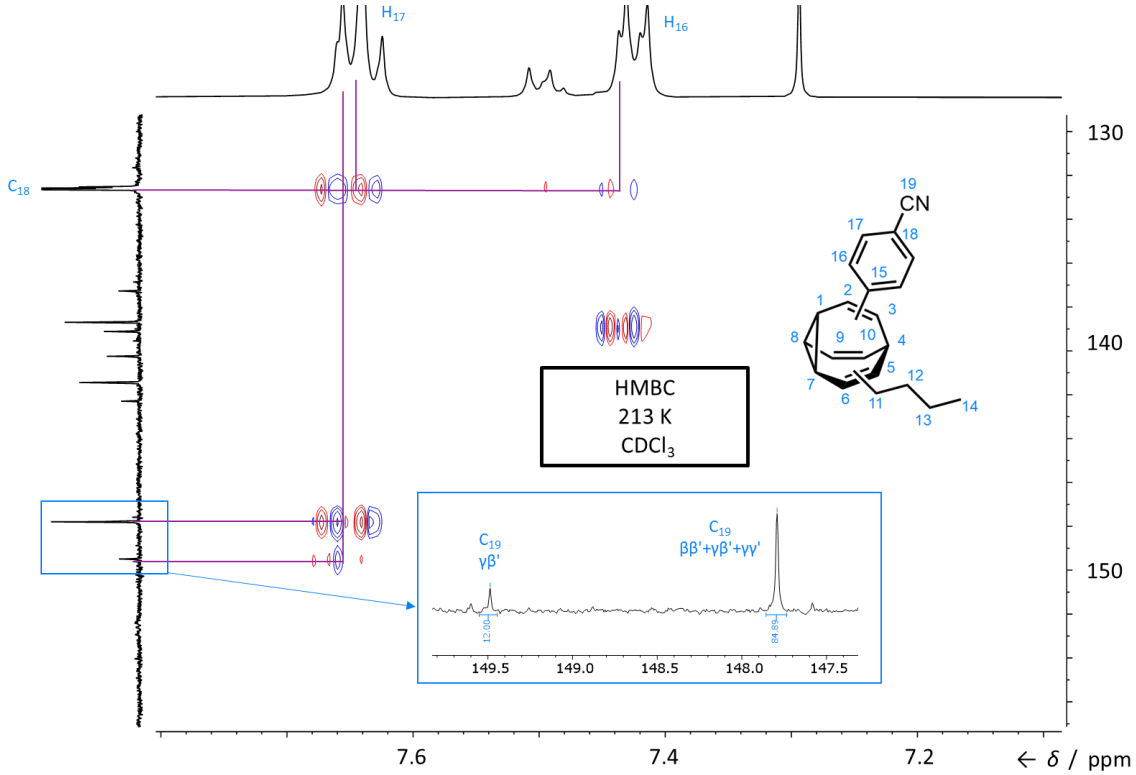

Figure 4.11. Partial HMBC spectrum of **1b**.

The remaining ^{13}C peaks are determined by looking for their corresponding ^{1}H peaks in the HSQC spectrum to finish the assignment of bullvalene **1b** (Figure 4.12). The ^{1}H and ^{13}C NMR spectra of bullvalene **1a** are assigned following the same procedure. The assumed distribution of four isomers is proved to be correct in the assignment process as it continuously matches up with the correlations observed in the 2D NMR.

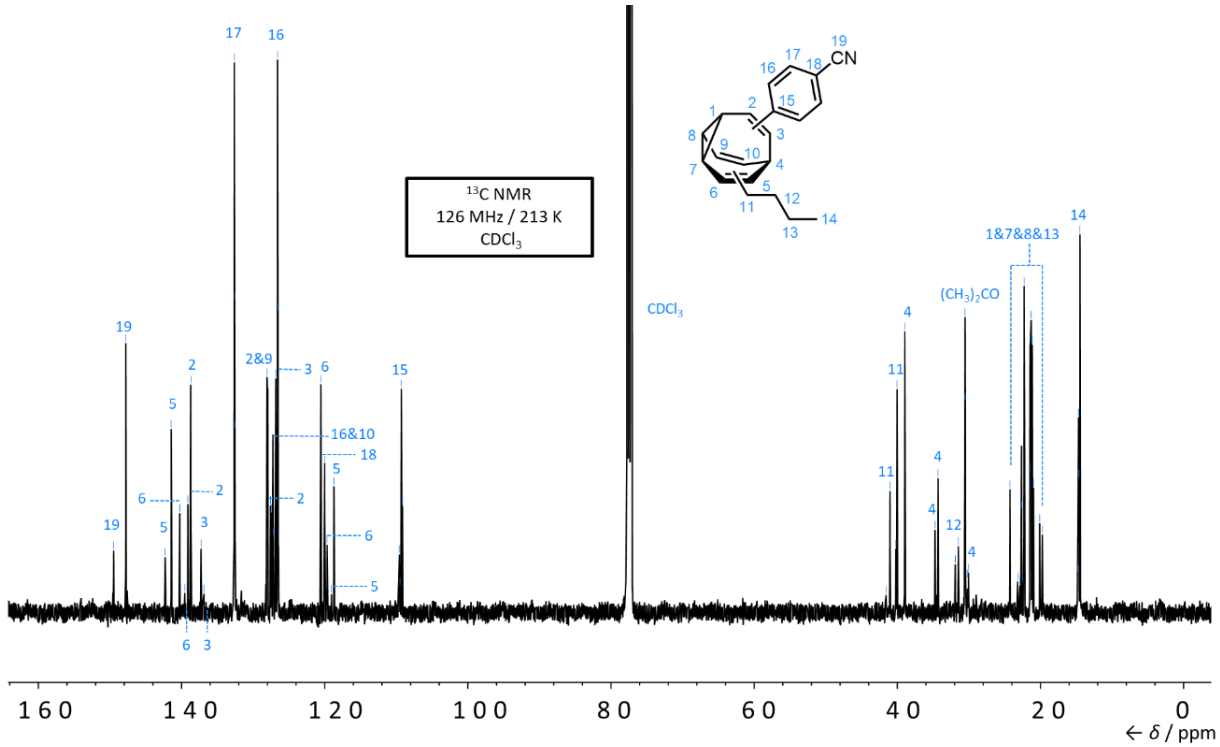

Figure 4.12. Fully assigned ^{13}C NMR spectrum of **1b**.

4.4.4 Table of Reported Compounds with Low Melting Points (＜−50 ℃)

The collection of compounds with ＜ − 50 ℃ melting points has been uploaded and can be accessed via the following link:

https://docs.google.com/spreadsheets/d/1jrwvzBv-1p9K2Fzxe5E_6SfbrOD1ZpJK/edit?usp=drive_link&ouid=109833257329170364271&rtpof=true&sd=true

4.4.5 Polarised Microscopy Results

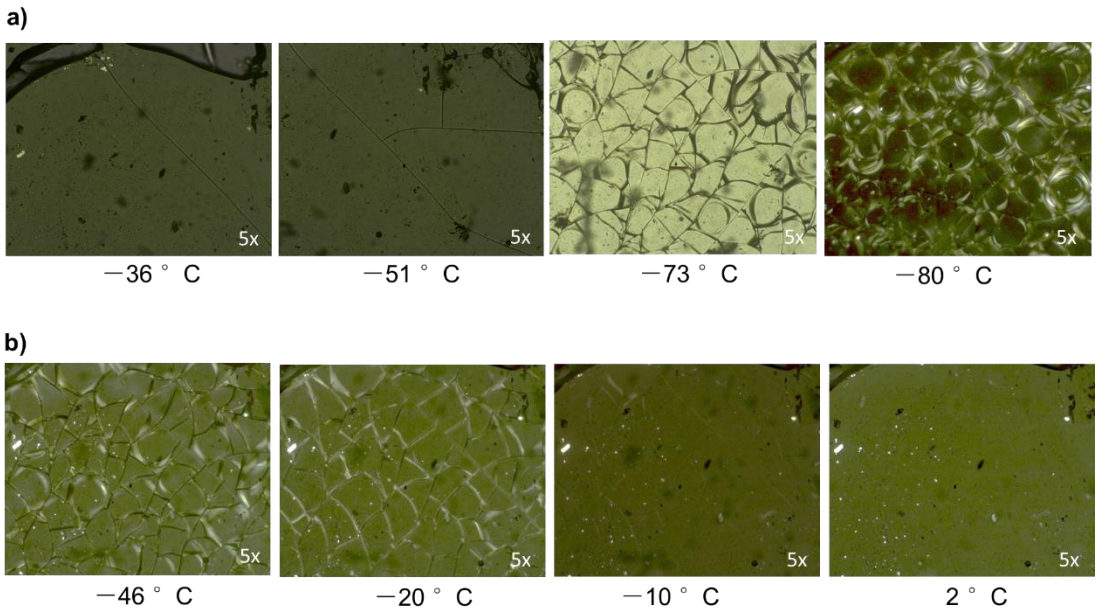

Figure 4.13. Polarised microscopy images of **1a** under variable temperature. a) cooling down; b) warming up.

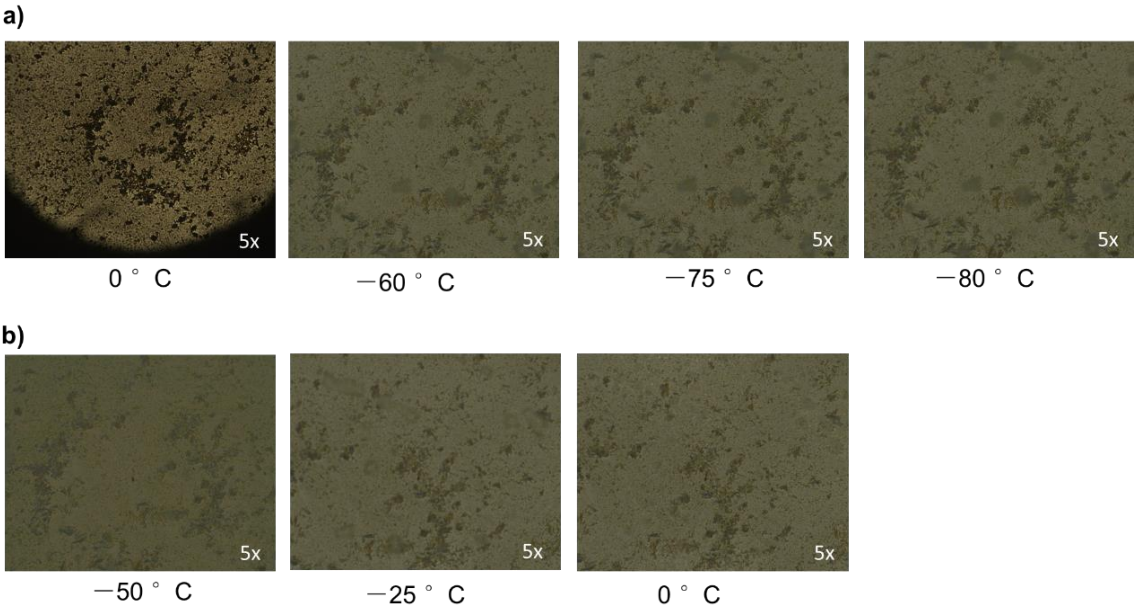

Figure 4.14. Polarised microscopy images of **1b** under variable temperature. a) cooling down; b) warming up.

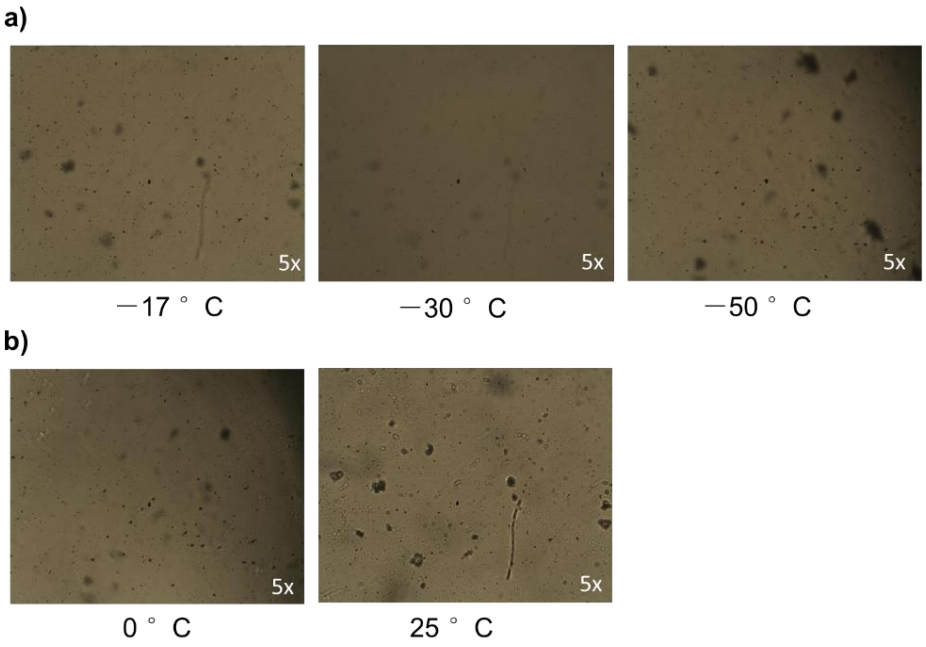

Figure 4.15. Polarised microscopy images of **2a** under variable temperature. a) cooling down; b) warming up.

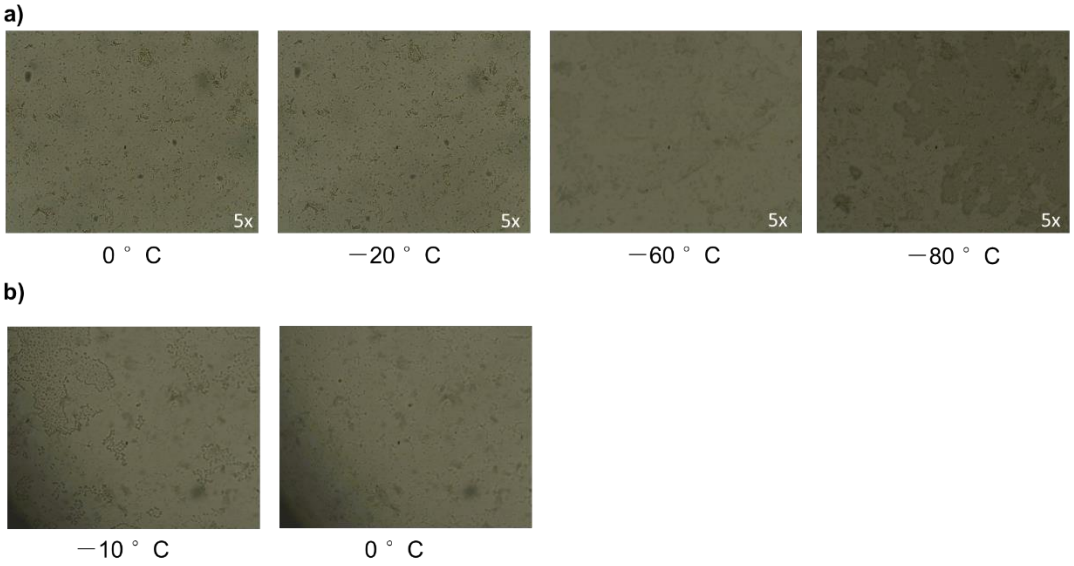

Figure 4.16. Polarised microscopy images of **2b** under variable temperature. a) cooling down; b) warming up.

4.4.6 Differential Scanning Calorimetry (DSC) Results

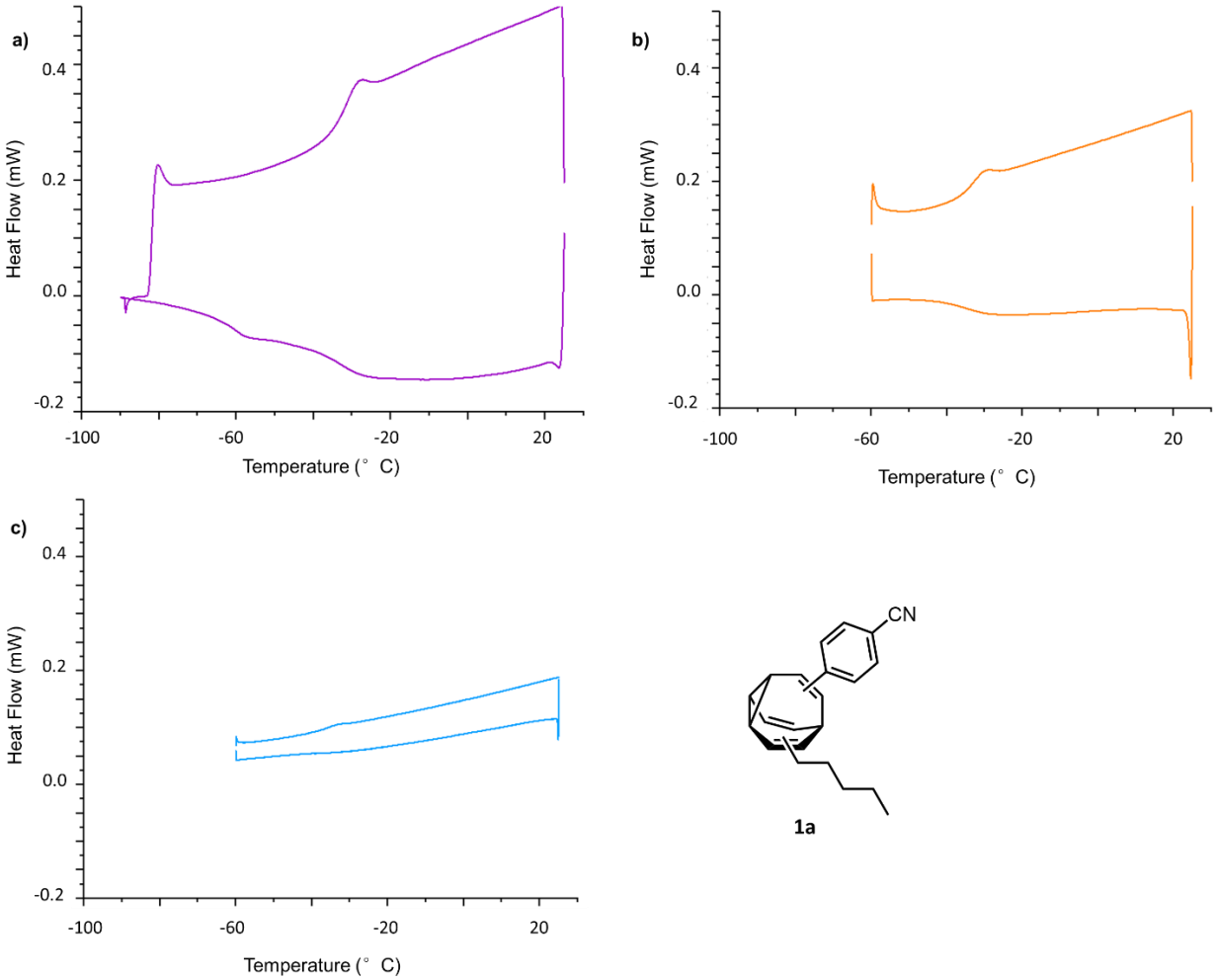

Figure 4.17. DSC diagrams of **1a** under different cooling and warming rates. a) 10 K / min; b) 5 K / min; c) 1 K / min.

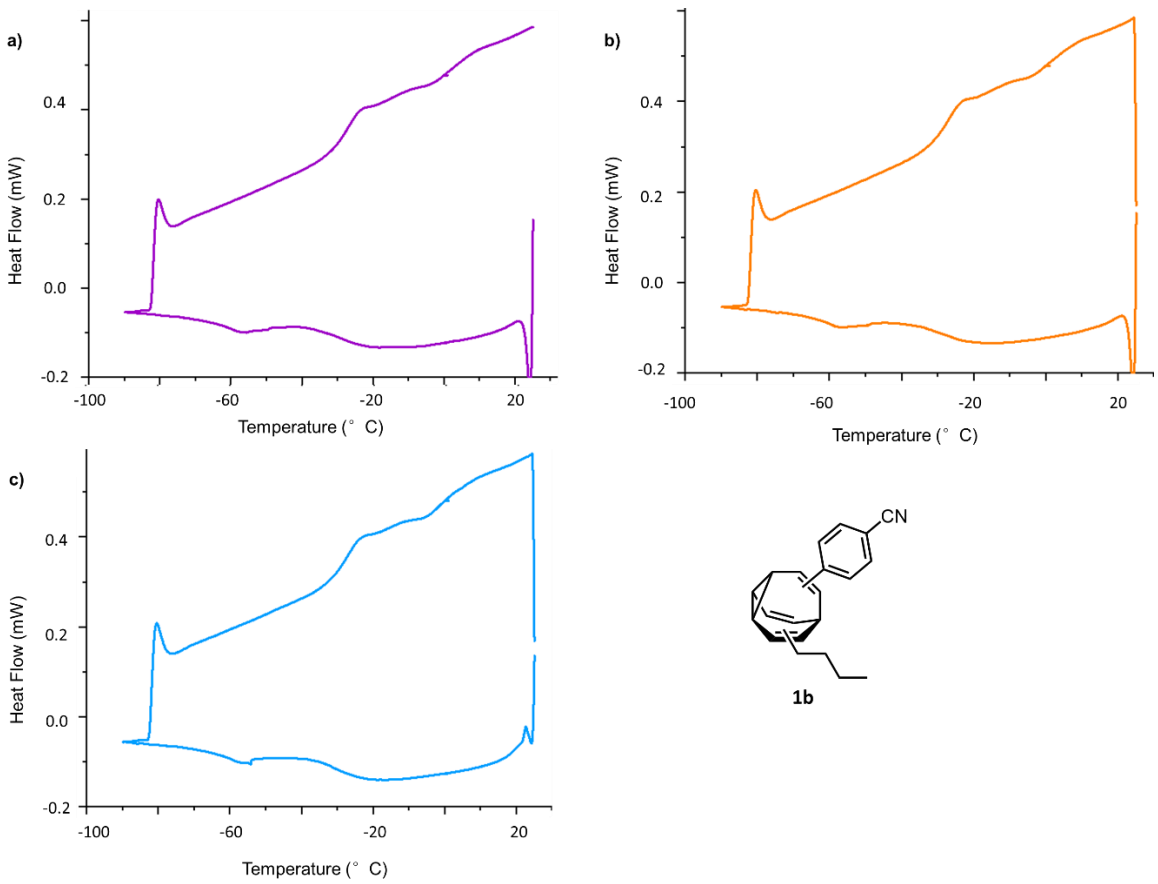

Figure 4.18. DSC diagrams of **1b** under different cooling and warming rates. a) 10 K / min; b) 5 K / min; c) 1 K / min.

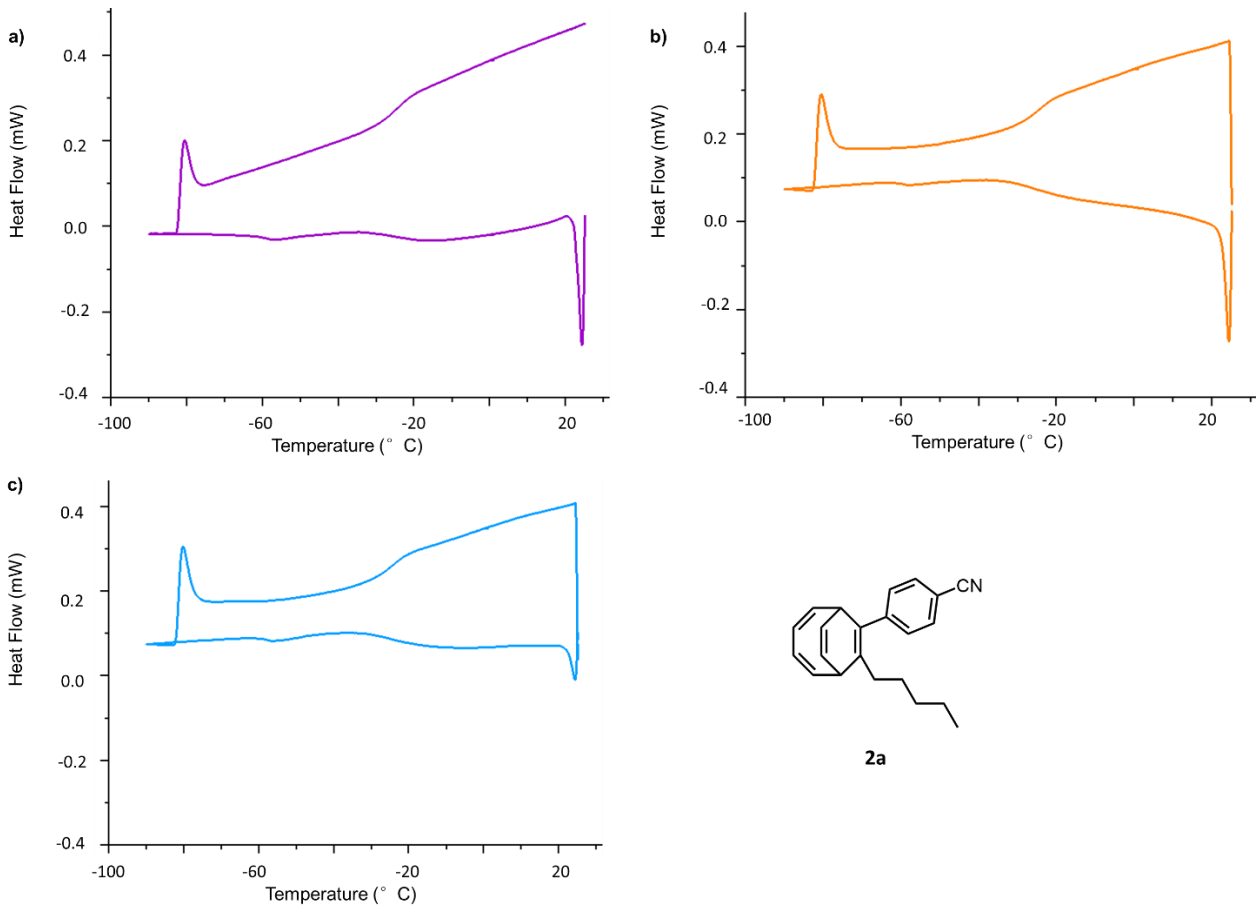

Figure 4.19. DSC diagrams of **2a** under different cooling and warming rates. a) 10 K / min; b) 5 K / min; c) 1 K / min.

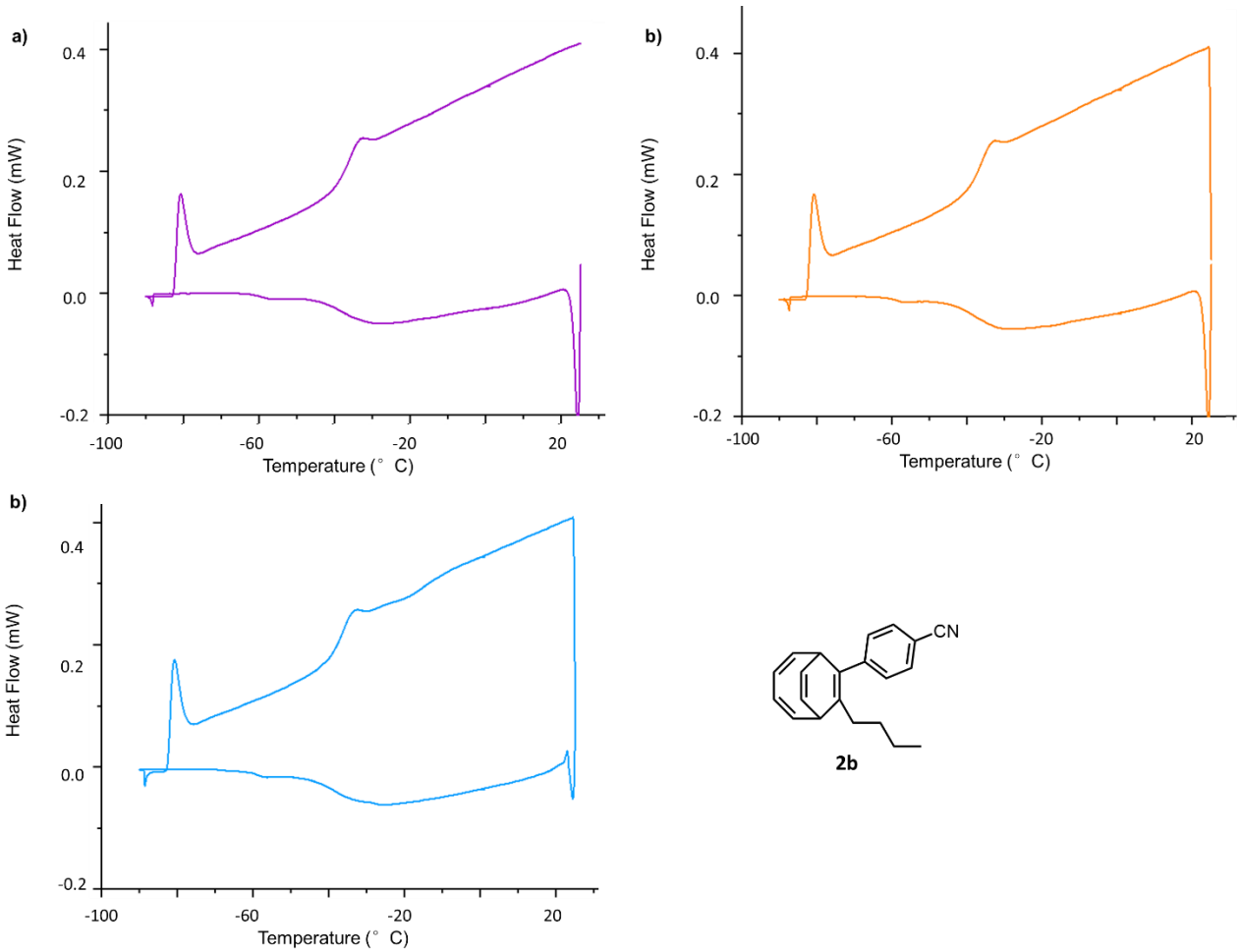

Figure 4.20. DSC diagrams of **2b** under different cooling and warming rates. a) 10 K / min; b) 5 K / min; c) 1 K / min.

	Warming up			Cooling down		
	T_g onset (℃)	T_g midpoint (℃)	ΔCp (J/g·K)	T_g onset (℃)	T_g midpoint (℃)	ΔCp (J/g·K)
1a (10 K / min)	– 35.1	–32.7	0.454	–20.0	–32.8	0.293
1a (5 K / min)	–36.0	–33.9	0.421	–39.4	–34.9	0.287
1a (1 K / min)	–37.5	–37.4	0.390	–38.1	–36.1	0.039
1b (10 K / min)	–32.0	–27.8	0.601	–18.4	–30.2	0.268
1b	–31.6	–27.6	0.586	–19.5	–30.0	0.211

(5 K / min)						
1b (1 K / min)	–31.4	–27.7	0.565	–18.4	–30.0	0.264
2a (10 K / min)	–29.2	–25.7	0.581	–16.9	–27.2	0.154
2a (5 K / min)	–29.52	–25.95	0.521	–13.9	–28.3	0.275
2a (1 K / min)	–29.2	–26.3	0.505	–17.8	–28.9	0.227
2b (10 K / min)	–39.3	–37.1	0.450	–26.4	–37.7	0.266
2b (5 K / min)	–39.2	–37.0	0.458	–27.8	–38.3	0.297
2b (1 K / min)	–39.2	–37.0	0.440	–26.1	–38.1	0.266

Table 4.2. T_g ranges and heat capacity changes of **1** and **2**.

4.5 References

1. (a) W. von E. Doering, W. R. Roth, *Tetrahedron* 1963, **19**, 715–737; (b) G. Schröder, *Angew. Chem. Int. Ed. Eng.* 1963, **2**, 481; (c) A. Adult, *J. Chem. Educ.* 2001, **78**, 924; (d) A. N. Bismillah, B. M. Chapin, B. A. Hussein and P. R. McGonigal, *Chem. Sci.* 2020, **11**, 324

2. (a) S. Ferrer, A. M. Echavarren, *Angew. Chem. Int. Ed.* 2016, **55**, 11178–11182; (b) O. Yahiaoui, L. F. Pašteka, B. Judeel and T. Fallon, *Angew. Chem. Int. Ed.* 2018, **57**, 2570; (c) H. D. Patel, T. H. Tran, C. J. Sumby, L. F. Pašteka and T. Fallon, *J. Am. Chem. Soc.* 2020, **142**, 3680-3685.

3. (a) O. Yahiaoui, L. F. Pašteka, C. J. Blake, C. G. Newton and T. Fallon, *Org. Lett.* 2019, **21**, 9574–9578; (b) B. A. Hussein, W. Maturi, M. K.Rylands, A. N. Bismillah, Y. Wen, J. A. Aguilar, R. Ayub, C. Rankine and P. R. McGonigal, *Correlated Shapeshifting and Configurational Isomerization*, under review.

4. (a) A. R. Lippert, V. L. Keleshian and J. W. Bode, *Org. Biomol. Chem.* 2009, **7**, 1529; (b) K. K. Larson, M. He, J. F. Teichert, A. Naganawa and J. W. Bode, *Chem. Sci.* 2012, **3**, 1825.

5. A. P. Birvé, H. D. Patel, J. R. Price, W. M. Bloch and T. Fallon, *Angew. Chem. Int. Ed.* 2021, **9**, e202115468

6. M. N. Pomfret, P. B. Sun, Z. Huang, A. C. Freund, T. Miyoshi and M. R. Golder, *Angew. Chem. Int. Ed.* 2023, **19**, e202301695

7. C. Dohmen, H. Ihmels and T. Paululat, *Eur. J. Org. Chem.* 2022, **45**, e202201172;

8. A. Ottonello, J. A. Wyllie, O. Yahiaoui, S. Sun, R. A. Koelln, J. A. Homer, R. M. Johnson, E. Murray, P. Williams, J. R. Bolla, C. V. Robinson, T. Fallon, T. P. Soares da Costa and J. E. Moses, Proc. *Natl. Acad. Sci.* 2023, **120**, e2208737120.

(a) J. S. McKechnie, M . G. Newton and I. C. Paul, *J. Am. Chem. Soc.* 1967, **89**, 4819-4825; (b) P. Luger, J. Buschmann, R. K. McMullan, J. R. Ruble, P. Matias and G. A. Jeffrey, *J. Am. Chem. Soc.* 1986, **108**, 7825-7827; (c) S. Schlick, Z. Luz, R. Poupko and H. Zimmermann, *J. Am. Chem. Soc.* 1992, **114**, 4315-4320; (d) A. Müller, U. Haeberlen, H. Zimmermann, R. Poupko and Z. Luz, *Mol. Phys.* 1994, **81**, 1239–1258; (e) B. H. Meier and W. L. Earl, *J. Am. Chem. Soc.* 1985, **107**, 5553-5555; (f) B. A. Hussein, W. Maturi, M. K.Rylands, A. N. Bismillah, Y. Wen, J. A. Aguilar, R. Ayub, C. Rankine and P. R. McGonigal, *Chem. Sci.* 2024, **15**, 14618-14624.

9. A. N. Bismillah, J. Sturala, B. M. Chapin, D. S. Yufit, P. Hodgkinson and P. R. McGonigal, *Chem. Sci.* 2018, **9**, 8631–8636.

10. C. Bhugra, and M. J. Pikal, *J. Pharm. Sci.* 2008, **97**. 1329-1349

11. A.De Silva, N. M. Felix, C. K. Ober, *Adv. Mater.* 2008, 20, 3355-3361

12. (a) Y. Chen,C. T. Powell and L. Yu, *J. Phys. Chem. B* 2017, **121**, 444−449; (b) R. Zallen, *The Physics of Amorphous Solids*, 1983, 23-32

14. Y. Sun, L. Zhu, K. L. Kearns, M.D. Ediger and L. Yu, *Proc. Natl. Acad. Sci. U. S. A.* 2011, **108**, 5990-5995.

15. (a) C. T. Powell, Y. Chen and L. Yu, *J. Non. Cryst. Solids* 2015, **429**, 122-128; (b) F. Chen, C.-H. Lam and O. K. C. Tsui, *Science* 2014, **343**,975-976; (b) L. Zhu, L. Wong and L. Yu, *Mol. Pharmaceutics.* 2008, **5**, 921–926; (c) L. Zhu, J. Jona, K. Nagapudi and T. Wu, *Pharm. Res.* 2010, **27**, 1558–1567; (d) V. Legrand, M. Descamps and C. Alba-Simionesco, *Thermochim. Acta.*1997, **307**, 77-83; (e) A. van der Wal, J. J. Mulder and R.J Gaymans, *Polymer* 1998, **39**, 5477-5481.

16. T. van de Ven and A. Soldera, *Advanced Materials*, 2020, 240-260.

17. A. N. Bismillah, T. G. Johnson, B. A. Hussein, A. T. Turley, P. K. Saha, H. C. Wong, J. A. Aguilar, D. S. Yufit and P. R. McGonigal, *Nature Chem.* 2023, **15**, 615–624.

18. W. M. Haynes, D. R. Lide and T. J. Bruno, *CRC Handbook of Chemistry and Physics*, 2016.

19. (a) O. E. Y. Kilinkissa, K. K. Govender and N. B. Báthori, *Cryst. Eng. Comm.* 2020, **22**, 2766-2771; (b) F. Ros and M. T. Molina, *Eur. J. Org. Chem.* 1999,**11**, 3179-3183; (c) S. Chen, H. Xi, R. F. Henry, I. Marsden and G. G. Z. Zhang, *Cryst. Eng. Comm.* 2010, **12**, 1485-1493.

20. (a) E. Donth, J. Korus, E. Hempel and M. Beiner, *Thermochimica acta.* 1997, **304**, 239-249; (b) P. Liu, L. Yu, H. Liu, L. Chen, and L. Li, *Carbohydr. Polym.* 2009, **77**, 250-253; (c) L. C. Thomas, *Am. Lab*. 2001, **33**, 26-31; (d) G. Wang and I. R. Harrison, *Thermochimica acta.* 1994, **231**, 203-213.

21. (a) R. Comesaña, M. A. Gómez, M. A. Álvarez and P. Eguía, *Thermochimica acta* 2012, **547**, 13-21; (b) R. Svoboda, L. P. Maqueda, V. Podzemná, A. Perejon and O. Svoboda, *J. Non. Cryst. Solids* 2020, **528**, 119738; (c) W. Sun, A. P. Vassilopoulos and T. Keller, *Int. J. Adhes. Adhes.* 2014, **52**, 31-39.

22. (a) I. M. Peterson and T. Y, Tien, *J. Am. Ceram. Soc.* 1995, **78**, 2345-2352; (b) A. Shyam, E. Lara-Curzio, A. Pandey, T. R. Watkins and K. L. More, *J. Am. Ceram. Soc.* 2012, **95**, 1682-1691.

23. J. K. Haleblian, *J. Pharm. Sci*. 1975, **64**, 1269-1288.

24. C. Y. Sun, S. X. Liu, D. D. Liang K. Z. Shao, Y. H. Ren and Z. M. Su, *J. Am. Ceram. Soc.* 2009, **131**, 1883-1888.

25. G. Schabert, R. Haase, J. Parris, L. Pala, A. Hery-Barranco, B. Spingler and U. Spitz, *Molecules* 2021, **26**, 2729.

CHAPTER 5
SUMMARY AND OUTLOOK

This Thesis has highlighted recent advances in the synthesis of fluxional carbon cages and understanding of their equilibria, dynamics and physical properties within different environments – all of which has been achieved in the period of October 2020 to April 2024. Research on these molecules since the 1960s have been mostly focused on its fundamental aspects such as synthetic methods and network analysis, and several explorations on their potential applications have come out over the last decade. The efficient preparation of target barbaralanes and bullvalenes in this Thesis are strongly based on the synthetic methods through gold(I) and Co(II) catalysts, established in 2012 and 2018 respectively.

Previous reports of the group in 2023 have demonstrated the control of dynamic sp^3-C stereochemistry of barbaralanes through covalent bonding. As a sequel, Chapter 2 of this Thesis described the control of barbaralane dynamic stereochemistry through noncovalent bonding. Host-guest interactions between barbaralanes and chiral macrocycles were studied in both solid and solution states. The co-crystals have clearly shown that the sp^3-C stereochemistry of barbaralanes is biased by the chiral β-CD in the solid state. Solution-state investigations are more complicated as the determination of enantioenrichment of the 'frozen' barbaralane remains challenging. ^{1}H-NMR titration studies showed that both β-CD monomers and dimers binds to guest barbaralanes with a 1:1 model, violating from the solid-state XRD results where a 2:2 self-sorting dimer was formed. The investigations revealed that the fluxional molecules can adapt their forms in response to the environment, which opens up their potential to be applied in molecular devices or sensors.

Chapter 3 is also a sequel to the previous work of the group: in 2018 the shape-selective crystallisations of barbaralane regioisomers were investigated, showing that the crystallisations are dictated by molecular size and shape instead of inherent energy levels. In this Chapter, a more systematic and broad study on the dynamic preferential crystallisations of barbaralanes is delivered. A series of novel barbaralane oligomers were synthesised and characterised, and their dynamic equilibria and crystallisations were analysed via XRD and computational modelling. The obtained XRD results showed that although various combinations of isomers are observed in the crystal structures, all barbaralane oligomers form racemic crystals containing 1:1 *R*- and *S*-barbaralyl cores, and the resolution of individual diastereoisomer can be influenced by

stereogenic information or the tendency of efficient packing. Computational studies confirmed that the resolution of isomers does not relate to inherent energy differences or specific noncovalent interactions, indicating that their crystallisation behaviours are mainly resulted from complementary isomerism and geometry. These results have revealed the regulations of dynamic resolution of barbaralanes and provided guidelines on predicting the crystal structures of not only barbaralanes but also other molecules with dynamic chirality. An additional discovery in this project is that a high proportion of barbaralanes exhibit high Z' values due to their awkward, irregular shapes, highlighting an exceptional regularity on the relatively rare high Z' crystals.

Chapter 4 is an attempt to investigate the thermal and mechanical properties of fluxional molecules and their potential in functional materials. Novel di-substituted bullvalenes were synthesised and their dynamic isomerism distributions were determined by low-temperature NMR spectroscopy. The structures are designed to possess both rigid and flexible components with different lengths for potential amorphous properties, and the non-fluxional analogue (BDT) of bullvalenes are also prepared as comparison. The initial hypothesis is that the fluxional bullvalene will have higher possibility to be amorphous. However, the polarised microscopy and DSC experiments gave unexpected results: both the bullvalenes and BDTs exhibit glass properties by showing glass transition in the DSC diagrams, and the bullvalenes showed fractures under cooling and solid-to-liquid peaks in the DSC diagrams while the BDTs did not, indicating that the fluxional bullvalenes exhibit some degrees of crystallinity, or higher coefficient of thermal expansion, and the non-fluxional BDTs are amorphous solids. These unexpected results indicated that the bullvalenes can spontaneously adjust their shapes to form ordered, stable solids, or even improved solubility and bioavailability, which is potentially valuable in the field of pharmaceuticals and functional materials.

In 2024 the fundamental aspects of fluxional molecules, including efficient synthesis and dynamic equilibria studies, have been intensively investigated and a solid background has been built for further explorations. Currently the bottleneck of investigating fluxional carbon cages is to precisely control and utilise their dynamic behaviour, and solution of these questions will lead to breakthrough in future applications.

PUBLISHED PAPERS

'*Correlated shapeshifting and configurational isomerization*' — B. A. Hussein, W. Maturi, M. K.Rylands, A. N. Bismillah, Y. Wen, J. A. Aguilar, R. Ayub, C. Rankine and P. R. McGonigal, *Chem. Sci.* 2024, **15**, 14618-14624.

Volume 15
Number 36
28 September 2024
Pages 14533–14990

Chemical Science

rsc.li/chemical-science

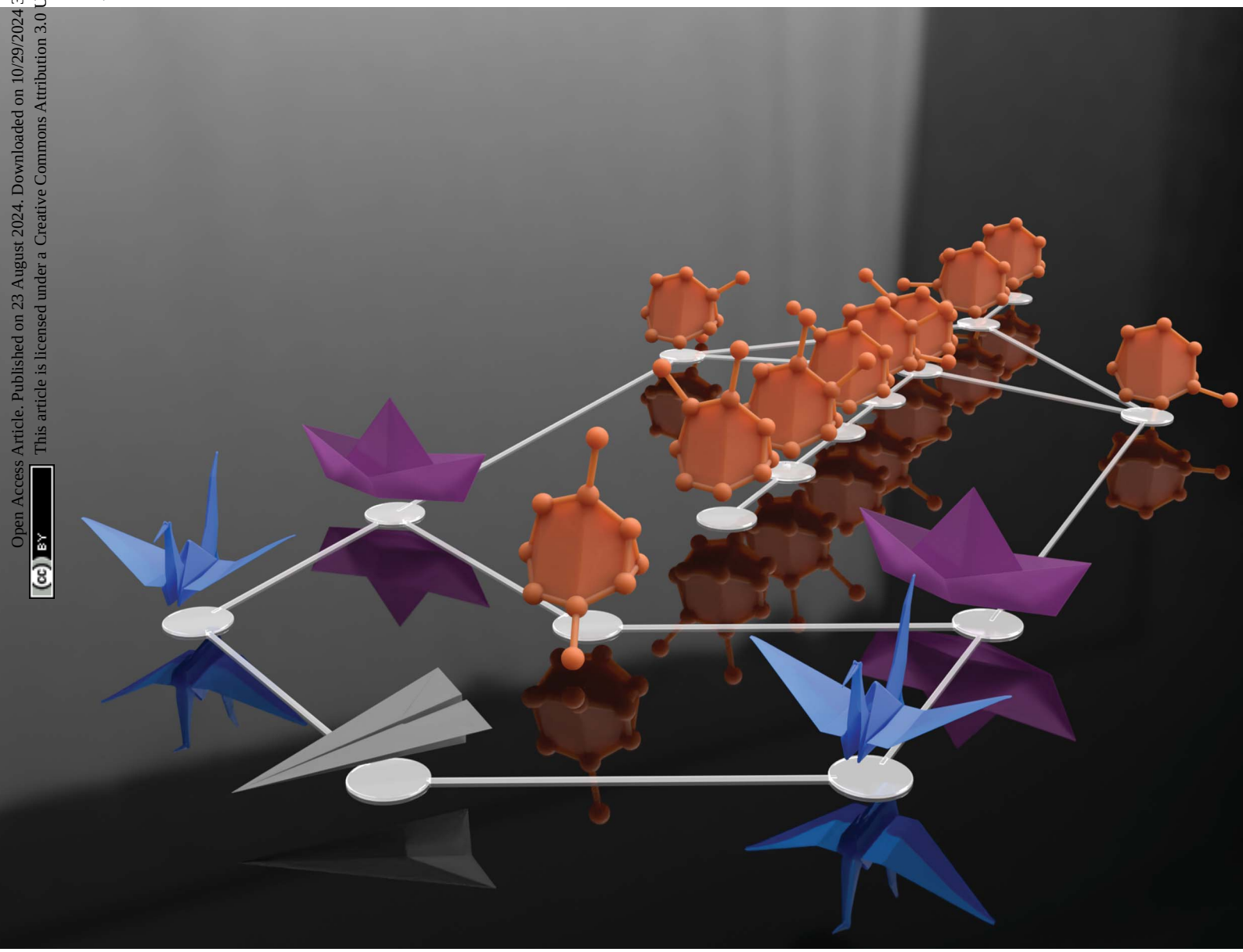

ISSN 2041-6539

ROYAL SOCIETY OF CHEMISTRY

EDGE ARTICLES
Paul R. McGonigal *et al.*
A guide to bullvalene stereodynamics
Correlated shapeshifting and configurational isomerization

Chemical Science

ROYAL SOCIETY OF CHEMISTRY

EDGE ARTICLE

Cite this: *Chem. Sci.*, 2024, **15**, 14618

All publication charges for this article have been paid for by the Royal Society of Chemistry

Received 6th June 2024
Accepted 23rd August 2024

DOI: 10.1039/d4sc03699a

rsc.li/chemical-science

Correlated shapeshifting and configurational isomerization†

Burhan A. Hussein,[a] William Maturi,[ab] Mary Kate Rylands,[a] Aisha N. Bismillah,[ab] Yuzhen Wen,[ab] Juan A. Aguilar,[a] Rabia Ayub,[b] Conor D. Rankine[b] and Paul R. McGonigal*[ab]

Herein we demonstrate that the rapid 'shapeshifting' constitutional isomerization of a substituted bullvalene is influenced by the *E*-to-*Z* configurational isomerization of a remote carbamate group, giving rise to correlated motion. We find that, while the *E*-configurational isomer of a bulky carbamate favors the *β*-bullvalene constitutional isomer, a noncovalent bonding interaction within the *Z*-carbamate tips the equilibrium toward the *γ*-bullvalene form. Using DFT modelling and NMR spectroscopy, this long-range interaction is identified as being between the bullvalene core and a pendant phenyl group connected to the carbamate. Coupling the constitutional changes of a bullvalene to a reciprocal configurational isomerization through a long-range interaction in this way will allow shapeshifting rearrangements to be exploited as part of collective motion in extended structures.

Introduction

The rapid, successive Cope rearrangements of bullvalenes[1] produce a series (Fig. 1a) of constitutional isomers. Recent advances in the synthesis of substituted derivatives,[2] alongside the development of related fluxional cages,[3] have led to renewed interest in exploiting these 'shapeshifting' structures as part of functional molecules and materials. Part of the appeal of using bullvalene derivatives is that they juxtapose the rigidity and well-defined bond angles[1e] that are typical of cage-like structures with the rapid structural dynamics that are commonly only found in flexible molecules. They exhibit 'rigid dynamics' at the single-molecule level.[4] Accordingly, investigations have been reported into bullvalene-containing fluorophores,[5] antibiotics,[6] small-molecule receptors,[7] transition metal complexes,[8] rigid-rod polymers,[9] and single-molecule junctions.[10]

By contrast, most organic structures, particularly those containing rotatable single bonds, rapidly sample stereoisomeric structures through changes in bond angles and dihedral angles.[11] The resulting isomerization (Fig. 1b) is not only influenced by local electronic and steric factors, but also by long-range interactions. Bond rotations of groups that are separated by several covalent bonds but are close together in space can, therefore, become correlated with one another,[12] *i.e.*, the isomerization or motion of one part of the molecule is coupled to a reciprocal conformational or configurational change in another part.

To exploit the shapeshifting rearrangements of bullvalenes in larger collective motions of extended structures,[12d–f] it is necessary to understand how their fluxional Cope rearrangements are influenced (Fig. 1c) by isomerization of surrounding groups. Here, we report the isomeric distribution of carbamate-functionalized bullvalenes **1** (Scheme 1) and demonstrate that,

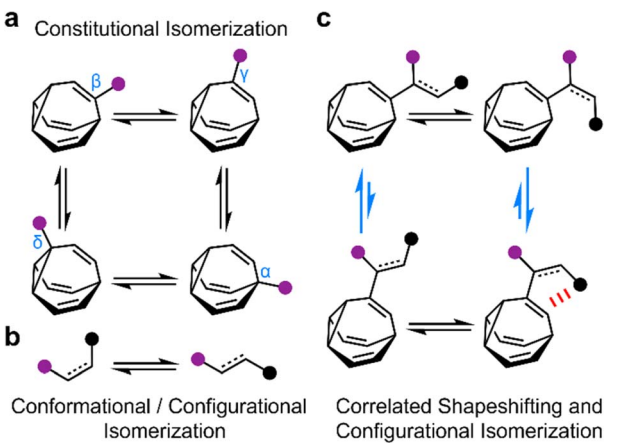

Fig. 1 The combination of (a) bullvalene shapeshifting rearrangements between constitutional isomers with (b) conformational and configurational changes by single bond rotations and *E*-to-*Z* isomerization are (c) correlated through noncovalent interactions (red) to bias the two bullvalene rearrangement equilibria in opposite directions (blue arrows). Black and purple circles represent appended functional groups.

[a]*Department of Chemistry, Durham University, Lower Mountjoy, Stockton Road, Durham, DH1 3LE, UK. E-mail: paul.mcgonigal@york.ac.uk*

[b]*Department of Chemistry, University of York, Heslington, York, YO10 5DD, UK*

† Electronic supplementary information (ESI) available. CCDC 2294194 (***E*,γ-1a**). For ESI and crystallographic data in CIF or other electronic format see DOI: https://doi.org/10.1039/d4sc03699a

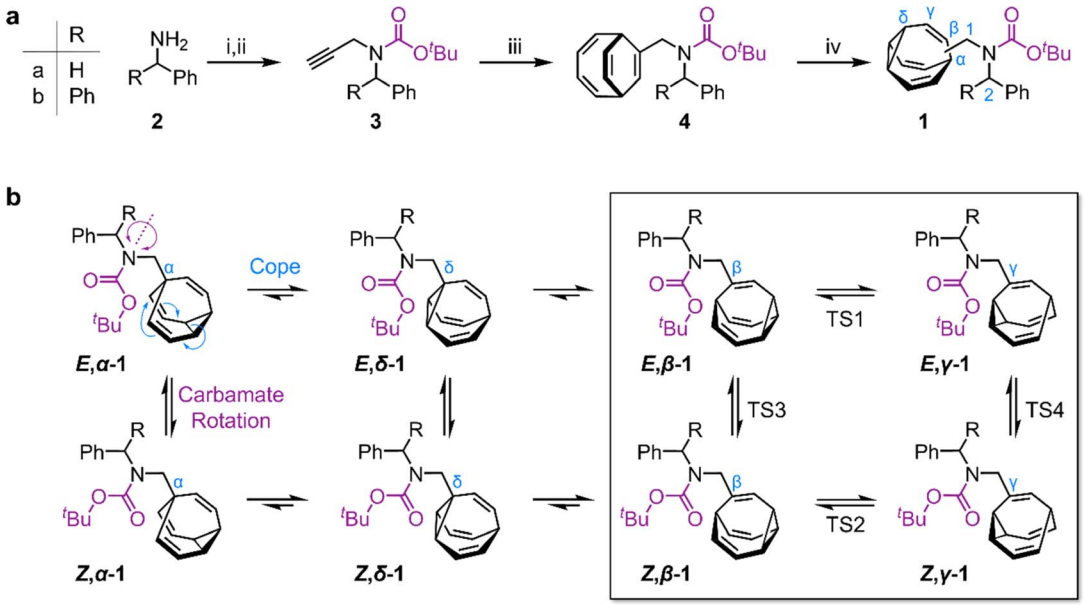

Scheme 1 (a) Synthesis of sterically crowded bullvalene carbamates. Reagents and conditions: (i) **2**, Boc_2O, NEt_3, CH_2Cl_2, rt, 24 h; (ii) **1**, NaH, DMF, 0 °C, 30 min, 2. propargyl bromide, rt, 5 h, 70% **3a** from **2a**, 64% **3b** from **2b**; (iii) **3**, cyclooctatetraene, $CoBr_2$(dppe), ZnI_2, Zn, TFE, 55 °C, 18 h, 55% **4a**, 50% **4b**; (iv) **4**, *hν* (365 nm), thioxanthone, THF, 25 °C, 3 h, 50% **1a**, 54% **1b**. DMF = dimethylformamide, dppe = 1,2-bis(diphenylphosphino)ethane, TFE = 2,2,2-trifluoroethanol, and THF = tetrahydrofuran. (b) Eight isomers interchange by Cope rearrangements (horizontal equilibria) and by rotation around the carbamate N–C bond (vertical equilibria).

even in this structurally simple case, conformational changes can become correlated to shapeshifting isomerization. For one of the compounds (benzhydryl derivative **1b**), we find that while the *E*-carbamate is most stable as its *β*-substituted bullvalene isomer, bond rotation to the *Z*-carbamate biases the bullvalene unit towards its *γ*-substituted form instead, *i.e.*, the energetics of bullvalene isomerization and carbamate rotation are coupled to one another. We show that through-space interactions subtly alter the energetics of the dynamic system. As part of this investigation, we have also assessed the extent to which this isomer distribution can be accurately modelled by comparing the calculated energies of the lowest energy conformers, as opposed to analyzing the full conformational landscape.

Results and discussion

We targeted (Scheme 1) tertiary carbamates **1a** and **1b** derived from benzylamine **2a** and benzhydrylamine **2b**, respectively. The partial double bond character of the carbamate C–N bond (*c.f.*, tertiary amide C–N bonds[13]) gives rise to *E*-to-*Z* configurational isomerization that can be slowed down and observed by dynamic NMR (DNMR) spectroscopy at low temperatures, which we reasoned would allow us to experimentally measure distributions of the configurational and constitutional isomers of **1a** and **1b**.

Starting from **2**, we performed (Scheme 1a) a sequence of carbamate formation, alkylation with propargyl bromide, and cobalt(I)-catalyzed [6 + 2] cycloaddition with cyclooctatetraene[2c,14] to produce bicyclo[4.2.2]deca-2,4,7,9-tetraene intermediates **4**. A final photochemical di-π-methane rearrangement step[15] using thioxanthone[2e] as a photosensitizer gave rise to the target bullvalenes **1**.

There are four possible constitutional isomers of **1** (Scheme 1b), which we label as *α*–*δ* according to the attachment point of the carbamate substituent to the bullvalene cage.[1e] Consecutive Cope rearrangements from the *α*-isomer lead to the *δ*-, *β*-, then *γ*-isomers in a reversible linear sequence. Alternatively, rotation around the carbamate C–N bond interconverts the *E*- and *Z*-configurational isomers. In combination, these two pathways give rise to a set of eight isomers (Scheme 1b).

^{1}H NMR Spectroscopic analysis of the benzyl derivative **1a** in $CDCl_3$ at 313 K (Fig. 2a) shows two broad resonances corresponding to the two sets of methylene protons, H1 and H2. Rapid chemical exchange at this temperature averages out the contributions from the different isomers to these two methylene resonances and causes the signals arising from the bullvalene methine groups, Hα–Hδ, to broaden and partially merge. At 219 K, the reduced rates of Cope rearrangements and carbamate rotation allow signals from the different species to be resolved.

Although there are eight possible isomers, the *α*- and *δ*-forms of mono-substituted bullvalenes are usually several kJ mol^{-1} higher in energy than the olefin-substituted *β*- and *γ*-forms,[16] so they are not present in sufficient concentrations to be observed. *β*-Substitution is usually preferred over *γ*-substitution by ∼1–2 kJ mol^{-1}.[2c] In keeping with this expectation, line fitting of the H1 peaks indicates (Fig. 1b) that four isomers are present in a 45 : 23 : 21 : 11 ratio, which can be assigned to ***Z,β*-1a**, ***E,β*-1a**, ***Z,γ*-1a**, and ***E,γ*-1a**, respectively, using 2D NMR (Fig. S15–S22†). Shape-selective crystallization‡[2e,17] from this mixture yields ***E,γ*-1a** (the least populated of the four isomers in solution) as the sole isomer

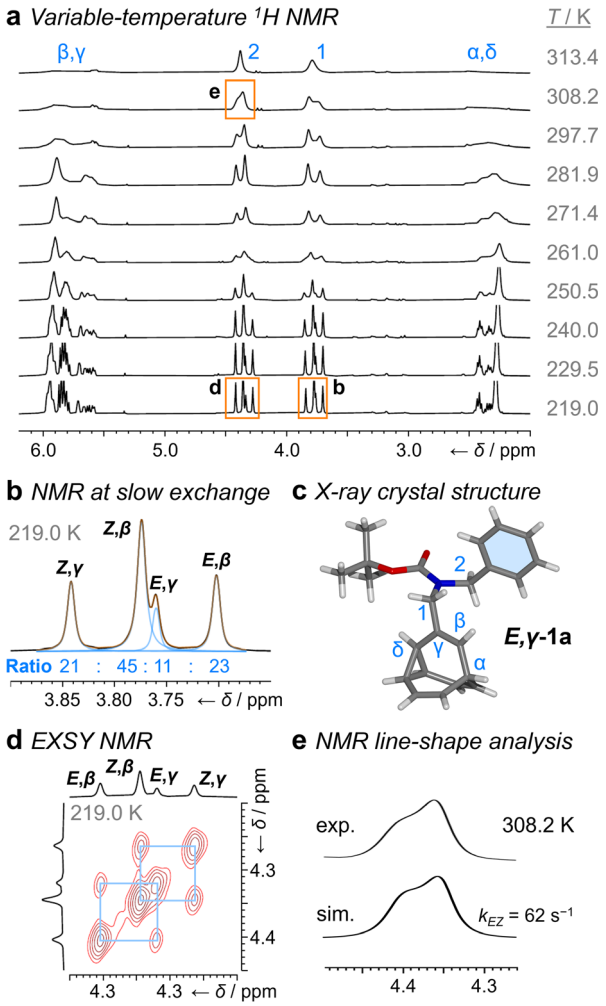

Fig. 2 ^{1}H DNMR (499 MHz, $CDCl_3$) and crystallographic analyses of **1a**. (a) Partial ^{1}H NMR spectra at temperatures ranging from 219 K to 313 K. Signals are assigned using the labels in Scheme 1. Regions in orange boxes correspond to those shown in panels b, d, and e. (b) Line fitting was used to deconvolute the H1 signals at 219 K. An overlay of the experimentally measured (black) and simulated (orange) traces is shown, including the integrals of the four simulated peaks (blue). (c) X-ray crystal structure of ***E*,γ-1a**. (d) Partial EXSY NMR spectrum (499 MHz, $CDCl_3$, t_m = 500 ms). Blue boxes indicate cross peaks arising from Cope rearrangements. (e) Line-shape analysis for the H2 signal at 308 K, comparing the experimentally measured (exp.) and simulated (sim.) line shapes. See Table S1† for simulation parameters.

in the solid state (Fig. 2c). In energetic terms (Table 1), the solution-phase population corresponds to small Gibbs energy biases ΔG_{exp} of ~1.3 kJ mol^{-1} toward both *β*-isomers over their γ-substituted counterparts, and ΔG_{exp} of ~1 kJ mol^{-1} for each *Z*-carbamate over its corresponding *E*-carbamate. Therefore, for **1a**, there is no evidence that the *E*/Z-state of the molecule substantially changes the energetics of *β*/γ-isomerization, or *vice versa*. The two isomerization processes do not appear to be correlated.

This system does, however, provide an unusual case of reversible covalent changes occurring in a molecule more rapidly than its bond rotation, *i.e.*, the carbamate isomerization of **1a** proceeds at a slower rate than its Cope rearrangement. Using ^{1}H–^{1}H Exchange NMR Spectroscopy[18] (EXSY) at 219 K (Fig. 2d), we found that the Cope rearrangements pass through transition states (TS1 and TS2, Scheme 1b) that are ~55–57 kJ mol^{-1} above the lowest energy isomer, ***Z*,*β*-1a**, which is typical[19] for bullvalene constitutional isomerization. There are no cross peaks visible between *E*- and *Z*-isomers at this temperature because of the slow carbamate rotation rate. At the higher temperature of 308 K, ^{1}H NMR line-shape analysis (Fig. 2e) gives an averaged rate of carbamate rotation, k_{EZ}, of 62 s^{-1}, indicating that TS3 and TS4 lie almost 10 kJ mol^{-1} higher than TS1 at ΔG_{exp} of ~65 kJ mol^{-1} relative to ***Z*,*β*-1a** (Table 1).

Unlike **1a**, the increased steric crowding present in the benzhydryl derivative **1b** leads to correlated isomerization. The additional phenyl ring of **1b** experiences long-range interactions with the bullvalene that influence the solution-phase isomerization equilibria. There are some key clues to this behavior in the variable-temperature NMR spectra (Fig. 3a). Crucially, the distribution of H1 methylene resonances (Fig. 3b) has been altered substantially relative to **1a**. The ***Z*,*β*-1b**, ***E*,*β*-1b**, ***Z*,γ-1b**, and ***E*,γ-1b** isomers are present in a 27 : 16 : 48 : 8 ratio, as assigned by 2D NMR (Fig. S15–S22†). Therefore, the *Z*,γ-isomer is the most favored form of **1b**, despite being only the third most populated isomer of **1a**. The changes in relative Gibbs energy (G_{rel}) between the **1a** and **1b** isomers is summarized graphically as a potential energy diagram in Fig. 4. A structural change from a hydrogen substituent to a phenyl group at a remote site has overridden the inherent preference[2c,16] for the bullvalene *β*-isomer in the reaction network, but only when the carbamate is in its *Z*-form (Fig. 5a). The benzhydryl carbamate of **1b** also rotates at a faster rate than the benzyl carbamate of **1a**, exhibiting near-identical energy barriers of ~54–58 kJ mol^{-1} for the four isomerization processes (Table 1).

To understand the unusual constitutional isomer distribution of **1b**, we carried out DFT modelling. We generated all the constitutional isomers of **1a** and **1b** and carried out distance-geometry-based generation of their configurational and conformational isomers before optimizing the geometries at the PBE0-D3/def2-SV(P) level of theory.[1e,20] As there are several rotatable single bonds in the structure of **1**, each of the isomers observed by low-temperature NMR itself represents a rapidly interconverting population of conformers. The relative energies of all the isomers are tabulated in Tables S3 and S4.† Cartesian coordinates are available in the ESI.† To take one representative example, there are six conformers of ***Z*,*β*-1a** spanning a range of ~16 kJ mol^{-1} in energy, of which the two lowest energy structures are within just 2.5 kJ mol^{-1} of one another.

Despite there being numerous different structures contributing to the overall energetics of *E*-to-*Z* and *β*-to-γ isomerization, the experimentally observed populations, p_{exp}, can be approximated reasonably well by analyzing just the lowest energy conformers (Table 1). For **1a**, the calculated energies, ΔG_{calc1}, of the lowest energy conformer for each of the four observable isomers gives a Boltzmann distribution, p_{calc1}, that matches closely to p_{exp}. For **1b**, however, this simplified approach incorrectly predicts that more of ***E*,*β*-1b** is present than ***Z*,*β*-1b**. Instead, it is necessary to perform a global

Table 1 Populations and relative Gibbs energies of the isomers present in the dynamic mixtures and their transition states

	1a, p/%			**1a**, ΔG/kJ mol^{-1}			**1b**, p/%			**1b**, ΔG/kJ mol^{-1}		
State	p_{exp}[a]	p_{calc1}[c]	p_{calcG}[d]	ΔG_{exp}[a]	ΔG_{calc1}[f]	ΔG_{calcG}[h]	p_{exp}[a]	p_{calc1}[c]	p_{calcG}[d]	ΔG_{exp}[a]	ΔG_{calc1}[f]	ΔG_{calcG}[h]
E,α	—[b]	<0.1	<0.1	—[b]	25.5	25.4	—[b]	<0.1	<0.1	—[b]	34.5	34.0
Z,α	—[b]	<0.1	<0.1	—[b]	23.1	23.2	—[b]	<0.1	<0.1	—[b]	26.5	26.8
E,β	23	18	22	1.2	1.7	1.4	16	24	23	1.9	1.4	1.2
Z,β	45	47	46	0.0	0.0	1.0	27	18	28	1.0	1.5	0.8
E,γ	11	10	13	2.5	2.8	2.3	8	6	5	3.2	3.8	3.8
Z,γ	21	14	18	1.4	2.2	1.7	48	51	44	0.0	0.0	0.0
E,δ	—[b]	<1	<1	—[b]	8.7	8.2	—[b]	<0.1	<0.1	—[b]	14.8	14.1
Z,δ	—[b]	<1	1	—[b]	7.2	6.8	—[b]	<1	<1	—[b]	9.5	8.8
TS1	—	—	—	55.6	—[g]	—[g]	—	—	—	54.5	—[g]	—[g]
TS2	—	—	—	57.2	—[g]	—[g]	—	—	—	57.4	—[g]	—[g]
TS3	—	—	—	64.9[e]	—[g]	—[g]	—	—	—	54.8	—[g]	—[g]
TS4	—	—	—	—	—[g]	—[g]	—	—	—	55.3	—[g]	—[g]

[a] Measured at 219 K in $CDCl_3$. [b] The population of α- and δ-isomers is below the detection limit of the equipment used to acquire ^{1}H NMR spectra. [c] Population calculated as a Boltzmann distribution based on the DFT calculated energies of the most stable conformer for each constitutional and configurational isomer (ΔG_{calc1}). [d] Population calculated as a global Boltzmann distribution by summing the populations of all accessible conformers calculated for each constitutional and configurational isomer (ΔG_{calcG}). [e] Apparent Gibbs energy barrier for carbamate rotation (weighted average of TS3 and TS4) at 308 K. [f] Relative Gibbs energies of only the most stable conformer for each isomer calculated at 219 K using PBE0-D3/def2-SV(P).[20i–k,p] [g] Transition states were not modelled. [h] Effective relative Gibbs energies based on the DFT calculated global Boltzmann distribution (p_{calcG}) for the purpose of comparison with ΔG_{exp}.

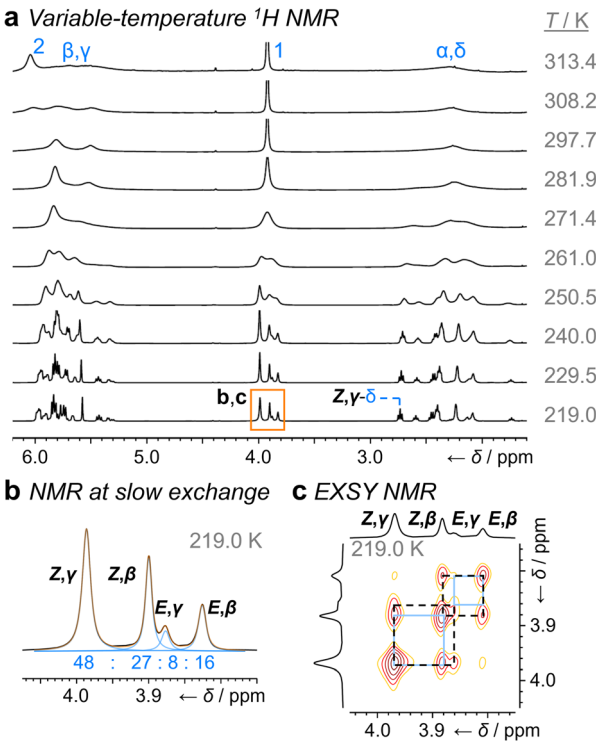

Fig. 3 ^{1}H DNMR analysis (499 MHz, $CDCl_3$) of **1b**. (a) Partial ^{1}H NMR spectra at temperatures ranging from 219 K to 313 K. Signals are assigned using the labels in Scheme 1. The region in an orange box corresponds to that shown in panels b and c. (b) Line fitting was used to deconvolute the H1 signals at 219 K. An overlay of the experimentally measured (black) and simulated (orange) traces is shown, including the integrals of the four simulated peaks (blue). (c) Partial EXSY NMR spectrum (499 MHz, $CDCl_3$, t_m = 500 ms). Blue boxes indicate cross peaks arising from Cope rearrangements. Dashed black boxes indicate cross peaks arising from carbamate rotation.

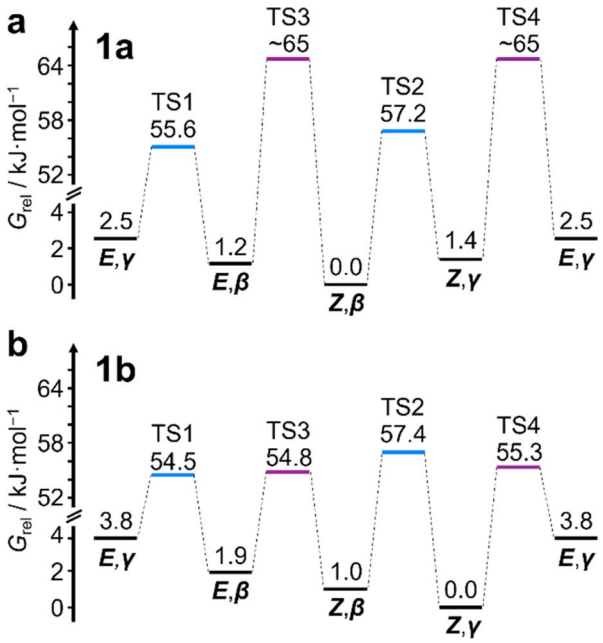

Fig. 4 Potential energy diagrams for the observed isomers of (a) **1a** and (b) **1b**, showing the relative stabilization of *Z*,γ-**1b**. Transition states in blue correspond to Cope rearrangement steps, those in purple correspond to *E*/*Z*-isomerisation.

Boltzmann population analysis (giving p_{calcG}) that takes into account all the accessible conformers in order to reproduce the experimentally observed hierarchy of isomers. This observation indicates that for bullvalene derivatives with several rotatable single bonds, accurate modelling of the shapeshifting rearrangements requires consideration of the full energetic landscape of accessible conformers.

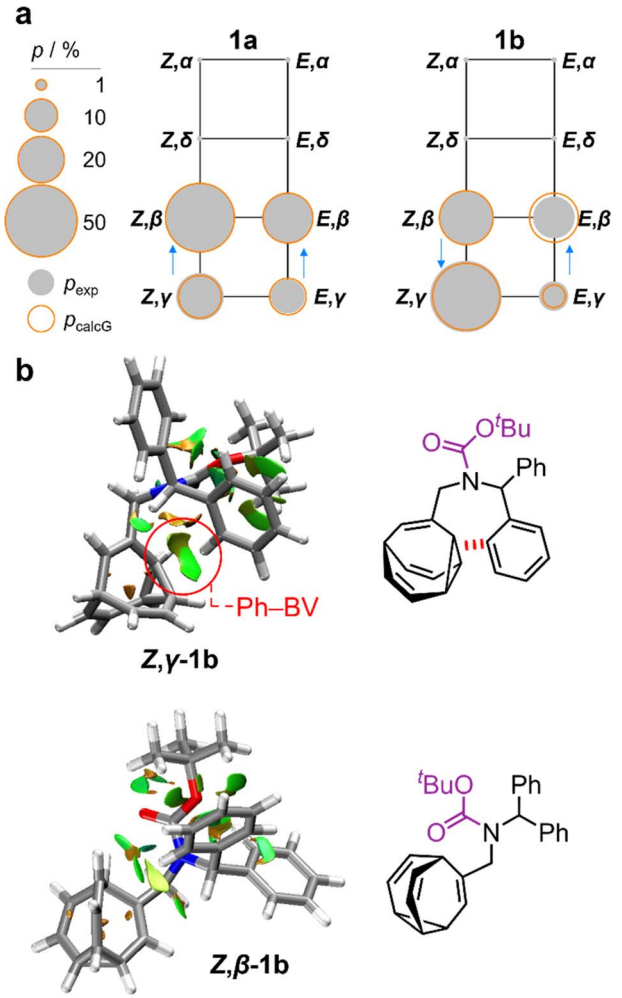

Fig. 5 (a) Network diagrams for the isomerization of **1a** and **1b** showing the experimentally measured populations (p_{exp}) of the β- and γ-isomers at 219 K as filled grey circles and the calculated populations (p_{calcG}) as hollow orange circles. According to DFT calculations, the α- and δ-isomers are present in <1%. Blue arrows point to the major species of each Cope rearrangement process, highlighting that the preference for the β- and γ-bullvalene isomers is correlated to the *E*-to-*Z* isomerization of **1b**. (b) NCI plots [LC-PBE/def2-TZVP][22] of ***Z*,γ-1b** and ***Z*,β-1b** showing the increased Ph–BV interaction in ***Z*,γ-1b**.

Noncovalent interaction (NCI) plots[21] generated using the DFT-optimized geometries reveal (Fig. 5b and S26–S29†) the interactions that are responsible for the correlated isomerization of **1b**. In addition to several close contacts between the crowded *tert*-butyl, carbonyl, and phenyl groups, which are present in all of the isomers, the lowest energy conformer of ***Z*,γ-1b** shows evidence of substantial interaction between an *ortho*-hydrogen of one phenyl ring with the bullvalene cyclopropyl ring (Ph–BV interaction, Fig. 5b). This long-range interaction is less significant in the NCI analyses of the other **1b** isomers (Fig. S26–S29†), such as ***Z*,β-1b** (Fig. 5b). Experimental evidence for the interaction in ***Z*,γ-1b** is apparent in its low-temperature ^{1}H NMR spectrum (Fig. 3a) as its Hδ resonance is shifted downfield relative to the Hδ signals of the other isomers of **1b**, which is indicative of deshielding caused by the aromatic ring current. The NOESY NMR spectrum (Fig. S23†) also confirms Hδ undergoes through-space interaction with a phenyl group. Although this Ph–BV interaction appears to be a relatively weak van der Waals contact, the combination of it together with other subtle differences in the attractive and repulsive noncovalent bonding interactions present in **1b** is evidently sufficient to provide enough of an energetic bias to overcome the ~1–2 kJ mol^{-1} preference for the β-isomer.

Conclusions

In summary, the shapeshifting constitutional rearrangements of even structurally simple bullvalenes can be influenced by a complementary, remote isomerization process. Given that the energetic differences between bullvalene isomers are often as little as a few kJ mol^{-1}, relatively subtle noncovalent bonding interactions, including weak van der Waals contacts, are sufficient to reshuffle the proportions of each isomer. In the system presented here, the introduction of an additional phenyl ring to the structure of **1a** causes the *Z*,γ-isomer to change from being the third most populous to being the major species of **1b** as a result of a Ph–BV interaction. Programming in switchable long-range interactions may allow for control to be exercised over the large number of constitutional isomers that arise in multi-substituted bullvalene derivatives.

Data availability

Experimental synthetic procedures, characterization data and theoretical calculation results are available in the ESI.†

Author contributions

Conceptualization: BAH, PRM. Investigation: BAH, WM, MKR, ANB, JAA, CR. Writing: BAH, WM, ANB, YW, RA, PRM.

Conflicts of interest

There are no conflicts to declare.

Acknowledgements

B. A. H. acknowledges an EPSRC SOFI CDT Studentship (EP/L015536/1) and an NSERC Scholarship. W. M. (EP/T518001/1), R. A (EP/X021564/1) and P. R. M (EP/V047817/2, EP/V040049/2) thank the EPSRC for funding. A. N. B. and P. R. M. acknowledge a Leverhulme Trust Research Project Grant (RPG-2020-218). Y. W. thanks the Chinese Scholarship Council. We thank Dr Dmitry Yufit for performing X-ray crystallography. We acknowledge the University of York High Performance Computing service, Viking.

Notes and references

‡ The energetics of crystal packing can outweigh the small solution-phase energetic bias towards certain isomers within fluxional mixtures.[2e,17]

1 (*a*) W. v. E. Doering and W. R. Roth, *Tetrahedron*, 1963, **19**, 715–737; (*b*) G. Schröder, *Angew. Chem., Int. Ed. Engl.*, 1963, **2**, 481–482; (*c*) S. Ferrer and A. Echavarren, *Synthesis*, 2019, **51**, 1037–1048; (*d*) A. N. Bismillah, B. M. Chapin, B. A. Hussein and P. R. McGonigal, *Chem. Sci.*, 2020, **11**, 324–332; (*e*) R. A. Ives, W. Maturi, M. T. Gill, C. D. Rankine and P. R. McGonigal, *Chem. Sci.*, 2024, DOI: **10.1039/D4SC03700F**.

2 (*a*) A. R. Lippert, J. Kaeobamrung and J. W. Bode, *J. Am. Chem. Soc.*, 2006, **128**, 14738–14739; (*b*) S. Ferrer and A. M. Echavarren, *Angew. Chem., Int. Ed.*, 2016, **55**, 11178–11182; (*c*) O. Yahiaoui, L. F. Pašteka, B. Judeel and T. Fallon, *Angew. Chem., Int. Ed.*, 2018, **57**, 2570–2574; (*d*) O. Yahiaoui, L. F. Pašteka, C. J. Blake, C. G. Newton and T. Fallon, *Org. Lett.*, 2019, **21**, 9574–9578; (*e*) H. D. Patel, T. H. Tran, C. J. Sumby, L. F. Pašteka and T. Fallon, *J. Am. Chem. Soc.*, 2020, **142**, 3680–3685; (*f*) A. Sanchez, V. M. Gonzalez, J. Sakamoto, A. Gurajapu and T. J. Maimone, *J. Am. Chem. Soc.*, 2024, **146**, 17573–17579.

3 (*a*) P. R. McGonigal, C. de León, Y. Wang, A. Homs, C. R. Solorio-Alvarado and A. M. Echavarren, *Angew. Chem., Int. Ed.*, 2012, **51**, 13093–13096; (*b*) X. Wang, O. Shyshov, M. Hanževački, C. M. Jäger and M. von Delius, *J. Am. Chem. Soc.*, 2019, **141**, 8868–8876; (*c*) M. Sanz-Novo, M. Mato, Í. León, A. M. Echavarren and J. L. Alonso, *Angew. Chem., Int. Ed.*, 2022, **61**, e202117045; (*d*) A. Sanchez and T. J. Maimone, *J. Am. Chem. Soc.*, 2022, **144**, 7594–7599; (*e*) A. Sanchez, A. Gurajapu, W. Guo, W.-Y. Kong, C. J. Laconsay, N. S. Settineri, D. J. Tantillo and T. J. Maimone, *J. Am. Chem. Soc.*, 2023, **145**, 13452–13461; (*f*) A. N. Bismillah, T. G. Johnson, B. A. Hussein, A. T. Turley, P. K. Saha, H. C. Wong, J. A. Aguilar, D. S. Yufit and P. R. McGonigal, *Nat. Chem.*, 2023, **15**, 615–624.

4 (*a*) H. Deng, M. A. Olson, J. F. Stoddart and O. M. Yaghi, *Nat. Chem.*, 2010, **2**, 439–443; (*b*) S. Krause and J. V. Milić, *Commun. Chem.*, 2023, **6**, 151; (*c*) P. K. Saha, T. Tran Ngoc, P. R. McGonigal and J. F. Teichert, *Nat. Synth.*, 2024, **3**, 684–697.

5 C. Dohmen, H. Ihmels and T. Paululat, *Eur. J. Org Chem.*, 2022, **2022**, e202201172.

6 A. Ottonello, J. A. Wyllie, O. Yahiaoui, S. Sun, R. A. Koelln, J. A. Homer, R. M. Johnson, E. Murray, P. Williams, J. R. Bolla, C. V. Robinson, T. Fallon, T. P. Soares da Costa and J. E. Moses, *Proc. Natl. Acad. Sci. U. S. A.*, 2023, **120**, e2208737120.

7 (*a*) K. K. Larson, M. He, J. F. Teichert, A. Naganawa and J. W. Bode, *Chem. Sci.*, 2012, **3**, 1825; (*b*) J. F. Teichert, D. Mazunin and J. W. Bode, *J. Am. Chem. Soc.*, 2013, **135**, 11314–11321.

8 (*a*) A. Birve, H. D. Patel, J. R. Price, W. M. Bloch and T. Fallon, *Angew. Chem., Int. Ed.*, 2021, **61**, e202115468; (*b*) C. Dohmen, T. Paululat and H. Ihmels, *Chem.–Eur. J.*, 2024, **30**, e202304311.

9 (*a*) M. N. Pomfret, P. B. Sun, Z. Huang, A. C. Freund, T. Miyoshi and M. R. Golder, *Angew. Chem., Int. Ed.*, 2023, **62**, e202301695; (*b*) P. B. Sun, M. N. Pomfret, M. J. Elardo, A. Suresh, Á. Rentería-Gómez, R. F. Lalisse, S. Keating, C. Chen, Shayna, L. Hilburg, P. Chakma, Y. Wu, R. C. Bell, S. J. Rowan and M. R. Golder, *J. Am. Chem. Soc.*, 2024, **146**, 19229–19238.

10 J. R. Reimers, T. Li, A. P. Birvé, L. Yang, A. C. Aragonès, T. Fallon, D. S. Kosov and N. Darwish, *Nat. Commun.*, 2023, **14**, 6089.

11 A. Mazzanti and D. Casarini, *Wiley Interdiscip. Rev.: Comput. Mol. Sci.*, 2012, **2**, 613–641.

12 (*a*) K. Mislow, *Acc. Chem. Res.*, 1976, **9**, 26–33; (*b*) M. Oki, *Angew. Chem., Int. Ed. Engl.*, 1976, **15**, 87–93; (*c*) Z. Rappoport and S. E. Biali, *Acc. Chem. Res.*, 1997, **30**, 307–314; (*d*) S. Erbas-Cakmak, D. A. Leigh, C. T. McTernan and A. L. Nussbaumer, *Chem. Rev.*, 2015, **115**, 10081–10206; (*e*) D. Dattler, G. Fuks, J. Heiser, E. Moulin, A. Perrot, X. Yao and N. Giuseppone, *Chem. Rev.*, 2020, **120**, 310–433; (*f*) S. Corra, C. de Vet, M. Baroncini, A. Credi and S. Silvi, *Chem*, 2021, **7**, 2137–2150; (*g*) C. L. F. Van Beek and B. L. Feringa, *J. Am. Chem. Soc.*, 2024, **146**, 5634–5642.

13 (*a*) E. R. Johnston, R. Fortt and J. C. Barborak, *Magn. Reson. Chem.*, 2000, **38**, 932–936; (*b*) J. Clayden and J. H. Pink, *Angew. Chem., Int. Ed.*, 1998, **37**, 1937–1939; (*c*) R. A. Bragg and J. Clayden, *Org. Lett.*, 2000, **2**, 3351–3354; (*d*) R. A. Bragg, J. Clayden, G. A. Morris and J. H. Pink, *Chem.–Eur. J.*, 2002, **8**, 1279–1289.

14 M. Achard, M. Mosrin, A. Tenaglia and G. Buono, *J. Org. Chem.*, 2006, **71**, 2907–2910.

15 (*a*) M. Jones and L. T. Scott, *J. Am. Chem. Soc.*, 1967, **89**, 150–151; (*b*) M. Jones, S. D. Reich and L. T. Scott, *J. Am. Chem. Soc.*, 1970, **92**, 3118–3126.

16 J. F. M. Oth, R. Merényi, J. Nielsen and G. Schröder, *Chem. Ber.*, 1965, **98**, 3385–3400.

17 (*a*) A. N. Bismillah, J. Sturala, B. M. Chapin, D. S. Yufit, P. Hodgkinson and P. R. McGonigal, *Chem. Sci.*, 2018, **9**, 8631–8636; (*b*) J. Nyman and G. M. Day, *CrystEngComm*, 2015, **17**, 5154–5165.

18 K. Nikitin and R. O'Gara, *Chem.–Eur. J.*, 2019, **25**, 4551–4589.

19 R. Merényi, J. F. M. Oth and G. Schröder, *Chem. Ber.*, 1964, **97**, 3150–3161.

20 (*a*) bullviso, 2024, **https://gitlab.com/conorrankine/bullviso**; (*b*) S. Riniker and G. A. Landrum, *J. Chem. Inf. Model.*, 2015, **55**, 2562–2574; (*c*) S. Wang, J. Witek, G. A. Landrum and S. Riniker, *J. Chem. Inf. Model.*, 2020, **60**, 2044–2058; (*d*) RDKit: Open-Source Cheminformatics. **https://rdkit.org**; (*e*) RDKit, 2023, **https://github.com/rdkit/rdkit**; (*f*) S. Grimme, C. Bannwarth and P. Shushkov, *J. Chem. Theory Comput.*, 2017, **13**, 1989–2009; (*g*) C. Bannwarth, S. Ehlert and S. Grimme, *J. Chem. Theory Comput.*, 2019, **15**, 1652–1671; (*h*) C. Bannwarth, E. Caldeweyher, S. Ehlert, A. Hansen, P. Pracht, J. Seibert, S. Spicher and S. Grimme, *Wiley Interdiscip. Rev.: Comput. Mol. Sci.*, 2020, **11**, e01493; (*i*) J. P. Perdew, K. Burke and M. Ernzerhof, *Phys. Rev. Lett.*, 1996, **77**, 3865–3868; (*j*) J. P. Perdew, K. Burke and M. Ernzerhof, *Phys. Rev. Lett.*, 1997, **78**, 1396; (*k*) C. Adamo and V. Barone, *J. Chem. Phys.*, 1999, **110**, 6158–6169; (*l*) S. Grimme, J. Antony, S. Ehrlich and H. Krieg, *J. Chem.*

Phys., 2010, **132**, 154104; (*m*) F. Neese, *Wiley Interdiscip. Rev.: Comput. Mol. Sci.*, 2012, **2**, 73–78; (*n*) F. Neese, *Wiley Interdiscip. Rev.: Comput. Mol. Sci.*, 2017, **8**, e1327; (*o*) F. Neese, F. Wennmohs, U. Becker and C. Riplinger, *J. Chem. Phys.*, 2020, **152**, 224108; (*p*) F. Weigend and R. Ahlrichs, *Phys. Chem. Chem. Phys.*, 2005, **7**, 3297–3305; (*q*) F. Weigend, *Phys. Chem. Chem. Phys.*, 2006, **8**, 1057–1065.

21 (*a*) H. Iikura, T. Tsuneda, T. Yanai and K. Hirao, *J. Chem. Phys.*, 2001, **115**, 3540–3544; (*b*) A. Najibi, M. Casanova-Paez and L. Goerigk, *J. Phys. Chem. A*, 2021, **125**, 4026–4035.

22 (*a*) E. R. Johnson, S. Keinan, P. Mori-Sánchez, J. Contreras-García, A. J. Cohen and W. Yang, *J. Am. Chem. Soc.*, 2010, **132**, 6498–6506; (*b*) J. Contreras-García, E. R. Johnson, S. Keinan, R. Chaudret, J.-P. Piquemal, D. N. Beratan and W. Yang, *J. Chem. Theory Comput.*, 2011, **7**, 625–632.